Development Of Improved Models And Designs For Coated-Particle Gas Reactor Fuels

Final Report Under The International Nuclear Energy Research Initiative (I-NERI)

A Collaboration of Work Performed by: The Idaho National Engineering and Environmental Laboratory (INEEL), The French Centre d'Etude Atomique (CEA), and The Massachusetts Institute of Technology (MIT)

December 2004

Idaho National Engineering and Environmental Laboratory
Bechtel BWXT Idaho, LLC

INEEL

Home of Science and Engineering Solutions

DEVELOPMENT OF IMPROVED MODELS AND DESIGNS FOR COATED-PARTICLE GAS REACTOR FUELS

**Final Report Under The International Nuclear
Energy Research Initiative (I-NERI)**

A Collaboration of Work Performed by:
The Idaho National Engineering and Environmental Laboratory (INEEL),
The French Centre d'Étude Atomique (CEA),
and The Massachusetts Institute of Technology (MIT)

December 2004

Idaho National Engineering and Environmental Laboratory
Idaho Falls, Idaho 83415

DEVELOPMENT OF IMPROVED MODELS AND DESIGNS FOR COATED-PARTICLE GAS REACTOR FUELS:

Final Report

Lead U.S. Investigating Organization:	**Idaho National Engineering and Environmental Laboratory (INEEL)**
Lead U.S. Principal Investigator:	**David Petti**
Lead Collaborating Investigating Organization:	**Centre Étude Atomique (CEA)**
Lead Collaborating Principal Investigator:	**Philippe Martin/ Mayeul Phélip**
Other Collaborating Institutions:	**Massachusetts Institute of Technology (MIT)**
Other Collaborating Principal Investigator:	**Ronald Ballinger**

DEVELOPMENT OF IMPROVED MODELS AND DESIGNS FOR COATED-PARTICLE GAS REACTOR FUELS: FINAL REPORT

EXECUTIVE SUMMARY

The objective of this INERI project was to develop improved fuel behavior models for gas reactor coated-particle fuels and to explore improved coated-particle fuel designs that could be used reliably at very high burnups and potentially in gas-cooled fast reactors. Project participants included the Idaho National Engineering Laboratory (INEEL), Centre Étude Atomique (CEA), and the Massachusetts Institute of Technology (MIT). To accomplish the project objectives, work was organized into the following five tasks:

- Task 1, information relative to material property databases and existing fuel models were exchanged,

- Task 2, an integrated fuel model was developed that includes the effects of multi-dimensional failure mechanisms and phenomena not beforehand in the models,

- Task 3, deterministic fuel performance calculations were performed to evaluate the capacity of classical TRISO fuel to reach extended burnups, and thereby establish requirements for fuel materials,

- Task 4, the feasibility of using particle fuel in a fast neutron environment was investigated, and

- Task 5, an irradiation testing strategy for prototype fuel particles was developed.

The CEA and INEEL exchanged their databases on coated particle fuel material property correlations. Comparison between the U.S. and European data revealed many similarities and a few important differences. These correlations are used in model predictions of fuel performance during irradiation. Such predictions are useful to understand the interplay of important phenomena that could occur outside of the existing irradiation envelope of temperature, burnup and fast neutron fluence. After reviewing and assessing the correlations, it was observed that property data are generally lacking for materials exposed to high fuel burnups and neutron fluences. This current lack of data will introduce uncertainty into model predictions of fuel performance. Several key material properties that affect fuel performance were identified and briefly described.

The INEEL continued from earlier efforts to develop an integrated fuel performance model

called PARFUME with the objective of physically describing both the mechanical and physico-chemical behavior of particle fuel under irradiation. In addition to the traditional pressure vessel failure mode, the model includes multi-dimensional failure mechanisms. These mechanisms include particle failure due to shrinkage cracks in the inner pyrolytic carbon (IPyC) layer (Figure i), partial debonding between the IPyC and SiC layers, particle asphericity (Figure ii), and kernel migration. A statistical approach is used to simulate detailed finite element calculations and allows for changes in fuel design attributes (e.g. thickness of layers, dimensions of kernel) as well as changes in important material properties which increase the flexibility of the code.
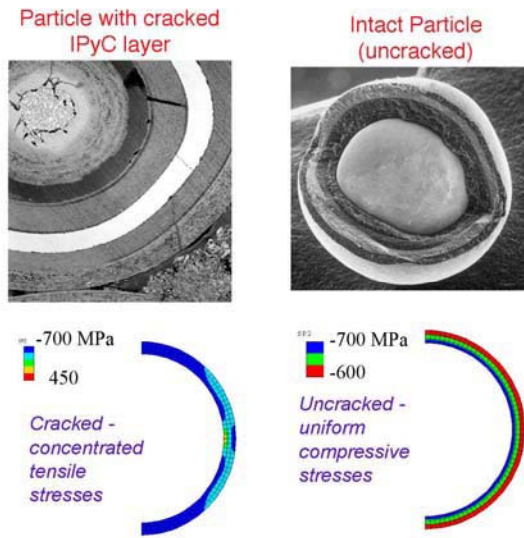

Figure ii. Effective particle asphericity on particle failure probability.

Figure i. Stress distributions in normal (uncracked) and cracked particles.

Time-dependent thermal modeling capabilities for either spherical or cylindrical fuel elements and for individual fuel particles are included in PARFUME. The thermal model accounts for changes in fission gas as well as shrinkage and swelling of the particle layers and kernel with the potential for formation of a gap between the buffer and IPyC layer. This effect is illustrated in the figures iii and iv. The CEA has developed a finite element, particle fuel simulation model called ATLAS (Figure v). This model and the material properties with constitutive relationships have been incorporated into a more general software platform called Pleiades. Pleiades is able to analyze various fuel

geometries from single particles to fuel elements and is able to account for the statistical variability in coated particle fuel. Preliminary benchmark calculations show good agreement between the French and U.S. models.
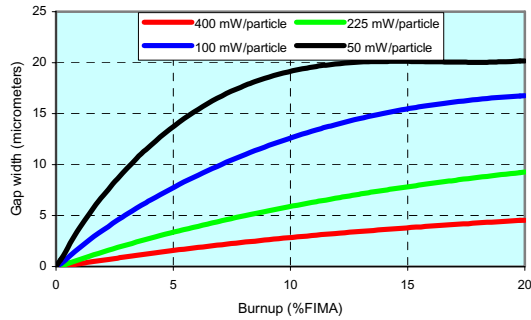

Figure iii. Gap development in a prismatic block core as a function of burnup and particle power.
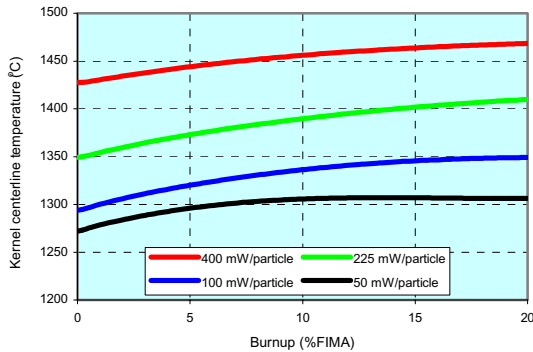

Figure iv. Kernel centerline temperatures in a prismatic block core as a function of burnup and particle power.
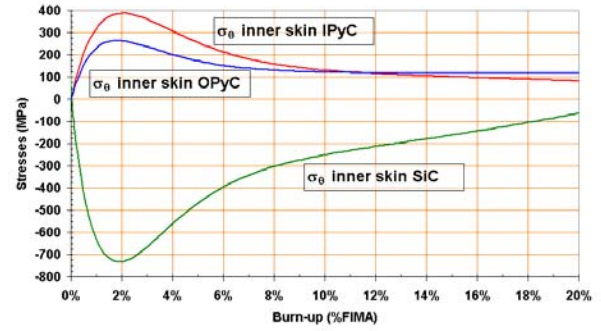

Figure v. Tangential stress history for the mean particle using ATLAS.

Deterministic fuel performance calculations were performed to evaluate the ability of particle fuel to reach extended burnups. These calculations illuminated the requirements that the fuel be able to withstand the stress levels and internal chemical environment that would be developed as a consequence of extended fuel life. For these evaluations, the INEEL developed, partially with internal funding, a fission product chemistry and transport module and incorporated it into PARFUME. This module calculates CO production, shown as the INEEL model in the figure below (Figure vi), release of gaseous fission products into particle void volume, and release to birth ratios for selected isotopes.

An extensive review of the literature was performed to understand the physical mechanisms for fission product transport in PyC and SiC. Mechanisms include: vapor transport via Knudsen diffusion for gaseous fission products and illustrated for Kr in Figure vii,

intercalation of alkali and alkali-earth fission products like Cs and Sr in the PyC layers, grain boundary diffusion, surface diffusion and bulk diffusion. Diffusivities for Ag, Xe, Cs, and Sr have also been gathered from the literature.
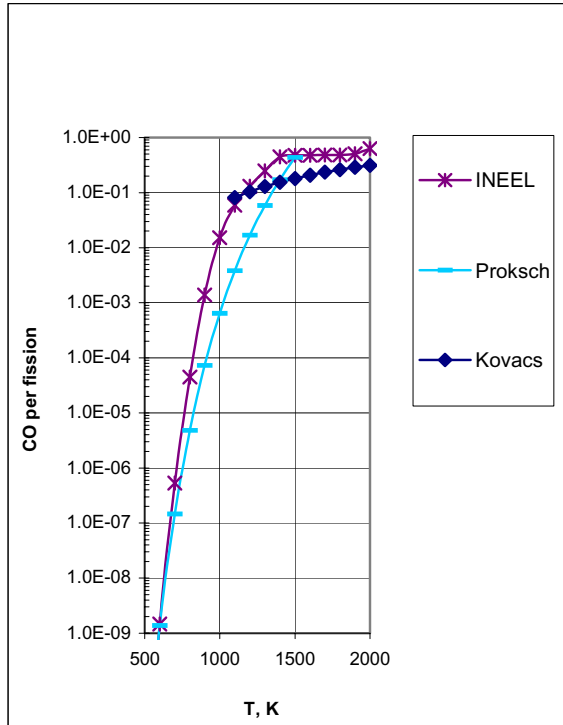

Figure vii. Effective diffusivities for Knudsen and viscous diffusion.

Figure vi. INEEL model predictions of CO yield per fission vs. temperature for a case with pure UO_2 fuel compared with German (Proksch) and historical U.S. (Kovacs) at t = 573 days (approximately 50MWd/kg).
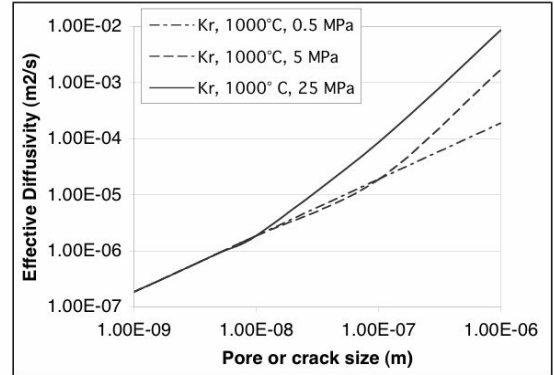
Scoping calculations were performed using a diffusion and trapping code called TMAP to model fission product transport from the particles. The code can model diffusion and trapping of multiple species and can model diffusion in the presence of a temperature gradient (the so-called Soret Effect). The code also has a thermal model that has been used to determine the temperature distribution and thermal gradient in each of the layers of the coated particle. Sensitivity studies have been conducted to look at thermal diffusion effects which are most important in the low density buffer where large thermal gradients could be expected depending on the power density in the fuel particle. The INEEL also investigated the effects of SiC layer thinning which may result from interactions with fission products. Preliminary results indicated that widening of

the thinned area more strongly increases particle failure probability than does deepening of the thinned area. A metallic Pd – SiC interaction model was developed and when combined with the SiC layer thinning evaluation will form an integrated model.

MIT performed diffusion couple experiments to study Ag and Pd transport through SiC (see Fig. viii). Results indicate that Knudsen pressure driven diffusion is the most likely mechanism for silver transport. This finding would imply transport via nanoporosity or nanocracks in the SiC. Knudsen and viscous pressure driven diffusion calculations have been performed to examine transport through sub micrometer size pores or cracks in the SiC layer.

Figure viii. Graphite shell substrate for the diffusion couples. Silver powder is placed inside the shell then SiC is coated on the outside.

Calculations have been performed to examine the feasibility of using TRISO-coated particles in a gas-cooled fast reactor. Damage rates as well as helium and hydrogen production in PyC and SiC were calculated using a gas cooled fast

reactor neutron spectrum. The calculated damage rates (~ 50 dpa) are high enough that radiation damage would be expected to influence the material properties. In particular the high radiation damage to the carbon layers would result in unacceptable dimensional change. At this level of radiation damage, SiC would also see significant property changes in terms of strength, swelling and other material properties. The use of the traditional TRISO coatings is not recommended for coated particle fuels in fast spectrum reactor applications.

Potential irradiation of prototype fuel particles in the Advanced Test Reactor (ATR) was examined. It was determined that the ATR would provide a near optimum balance of burnup accumulation and fast neutron fluence for irradiation testing of particle fuel. The CEA have investigated particle fuel irradiation in the French Material Testing Reactor, OSIRIS. Initial experiments utilizing historical German fuel and newly manufactured French fuel have been planned and are being implemented under a separate European program.

PROJECT ORGANIZATION:

Task	Task Title	Responsible Lead	Principal Investigators
1	Information Exchange	INEEL, CEA	David Petti, John Maki, and Philippe Martin, Mayeul Phélip
2	Model Development	INEEL, CEA	Gregory Miller, John Maki, David Petti, Mayeul Phélip
3	Concept Improvements	MIT, INEEL	Ron Ballinger and David Petti
4	Feasibility of the concept in a hard spectrum	CEA, INEEL	Philippe Martin and David Petti
5	Irradiation of prototype particles	INEEL, CEA	David Petti and Philippe Martin

TABLE OF CONTENTS

TABLE OF FIGURES

Enhanced Thermal Model

TABLE OF TABLES

Filename: 1. Introduction.doc
Directory: C:\Documents and Settings\talbhd\Desktop\FINAL INERI JAN3
Template: \\Hugh\publications\Templates\Reports\EXTERNAL-May-
     01.DOT
Title: INEEL/EXT-97-
Subject:
Author: pys
Keywords:
Comments:
Creation Date: 1/11/2005 9:56:00 AM
Change Number: 11
Last Saved On: 1/17/2005 3:31:00 PM
Last Saved By: test
Total Editing Time: 48 Minutes
Last Printed On: 1/18/2005 10:46:00 AM
As of Last Complete Printing
     Number of Pages: 26
     Number of Words: 5,689 (approx.)
     Number of Characters: 31,808 (approx.)

1. TASK 1: INFORMATION EXCHANGE ON EXISTING PARTICLE FUEL DATA, MODELS, AND COMPREHENSION

Responsible Leads: INEEL, CEA

Brief Description of Objectives:

The CEA and INEEL exchanged their current databases on coated particle fuel performance during irradiation and the computer models and material property correlations that have been developed to describe that performance. This information included fission gas release data from irradiation experiments, and post-irradiation examination results documenting the physical state of the TRISO coatings and kernels after irradiation. In addition, information on the pedigree of the fuel including fabrication conditions was included where available. (Much of the previous U.S. database was obtained from the open literature or from GA.) Included with this information, the INEEL provided detailed results from the NPR-1, NPR-1A and NPR-2 experiments that were conducted at the INEEL as part of the New Production Reactor program. Once received, the particle fuel databases were reviewed and critically assessed. This assessment identified data needs in regard to implementation and further development of fuel behavior models. Attempts were made to fulfill those data needs.

1.1 Task Technical Overview - INEEL

Work was conducted on reviewing and assessing particle fuel material property correlations. These correlations are used in model predictions of fuel performance during irradiation. Such predictions are useful to understand the interplay of important phenomena that could occur outside of the existing irradiation envelope of temperature, burnup and fast neutron fluence. It has been observed that property data are generally lacking for materials exposed to high fuel burnups and neutron fluences. This current lack of data will introduce uncertainty into model predictions of fuel performance. Several key material properties that affect fuel performance are briefly discussed below.

PyC Shrinkage and Swelling

Under irradiation, the PyC layers of the fuel particle experience either shrinkage or swelling which affects the amount of stress experienced by the SiC layer. The correlations currently used

to represent shrinkage, or swelling, of the PyC layers were obtained from empirical fits to data as compiled by the CEGA Corporation (CEGA 1993). These correlations are good up to fluences of 3.7 x 10^{25} n/m^2 and are functions of temperature, anisotropy, density and fast neutron fluence. Figure 1-1 displays several fits and the underlying data at various temperatures. The amount of data is rather sparse, which introduces significant uncertainty when the correlations are extrapolated beyond neutron fluences of 5 x 10^{25} n/m^2.
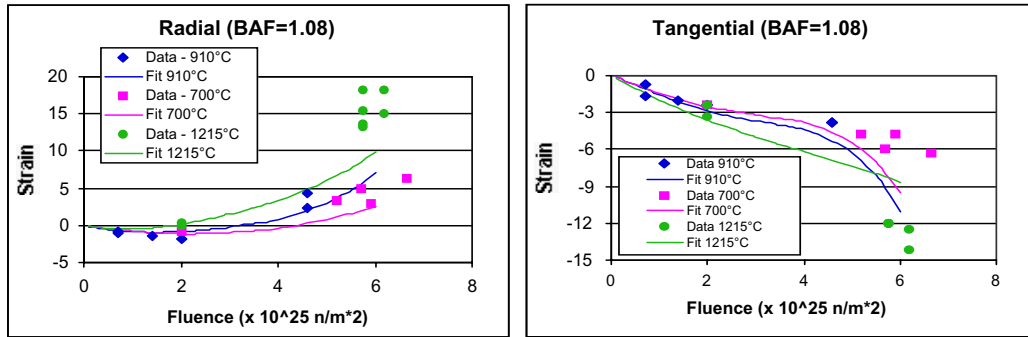
Figure 1-1. Database underlying the CEGA PyC shrinkage correlation expressed in units of % strain.

Figure 1-2 displays the CEGA shrinkage correlation for several PyC anisotropies (as indicated by the BAF values). The CEGA correlations are also compared to the UK STRESS3 correlations (Martin 2001) in Figure 1-3, for both high-temperature isotropic (HTI) and low-temperature isotropic (LTI) high density, low anisotropy PyC. These correlations generally display the same shrinkage trends but differ in magnitude, especially at high neutron fluences.
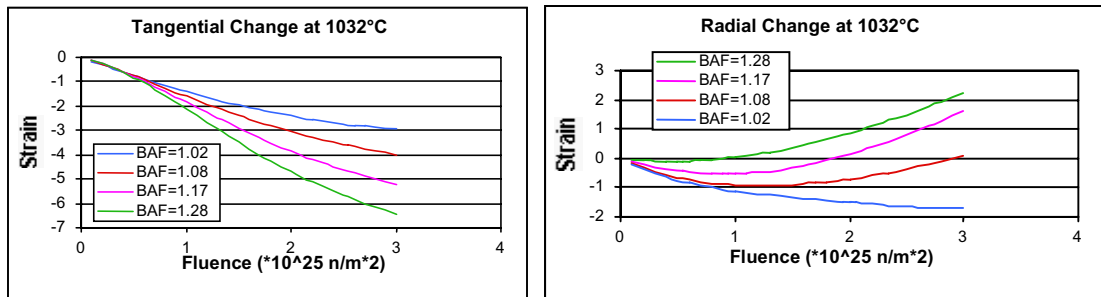
Figure 1-2. CEGA correlation of PyC shrinkage for various anisotropies expressed in units of % strain.
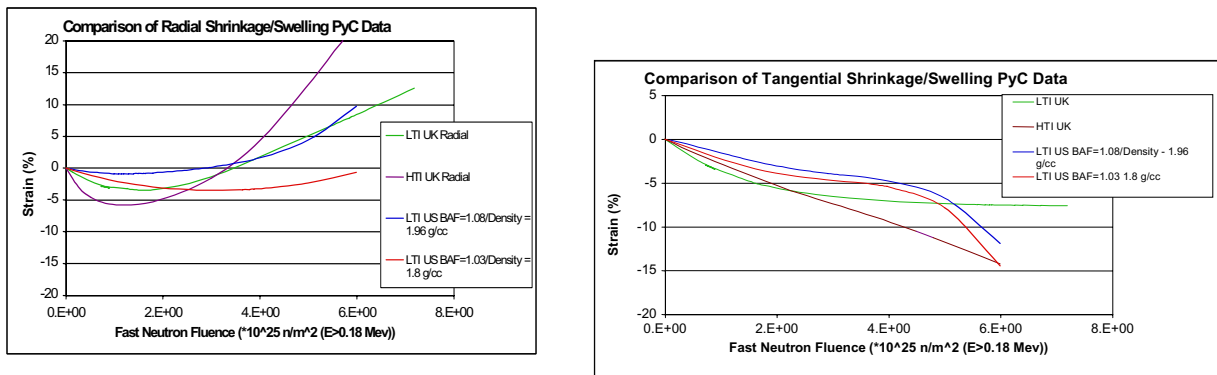
Figure 1-3. STRESS3 and CEGA correlations for PyC shrinkage.

PyC Irradiation-Induced Creep

Irradiation-induced creep in the PyC layers is another important property that affects the stress-state of the particle. However, there is a considerable range of values reported in the literature as indicated by the sources listed in Table 1-1. Even by disregarding the value from Morgand (which is generally considered to be suspect), the creep constant varies by a factor of about five.

Table 1-1. Selected irradiation induced creep constants for PyC (expressed for neutron fluences with E > 0.18 MeV).

Author	Creep constant 10^{-29} (MPa n/m^2)$^{-1}$
Kaae et al. (1972)	1.0
Price and Bokros (1967)	1.3
Buckley et al (1975)	4.9
Buckley et al. (1975)	4.0
Brocklehurst and Gilchrist (1976)	3.3
Brocklehurst and Gilchrist (1976)	1.7
Morgand (1975)	13.3

One of the current creep correlations used in the INEEL particle fuel performance code, called PARFUME, is the correlation compiled by the CEGA Corporation (CEGA 1993) and is referred to as the base creep value. However, it has been shown that PARFUME particle failure calculations of past NPR irradiation experiments (Miller 2002) best match actual test results when this base creep value is multiplied by a factor of 2.5 (when coupled with a Poisson's ratio in creep of 0.5). An amplification factor of 2.0 may be better yet when coupled with a creep Poisson's ratio of 0.4. This amplified value is closer in magnitude to the historical U.S. value

and the currently used STRESS3 value than the base value. STRESS3 is the standard particle
fuel performance code used primarily by European investigators (Martin 2001). Table 1-2 lists
these creep constants at a temperature of 1200 °C.   The most recent analysis, discussed in the
Task 2 section, suggests that an amplification value of 1.8 with the latest statistical method may
be somewhat better.

Table 1-2.   Various PyC irradiation induced creep constants at 1200 °C (expressed for neutron
fluences with E > 0.18 MeV).

Correlation	Creep constant 10^{-29} (MPa n/m^2)$^{-1}$
Base (CEGA correlation)	2.0
Amplified value (base x 2.5)	5.0
Historical U.S.	6.2
STRESS3	4.9

The magnitude of the PyC irradiation creep value has a large influence on the stress state of the
SiC layer. This is evident in Figure 1-4 which displays the stress experienced by the SiC layer
(with a cracked inner PyC layer) assuming the base and amplified creep values at 1200 °C.
Clearly more data are needed here.
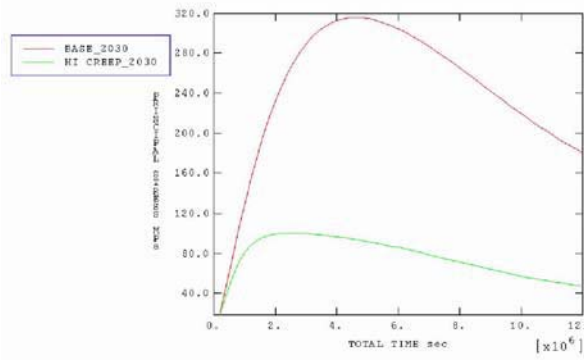
Figure 1-4. Calculated SiC stress using different values of irradiation-induced creep.

PyC Poisson's Ratio in Creep

The magnitude of Poisson's ratio in creep for the PyC layer also has a significant affect on the stress-state of the particle. This parameter is quoted with a range of 0.3 to 0.5 in the literature. However, a value of 0.5 implies no volume change and it is generally acknowledged that a realistic value is closer to 0.4. As illustrated by PARFUME calculations listed in Table 1-3, the stress in the fuel particle can vary by over 20% depending upon the value of Poisson's ratio.

Table 1-3. Effect of Poisson's ratio in creep on calculated stress levels.

Case	IPyC Stress (MPa, tension)		SiC Stress (MPa, compression)	
	$\nu_c = 0.4$	$\nu_c = 0.5$	$\nu_c = 0.4$	$\nu_c = 0.5$
Nominal, T = 1273 K	351	475	697	847
Nominal, T = 873 K	488	627	948	1107
NPR-1, compact A9	307	430	610	784
NPR-2, compact A4	449	599	895	1101

PyC Anisotropy Change Under Irradiation

Under high strains, some PyC will reorient itself and become more anisotropic leading to higher stresses and the potential for particle failure at high neutron fluences. This phenomenon is dependent on the initial structure of the PyC. The data, as displayed in Figures 1-5 (Tempest 1978) and 1-6 (CEGA 1993), suggests that this effect is more prevalent for lower density PyC and/or for material produced at lower coating rates. However, this effect is not consistent with the German irradiation database which used high density PyC produced at high coating rates (Approximately 1.9 g/cm^3 produced at high coating rates of 4 to 6 μm/ min).
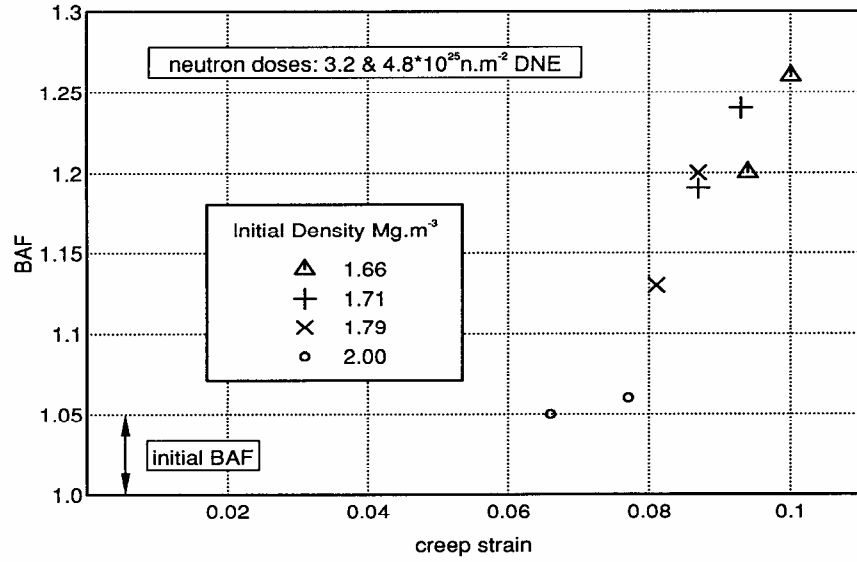
Figure 1-5. Changes in PyC anisotropy due to irradiation (Tempest 1978).
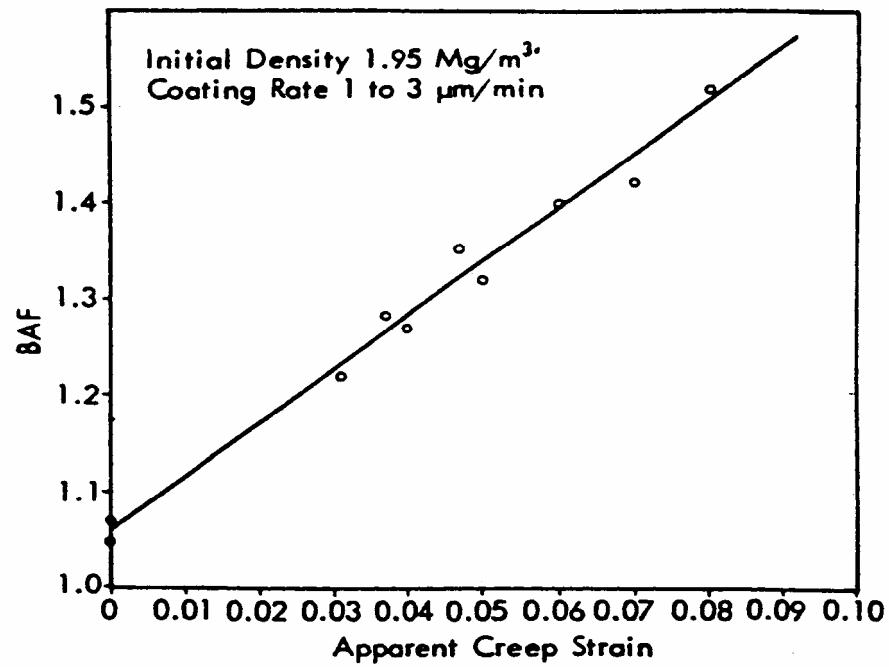
Figure 1-6. Changes in PyC anisotropy due to irradiation (CEGA 1993).

PyC and SiC Fracture Strength

Weibull theory is widely used to predict particle layer failures. The Weibull failure probability, $P_{failure}$, may be expressed as:

$$P_{failure} = 1 - \exp\left(-\sigma_c / \sigma_{ms} \right)^m$$

where σ_c is the calculated maximum stress in the material, σ_{ms} is the Weibull mean fracture strength, and m is the Weibull modulus. The parameters used in the Weibull formulation are indicative of the flaw distribution in a given volume of a material. These values may then be dependent upon a particular production batch of the material. Considerable variation does exist in these parameters among various sources. Table 1-4 lists Weibull parameters from selected sources and the corresponding stress required to reach a failure fraction of 1×10^{-4}. As suggested by Table 1- 4, there is a considerable range in predicted failure levels depending upon the choice of Weibull parameters.

Table 1- 4. Weibull parameters for particle fuel.

Material	Source	Weibull mean Fracture strength (MPa)	Modulus	WeibullStress required for 10^{-4} failure fraction (MPa)
PyC	CEGA	300	9.5	114
	German	-200	5	34
SiC	CEGA	500	6	107
	STAPLE (UK)	200	5	34
	German (unirrad.)	834	8	276
	German (irrad.)	667	6	157

PyC CTE and Elastic Modulus

The coefficient of thermal expansion (CTE) and the elastic modulus of PyC are important material properties especially needed to describe the behavior of particle fuel during thermal transients where differential thermal expansion of the particle layers may lead to significant mechanical interactions. CTE for PyC is different in the radial and tangential orientations and depends upon the anisotropy of the material. The effect of irradiation on this property is unknown. Figure 1-7 displays PyC CTE data at various temperatures. (Martin 2001) Figure 1-8 displays the elastic modulus for PyC which is a function of anisotropy, neutron fluence, density, and temperature (CEGA 1993).
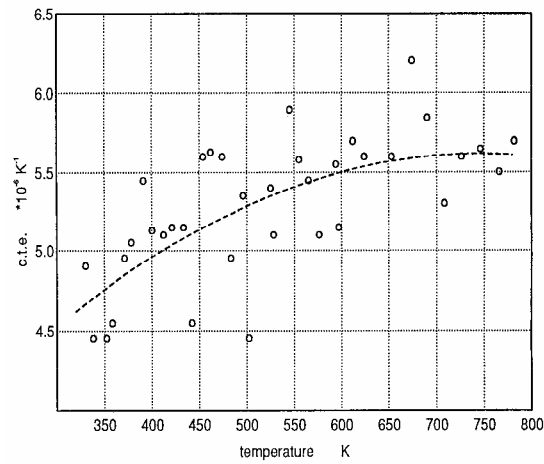
Figure 1-7. Coefficient of thermal expansion for PyC.
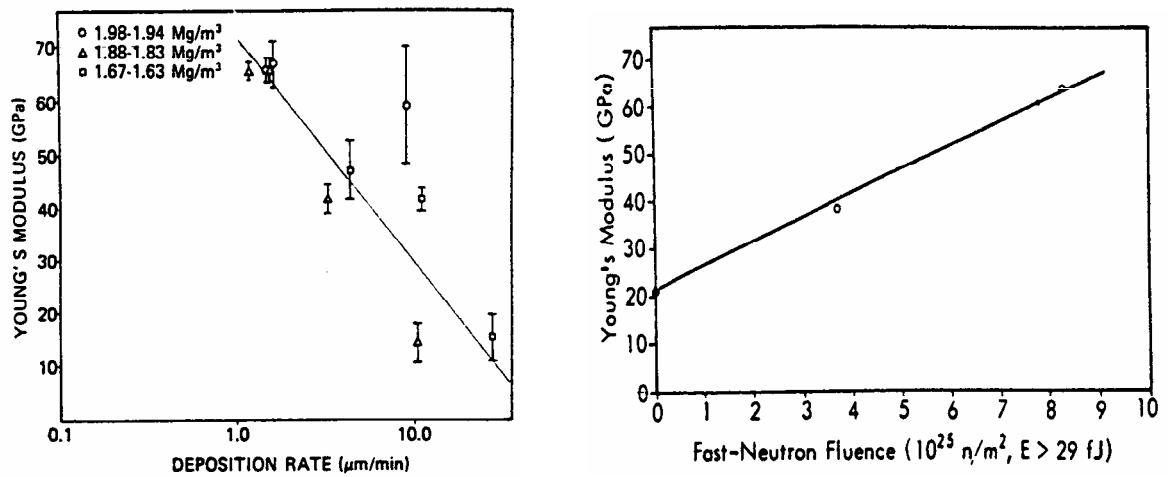
Figure 1-8. Elastic modulus for PyC (CEGA 1993).

Kernel Swelling

Solid fission product fuel swelling is an important phenomena at high burnups because it can reduce the void volume within the particle which increases the internal gas pressure. Under some conditions, fuel swelling can also lead to kernel − coating layer mechanical interaction which may result in particle failure. Theoretical estimates (Olander 1976) of swelling range

from 0.3 to 0.45 % ΔV/V per atom percent burnup. However, experimental measurements indicate larger values in the range of 0.6 to 1.5% ΔV/V per atom percent burnup (these larger values may be due to intergranular fission gas bubbles). At 20 %FIMA, this amount of swelling corresponds to a 6 to 30% increase in the volume of the kernel. For particles with sufficiently thin buffer layers (due to the high coating rates for the buffer, this layer displays the greatest variability in thickness among the particle layers), kernel – coating mechanical interaction may occur. Figure 1-9 presents a STRESS3 calculation indicating such an interaction (Martin 2002).
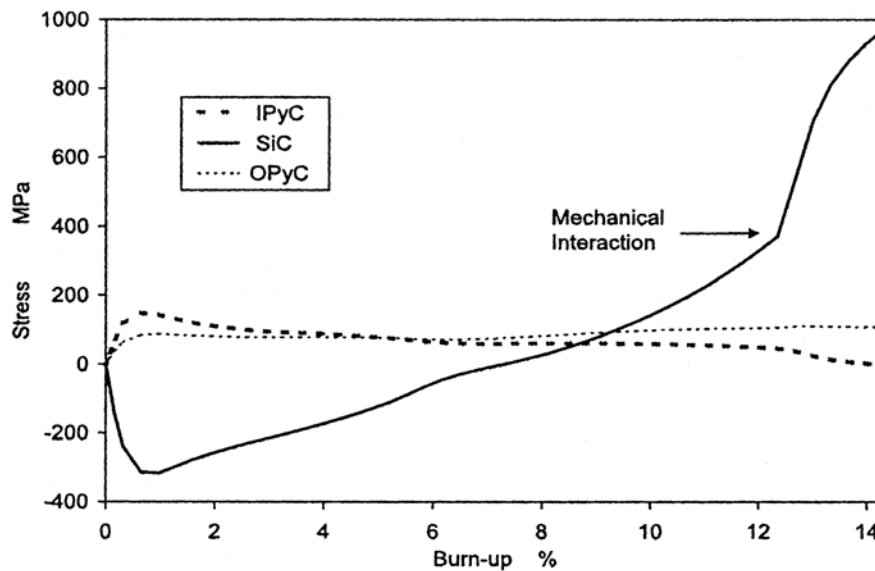
Figure 1- 9. A STRESS3 calculation indicating kernel – coating layer mechanical interaction.

CO Production

The release of excess oxygen in UO_2 fuels causes CO production to become significant at high burnups. Existing experimental data of CO production is sparse and displays large scatter (by over an order of magnitude). Furthermore, there are no data at high burnups. Figure 1-10 displays the Proksch correlation (Proksch 1982) which is an empirical fit to the data for excess oxygen yield from UO_2 fuel and is limited to 550 full power days of irradiation (about one half of full burnup) and displays a quadratic time dependency. Also displayed in Figure 1-10 are historic General Atomics (GA) correlations for oxygen yield from low enriched uranium fuel (Kovacs et al. 1985). The GA correlations depend upon only temperature. A detailed

thermodynamic model for CO production, described in the Task 2 section, has recently been completed and is used in the PARFUME code (INEEL 2002).
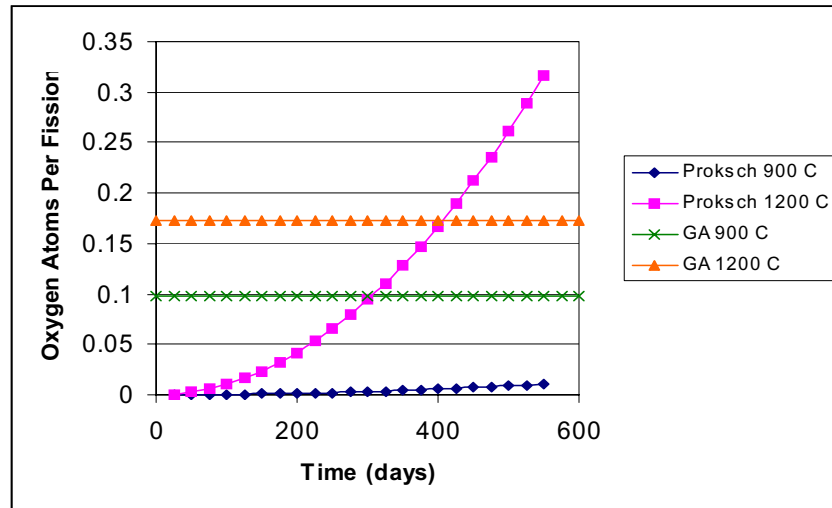
Figure 1-10. Correlations for oxygen release per UO_2 fission.

Fission Gas Release

Particle fuel performance evaluations almost universally use the classic Booth equivalent sphere diffusion model for fission product gas release. Differences in this application arise from different gas diffusivities being used. Generally, the impact of these differences on the fractional gas release is fairly small. This is evident from Table 1-5 which lists fission gas release fractions as calculated by PARFUME and MINIPAT (Martin 1982) which use different fission product gas diffusion coefficients. The diffusivity used in MINIPAT is based upon the work of Horsley (Horsley 1976) and has been also used in German coated particle fuel performance models.

Table 1-5. Calculated fission product gas release fractions.

	German Fuel 8.5 %FIMA, 900°C, 3 yr irrad.	U.S. HEU NPR Fuel 79 %FIMA, 1200°C, 3 yr irrad.
PARFUME	.23	.86
MINIPAT	.33	.95

1.2 Task Technical Overview - CEA

UO$_2$ Kernel

CEA brought to the INERI collaboration its experience with UO$_2$ and (U,Pu)O$_2$ fuels behavior under irradiation. In carrying out the work, the CEA sought to establish a set of properties and models for the kernel of the coated particle. A collection of physical and mechanical properties for UO$_2$ and (U, Pu)O$_2$ fuels were gathered, taking into account the effects of a number of important parameters such as temperature, burn-up and porosity. In addition, a number of fuel behavior models including in pile densification, fuel swelling, fission gas release and CO production were analyzed.

The proposed fuel models are based upon CEA knowledge of PWR and FBR oxide fuels. Most have been used in CEA codes for several years and have been validated. In regards to CO production, an empirical model was developed based upon experimental data from the open literature. This model had been used previously in other HTR codes.

Most of the properties for UO$_2$ fuel proposed below are based on measurements of sintered PWR fuel. There is limited data for UO$_2$ prepared by the Sol gel process. Therefore, it is recommended for future kernel fabrications that measurements of certain properties be carried out to validate the merits of the present recommendations.

Linear Thermal Expansion

The linear thermal expansion of UO$_2$ is given by the following expressions:

For $T_K < 923$ K:

$$\frac{l_{T_K}}{l_{273}} = 9.9734 \times 10^{-1} + 9.802 \times 10^{-6}\, T_K - 2.705 \times 10^{-10} T_K^2 + 4.391 \times 10^{-13} T_K^3$$

For $T_K \geq 923$ K:

$$\frac{l_{T_K}}{l_{273}} = 9.9672 \times 10^{-1} + 1.179 \times 10^{-5} T_K - 2.429 \times 10^{-9} T_K^2 + 1.219 \times 10^{-12} T_K^3$$

with T_K in K.

The averaged linear thermal expansion coefficient between 273 and T_K is given by:

$$\alpha_{(273-T_K)} = \frac{1}{(T_K - 273)}\left(\frac{l_{T_K}}{l_{273}} - 1\right)$$

The correction for substoichiometric mixed oxide fuels (O / M < 2) is as follows:

$$\left(\frac{l_{T_K} - l_{273}}{l_{273}}\right)_{2-X} = \left(\frac{l_{T_K} - l_{273}}{l_{273}}\right)_{2} (1+3.9x) \text{ with: } x = 2-(O/M)$$

Thermal Conductivity

A study of UO_2 thermal conductivity, available in the open literature, was recently carried out. This study resulted in a new recommendation, inspired by the "Lucuta's law" of 1996, which has been validated with measurements to 1900 K. This correlation, applicable for stoichiometric UO_2 fuel, is also used in the current version of the PWR rod code METEOR:

$$\lambda = K_{1d} \ K_{1p} \ K_{2p} \ K_{4r} \ \lambda_0$$

With:

The correlation proposed by Harding and Martin for the unirradiated UO_2:

$$\lambda_0(T_K) = \frac{1}{0.0375 + 2.165 \times 10^{-4} T_K} + \frac{4.715 \times 10^9}{T_K^2} \exp\left(-\frac{16.361}{T_K}\right)$$

The correction due to FP in solid solution:

$$K_{1d} = \left(\frac{1.09}{\tau^{3.265}} + \frac{0.0643}{\sqrt{\tau}} \sqrt{T_K} \right) \arctan\left[\frac{1}{\left(\frac{1.09}{\tau^{3.265}} + \frac{0.0643}{\sqrt{\tau}} \sqrt{T_K} \right)} \right]$$

The correction due to FP precipitates:

$$K_{1p} = 1 + \frac{0.019\,\tau}{3 - 0.019\,\tau} \frac{1}{\left(1 + \exp\left(-\frac{(T_K - 1200)}{100} \right) \right)}$$

The correction due to porosity:

$$K_{2p} = \frac{1 - P}{1 + 2\,P}$$

The correction due to irradiation damages:

$$K_{4r} = 1 - \frac{0.2}{\left(1 + \exp\left(\frac{(T_K - 900)}{80} \right) \right)} (1 - \exp(-\tau))$$

where:

λ, λ_0	:	thermal conductivity	(W/(mK))
T_K	:	temperature	(K)
τ	:	burn-up	(at% FIMA)
P	:	pore fraction	(/)
x	:	2 - O/M	(/)

13
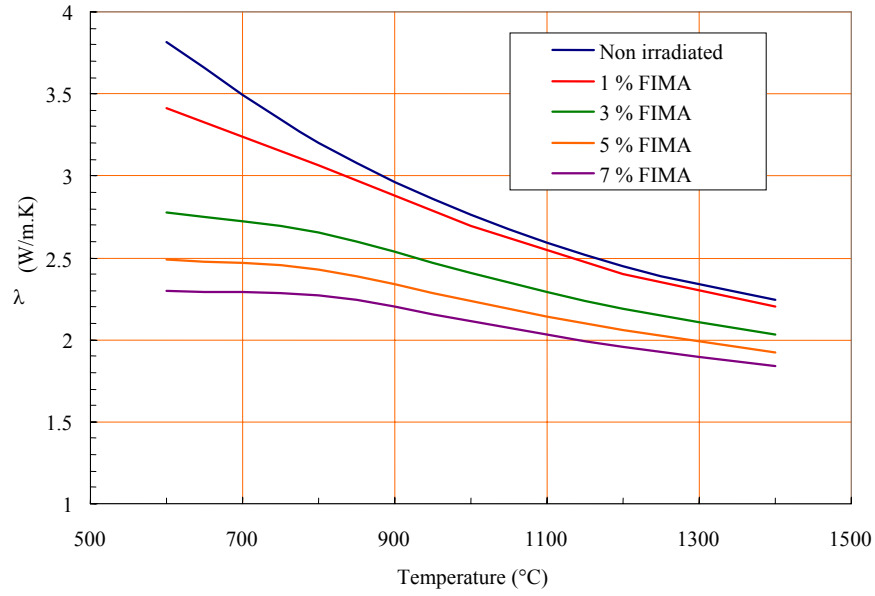
Figure 1-11. Thermal conductivity of UO_2...

Young's Modulus

The evolution of the UO_2 Young's modulus with both temperature and porosity is given by the following equations:

For $273 \leq T_K \leq 2.610$ K:
$$E_0 = 2.2693 \times 10^2 - 1.5399 \times 10^{-2} T_K - 9.597 \times 10^{-6} T_K^2$$

For $T_K > 2.610$ K:
$$E_0 = -1.33445 \times 10^3 + 1.18106 T_K - 2.38803 \times 10^{-4} T_K^2$$

The correction due to porosity is as follows:

If $P \leq 0.3$:
$$E = (1 - 2.5 P) E_0$$

If $P > 0.3$:
$$E = \frac{1 - P}{1 + 6 P} E_0$$

where:

$$E, E_0 \ : \quad \text{Young's modulus} \qquad \qquad \text{(GPa)}$$

$$T_K \quad : \quad \text{temperature} \qquad \qquad \qquad \text{(K)}$$

$$P \quad : \quad \text{fuel pore fraction} \qquad \qquad \text{(/)}$$

Models

Densification

The densification of UO_2 at the beginning of the irradiation, results from sintering due to both temperature and the fission spikes. It is the fine porosity population ($\Phi < 1.5 \ \mu m$), which is the result of fabrication, that is mainly removed. The different modes of manufacture for sintered PWR pellets and Sol gel-produced HTR kernels can lead to differences in the size distribution of the porosity. This implies that most of empirical densification models developed from sintered fuels would not be suitable for Sol gel fuels. The manufactured kernel density of future HTR fuel is required to be $\geq$ 95%TD. Consequently, for a first approach, it is not necessary to take into consideration the in pile densification because it is of little consequence compared to fuel swelling.

Swelling

Solid FP swelling

The fuel is considered to be an isotropic material. The swelling rate, which was determined from density measurements, reflects the "solid swelling". The density measurements carried out on post-irradiated PWR and FBR fuels clearly display a linear behavior in relation to the burn-up. This solid swelling includes not only the contribution of solid FP, but also that of the fission gas in super saturation in the fuel, or partly precipitated as nanometric bubbles.

The solid swelling rate, $\dot{S}_s$ is given by the equation:

$$\dot{S}_s = \frac{dS_s}{d\tau} = \frac{d\left(\dfrac{\Delta V}{V_0}\right)}{d\tau} = 0.06$$

with: $\dot{S}_s$: solid swelling rate (% / GWd/t_{HM})

Gaseous swelling

The fuel swelling due to gaseous fission products (Xe, Kr) results mainly in an increase of bubble population and bubble size in the matrix and grain boundaries. The mechanisms which lead to this swelling are complex. For this reason, gaseous swelling models are often empirical correlations which depend only upon some parameters, the most important of which are temperature and burn-up. Some models are available in open literature, and the CEA proposes using the MATPRO model for HTR UO_2 fuel. This empirical model simulates the gaseous steady state free swelling between 1000 and 2000 K. The gaseous swelling rate in relation to local temperature is as follows:

$$\dot{S}_g = \frac{dS_g}{d\tau} = 2.19912 \, x10^{-28} \left(2800 - T_K\right)^{11.73} \exp\left[-0.0162\left(2800 - T_K\right)\right]$$

with:

$\dot{S}_g$: gaseous swelling rate   (% / GWd/t$_{HM}$)

T_K : temperature   (K)

Fission Gas Release

A number of fission gas release (FGR) models are available for steady state conditions. The release process is relatively complex, but it may be reduced to a two-stage process. In the first stage, the gas atoms in the grain migrate by several mechanisms towards the grain boundaries. In the second stage, the gas migrates from these boundaries to the free surfaces of the fuel and is released in the free volume.

For its simplicity, the equivalent sphere diffusion model or Booth model is usually used to estimate the FGR of coated particles. More refined FGR models, which are for the most part built on the original Booth model, take into account other contributions. These include the trapping of gas atoms by matrix defects and the resolution of gas atoms from bubbles by fission spikes. In addition, for high burn-up there is the principle of a gas saturation threshold which leads to an increase of the kinetic of release, even at low temperatures.

The CEA model, developed for the FBR mixed oxide fuel, accounts for fission gas release becoming more intense when the fuel structure changes at high burn-up. This change occurs particularly in the

600 – 1200 °C temperature range. Consequently, this model seems better adapted for fuel burn-up in excess of 10 %FIMA. In addition, the model takes into account an athermal diffusion of the fission gas atoms, which dominates below 1000°C, and a gas saturation threshold which is a function of the temperature. For the calculation of the saturation threshold, the model adopts the Speight theory which considers that the phenomena is controlled by the resolution of the gas atoms from the bubbles into the matrix as a result of fission spikes. The main consequence of this is the formation of an intra and inter granular gaseous porosity, which interconnects and favors the fission gas release. Although it is impossible to provide a comprehensive description of the model in the frame of the present document, graphics of the CEA FGR model application are provided below:
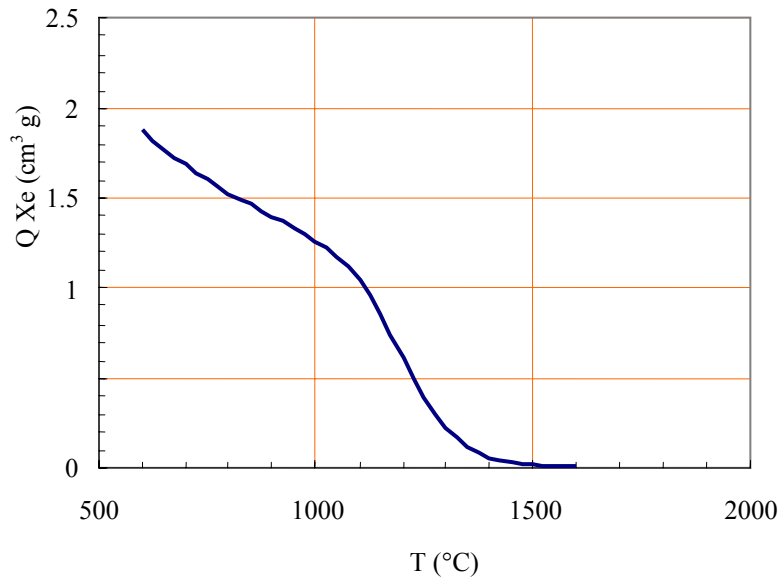
Figure 1-12. Limit of the gas saturation (super saturation in the matrix and in nanometer bubbles) in oxide fuel versus the fuel temperature.
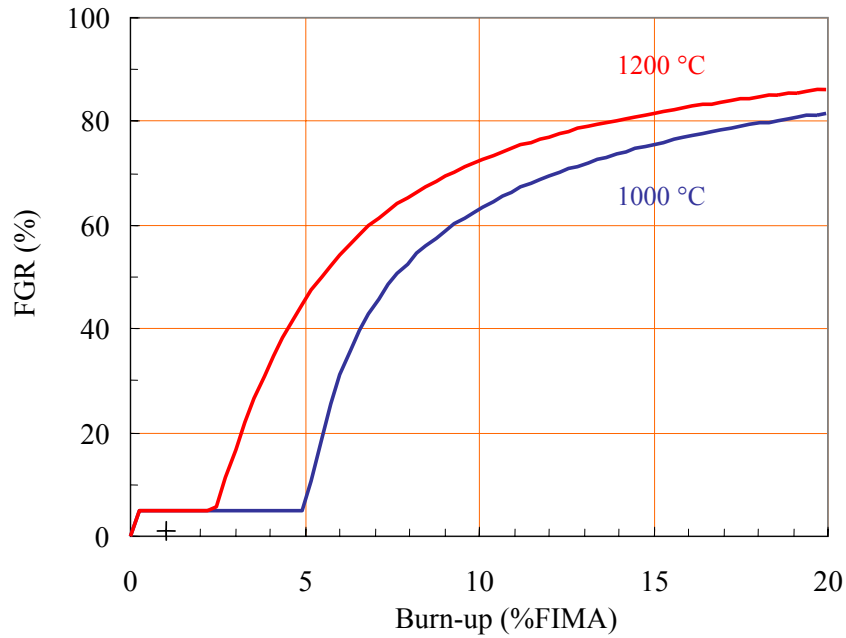
Figure 1-13. Evolution of the fission gas release rate with the fuel burn-up.

CO Production

Several different gases contribute to the pressure build-up in the coated particle. Among them, the CO production from the reaction between the free oxygen liberated by fissions, and the carbon of the inner coatings may become significant. The production of free oxygen depends on the nature of the fuel: oxide or oxycarbide and on the type of fissile material, either uranium or plutonium. It has been proven that unlike UO_2, fuels containing carbon do not produce excess free oxygen. The formulation proposed by Homan for low-enriched uranium fuels ($U^{235} < 20$ wt%) takes into account the effect of plutonium fissions on the oxygen production. It is assumed that negligible CO_2 is formed under normal operating conditions.

The following equations have been proposed:

$$O / f = 1.64 \exp[-3311/T]$$

and

$$O / f_{max} = 0.61$$

with:

O / f: atomic oxygen release per fission   (/)
T :   temperature (K)

In addition to the Homan formulation, the Proksch model and the "STRESS3" model have been investigated. The empirical expression proposed by Proksch, based on a large number of mass-spectrometric CO measurements seems to be the best at present to describe this phenomenon. It takes into account both the role of plutonium fissions on the oxygen production and the irradiation time. Proksch proposes the following equations for the oxygen atoms per fission.

$$\log_{10}[(O/f)/t^2] = -0.21 + (-8500/T)$$

and

$$O/f_{max} = 0.4\, f_U + 0.85\, f_{Pu} \text{ with a upper limit of } 0.625$$

with:

O/f : atomic oxygen release per fission (/)
t : irradiation time (days)
T : particle surface temperature (K)
f_U : U fission rate (/)
f_{Pu} : Pu fission rate (/)

In principle, the validity of the equation is strictly held only in the region covered by the supporting experiments:

$$950 < \theta < 1525°C$$

$$66 < t < 550 \text{ days}$$

The "STRESS3" model, proposed by D.G. Martin, assumes that the number of oxygen atoms released during irradiation is proportional to the number of fissions occurring via plutonium. The temperature dependence is given by:

$$O/f_{Pu} = 1.641 \exp\left(-\frac{3311}{T}\right)$$

For a LEU UO_2 fuel, the ratio between plutonium fissions and total fissions depends both on the ^{235}U enrichment of the fuel and on the burn up.
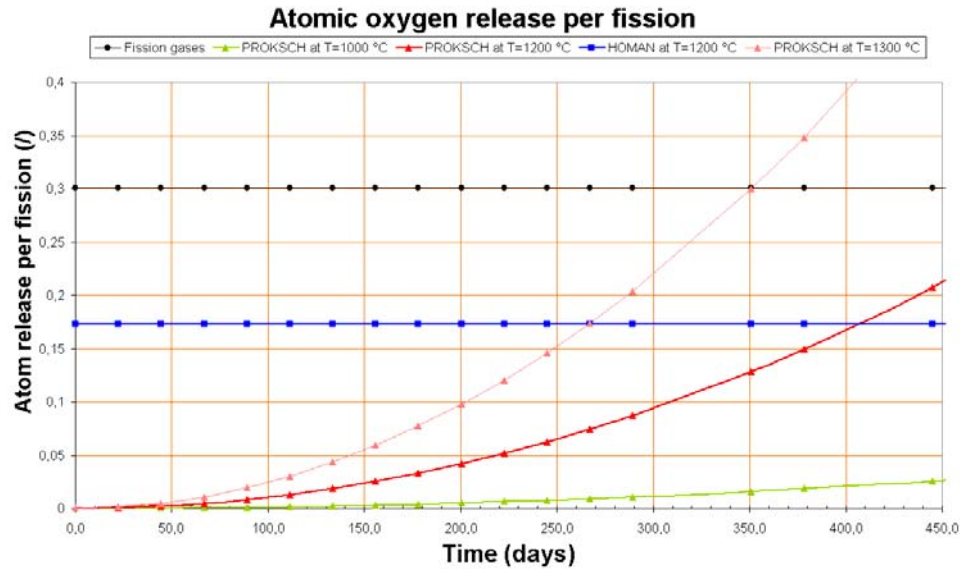
Figure 1-14. Atomic oxygen release per fission.

Pressure Calculation

Because the classical ideal gas law is inadequate to calculate the internal pressure of the coated particle, a new model of pressure calculation has been included. The earlier model failed to take in account the particular conditions which prevail inside the particle: low volume, low to high temperature and pressure. In addition, it neglects the volume that gas atoms and molecules occupy. As a consequence, it is necessary to use a more appropriate equation of state. Among the numerous equations of state for gases, the model proposed by Redlich and Kwong seems to be the best adapted for calculating gas pressure within coated particles, combining a simple formula with a high level of accuracy.

The Redlich-Kwong equation of state is:

$$\left[RT = P + \frac{a}{T^{1/2} \, V \, (V+b)} \right] (V - b)$$

where:

P: pressure   Pa

V: volume per mole m^3/mol

T: temperature   K

R: gas constant   8.31441 J/ (K mol)

"a" and "b" are gas constants whose values are obtained by noting that at critical point:

$$\left(\frac{\partial P}{\partial V} \right)_T = \left(\frac{\partial^2 P}{\partial V^2} \right)_T = 0$$

implying for each gas that:

$$a = \frac{R^2 T_c^{2.5}}{9 \, \xi \, P_c} \quad \text{and} \quad b = \frac{\xi \, R \, T_c}{3 \, P_c}$$

Values of the critical temperatures and pressures, together with the derived "a" and "b" values for the four gases of interest (CO, CO_2, Xe, Kr) are given in the following table.

Table 1-6. Redlich-Kwong gas constants.

Gas	T_c (K)	P_c (MPa)	a (N m^4 $K^{0.5}$/mol^2)	b (m^3/mol)
CO	132.91	3.5	1.72	2.736×10^{-5}
CO_2	304.14	7.38	6.46	2.969×10^{-5}
Kr	209.45	5.5	3.411	2.743×10^{-5}
Xe	289.75	5.9	7.158	3.538×10^{-5}

The coefficient "ξ" in the equations of "a" and "b" is equal to $(2^{1/3} - 1) \cong 0.259921$.

In the case of gas mixture, mean values of "a" and "b" are required. They are given by:

$$\overline{a} = \left[\sum_{i=1}^{n} x_i \, a_i^{1/2} \right]^2$$

$$\overline{b} = \sum_{i=1}^{n} x_i \, b_i$$

where:

n: number of gas species

x_i: fraction of gas specie i

Pyrocarbons

Pyrolytic carbons (PyCs) are key protective materials in the design of the classical HTR coated fuel particles. PyCs are basically used for the constitution of the first porous coating (50% dense) called the "buffer" layer and for the two "dense" layers: the inner pyrolytic carbon (IPyC) layer and the outer pyrolytic carbon (OPyC) layer. These, in turn, enclose the silicon carbide layer (SiC) of the TRISO particle. According to both the temperature of the pyrolysis process and the nature of the hydrocarbon, two classes of "dense" PyC materials exist: the high-temperature isotropic (HTI) PyC ($\theta > 1800$ °C and CH_4 - Ar mixture) and the low-temperature isotropic (LTI) PyC ($\theta < 1500$ °C and generally C_3H_6 - Ar mixture). Much available data comes from the first class (HTI), because the greatest amount of tests on these materials was performed during the 1960's and 70's.

Three distant sets of data may be found:

- Data from the German experience
- Data from the UK experience, especially from the DRAGON program
- Data from the U.S. experience

Density

The theoretical density of graphite material is 2.27 g/cm^3. The value for 100 % dense PyC is a little lower than this value as shown in the table below:

Table 1-7. PyC density.

Value	German	UK
Theoretical density (g/cm^3)	2.2	
Fabricated density for:		
"Buffer" layer (g/cm^3)	$0.9 < \rho < 1.1$	
Dense PyC layers (g/cm^3)	$1.8 < \rho < 2$	

Coefficient of thermal expansion

Very often, the data reported in the literature is not the true linear thermal expansion coefficient (α) but the mean value ($\bar{\alpha}$) given between two temperatures T_1 and T_2. The PyC thermal conductivity depends on porosity and, consequently on the as-fabricated density.

Table 1-8. PyC coefficient of thermal expansion.

Value	German	UK	US[1]
"buffer" layer α (10^{-6} K^{-1})	$\alpha = 3.5$	$\alpha = 3.5$	*For BAF < 3 (R_1 < 0.8 and R_3 > 0.4)* *And in the range of temperature around 1100°C:*
dense isotropic PyC layers α (10^{-6} K^{-1})	$\alpha = 5.5$	$\alpha = 5.6$	$\alpha_1 = 40 (R_1 - 1)^2 + 1.11$ $\alpha_3 = -41.67 R_3 + 33.33$

[1] The parallel and normal directions are represented by subscripts 1 and 3, respectively.

Thermal conductivity

Table 1-9. PyC thermal conductivity.

Value	Germany	UK
"buffer" layer λ (W m^{-1} K^{-1})	$\lambda = 0.5$	$\lambda = 10.98222 \left(\dfrac{1-P}{1+2P} \right) + 0.00444$
dense isotropic PyC layers λ (W m^{-1} K^{-1})	$\lambda = 4$	For P = 0.5 $\quad \lambda = 2.75$ For P = 0.2 $\quad \lambda = 6.28$ P = porosity fraction

Young's Modulus

Values for PyC Young's modulus are listed in the table below and plotted in the following figures.

Table 1-10. Young's modulus**.**

Reference	German	UK
"buffer" layer E (MPa) Φ (10^{25} n/m^2 >0.1 MeV)	*For 0 < D < 0.5* E = 7000 + 6000 D *For D > 0.5* E = 10,000	E = 12,500 (1 + 0.18 Φ)
dense isotropic PyC layers E (MPa) Φ (10^{25} n/m^2 >0.1MeV)	E = 29,000	E = 25,000 (1 + 0.18 Φ)

[1] Polynomial adjustment according to the German recommendation.

[2] Polynomial adjustment according to the constants of compliance used in the code STRESS 3. The Young's modulus is deduced from the constants by the relation: E = 1/E_{11}.

Table 1-11. Young's modulus, continued.

Value	US
Buffer layer E(MPa) P (/)	For 0.2 <P < 0.6 $\quad$ E = 34,500 exp(-2.03 P)
Dense PyC layers : $\quad$ E(MPa) $\quad$ θ (°C) $\quad$ ρ (g/cm^3) $\quad$ Lc (nm) ** $\quad$ Φ (10^{25} n/m^2 >0.1MeV)	$E_1 = k_\rho \, k_{BAF01} \, k_{Lc} \, k_\phi \, k_T \, E_{01}$ $\quad$ and $\quad$ $E_3 = k_\rho \, k_{BAF03} \, k_{Lc} \, k_\phi \, k_T \, E_{03}$ *With:* $\quad$ $E_{01} = E_{03} = 25500$ $\quad$ $k_\rho = 0.384 + 0.324 \, \rho$ $\qquad$ $(1.8 < \rho < 2)*$ $\quad$ $k_{Lc} = 2.985 - 0.662 \, Lc$ $\qquad$ $(2.5 < Lc < 3.5)*$ $\quad$ $k_\Phi = 1 + 0.23 \, \Phi$ $\qquad\qquad$ (4×10^{25}) $\quad$ $k_T = 1 + 0.00015 \, (\theta - 20)$ $\quad$ $(20 < \theta < 2000)*$ $\quad$ $k_{BAF01} = 0.481 + 0.519 \, BAF_0$ $\quad$ $k_{BAF03} = 1.463 - 0.463 \, BAF_0$ $\quad$ $(1 < BAF_0 < 2)*$

$\quad$ * Recommended ranges of variation of the parameters
$\quad$ ** Lc: crystallite size
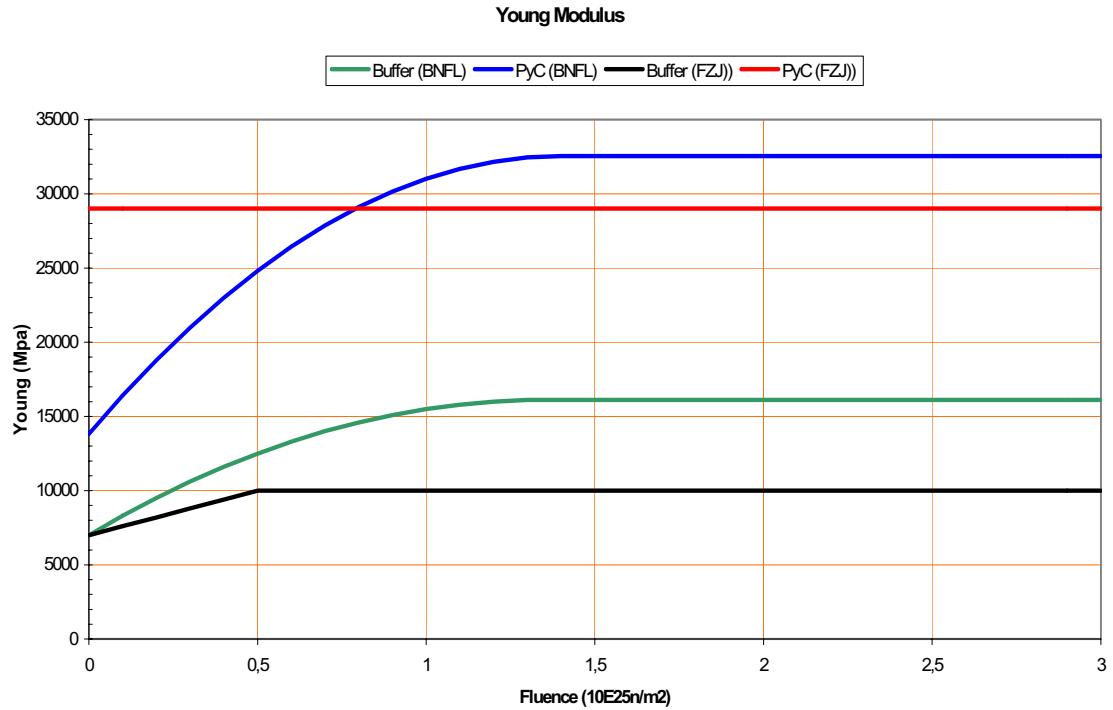
Figure 1-15. PyC Young's modulus from German and U.K. sources.

Young Modulus
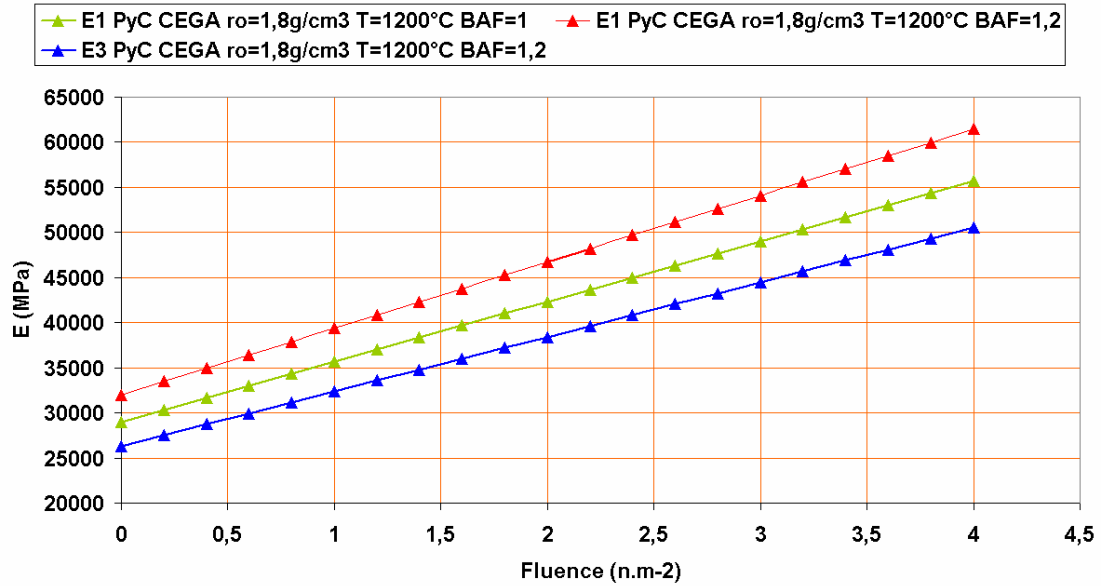
Figure 1-16. PyC Young's modulus from U.S. source.

Poisson's Ratio

Values for PyC Poisson's ration are listed on the table below:

Table 1-12. Poisson's Ratio.

Value	Germany	UK	US[1]
"buffer" layer ν (/)	$\nu = 0.3$	$\nu = 0.21$	$\nu = 0.23$
"dense" PyC layers ν (/)	$\nu = 0.3$	$\nu = 0.21$	$\nu_{12} = 0.766\ R_3 - 0.275$ $\nu_{13} = -0.884 R_3 + 0.825$ $\nu_{31} = \nu_{13}\ E_3 / E_1$

[1] Preferred orientation parameter, R3 in the direction normal to the deposition plane.

Ultimate Tensile Strength

Pyrolytic carbons are generally treated as brittle materials. The scatter in the fracture strength (UTS) is often rather large because failure starts from the defects existing inside and at the surface of the material. The distribution density of failure "f" is given by a statistical distribution expressed in terms of a Weibull equation whose usual expressions are:

$$f = 1 - \exp\left\{-\ln 2\left(\frac{\sigma}{\sigma_{med}}\right)^m\right\} \qquad \text{or} \qquad f = 1 - \exp\left\{-\int_V\left(\frac{\sigma}{\sigma_{0V}}\right)^m dV\right\}$$

where σ_{med} or σ_0 and m are constants whose values are determined from experiments.

Table 1-13. PyC strength parameters.

Value	UK[1]	US
"buffer" layer σ_{med} (MPa)	σ_{med} = 50	No recommendation
"dense" PyC layers σ_{med} (MPa) σ_{0V} (MPa m$^{(3/m)}$) m (/)	σ_{med} = 190 m = 7	σ_{0V} = 154.46 BAF$_0^2$ – 141.1 BAF$_0$ m = 9.5

[1] Linear adjustments for σ_{med} and m versus the density according to the data from Bongartz *et al* (1976) on results obtained from propylene derived PyC with densities between 1.73 to 1.95 g/cm^3.

Irradiation induced creep

The irradiation induced creep rate is given by the following expression:

$$\dot{\varepsilon}_1 = K\left[\sigma_1 - \nu_c(\sigma_2 + \sigma_3)\right]\frac{dD}{dt}$$

where:

K:	creep constant
σ_1, σ_2 and σ_3:	components of the stress tensor
ν_c:	Poisson's coefficient for creep
$\dfrac{dD}{dt}$:	fast neutron flux

Values of the creep constant, K, display much scatter among the different sources.

Table 1-14. PyC creep parameters.

Value	German	UK[1]	US
"buffer" layer K [MPa n m^{-2}(E> 0.1 MeV)]$^{-1}$ ν_c (/)	K = 9.6 x 10^{-30} ν_c = 0.5	K = 4.4 x 10^{-29} ν_c = 0.4	*For 1 < ρ < 2* K = K$_0$ [1 + 2.38 (1.9 - ρ)]
"dense" PyC layers K [MPa n m^{-2} (E > 0.1 MeV)]$^{-1}$ ρ (g/cm^3) θ (°C) ν_c (/)	K = 1.4 x 10^{-29} ν_c = 0.5	K = 4.4 x 10^{-29} ν_c = 0.4	*For 600 < θ < 1300* K$_0$ = 1.996 x 10^{-29} – 4.415 x 10^{-32} θ + 3.6544 x 10^{-35} θ^2 ν_c = 0.5

[1] data from Buckley et al (1975) used in STAPLE code.
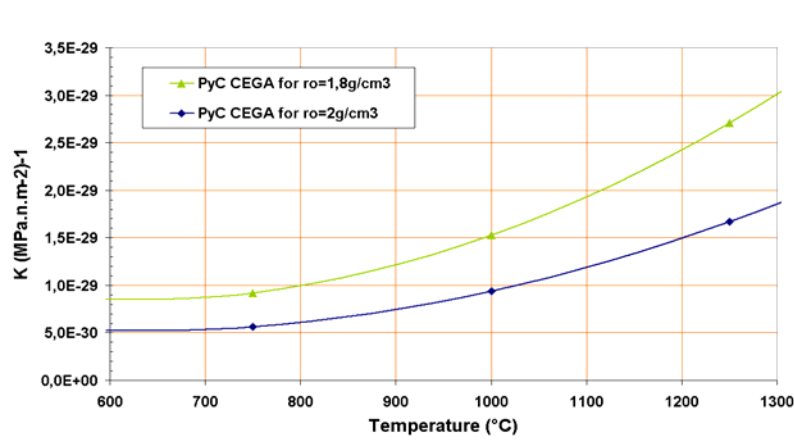
Figure 1-17. PyC irradiation induced creep constant K.

Irradiation induced dimensional change rate

Under irradiation, the buffer and the dense PyC are exposed to a fast neutron flux causing an irradiation induced dimensional change. The dimensional change rate is a strong function of the

initial density and initial anisotropy. A considerable number of measurements of dimensional change in unrestrained PyC has been reported in the open literature as shown below.

Table 1-15. PyC irradiation induced dimensional change rates.

Value	German [1]	UK [2]
"buffer" layer $\dot{\varepsilon}_r$ $\dot{\varepsilon}_\theta$ Φ $[10^{25}\,\mathrm{n\,m^{-2}}\,(>0.1\mathrm{MeV})]^{-1}$	$\dot{\varepsilon}_r = \dot{\varepsilon}_\theta = -0.176\exp(-1.75\,\Phi)$	$\dot{\varepsilon}_r = \dot{\varepsilon}_\theta = -0.241\exp(-2.2\,\Phi)$
"dense" PyC layers $\dot{\varepsilon}_r$ $\dot{\varepsilon}_\theta$ Φ $[10^{25}\,\mathrm{n\,m^{-2}}\,(>0.1\mathrm{MeV})]^{-1}$	$\dot{\varepsilon}_r = -0.077\exp(-\Phi)+0.031$ $\dot{\varepsilon}_\theta = -0.036\exp(-2.1\,\Phi)-0.01$	$\dot{\varepsilon}_r = -0.1335\exp(-1.5\,\Phi^{0.8})$ $\quad -1.12\,10^{-3}\Phi^2 + 1.85\,10^{-2}\Phi$ Approached formula for the radial deformation: If $\Phi < 4$ $\varepsilon_r = 0.164253\,\Phi^4 - 1.64495\,\Phi^3 + 6.6379\,\Phi^2 \quad - 10.4153\,\Phi$ If $\Phi > 4$ $\varepsilon_r = 0.472672\,\Phi^2 + 2.29629$ $\Phi - 15.6717$ $\dot{\varepsilon}_\theta = -0.0225\exp(-0.7\,\Phi)$ $\quad -2.1\,10^{-3}\Phi - 8\,10^{-3}$

[1] Adjustment from German source
[2] Adjustment from the data used in the code STRESS 3 (i.e. the Williams/Shipp correlation at 1200°C for a density range: 1.75 – 1.86)
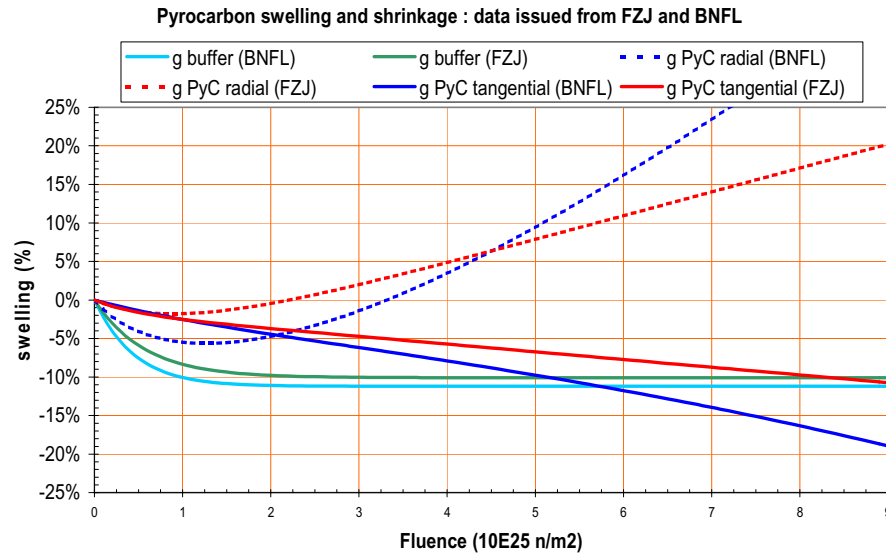
Figure 1-18. Pyrocarbon swelling and shrinkage: data from FZJ and BNFL.

The formulas below give the tangential dimensional change rate:

$$\dot{\varepsilon}_\theta \, [\%/(10^{25} \, \text{n/m}^2 \, E > 0.18 \, \text{MeV})]$$

$$\dot{\varepsilon}_\theta = CT1 + 2 \, CT2 \, \Phi$$

For $\phi > 4 \times 10^{25}$ n/m², $\dot{\varepsilon}_\theta$ is assumed to remain constant and equal to $(\dot{\varepsilon}_\theta)_{\phi = 4 \times 10^{25}}$
Coefficients CT1 and CT2 can be obtained from the following equations:

$$CT1 = CT1T2 \, \theta^2 + CT1T1 \, \theta + CT1T0$$
$$CT2 = CT2T2 \, \theta^2 + CT2T1 \, \theta + CT2T0$$

In which coefficients CTjTi are given by:

For j = 1

$$CT1Ti = c_{3i} \, BAF_0{}^3 + c_{2i} \, BAF_0{}^2 + c_{1i} \, BAF_0 + c_{0i}$$

i =	c_{3i}	c_{2i}	c_{1i}	c_{0i}
0	-2056.865	6492.003	-6837.18	2401.046
1	4.75697	-15.01806	15.82031	-5.559754
2	-2.174319×10^{-3}	6.850273×10^{-3}	-7.207533×10^{-3}	2.531618×10^{-3}

For j = 2

$$CT2Ti = d_{3i} \, BAF_0{}^3 + d_{2i} \, BAF_0{}^2 + d_{1i} \, BAF_0 + d_{0i}$$

i =	d_{3i}	d_{2i}	d_{1i}	d_{0i}
0	635.02826	-1992.5331	2084.7227	-727.22875
1	-1.4607633	4.5802947	-4.7891012	1.6699538
2	6.6869010×10^{-4}	$-2.0855729 \times 10^{-3}$	2.1688388×10^{-3}	$-7.5212054 \times 10^{-4}$
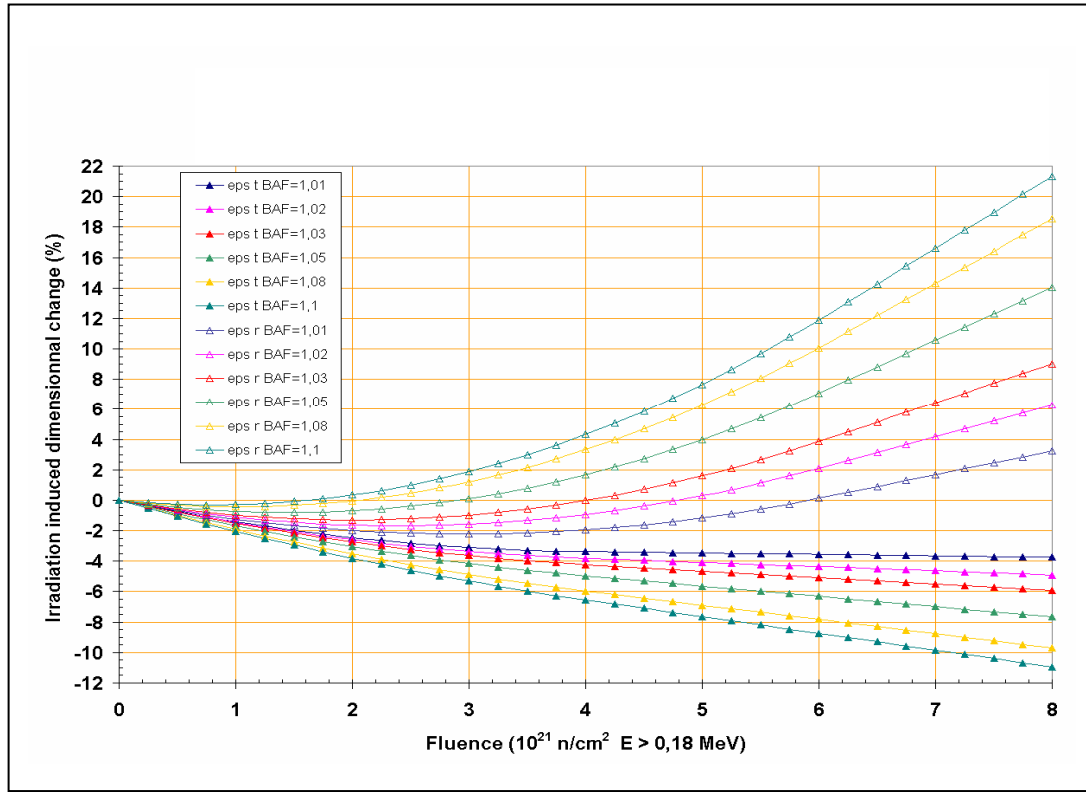
Figure 1-19. Tangential and radial irradiation induced dimensional change for PyC at T = 1200˚ C versus fluence and BAF_0.

Silicon Carbide

As for PyC layers, silicon carbide (SiC) layers of the coated particle are deposited from a mix of gases, most commonly, methyltrichlorosilane (MTS) with H_2/Ar. The microstructure of pyrolytic SiC depends on temperature and rate of deposition. The β (cubic) structure dominates, but α phase and free silicon may be present at low (<1250 °C) deposition temperature.

Material property considerations are generally less of a problem for the SiC, compared to the PyC materials. However, this layer plays a fundamental role for the mechanical and diffusion resistance of the coated particle. Consequently, a good knowledge of the ultimate tensile strength (UTS) of the SiC layer, which can be enhanced by reducing its flaws, is very important for achieving high burn-up. In this section, the properties for pyrolytic SiC are presented.

Thermal conductivity

Due to the silicon carbon covalent bond, thermal conductivity is proportional to the mean free path of phonons. This is impurity, isotropy and grain boundary type-dependent. Parameters inducing high thermal conductivity of ceramic compounds are:

- Simple crystal structure with high network symmetry
- Mono-carbide formulation
- Elements with similar atomic weight and with few isotopes
- Covalent bonds

All of the above criteria are represented in β-SiC. However, the disparity of thermal conductivity values may be significant. For example, at room temperature the values are about 500 W/ (mK) for a monocrystal, 200 W/ (m-K) for a self-bonded SiC and only 10 W/ (m-K) for a bad pyrolitic SiC.

The CEA SiC thermal conductivity model was obtained by fitting data from (Price 1973) for CVD β-SiC and is as follows:

$$\lambda (T) = A + B/T + C/T^2 + D/T^3$$

with T(K), λ(W/(mK)) and A=42.58, B=-1.5564 x10^4, C=1.2977 x 10^7 and D=-1.8458 x10^9

Thermal conductivity decreases under irradiation. A saturation phenomenon at low fluence occurs and the selected model beyond saturation was obtained by fitting Senor data (1996) and is given as follows:

$$\lambda_{irradiated}/\lambda_{unirradiated}(T) = a \cdot \exp (b \cdot T)$$

with a = 3.91112 x 10^{-2} and b = 2.24732 x 10^{-3}

To take into account the effect of porosity, a simplified correlation, $\lambda(T \cdot p) = \lambda_0 (T)(1-p)$

is used, where p is the porosity and λ_0 the dense compound conductivity.
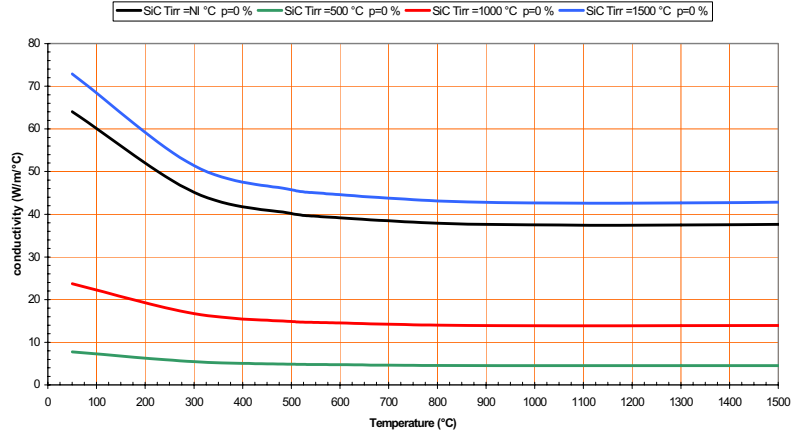
Figure 1-20. Beta-SiC thermal conductivity.

Thermal expansion

The silicon carbide thermal expansion rate is low (4-5 x 10^{-6} C^{-1}) compared to refractory carbide like WC, TiC or ZrC (7-8 x 10^{-6} C^{-1}) or oxides like Al_2O_3 (8.5 x 10^{-6} C^{-1}) or MgO (13.8 x 10^{-6} C^{-1}). The selected thermal expansion rate model, well adapted to β-SiC, was obtained by scanning Popper and Mohyuddin data and is as follows (average value):

$$\alpha(20°C \cdot T) = 3.43846 \text{ x } 10^{-6} + 1.19402 \text{ x } 10^{-9} \text{ T} - 2.05716 \text{ x } 10^{-13} \text{ T}^2$$

The thermal expansion rate doesn't change under irradiation.

Young's Modulus

The scatter among Young's modulus values is significant, which is typical of brittle materials. Nevertheless, Young's modulus decreases with increasing temperature at a rate of about one hundred GPa between 350°C and 1000°C. The selected Young's modulus model was obtained from Gulden data which appears as the most consistent data and is as follows:

$$E(T) = 432 - 0.0741T + 1.541 \text{ x } 10^{-4}T^2 - 5.401 \text{ x} 10^{-7}T^3$$
$$+ 8.142 \text{ x } 10^{-10}T^4 - 5.18 \text{ x } 10^{-13}T^5 + 1.043 \text{ x } 10^{-16}T^6$$

where E is in GPa.

32

At room temperature, CVD β-SiC is about 430 GPa. To take into account the effect of porosity, the empirical correlation $E = E_0 \cdot \exp(-C \cdot p)$ is used, where $C = 3.12$ (data available for CVD β-SiC) and p is the porosity. The Young's modulus of pyrolitic SiC doesn't change under irradiation.
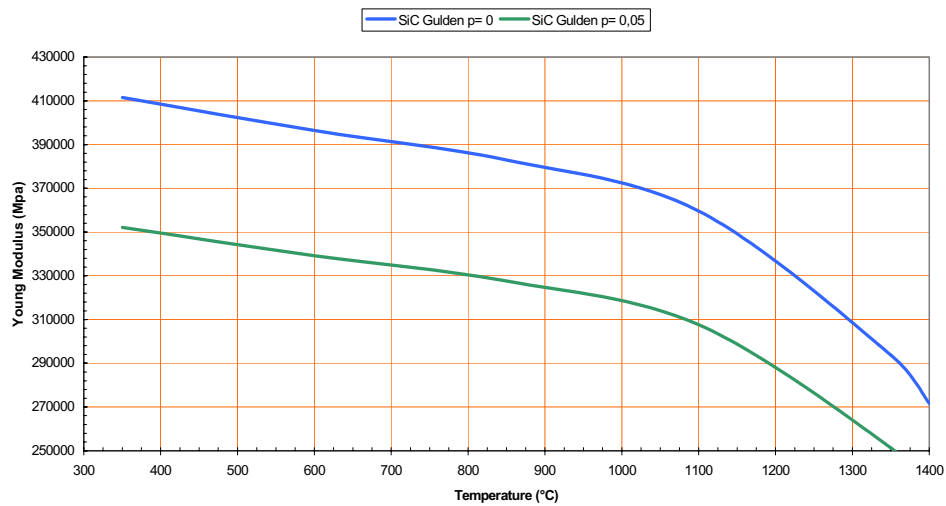
Figure 1-21. Beta-SiC Young's modulus.

Poisson's ration

A few values for Poisson's ratio as reported in the literature are listed in the following table.

Table 1-16. Poison ratio for SiC.

Reference	SiC	Density	ν
R. G. Munro	α–SiC Hexoby SA ™(2500˚C)	0.98	0.160
R.D. Carnahan	α–SiC "pressure sintered" (2100˚C)	0.99930	0.168
Compilation Battelle Institute	"reaction sintered"	0.975	0.13 to 0.24
J. Gibson	Deposition		0.18
Handbook H.O. Pierson -1996			0.142
B.O.Yavuz et R.E. Tressler	CVD β-SiC		0.13 ± 0.02
M.J. Slavin & G.D. Quinn	"Sintered" β-SiC	~0.97	0.17

Swelling

Three different areas may be distinguished concerning the neutron-induced swelling:

- Low temperature: swelling is the result of amorphisation and the volume increase is about 11 % for a total phase transformation.

- Intermediate temperature: swelling is moderate and is the result of Frenckel pairs or Frank dislocation loops accumulation.

- Elevated temperature: swelling is the result of voids creation due to lacuna migration and coalescence.

The CEA neutron-induced swelling model was obtained by fitting data from Price for CVD β-SiC and is as follows:

- Between 25°C and 800°C :

    $G_{sat}[\%] = -3.3283 \times 10^{-3}T + 3.1133$ and $G = G_{sat}.(1-\exp(-\Phi/\Phi_0))$

- Between 800°C and 1000°C :

    $G_{sat}[\%] = -1.3528 \times 10^{-3}.T + 1.5329$ and $G = G_{sat}.(1-\exp(-\Phi/\Phi_0))$

- Between 1250°C and 1500°C :

    $G[\%] = 0.18.(1-\exp(-\Phi/\Phi_0)) + 1.297 \times 10^{-26}.\Phi$

where T(K), $\Phi(n/m^2)$, E>0.1 MeV, and $\Phi_0 = 0.3396 \times 10^{25}$ n/m².

Between 1000 ˚C and 1250 ˚C, linear interpolation is required.
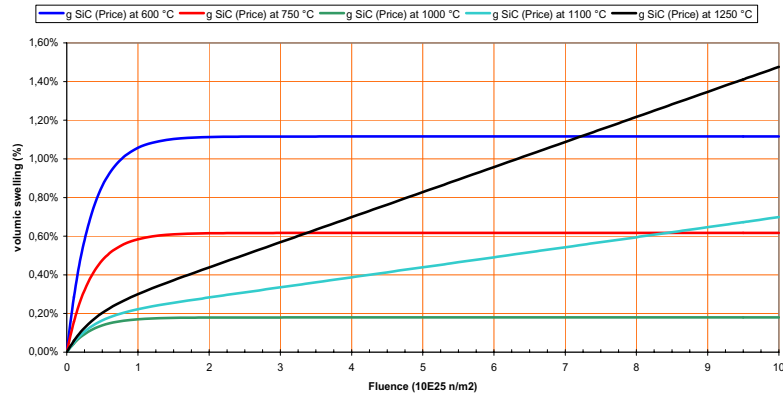
Figure 1-22. Pyrolytic beta-SiC swelling.

Irradiation creep

For neutron induced creep, the classical relation between creep equivalent strain rate, equivalent stress, and neutron flux was selected and is as follows:

$$\dot{\varepsilon}_{\text{creep}} = K_I . \dot{\Phi} . \sigma_e$$

where different values of K_I listed below depend on temperature (and are about hundred times as small as pyrocarbon values).

SiC	$T \, [°C]$	Reference	Max. fluence	Irradiation type	$K_I \, [MPa^{-1} \cdot (n/m^2)^{-1}]$
β-SiC *	650	Price	4.18 x 10^{25} n/m^2	Neutronic	0.2 to 0.264 x 10^{-31}
β-SiC *	800	Price	7.7 x 10^{25} n/m^2	Neutronic	0.4 x 10^{-31}
β-SiC *	900	D.G.Martin	4.62 x 10^{25} n/m^2	Neutronic	0.4 x 10^{-31}
β-SiC *	> 1100	CEGA		Neutronic	1.82 x 10^{-31}

Fracture strength

CVD β-SiC mean fracture strength value varies within the range of 60 to 3100 MPa. The wide range of ceramic fracture strength is due to the differences in size, shape, location and direction of the micro-defects coupled with the lack of ductility of such material. SiC displays:

- A large dispersion of results for exactly identical test specimens and

- close correlation between fracture strength mean values and associated loading types, specimen volume, test type (bending, crushing, bursting…).

The fracture strength is not an intrinsic feature of a given ceramic and needs a probabilistic approach. The most useful approach is the Weibull theory, which supposes that:

- The solid is statistically homogeneous (juxtaposition of independent micro-structural elements).

- The fracture of the least resistant element causes the total collapse of the structure.

The cumulative failure probability of ceramic material is given by the following conventional expression:

$$P_R = 1 - \exp\left[-\int_D \left(\frac{\sigma(x,y,z)}{\sigma_{0D}} \right)^m \cdot dD \right]$$

where D is a dimension (Volume, Surface or Line), σ is a tensile stress dependent of the location (x, y, z), m is the Weibull modulus and σ_{0D} is a characteristic strength (homogeneous to a stress multiplied by a length to the power i/m with i = 1 (line), 2 (surface) or 3 (volume)).

Values for the modulus m, given by the literature are scattered and are dependent upon the fabrication method of the SiC. At room temperature, m varies within the range of 1.5 to 14. For CVD β-SiC, a recommended value is 6.

For σ_{0D}, a few values are given by the literature but results are not very consistent as shown below:

- CEGA $\qquad\qquad\qquad\qquad$ $\sigma_{0V} = 9.64$ MPa m$^{3/6}$ (m=6)
- CEA re-analysis $\qquad\qquad\quad$ $\sigma_{0V} = 24.6$ MPa m$^{3/5.8}$ (m=5.8)

Another widely used approach is to express the cumulative failure probability as:

$$P_R = 1 - \exp\left[-\ln(2) \cdot \left(\frac{\sigma_R}{\sigma_{R\frac{1}{2}}} \right)^m \right]$$

where σ_R is the calculated maximum stress in the material and $\sigma_{R1/2}$ the mean fracture strength, which is dependent upon the specimen and its loading.

Weibull distribution

- SiC (FZJ) fluence = 0 10E25n/m2 T(°C) = 1200 sigmean = 834 MPa m = 8,02
- SiC (FZJ) fluence = 1 10E25n/m2 T(°C) = 1200 sigmean = 750 MPa m = 6,84
- SiC (FZJ) fluence = 5 10E25n/m2 T(°C) = 1200 sigmean = 414 MPa m = 2,16
- SiC (FZJ) fluence = 5 10E25n/m2 T(°C) = 900 sigmean = 510 MPa m = 3,5
- SiC (FZJ) fluence = 0,15 10E25n/m2 T(°C) = sigmean = 572 MPa m = 5,89
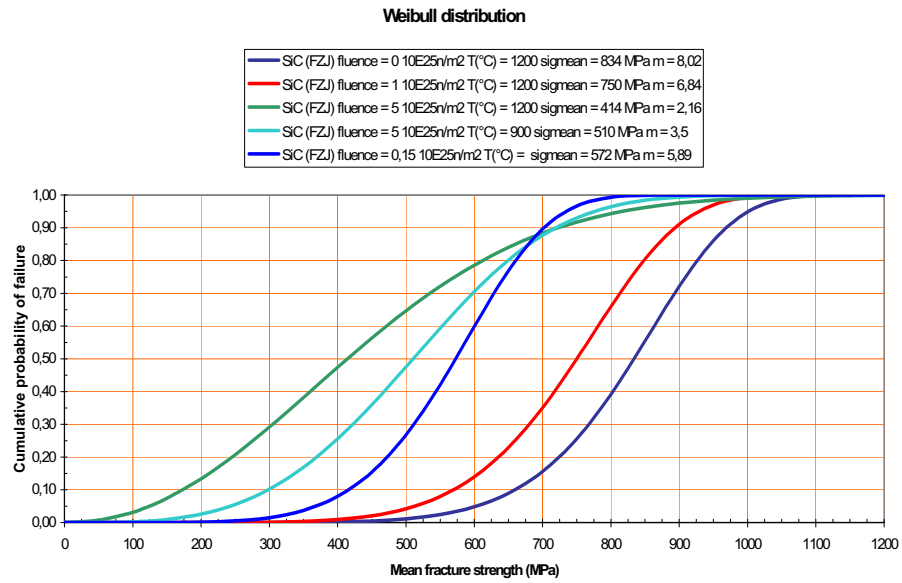
Figure 1-23. Weibull distribution.

Filename: 2. I-NERI Task 1.doc
Directory: C:\Documents and Settings\talbhd\Desktop\FINAL INERI JAN3
Template: C:\Documents and Settings\talbhd\Application
    Data\Microsoft\Templates\Normal.dot
Title: TASK 1: INFORMATION EXCHANGE ON EXISTING PARTICLE
    FUEL DATA, MODELS, AND COMPREHENSION
Subject:
Author: test
Keywords:
Comments:
Creation Date: 1/5/2005 12:31:00 PM
Change Number: 3
Last Saved On: 1/6/2005 9:43:00 AM
Last Saved By: test
Total Editing Time: 2 Minutes
Last Printed On: 1/18/2005 10:47:00 AM
As of Last Complete Printing
    Number of Pages: 37
    Number of Words: 7,120 (approx.)
    Number of Characters: 35,530 (approx.)

2. TASK 2: DEVELOPMENT OF AN INTEGRATED MODEL TO EVALUATE THE MECHANISMS OF FAILURE FOR CLASSICAL TRISO PARTICLES IN THERMAL GAS REACTOR SPECTRUM

Responsible Lead: INEEL

Brief Discussion of Objectives:

The purpose of this task was to develop an integrated fuel performance model to evaluate mechanisms that contribute to particle failure. Information obtained from the exchanged of existing models and material property databases were used in this development. The existing models were used as the basis for developing the extended model.

2.1 Task Technical Overview – INEEL

The INEEL is developing an integrated fuel performance model called PARFUME with the objective of physically describing both the mechanical and physico-chemical behavior of the fuel particle under irradiation. The model includes multi-dimensional failure mechanisms in addition to the traditional pressure vessel failure. For example, studies conducted at the INEEL (Miller et al. 2001) indicated that shrinkage cracks in the IPyC could contribute significantly to particle failures. Much effort to date has been directed toward including this failure mechanism in the model in addition to other multi-dimensional mechanisms, such as partial debonding between the IPyC and SiC layers and particle asphericity.

A typical TRISO-coated particle is shown in Figure 2-1. Fission gas pressure builds up in the kernel and buffer regions, while the IPyC, SiC, and OPyC act as structural layers to retain this pressure. The basic behavior modeled in these analyses is shown schematically in Figure 2-2. The IPyC and OPyC layers both shrink and creep during irradiation of the particle while the SiC exhibits only elastic response. A portion of the gas pressure is transmitted through the IPyC layer to the SiC. This pressure continually increases as irradiation of the particle progresses, thereby contributing to a tensile hoop stress in the SiC layer. Countering the effect of the pressure load is the shrinkage of the IPyC during irradiation, which pulls inward on the SiC. Likewise, shrinkage of the OPyC causes it to push inward on the SiC. Failure of the particle is normally expected to occur if the stress in the SiC layer reaches the fracture strength of the SiC.

Failure of the SiC results in an instantaneous release of elastic energy that should be sufficient to cause simultaneous failure of the pyrocarbon layers.

Numerous material properties are needed to represent fuel particle behavior in the performance model. These include irradiation-induced strain rates used to represent shrinkage (or swelling) of the pyrocarbon layers, creep coefficients to represent irradiation-induced creep in the pyrocarbon layers, and elastic properties to represent elastic behavior for the pyrocarbons and silicon carbide. The properties currently used were obtained from data that was compiled in a report by the CEGA Corporation (CEGA 1993).

OPyC
SiC
IPyC
Buffer
Kernel

631 μm
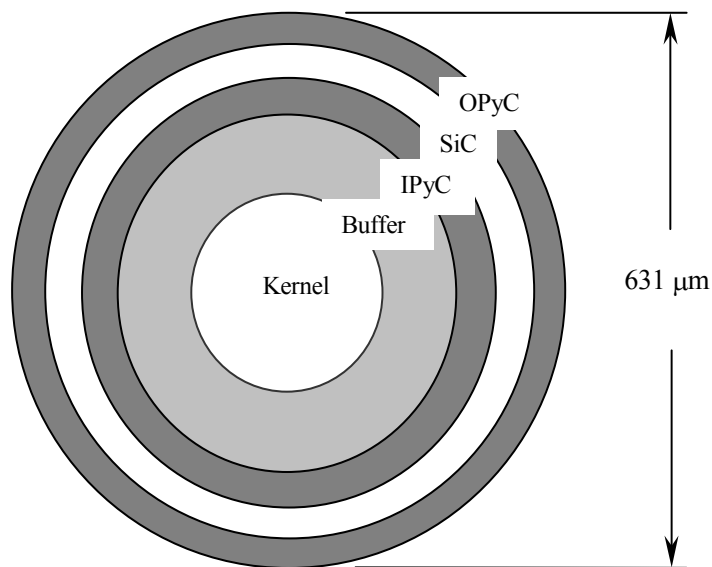
Figure 2-1. Representative fuel particle.

IPyC　　　　　**SiC**　　　　　**OPyC**

shrinks and creeps　　　elastic　　　shrinks and creeps

Gas Pressure

| 1 |
| 2 |
| 3 |
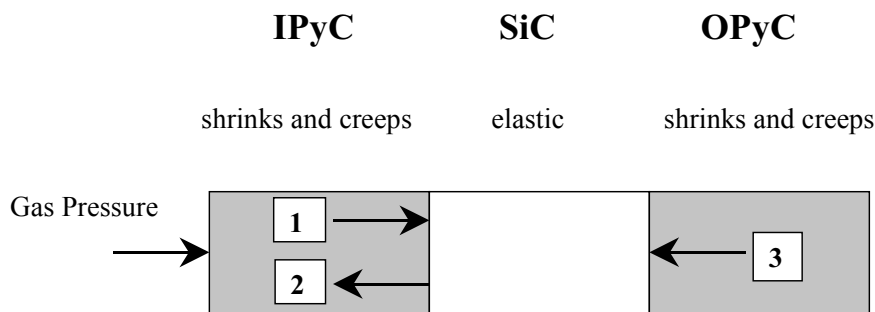
1　Gas pressure is transmitted through the IPyC

2　IPyC shrinks, pulling away from the SiC

3　OPyC shrinks, pushing in on SiC

Figure 2-2. Fuel particle behavior.

The stresses in a perfectly spherical TRISO-coated particle can be accurately predicted with a closed-form solution. One-dimensional models such as this have historically been used to evaluate fuel particles for potential failures caused by the buildup of internal fission gas pressure. The coated fuel designed in the US, however, has incurred significantly greater levels of failure than are predicted considering just one-dimensional pressure vessel failures, indicating that other mechanisms contributed to failure of the particles. Post-irradiation examinations have revealed the presence of radial shrinkage cracks in the IPyC and OPyC layers, partial debonding between the IPyC and the SiC, and deviations from a spherical shape. It has previously been shown that shrinkage cracks in the IPyC layer can contribute significantly to the failure of fuel particles (Miller et al. 2001). This section documents the effects of partial debonding and asphericity on particle failure probability. The results presented serve to identify circumstances where these multi-dimensional effects may contribute to the failure of fuel particles.

New Statistical Method

A new statistical method was developed and incorporated into the PARFUME code that treats parametric variations in the multi-dimensional behavior of fuel particles. Multi-dimensional behavior includes cracking of the IPyC layer, partial debonding between the IPyC and SiC layers, and asphericity in the particle geometry. The statistical approach was needed to develop equations that can be used to efficiently calculate stresses in a random particle, where several design or fabrication parameters may deviate from their nominal values. These equations are used in a Monte Carlo simulation to calculate failure probabilities for a batch of fuel particles. The method has been used to predict failure probabilities for several experiments, considering the effect of shrinkage cracks in the IPyC layer on fuel particle behavior.

Our initial statistical approach was to perform regression analyses using the Design Expert program (Whitcomb et al. 1993) to produce an algorithm that predicts the stress level in the SiC layer of particles that have a cracked IPyC. This program used response surface analysis to develop a sixth-order polynomial that statistically fit stress data (obtained from finite element analyses) to a high level of accuracy when variations in six parameters were considered. This involved full-factorial regression analysis that required a total of 972 finite element (FE) analysis runs using the ABAQUS computer program (Hibbitt, Karlsson, and Sorenson 1998). A problem with this statistical treatment is that the number of finite element analyses required becomes overwhelming when 1) additional parametric variations are introduced, 2) the fundamental material properties that were used in the analyses (such as the shrinkage of the pyrocarbons) are changed, or 3) a different failure mechanism is considered.

Therefore, an alternative method was developed that greatly reduces the number of finite element analyses needed. The approach is to perform finite element analyses on just enough cases to determine the effects of varying each parameter individually. The same cases are then analyzed using a closed-form solution that solves for stresses in a normal (uncracked) TRISO fuel particle (Miller and Bennett 1993). Finally, statistical fits are performed on the results of the analyses and a correlation is drawn between the stress in an uncracked particle with the stress in a cracked particle for the same parametric variations. Implementing this in the performance model, the stress in the SiC layer of a particle having a cracked IPyC is determined by first computing the stress for the same particle having an intact IPyC. This stress is then converted to a stress for a cracked particle by applying the correlations. The equation used to estimate stress in the SiC layer, which is a function of multiple parameters, is:

$$\sigma_c(v_j, v_k, v_l,...) \cong \frac{\sigma_{c\bar{v}}}{\sigma_{u\bar{v}}} \sigma_u(v_j, v_k, v_l,...) h_j(\Delta v_j) h_k(\Delta v_k) h_l(\Delta v_l)... \qquad (1)$$

where,

$\sigma_c(v_j, v_k, v_l,...) =$ maximum stress in the SiC layer of a cracked particle as a function of multiple parameters,

$\sigma_u(v_j, v_k, v_l,...) =$ maximum stress in the SiC layer of an uncracked particle for the same parameters,

$\sigma_{c\bar{V}} =$ maximum stress in the SiC layer of a cracked particle having mean values for all parameters,

$\sigma_{u\bar{V}} =$ maximum stress in the SiC layer of an uncracked particle having mean values for all parameters,

$h_j(\Delta v_j) =$ correlation function for parameter v_j,

$\Delta v_j =$ variation of parameter v_j from its nominal value.

It was shown through benchmark analyses (as shown in Table 2-1) that results obtained from using this equation correlated very well with results from the Design Expert algorithm. The two equations were used in calculating failure probabilities for hypothetical fuel particle batches having statistical variations in six parameters as shown in the table. The difference between the two cases was in the size of the standard deviations for the six parameters. In these calculations, a particle was considered to fail if the SiC layer was determined to fail.

Table 2-1. Comparison of failure probability calculations for two statistical methods.

Case	Mean values and standard deviations						% Failed	
	IPyC thick. (μm) [Std. Dev.]	SiC thick. (μm) [Std. Dev.]	OPyC thick. (μm) [Std. Dev.]	IPyC dens. (10^6g/m^3) [Std. Dev.]	IPyC BAF [Std. Dev.]	Irrad. temp. (°C) [Std. Dev.]	Design Expert	New method, Eq. (1)
1	40 [5]	35 [5]	43 [5]	1.90 [0.02]	1.16 [0.02]	1000 [30]	0.80	0.80
2	40 [8]	35 [8]	43 [8]	1.90 [0.05]	1.16 [0.05]	1000 [50]	1.24	1.18

Because the equation above does require performing several finite element analyses to develop the correlation functions h_i, using this equation still entails significant effort if a new set of correlation functions must be developed for every batch of particles considered. This generally is the case if the parametric mean values change significantly from one batch to the next. Therefore, a simplified form of the equation was developed by simply setting the h functions equal to one. The rationale for doing this was that the product of the h functions for the particles in a batch tends to fluctuate (from particle to particle) about an average value that is very near to 1.0. The resulting equation then requires that only one finite element analysis (to calculate $\sigma_{c\bar{v}}$) be performed to determine the failure probability for a particle batch:

$$\sigma_c(\nu_j, \nu_k, \nu_l, \ldots) \cong \frac{\sigma_{c\bar{v}}}{\sigma_{u\bar{v}}} \sigma_u(\nu_j, \nu_k, \nu_l, \ldots) \qquad (2)$$

To evaluate the accuracy of Equation 2, results obtained from its use were compared to results obtained from Equation 1 for four cases involving variations in six parameters (Table 2-2). A new set of correlation equations, h, was developed for each of the four cases. It is seen that reasonable correlations were attained in all cases. Finally, two cases were evaluated where the number of varying parameters was increased from six to eleven, as shown in Table 2-3. Results from these cases again show a favorable correlation between Equations 1 and 2.

Table 2-2. Comparison of failure probability calculations for new method, Equation 2 vs. Equation 1.

Case	Mean values						% Failed	
	IPyC thick. (µm)	SiC thick. (µm)	OPyC thick. (µm)	IPyC dens. (10^6g/m^3)	IPyC BAF	Irrad. Temp. (°C)	w/ h functions (Eq. 1)	wo/ h functions (Eq. 2)
1	40	35	43	1.90	1.16	1000	0.80	1.10
2	45	30	40	2.00	1.10	700	13.8	14.6
3	35	40	50	1.82	1.24	900	0.64	0.81
4	30	45	53	1.80	1.32	600	1.51	1.62

Table 2-3. Statistical variations and results for eleven-parameter cases.

Parameter	Mean value (case 1)	Mean value (case 2)	Standard deviation
IPyC thickness (μm)	50	40	5
SiC thickness (μm)	25	35	5
OPyC thickness (μm)	50	40	5
IPyC density (10^6 g/m^3)	1.8	1.9	0.02
OPyC density (10^6 g/m^3)	1.8	1.9	0.02
IPyC BAF	1.24	1.06	0.02
OPyC BAF	1.04	1.06	0.02
Irradiation temp. (°C)	700	1000	30
Creep amplification	3	2	0.2
Kernel diameter (μm)	200	500	20
Buffer thickness (μm)	120	100	10
	Results		
	Case 1	Case 2	
% failed, per Eq. 1	1.31	0.004	
% failed, per Eq. 2	1.05	0.003	

Results above indicate that Equation 2 can typically be used to produce reasonable estimates for failure probabilities in a general batch of fuel particles. Equation 1 can be used in situations where a more accurate estimate is desired. This approach has the capacity to treat statistical variations in all of the design parameters for TRISO-coated fuel particles. It has been described above in terms of fuel particles having a cracked IPyC, but should also be applicable to other multi-dimensional behavior. It is therefore anticipated that this method will facilitate the development of a fuel performance code that is capable of treating multi-dimensional failure mechanisms together with statistical variations in a wide range of design parameters.

Approach for Determining Whether the SiC Fails

The correlation equations developed for particles having a cracked IPyC were programmed into the fuel performance code. The next step was to utilize the stresses calculated to determine particle failure probabilities in the fuel performance model. Using a fracture mechanics approach to determine whether a cracked IPyC layer results in failure of the SiC would require calculation of a stress intensity at the crack tip. Such a calculation is greatly complicated by the fact that there is a material discontinuity at the interface between the IPyC and SiC layers. It is

believed that the SiC failures will follow a Weibull statistical distribution, having a mean strength σ_{mc} and a modulus m. The mean strength is a function of the stress distribution and geometry of the SiC layer, and is derived below from the characteristic strength σ_0. In the Weibull theory, the failure probability for the SiC is given by:

$$P_f = 1 - e^{-\int_V (\sigma/\sigma_0)^m \, dV} \tag{3}$$

where,

$P_f =$ probability of failure of the SiC,

$\sigma =$ stress in the SiC layer,

$\sigma_0 =$ Weibull characteristic strength for the SiC material,

$m =$ Weibull modulus for the SiC material,

$V =$ volume of the SiC layer.

Once finite element results are obtained from the analysis of a cracked particle, the stress integration above can be performed using the principle of independent action (PIA) model for treating multiaxial stress states (Nemeth et al. 1989):

$$\int_V \sigma^m \, dV = \int_V (\sigma_1^m + \sigma_2^m + \sigma_3^m) \, dV \tag{4}$$

where,

$\sigma_1, \sigma_2, \sigma_3 =$ the three components of principal stress.

Since only tensile stresses contribute to fracture of the material, compressive stresses are not included in the integration. Only stresses in the finite elements of the SiC layer in the immediate vicinity of the crack tip make a meaningful contribution to the integral. The integration is performed using stress values calculated at integration points in the ABAQUS analysis. The minimum principal stress σ_1 is always negative, and therefore makes no contribution. This component is neglected in these analyses.

Based on the magnitude of stresses calculated at integration points near the crack tip, the integral above assumes a value which can be written as follows:

$$\int_V \sigma^m \, dV = \sigma_c^m \int_V f(V) \, dV = \sigma_c^m (I) \tag{5}$$

where σ_c is the maximum value calculated for the stress anywhere in the volume. The integral I is a normalized integration of the stress distribution, where the maximum stress (taken to the m power) has been factored out. The failure probability then becomes

$$P_f = 1 - e^{-\sigma_c{}^m (I) / \sigma_0{}^m} \qquad (6)$$

The fuel performance model is set up to calculate the failure probability according to the following:

$$P_f = 1 - e^{-(\sigma_c / \sigma_{ms})^m} \qquad (7)$$

The mean strength σ_{ms} is the stress level at which 63.2% of the particles would fail if all were stressed equally, as seen by setting $\sigma_c = \sigma_{ms}$ in Equation (7). PARFUME executes Equation (7) in a Monte Carlo simulation by calculating a stress σ_c for each particle and comparing that stress to a strength σ_s that is sampled for that particle according to the following equation (which is obtained from Equation 7):

$$\sigma_s = \sigma_{ms} e^{[\ln(-\ln F)] / m} \qquad (8)$$

where F is a random number between 0 and 1.

The mean strength is determined by applying the condition that the failure probability calculated by the fuel performance model per Equation (7) essentially equal that of Equation (6). This is done by equating the exponents for the two equations and using stresses obtained from a finite element analysis on a particle having nominal values for all parameters to determine the integral I. The effective mean strength for the SiC layer of a particle having a cracked IPyC is then defined to be:

$$\sigma_{ms} = \sigma_0 / I_n{}^{1/m} \qquad (9)$$

where the subscript n denotes a particle having nominal values for all parameters. This value for σ_{ms} is used in the fuel performance model per Equation (7) to perform Weibull statistical evaluations of failure on those particles having a cracked IPyC.

Flow Diagram for PARFUME Methodology

The methodology currently envisioned in PARFUME is summarized in Figure 2-3.

Finite element analysis

Analysis of nominal particle

Statistical analysis

Input parameters

Perform finite element analysis (to calculate SiC stress) on selected cases for particle having a cracked IPyC.

Calculate SiC stress for a nominal (uncracked) particle (using closed-form solution) for the same cases.

Perform regression analysis on analysis results.

Develop correlation equations that convert the SiC stress from the closed-form solution to a stress for the cracked particle (for any combination of parametric variations).

Determine Weibull mean strengths

Failure probability determination

Cumulative failure probability

Use results of analyses on particle having nominal parameters to determine Weibull mean strengths for the IPyC and SiC layers. The SiC layer has different strengths for the cracked vs. uncracked particle.

Input correlation equations and Weibull mean strengths into PARFUME. (Correlation equations are not needed when using Eq. 2.)

Use Monte Carlo sampling and Weibull statistics to determine a failure probability for particles having a cracked IPyC (considering all relevant parametric variations). First, determine whether the IPyC cracks. If so, then determine whether the particle fails.

If the IPyC layer in a sampled particle does not crack, then determine whether the particle fails due to a traditional pressure vessel failure. If so, then include these in a cumulative failure probability.

Similarly, calculate failures due to other failure mechanisms and add these to total.

Figure 2-3. Flow diagram for PARFUME Methodology.

Predictions for NPR Experiments

Predictions for fuel particle failure probabilities have been made for three irradiation experiments conducted as part of the New Production – Modular High Temperature Gas-Cooled Reactor (NP-MHTGR) program in the early 1990s. These predictions reflect the latest pyrocarbon creep and shrinkage properties and current gas release model used in the PARFUME code. In these experiments, fuel compacts were irradiated at the High Flux Isotope Reactor (HFIR) and the Advanced Test Reactor (ATR) in the United States. TRISO-coated particles containing high-enriched uranium were irradiated at temperatures between 750 and 1250 °C, burnups between 65 and 80 %FIMA, and fluences between 2 and 3.8×10^{25} n/m^2. On-line fission gas release measurements indicated significant failures during irradiation. Post-irradiation examination (PIE) of individual fuel compacts revealed the presence of radial cracks in all layers of the TRISO coating. The irradiation conditions for the experiments are summarized in Table 2-4, while the levels of cracking measured during PIE are shown in Table 2-5. The particle dimensions, burnup, end-of-life fluence, irradiation temperature, ^{235}U enrichment, densities and BAF for the pyrocarbons, etc., were based on fabrication records for the fuel and on the service conditions measured during irradiation for each experiment.

To assess the effect of temperature variability during irradiation on particle stresses, ABAQUS calculations were performed with both the actual volume averaged temperature history and the time averaged volume averaged temperature for NPR-1 compact A5. The actual volume averaged temperature for the compact varied from about 1150 to 870 °C during the experiment, while the time averaged, compact volume averaged temperature was 987 °C (Baldwin et al. 1993). Calculated time histories for principal stresses in the SiC layer are presented in Figure 2-4, which show that the stress histories compare closely for these two cases. These results indicate that using a time averaged volume averaged temperature in the PARFUME predictions is a good approximation to the use of actual temperature histories.

Included in the results shown in Table 2-5 (column 5) are the percentage of particles predicted to have a cracked IPyC and the percentage of particles predicted to fail because of a cracked SiC. It is seen that PARFUME predicts that the IPyC layer cracks in 100% of the particles for every compact tested. In reality, the PIE revealed that the actual failure fractions were less than this, as shown in the table. Based on historical literature sources, it is believed that the creep coefficients recommended in (CEGA 1993) and currently used in the PARFUME code may be too low, which would allow the calculated shrinkage stresses to reach too high a value before

creep relaxation takes effect. If the creep coefficients used in the analyses were amplified by a factor of 1.8, which is closer to values used in older performance codes (Kaae et al. 1971; Martin 2001), the number of failures in the IPyC and SiC decrease as shown in Table 2-5 (column 6). The higher creep gives better agreement with the experimental results.

It is noted that because the ratio $\sigma_{c\bar{V}} / \sigma_{u\bar{V}}$ in Equation 2 maintained essentially the same value for all four NPR compacts (~0.79), only one finite element analysis of a cracked particle would have been needed to generate the failure probabilities of Table 2-5.
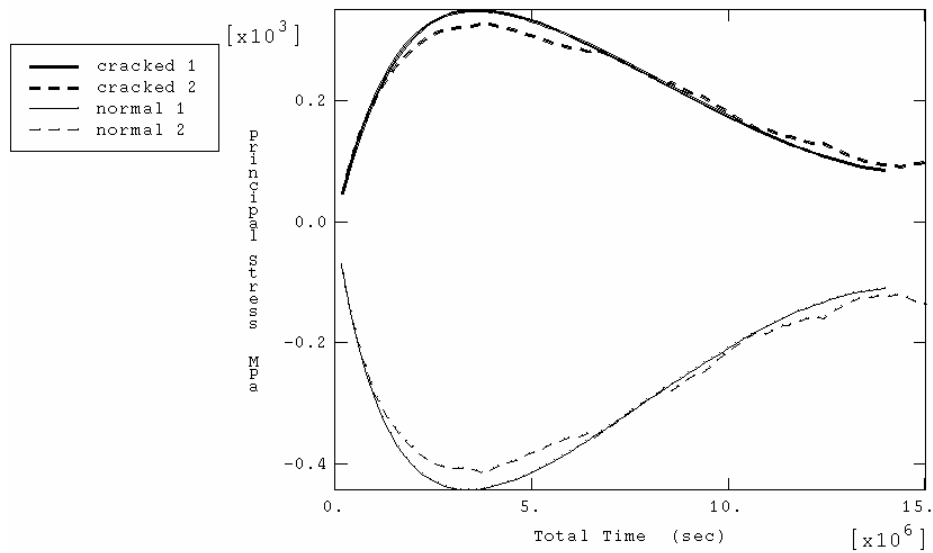
Figure 2-4. SiC stress history comparisons for 1) time averaged temperature vs. 2) actual temperature in cracked and uncracked particles of NPR-1 A5 irradiation experiment.

Table 2-4. Irradiation conditions for NPR experiments.

Fuel Compact ID	Fast Fluence $(10^{25}$ n/m$^2)$	Irradiation temp. (°C), average	Burnup (%FIMA)
NPR-2 A4	3.8	746	79
NPR-1 A5	3.8	987	79
NPR-1 A8	2.4	845	72
NPR-1A A9	1.9	1052	64

Table 2-5. Comparisons of ceramographic observations to PARFUME calculations for TRISO coated fissile fuel particles.

IPyC Layer(a)					
Fuel Compact ID	Sample Size	% Failed	95% Conf. Interval (%)	Calc.	Calc. with 1.8x creep
NPR-2 A4	83	65	54<p<76	100	99.8
NPR-1 A5	39	31	17<p<47	100	34.8
NPR-1 A8	53	6	2<p<16	100	94.0
NPR-1A A9	17	18	5<p<42	100	14.5
SiC Layer (a)					
	Sample Size	% Failed	95% Conf. Interval (%)	Calc.	Calc. with 1.8x creep
NPR-2 A4	287	3	2<p<6	9.2	3.4
NPR-1 A5	178	0.6	0<p<3	1.8	0.22
NPR-1 A8	260	0	0<p<2	5.9	1.8
NPR-1A A9	83	1	0<p<5	1.1	0.044

a. Layer failure is considered to be a through wall crack as measured by PIE.

HRB-21 Experiment

Initial failure probabilities were also calculated for the HRB-21 experiment. Irradiation conditions for this test are listed in Table 2-6, where it is seen that the primary differences between the compacts are the fast fluence and the irradiation temperature.

Table 2-6. Irradiation conditions for HRB-21 experiment.

Fuel Compact ID	Fast Fluence (10^{25} n/m^2)	Irradiation temp.(°C), average	Burnup (%FIMA)
1C	1.5	800	14.0
2B	2.3	980	18.0
4A	3.5	1000	22.5

The observed and calculated failure fractions for the IPyC and SiC layers in the HRB-21 experiment are presented in Table 2-7. The calculated failures for the IPyC and SiC layers (based on $1.8 \times$ creep) were greatest for compact 1C and least for compact 4A, contrary to what occurred in the tests. This suggests that the material properties used in the calculations may not accurately represent these particles, or that there was an effect in the experiment not captured in the calculations. Further analyses of this experiment, incorporating more exact experimental conditions will be conducted. Since HRB-21 displayed wide temperature variations over time

and across the compacts (much wider than that in the NPR experiments), future calculations will first investigate the use of actual temperature histories (as opposed to the time and volume averaged temperature used in the initial calculations).

Table 2-7. Failure fractions during irradiation for HRB-21 experiments.

IPyC Layer				
Fuel Compact ID	Sample Size	% Failed	95% Conf. Interval (%)	Calc. (with 1.8× creep)
1C	96	1	0<p<5	70.6
2B	70	3	0<p<9	9.7
4A	61	33	18<p<48	7.3
SiC Layer				
	Sample Size	% Failed	95% Conf. Interval (%)	Calc. (with 1.8× creep)
1C	96	0	0<p<4	5.4
2B	70	0	0<p<6	0.16
4A	61	5	0<p<13	0.10

Debonding Between the IPyC and SiC Layers

The failure predictions above focus on failures associated with shrinkage cracks that develop in the IPyC layer during irradiation. Another form of multi-dimensional behavior that may contribute to particle failures is debonding between the IPyC and SiC layers. The statistical methodology presented above can be used to evaluate failures caused by debonding as well as failures caused by a cracked IPyC layer.

Partial debonding between the IPyC and the SiC has been observed in PIE of the NP-MHTGR fuel particles. During irradiation, shrinkage of the IPyC layer induces a radial tensile stress at the interface between the IPyC and SiC layers. If the stress exceeds the bond strength between layers, then debonding of the IPyC from the SiC occurs. The debonding process is not likely to be an instantaneous detachment over the entire surface of the interface. Rather, it begins at an initiation point from which the layers progressively unzip during irradiation. An axisymmetric finite element model for the debonded geometry is shown in Figure 2-5. The model plotted is a deformed shape as it appears part way through irradiation, after the unzipping process has begun.

51
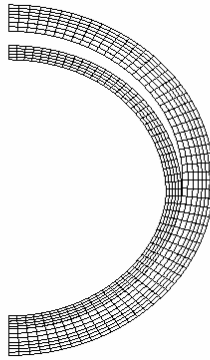
Figure 2-5. Finite element model for a partially debonded particle.

A typical debonded particle was analyzed in a viscoelastic time-integration analysis that progressed until the fluence reached a value of 3×10^{25} n/m^2, occurring at a time of 1.2×10^7 sec in the analysis. In the ABAQUS analysis, the IPyC and SiC were initially assumed to be debonded at an arbitrary point in the model. Continued debonding, if it occurred, then progressed from this point. The criterion used was that the next node ahead of the crack tip debonds when the local stress across the interface at a specified distance ahead of the crack tip reaches the specified bond strength. Figure 2-6 shows the stress concentration that occurs in the SiC layer at the tip of the debonded region. The stress plotted is the maximum principal stress, which is tensile at the tip of the crack. As with a cracked IPyC, this stress concentration can contribute to failure of the SiC. Figure 2-7 plots a time history for the maximum calculated principal stress at a point (point 1) on the inner surface of the SiC layer along the debonded path. The stress at this point rose to a peak as the tip of the debonded region passed through this location. With continued unzipping between layers, the stress at this location rapidly diminished. Also shown in Figure 2-7 is a stress history at a point further down the debonded path (point 2). As would be expected, the stress at this point peaked at a later time during irradiation.
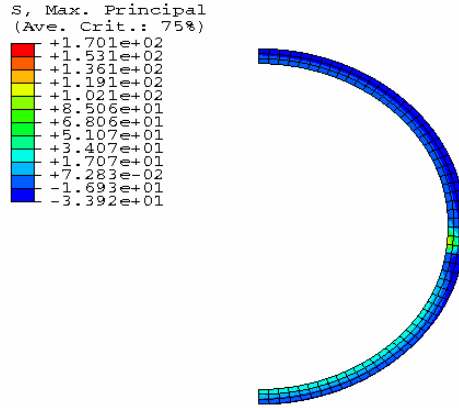
Figure 2-6. Stress concentration at the tip of the debonded region.
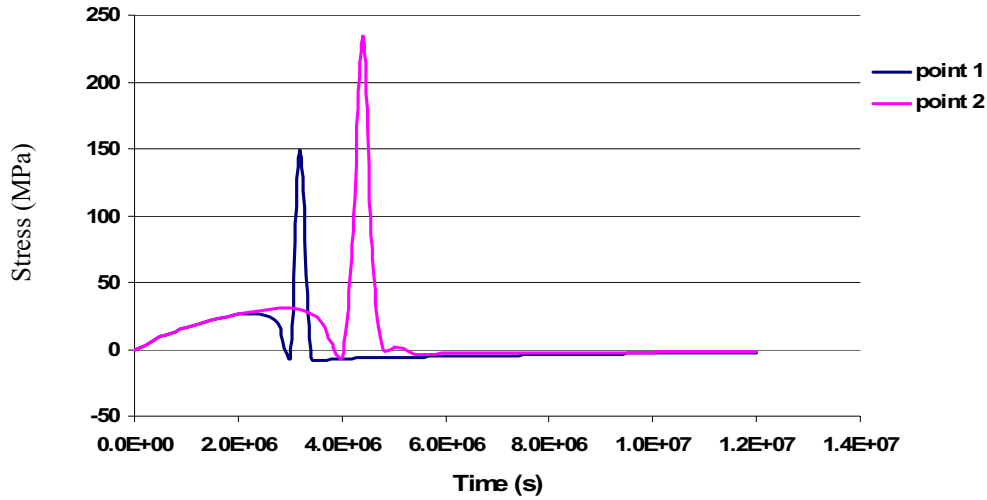
Figure 2-7. Stress histories at two points along the debonded path.

To evaluate particles for potential failure due to debonding, PARFUME first determines whether debonding occurs. It calculates the radial stress at the interface between the IPyC and SiC layers using the closed-form solution, and compares this stress to the bond strength between layers. If PARFUME determines that debonding occurs, it then calculates a maximum stress for the SiC layer utilizing the statistical method described above (Eq. 1 or 3). Calculations performed herein utilized Eq. (3), which required that only one FE analysis be performed for each batch of particles considered. PARFUME compares this stress to a strength that is sampled from a

Weibull distribution having mean strength σ_{ms} and modulus m. The mean strength is calculated from Eq. (4), where the integral I_n represents a stress distribution obtained from the ABAQUS analysis of a debonded particle having mean values for all parameters (referred to as a nominal particle). With the moving crack tip, significant stress concentrations may occur at numerous points along the debonded path. These stress concentrations are typically not as severe as those at the crack tip of a cracked IPyC, but they occur over a larger portion of the SiC volume. Because the peak stresses at these points do not occur simultaneously, caution must be exercised in calculating I_n to ensure that the stress distribution is based on the maximum stresses that occur at any time during irradiation.

The effects of partial debonding were evaluated by performing failure probability calculations on representative particles assuming a range of values for the bond strength between the IPyC and SiC layers (0 to 60 MPa). The input parameters for four cases are summarized in Table 2-8. Each value for the bond strength considered in these calculations was represented by its own batch of particles. Within each batch of particles, the primary statistical variation from particle to particle was a Weibull distribution in the SiC strength. Because the stress distribution in the particle layers change with variations in the bond strength, the Weibull mean strength σ_{ms} from Eq. (4), which is obtained by integrating tensile stresses over the volume of the SiC, indirectly becomes a function of the bond strength. Thus, a new value was calculated for σ_{ms} for each bond strength considered. Statistical variations of small standard deviations were applied to several of the parameters of Table 2-8, but these had only a slight effect on the calculated failure probabilities.

Table 2-8. Input parameters for debonding calculation.

Parameter	Units	Case 1	Case 2	Case 3	Case 4
Kernel diameter	μm	500			
Buffer thickness	μm	100			
IPyC thickness	μm	40			
SiC thickness	μm	35			
OPyC thickness	μm	40			
End-of-life fluence	10^{25} n/m^2	3.0			
Irradiation temperature	°K	973	973	1473	1473
Gas pressure	MPa	4.61			
Ambient pressure	MPa	0.1			
IPyC density	g/cm^3	1.90			
OPyC density	g/cm^3	1.90			
IPyC BAF		1.06	1.03	1.06	1.03
OPyC BAF		1.06	1.03	1.06	1.03

Results of the debonding calculations are presented in Figure 2-8, which shows failure probabilities caused by debonding alone. It is shown that the maximum failure probability for Case 1 occurred when the bond strength between the IPyC and SiC layers was 28.5 MPa. At very low bond strengths, the IPyC debonded from the SiC layer, but the stress between layers was very small. The resulting stresses in the SiC were small, resulting in low failure probabilities. At large bond strengths (>60 MPa in this case), the radial stress between layers was not sufficient to overcome the bond strength, and there were no failures caused by debonding. In Case 2, the coating layer stresses diminished with a lower BAF, and the failure probabilities due to debonding decreased. Because the radial stress between the IPyC and SiC layers is diminished with the lower BAF, the peaks in the curve also shifted somewhat to lower bond strengths. In this case, the maximum failure probability occurred at a bond strength of 36.5 MPa.

At the higher irradiation temperature of Cases 3 and 4, the radial stress between the IPyC and SiC layers decreased significantly. This was the result of the higher creep coefficient for the pyrocarbons at the higher temperature, which relieved stresses in the coating layers. These stresses were not high enough to generate any failures due to the debonding process.

Results of the debonding calculations show that failures caused by debonding are highly dependent on the irradiation temperature and bond strength. Material properties such as BAF can also have a significant effect.
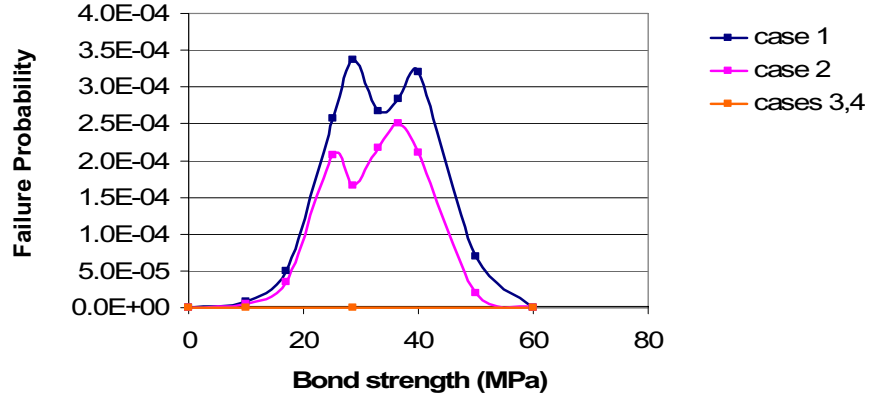
Figure 2-8. Failure probability due to debonding as a function of bond strength.

Asphericity

Another form of multi-dimensional behavior modeled in PARFUME is asphericity. The program incorporates the effects of asphericity for particles that have a flat facet but that are otherwise spherical. An axisymmetric finite element model for this faceted shape is shown in Figure 2-9. A faceted geometry is typical of what has been observed in fabricated particles. Another form of asphericity is an ellipsoidal shape, but this is not characteristic of what has been observed. Furthermore, the effects of an ellipsoidal shape are negligible relative to the faceted geometry. Therefore, this form of asphericity is not included in PARFUME.

The degree of asphericity for a particle is defined in terms of an aspect ratio, which is the ratio of the major diameter to minor diameter. A reason for defining this parameter is that it is a commonly used measure of the severity of deformity in a particle, and is thereby used as a criterion for particle acceptability. Using dimensions shown in Figure 2-9, the aspect ratio (A) is

$$A = \frac{2R}{R + \sqrt{R^2 - r^2}} \qquad (5)$$

where:

A: aspect ratio for an aspherical particle, or ratio between
the major and minor outer diameters for the particle (used
to measure the degree of asphericity)

R: is the outer radius of the particle and *r* is the radius of the facet

r: radius of the facet in an aspherical fuel particle.
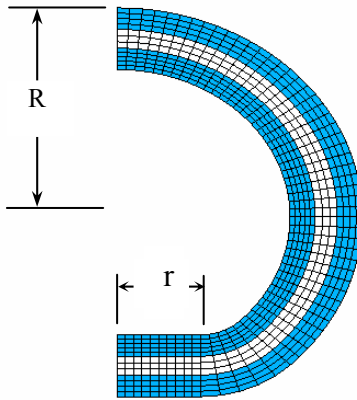
Figure 2-9. Finite element model for an aspherical fuel particle.

During irradiation, the faceted portion of the particle acts a flat plate that restrains the internal gas pressure. If the pressure builds up high enough, a local region of tensile stress develops in the central portion of the plate, which can contribute to particle failures. This is shown in the contour plot of Figure 2-10, where tensile bending stresses in the SiC layer occur in the outer face of the facet. Unlike failures caused by cracking of the IPyC or partial debonding of the IPyC, which are governed by shrinkage of the pyrocarbons, failures caused by asphericity are controlled by the internal pressure. Therefore, while failures due to IPyC cracking and debonding tend to occur early during irradiation when shrinkage stresses are at their highest, failures due to asphericity are likely to occur later when the internal pressure is highest.

57
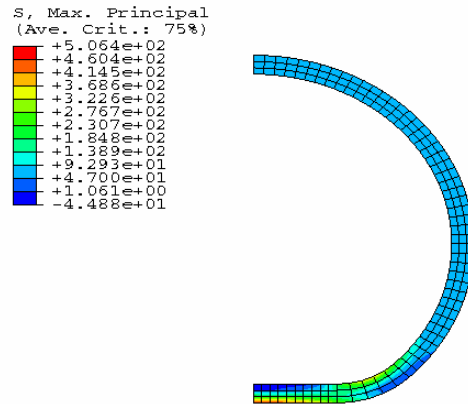
Figure 2-10. Stress intensification in the faceted portion of a fuel particle.

A typical faceted particle was analyzed in a viscoelastic time-integration analysis that progressed until the fluence reached a value of 3×10^{25} n/m^2, occurring at a time of 1.2×10^7 sec in the analysis. Figure 2-11 plots a time history for the principal stress in the SiC at the center of the faceted portion of the particle. Also plotted is the corresponding time history for the tangential stress in a perfectly spherical particle. A comparison of these stress histories shows that the facet intensifies the stress in that local region of the particle. Depending on its severity, this stress intensification can lead to increased particle failures.
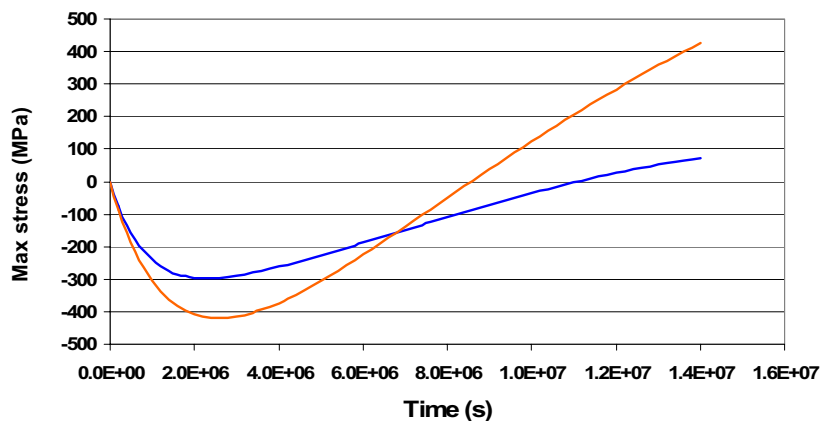
Figure 2-11. Stress histories for the faceted vs. spherical fuel particle.

In evaluating asphericity, PARFUME calculates a maximum stress for the SiC layer utilizing the statistical method described above (Eq. 1 or 3). However, a second term is added to the right hand side of these equations to correctly estimate the maximum stress σ_c for an aspherical particle, as follows for Eq. (3):

$$\sigma_c(\nu_j, \nu_k, \nu_l, ...) \cong \frac{\sigma_{c\bar{\nu}}}{\sigma_{u\bar{\nu}}} \sigma_u(\nu_j, \nu_k, \nu_l, ...) + \frac{\Delta\sigma_{c\bar{\nu}}}{\Delta\sigma_{u\bar{\nu}}} \Delta\sigma_u(\nu_j, \nu_k, \nu_l, ...) \qquad (6)$$

where:

σ_c: maximum principal stress in the volume of the SiC layer for an aspherical particle, MPa

σ_u: tangential stress in the SiC layer of an intact spherical particle, MPa

$\sigma_{c\bar{\nu}}$: maximum principal stress in the volume of the SiC layer for a debonded or aspherical particle having all parameters set at mean values for a particle batch, MPa

$\sigma_{u\bar{\nu}}$: tangential stress in the SiC layer of an intact spherical particle having all parameters set at mean values for a particle batch, MPa

$\Delta\nu$: variation in parameter ν from its mean value

and $\Delta\sigma_{c\bar{\nu}}$, $\Delta\sigma_{u\bar{\nu}}$, and $\Delta\sigma_u$ are changes in the stresses $\sigma_{c\bar{\nu}}$, $\sigma_{u\bar{\nu}}$, and σ_u in going from the first extremum (or minimum) to the end of irradiation in each respective stress time history. If a second extremum (or maximum) occurs before the end of irradiation is reached, then $\Delta\sigma_{c\bar{\nu}}$, $\Delta\sigma_{u\bar{\nu}}$, and $\Delta\sigma_u$ are taken as changes in these stresses in going from the minimum to the maximum. This ensures calculation of the largest value of stress that occurs anytime during the irradiation history. In Eq. (6), $\sigma_{c\bar{\nu}}$, $\sigma_{u\bar{\nu}}$, and σ_u are stress values occurring at the time of the minimum in each time history. The first term then takes the solution from time zero to the time of the minimum in the stress history, while the second term takes the solution from the minimum to the end of irradiation or to a maximum, whichever occurs first. The additional term is needed for asphericity evaluations because failures due to asphericity occur after the first extremum for σ_u has been reached, when shrinkage effects from the pyrocarbons are diminishing.

With the addition of a second term, Eq. (1) becomes

$$\sigma_c(\nu_j, \nu_k, \nu_l) \cong \frac{\sigma_{c\bar{\nu}}}{\sigma_{u\bar{\nu}}} \sigma_u(\nu_j, \nu_k, \nu_l, ...) h_{1j}(\Delta\nu_j) h_{1k}(\Delta\nu_k) h_{1l}(\Delta\nu_l)...$$

$$+ \frac{\Delta\sigma_{c\bar{\nu}}}{\Delta\sigma_{u\bar{\nu}}} \Delta\sigma_u(\nu_j, \nu_k, \nu_l, ...) h_{2j}(\Delta\nu_j) h_{2k}(\Delta\nu_k) h_{2l}(\Delta\nu_l)... \qquad (7)$$

The second set of correlation functions h_{2i} is determined in the same way as the first set h_{1i} (Ref. 3), using output from the same ABAQUS finite element analyses.

Eq. (6) was utilized to perform the calculations described below, since this required that only one ABAQUS finite element analysis be performed for each batch of particles considered. In these calculations, PARFUME compared the maximum calculated stress (from Eq. 6) to a strength that is sampled from a Weibull distribution having mean strength σ_{ms} and modulus m. The mean strength is calculated from Eq. (4), where the integral I_n represents a stress distribution obtained from the ABAQUS analysis of a faceted particle having mean values for all parameters.

Effects of Asphericity on NPR-1, HRB21, and German Particles

The effects of asphericity were evaluated by performing failure probability calculations on representative NPR-1, HRB21, and German particles, using the input parameters shown in Table 2-9.

Table 2-9. Input parameters for three types of particles.

Parameter	Units	NPR-1	HRB21	German
Kernel diameter	μm	200	351	500
Buffer thickness	μm	102	105	95
IPyC thickness	μm	53	52.8	40
SiC thickness	μm	35	32.6	35
OPyC thickness	μm	39	46.8	40
End-of-life fluence	10^{25} n/m^2	3.8	3.5	2.3
Irradiation temperature	K	1260	1273	1173
Gas pressure	MPa	23.31	15.82	10.65
Ambient pressure	MPa	0.1	0.1	0.1
IPyC density	g/cm^3	1.923	1.90	1.90
OPyC density	g/cm^3	1.855	1.84	1.90
IPyC BAF		1.0579	1.074	1.04
OPyC BAF		1.0515	1.038	1.04

Failure probability calculations for the three types of particles were performed over a range of values for the aspect ratio. The only statistical variation considered among particles in a batch was a Weibull distribution in strength for the SiC layer. Each aspect ratio considered was represented by a batch of particles. Including statistical variations in other parameters would likely increase the failure probabilities to some extent, but the trends should be very similar. Only failures caused by internal pressure were considered in the calculations, which isolated the

effects of asphericity. Because the stress distributions in the particle layers change with variations in the aspect ratio, a new Weibull mean strength was calculated from Eq. (4) for each aspect ratio considered. Results of the calculations are presented in Figure 2-12, where it is shown that none of the particles were predicted to fail at very low aspect ratios (a situation of zero failures was assigned a probability of 10^{-9}). The NPR-1 and HRB21 particles experienced an increase in failure probability at aspect ratios greater than 1.05. The German particles, however, showed no propensity to fail at any aspect ratio. This was due primarily to the lower irradiation temperature and corresponding lower internal pressure for these particles.
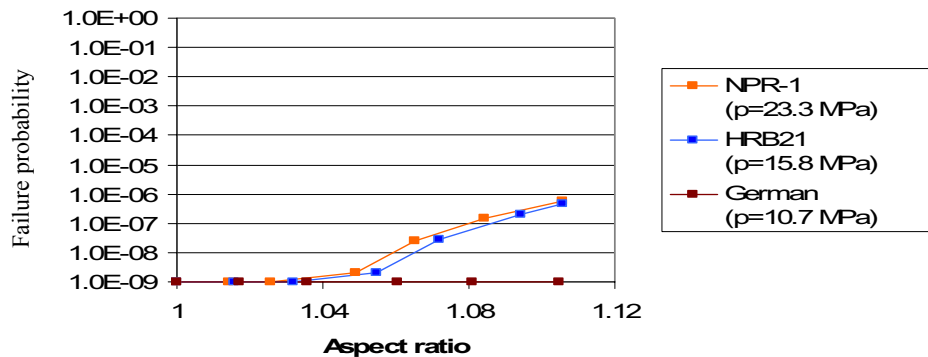
Figure 2-12. Failure probabilities as a function of aspect ratio for three types of fuel particles.

Effect of Asphericity on Particles Proposed for the DOE Advanced Gas Reactor (AGR) Program

Failure probability calculations were also performed on AGR particles over a range of aspect ratios (1.0 to 1.11) and internal gas pressures (7.3 to 32.3 MPa in increments of 5 MPa). The input parameters for these calculations are summarized in Table 2-10. The material properties in all cases corresponded to an irradiation temperature of 1273 °K.

Table 2-10. Input parameters for AGR particles.

Parameter	Units	AGR
Kernel diameter	μm	350
Buffer thickness	μm	100
IPyC thickness	μm	40
SiC thickness	μm	35
OPyC thickness	μm	40
End-of-life fluence	10^{25} n/m^2	3.5
Irradiation temperature	K	1273
Gas pressure	MPa	Varied
Ambient pressure	MPa	0.1
IPyC density	g/cm^3	1.90
OPyC density	g/cm^3	1.85
IPyC BAF		1.03
OPyC BAF		1.03

Again, the only statistical variation considered among particles in a batch was a Weibull distribution in strength for the SiC layer. Only failures caused by internal pressure were considered in the calculations, isolating the effects of asphericity. As before, a variation in the Weibull mean strength across the range of aspect ratios was incorporated in the calculations. Results of the calculations are presented in Figure 2-13, where it is evident that failures due to asphericity are highly dependent on the pressure and aspect ratio. The failure probability generally increased by several orders of magnitude over the range of 1.0 to 1.11 in aspect ratio. The high failure probabilities at the higher pressure (32 MPa) suggest that asphericity could be very important under accident conditions.
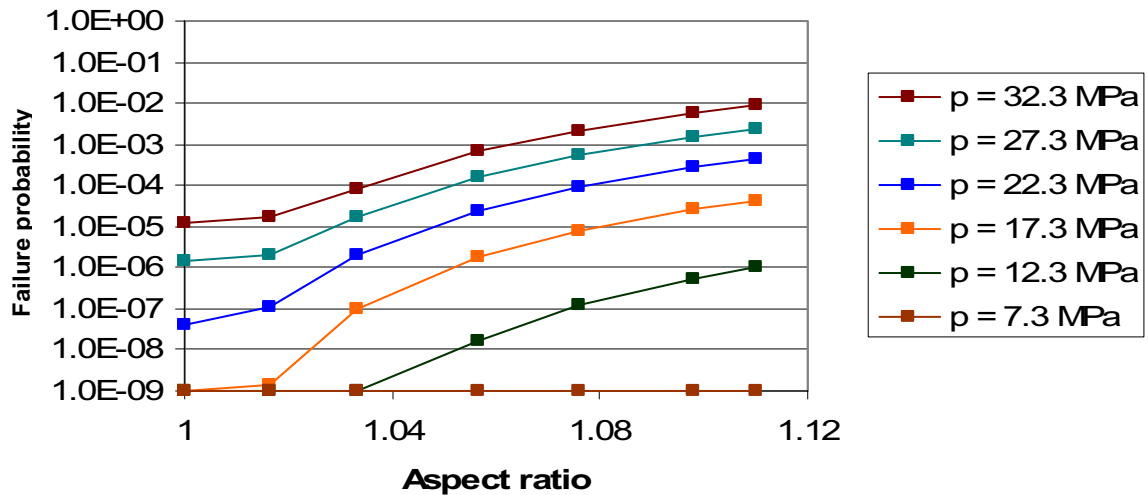
Figure 2-13. Failure probability of AGR particles as a function of aspect ratio and gas pressure.

Thermo-mechanical Particle Performance Summary

The PARFUME code, which is under development at the Idaho National Engineering and Environmental Laboratory, has been used to evaluate the effects of layer cracking, partial debonding (between the IPyC and SiC) and asphericity on the performance of TRISO-coated fuel particles. Results of the studies on debonding indicate that

- Debonding occurs when the radial stress that develops between the IPyC and SiC layers, due to shrinkage of the IPyC layer, exceeds the bond strength between layers.

- The debonding process is likely to be a progressive unzipping of the two layers that starts at a weak point on the interface between layers.

- Stress concentrations occur at the tip of the debonded region, inducing tensile stress components in the SiC layer that can contribute to particle failures.

- The number of particle failures that occur as a result of debonding is strongly a function of the bond strength between layers. At low bond strengths, the layers readily debond, resulting in low stress in the SiC layer and consequently a low number of failures due to debonding. At a high bond strength, the radial stress between layers may not be sufficient to overcome the bond strength, which again results in a low number of failures due to debonding. Thus, the number of failures due to debonding is greatest at intermediate values for the bond strength.

- The number of failures caused by debonding is also strongly a function of the irradiation temperature. At high temperatures, the creep in the pyrocarbons tends to relax stresses caused by shrinkage, which can in turn greatly reduce the number of failures that would occur due to debonding.

- Material properties such as the anisotropy of the pyrocarbons as measured by BAF can also have a measurable effect on the number of failures caused by debonding.

Results of the studies on asphericity indicate that:

- Asphericity is likely to have its greatest effects for particles that have a faceted geometry. The faceted portion of the particle acts as a flat plate that can incur tensile bending stresses as the gas pressure in a fuel particle builds up, which can contribute to particle failures.

- The number of particle failures caused by asphericity is strongly a function of the internal pressure. The stresses in the faceted portion of a particle are highest when the shrinkage of the pyrocarbons diminishes and the internal gas pressure increases.

- The number of particle failures due to asphericity is also largely dependent on the degree of asphericity, as measured by the aspect ratio for the particle (the ratio between major and minor outer diameters).

- Failure predictions for fuel particles from the NPR-1 and HRB21 experiments showed that these particles experienced a significant increase in failures (relative to spherical

particles) at aspect ratios greater 1.05. Meanwhile, predictions for German particles showed no increase in failure probability at any aspect ratio. This was attributable primarily to a lower irradiation temperature, and a corresponding lower internal pressure for these particles.

- Predictions were made over a range of aspect ratios and gas pressures for particles from the proposed AGR program. These showed that the failure probability typically increased by several orders of magnitude over a range of 1.0 to 1.11 in aspect ratio. The large failure probabilities predicted for an internal pressure of 32 MPa suggest that asphericity could be very important under accident conditions.

Equation of State

The Redlich-Kwong equation of state has been incorporated into the PARFUME code. It consists of the same formalism and gas specie mixing rules as used by CEA (presented later in this section). However, slight differences exist in the values of critical temperatures and pressures used to derive the Redlich-Kwong constants a_i and b_i. Values of critical temperatures, pressures (Reid, Prausnitz, and Poling 1987) and the derived constants as used in PARFUME are presented in Table 2-11.

Table 2-11. Parameters used in PARFUME's Redlich-Kwong equation of state.

Gas	Critical Temp. T_c (K)	Critical Pressure P_c (MPa)	Redlich-Kwong Constant a_i ($Nm^4K^{0.5}/mol^2$)	Redlich-Kwong Constant b_i (m^3/mol)
CO	132.9	3.50	1.720	2.737×10^{-5}
Kr	209.4	5.50	3.412	2.744×10^{-5}
Xe	289.7	5.84	7.234	3.576×10^{-5}

A comparison of internal gas pressures as calculated by the Ideal Gas Law and by the Redlich-Kwong equation of state is presented in Figure 2-14. This comparison considers a 502 μm diameter, 16.7 % enriched UO_2 fuel kernel irradiated to 20 % FIMA that contains 3.67×10^{-7} g-mol CO, 4.49×10^{-8} g-mol Xe and 1.02×10^{-8} g-mol Kr. For this case, the Redlich-Kwong equation of state determines internal pressures that are slightly more than 20 % higher than those determined by the Ideal Gas Law.
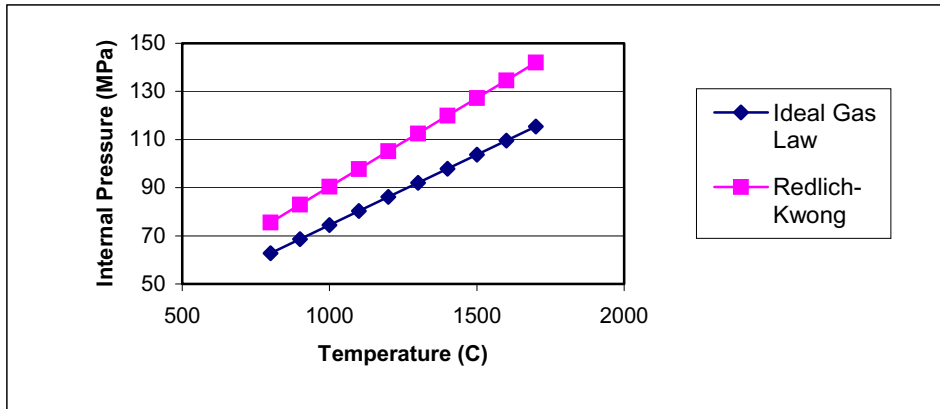
Figure 2-14. Comparison of particle internal pressure as calculated by the Ideal Gas Law and by the Redlich-Kwong equation of state for a representative 502 μm diameter UO_2 fuel particle.

CO Yield Model Input Criteria

A detailed thermochemistry model based on the HSC thermochemical free energy minimization code was used to determine the free oxygen released per fission and the corresponding CO production (Petti et al. 2002). These calculations were done over a range of burnups, temperatures, enrichments, and UO_2 + UC_2 compositions that might be considered for TRISO-coated fuel.

One of the input parameters to the HSC CO yield model, as implemented in the PARFUME code, is the fraction of UC_2 used, along with UO_2, to produce the UC_xO_y fuel being analyzed. This particular fraction, as used in the model, assumes no lost or gain of constituent atoms, which dictates that the sum of x and y is two. However, during fabrication of UC_xO_y fuel, a partial pressure of CO is used to control composition whereby the sum of x and y is not necessarily two. Due to this composition influx and the complex U-C-O phase equilibrium, simple scaling from the initial to final (or vice versa) mixture is not possible. Furthermore, since initial UC_2 fractions are generally not reported (in QC data reports or test reports) in the description of UCO fuel (but final carbon to uranium and oxygen to uranium ratios are), some criteria must be established regarding the use of reported atom ratios as input to the HSC CO yield model.

Considering the simple scaling as used in the HSC model implies that:

$$UC_xO_y = f(UC_2) + (1 - f)(UO_2) = UC_{2f}O_{2(1-f)}$$

65

where   x = C/U = carbon to uranium atom ratio
                     y = O/U = oxygen to uranium atom ratio
                     f = fraction of UC_2 in the UC_xO_y fuel.

Solving for the UC_2 fraction, f, yields:

$$f = (x/2) = 1 - (y/2)$$

which may result in two different values. Using the following NPR QC data as an example,

$$x = C/U = 0.3618$$
$$y = O/U = 1.5098$$

two UC_2 fractions are determined as:

$$f = 0.3618 / 2 = 0.181 \text{ and}$$
$$f = 1 - (1.5098/2) = 0.245.$$

Since it is more conservative to calculate a higher CO yield, a lower UC_2 fraction would be used in the HSC model. This implies that performance calculations (PARFUME) for NPR fuel would use a conversion of the carbon to uranium ratio, x, as input for the UC_2 fraction. The HSC model input criteria then can be stated as: On input, PARFUME will test for the lowest derived UC_2 fraction and use it as input to the HSC model. Also on input, "out of bounds" UC_2 fractions greater than one will be flagged and set equal to one (as for $UC_{5.45}O_{1.75}$ fuel used in OF-2).

SiC Thinning

INEEL investigated the effects on particle behavior from thinning of the SiC layer, which would be caused by interaction of fission products with the SiC. This was done by performing finite element analysis on a typical AGR fuel particle using the ABAQUS program, where elements in the thinned portion of the SiC layer were effectively removed from the model. This was accomplished by either simply not including these elements in the model (Figure 2-15), or by substantially decreasing the stiffness of the affected elements at the time that the material is removed during irradiation. Several configurations were considered involving variations in the depth or width of the thinned region. Results of the thinning analysis show that stress concentrations occur during irradiation at the edges of the thinned region. As with a cracked IPyC or a partially debonded IPyC, these stress concentrations include tensile stress components that reach a maximum value early during irradiation, due to shrinkage of the pyrocarbon layers (Figure 2-16), red curve). Once creep in the pyrocarbon layers takes effect, then these stress concentrations diminish rapidly. The red curve of Figure 2-16 was based on eliminating the

thinned elements (to a depth of 1/6 the wall thickness) from the beginning of the solution. The green curve of Figure 2-16 was based on thinning the wall to a depth of one-half the wall thickness in three steps (1/6 the thickness in each step at time intervals of 4×10^6 s). When the first step of wall thinning was applied (at time 4×10^6 s), the green curve suddenly rose to a value that nearly meets the red curve. This tendency was observed in other cases where thinning was applied in stages. This suggests that the maximum stress due to thinning may be obtained by 1.) determining the time at which stresses reach a peak value due to shrinkage of the pyrocarbons, 2.) determining how much thinning has occurred at that time, and 3.) solving for stresses at that time in an ABAQUS analysis assuming that level of thinning from the start of the analysis. Failure probability calculations performed for AGR particles having a locally thinned SiC layer showed that resulting failure probabilities were of the same order of magnitude as those associated with a cracked IPyC. It was also shown that either deepening or widening the thinned area increased the failure probability, but that widening the thinned area had a more significant effect.
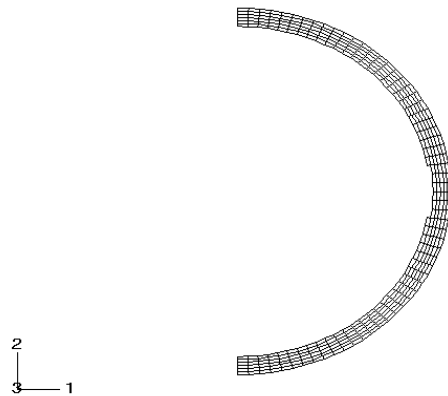
Figure 2-15. Finite element model of an SiC layer having a thinned region.
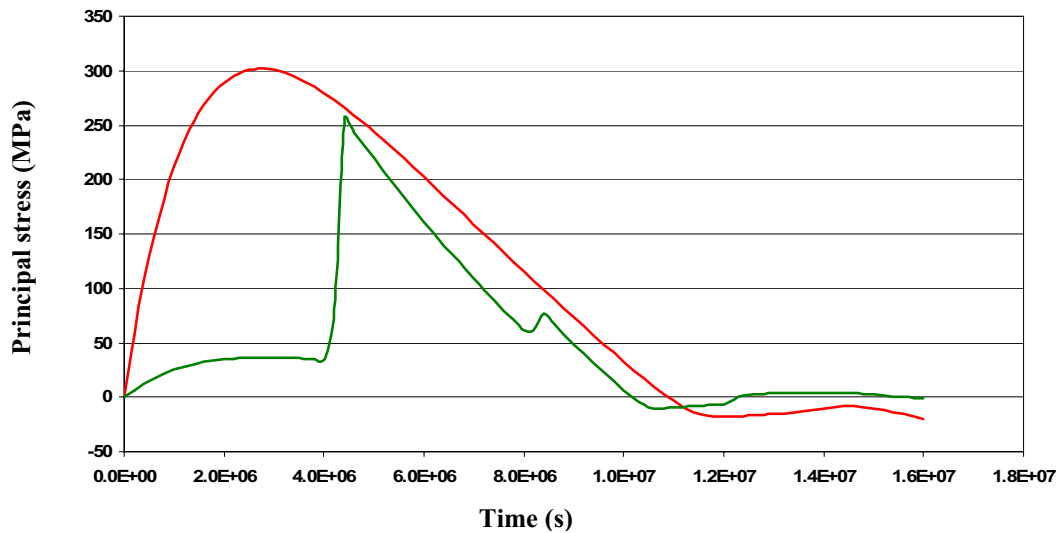
Figure 3-16. Stress histories for local stress in thinned region of SiC layer.

This is illustrated by performing finite element analyses on an AGR fuel particle using the ABAQUS program, where elements in the thinned portion of the SiC layer were removed from the model. In these analyses, the irradiation temperature was assumed to be 1173K, and the internal gas pressure was assumed to reach 30 MPa. The configurations shown in Table 2-12 were considered, which involve variations in the depth and width of the thinned region. Included is a case where the SiC is thinned at several locations, representing the situation where fission products attacked the SiC in several areas. As discussed in the first quarter 2004 report, stress concentrations occur during irradiation at the edges of the thinned regions. These include tensile stress components (typically peaking early during irradiation due to shrinkage of the pyrocarbon layers) that can contribute to particle failures.

The results in Table 2-12 show that widening the thinned area more strongly increases the particle failure probability than does deepening the thinned area. In the case "Narrow 5", an SiC layer that was thinned through 5/6 of its thickness in a local area had a failure probability of 4.8×10^{-4}. In the case "Narrow 3", an SiC layer that was thinned through 2/3 of its thickness in several locations had a failure probability of 9.7×10^{-5}. These results indicate that the SiC layer can sustain a significant amount of thinning in local areas without failure. It is planned to use results from analyses such as those of Table 2-12 to establish a simplified failure criterion for particles that undergo thinning of the SiC layer during irradiation.

68

Table 2-12. Calculated failure probabilities for several configurations of a thinned SiC layer.
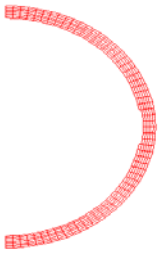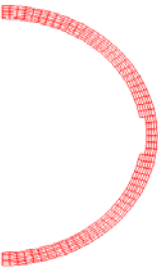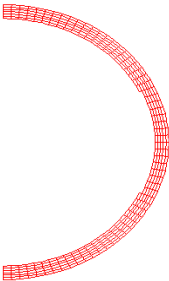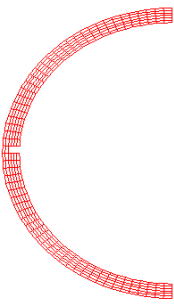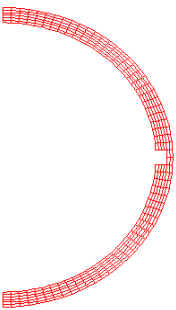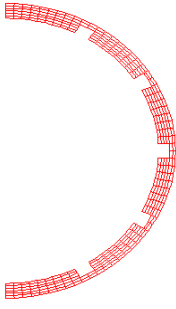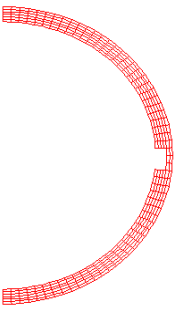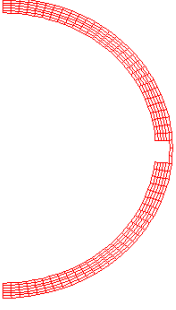
Model	Label	Size, depth × width (μm)	Failure Probability
	Base Case	5.8 X 104	1.78×10^{-4}
	Deep	11.7 x 104	3.00×10^{-4}
	Wide	5.8 x 279	1.62×10^{-3}
	Narrow 1	23.3 x 17.4	9.38×10^{-6}

Table 2-12., continued

Model	Label	Size, depth × width (μm)	Failure Probability
	Narrow 2	23.3 x 34.8	2.65×10^{-5}
	Narrow 3	23.3 x 34.8, 5 places	9.70×10^{-5}
	Narrow 4	23.3 x 52.2	7.11×10^{-5}
	Narrow 5	29.2 x 52.2	4.82×10^{-4}

SiC Swelling

The INEEL also studied the effect on particle stresses from swelling in the SiC layer. To do this, an ABAQUS finite element analysis on an AGR fuel particle was performed, where the SiC was assumed to swell steadily throughout irradiation to a final value of 1% volumetric swelling. Figure 2-17 compares the calculated stresses for the IPyC and SiC layers to those for the case of no swelling in the SiC layer. Peak magnitudes for the IPyC stress and SiC stress increased from 184 to 193 MPa and from 310.9 to 326.8 MPa, respectively. The magnitudes for the IPyC and SiC stresses at end-of-fluence increased from 40.6 to 50 MPa and from 90.4 to 106.1 MPa, respectively.
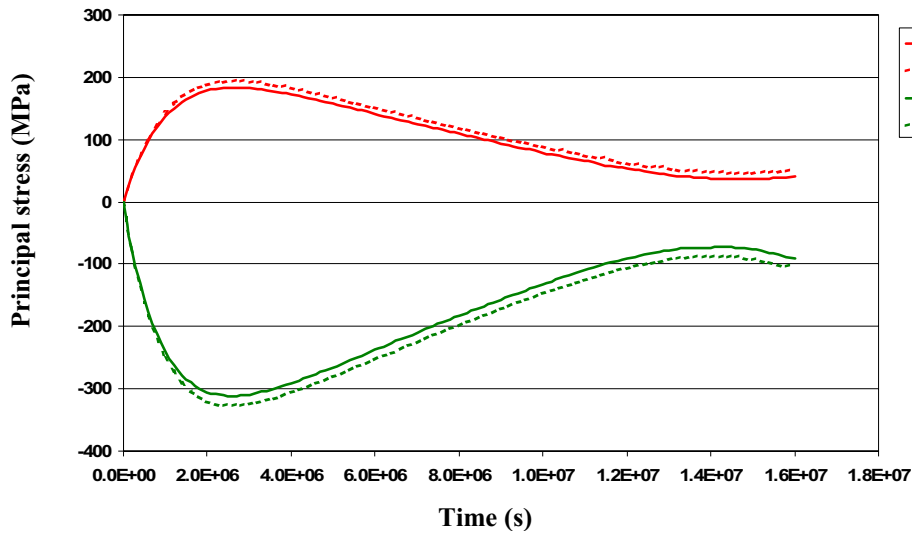
Figure 2-17. Stress histories showing the effect of 1% swelling in the SiC.

Enhanced Thermal Model

INEEL enhanced the thermal modeling capabilities of the PARFUME code. These new capabilities allow the time-dependent prediction of temperature profiles through TRISO-coated fuel particles. The fuel temperatures can be calculated for particles embedded in either pebble bed spheres or prismatic block cores (as specified by the user) based on fuel particle positions determined internally through statistical sampling. Both steady state and transient models of pebble bed spheres and prismatic block cores were completed to facilitate calculation of the fuel temperatures. Those models are depicted in Figures 2-18 and 2-19. As indicated in Figure 2-18, the pebble bed model is a spherical representation of an unfueled shell and a central fueled

71

region. The outer boundary of the model (corresponding with the outer surface of a pebble) is assumed to be at a user specified irradiation temperature. The prismatic model is a cylindrical representation of an outer-fueled region and a central unfueled region based on a hexagonal unit cell approach as shown in Figure 2-19. The inner boundary of the model (corresponding with the surface of a coolant hole) is assumed to be at a user specified irradiation temperature. Both steady state and transient algorithms were needed in both models because user specified irradiation (boundary) temperatures may be time dependent.

The modeling approach involves calculating pebble bed or prismatic temperature distributions (as appropriate), assignment of fuel particle surface temperatures based on interpolation within pebble bed or prismatic distributions at statistically-determined particle positions, and then calculation of particle temperature profiles for assigned surface temperatures. Predicted fuel particle temperatures have also been applied to all appropriate interfaces with existing pressure, stress, and fission product release models. Improved prediction of fuel particle performance is assured as a result.
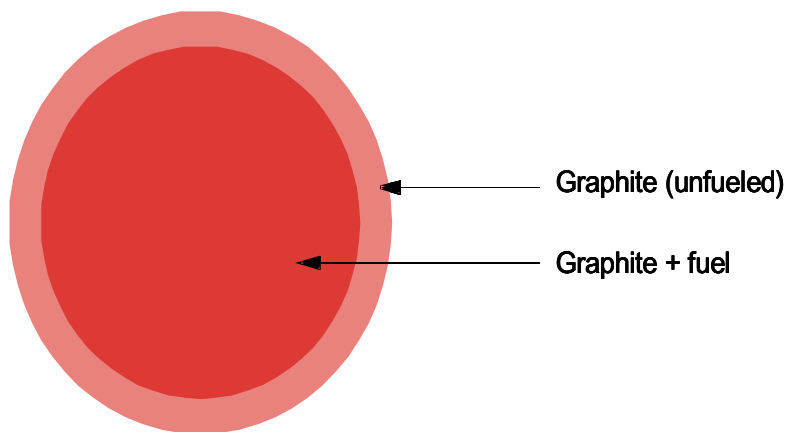
(a) Cross-section of pebble bed sphere

Graphite (unfueled)

Graphite + fuel

Boundary set at user
specified irradiation temperature

Graphite + fuel (smeared)

Graphite (unfueled)

R_f

R_g
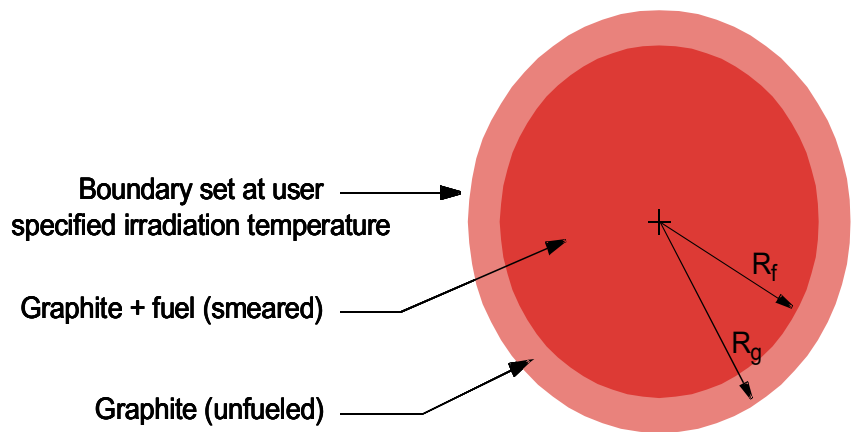
(b) Spherical model for pebble bed

Figure 2-18. Pebble bed thermal model used in calculating TRISO coated fuel particle temperature profiles.
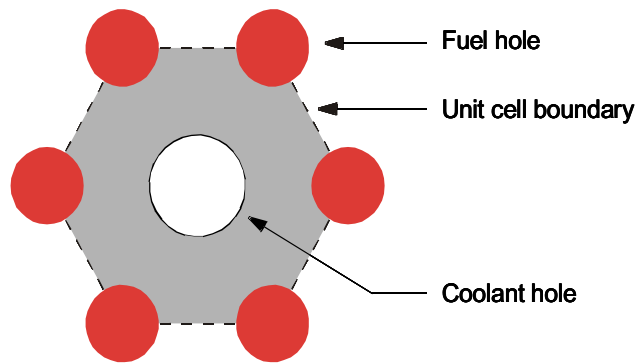
(a) Cross-section of hexagonal unit cell for prismatic core
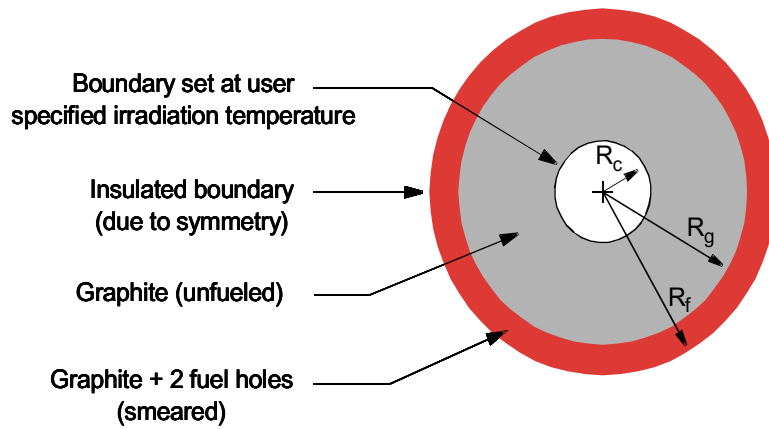
(b) Cylindrical model for prismatic core

Figure 2-19. Prismatic core thermal model used in calculating TRISO-coated fuel particle temperature profiles.

Additional improvements to the PARFUME code include modeling to allow the (potential) development of a gap between the buffer and the IPyC. Simulating the potential development of a buffer/IPyC gap was built into the fuel particle thermal models as outlined below.

The potential for development of a gap was assumed to be due to the net effects of kernel swelling, buffer shrinkage and creep, the associated kernel/buffer contact pressure, and IPyC shrinkage and creep. These effects were incorporated into the thermal models because development of a gap and changes in (kernel, buffer, and IPyC) geometry will impact particle temperature profiles. Accordingly, the thermal solution now includes:

1. Time-dependent prediction of a temperature profile through a pebble bed sphere or a prismatic block core (as defined through input) for an irradiation boundary temperature and a fuel element power (as specified by the user)

2. Statistical determination of a particle position within the fuel element

3. Interpolation within the fuel element profile at the particle position to determine a particle surface temperature

4. Calculation of particle temperature profiles at each step in an irradiation history based on:

   - Particle power and surface temperature

   - Kernel swelling as a function of burnup

   - Buffer displacement, accounting for buffer shrinkage and creep as a function of fluence and temperature

   - Kernel/buffer contact pressure as a function of fluence, temperature, and geometry

   - IPyC displacement, accounting for IPyC shrinkage and creep as a function of fluence and temperature

   - CO production and release into the gap as a function of burnup

   - Fission gas production and release into the gap as a function of burnup and temperature

   - Pressure of gases in the gap as a function of temperature and geometry

   - Material thermal conductivities as a function of temperature

5. Iteration within step 4 until particle temperature convergence is achieved.

It should be noted that the gap thermal conductivity is calculated as a function of released fission gas mole fractions and the gas temperature and pressure. In addition, kernel and buffer densities are modified as the geometry changes with the limitation that the buffer cannot shrink to a density above its theoretical value. Buffer conductivity is allowed to increase as densification proceeds, although the temperature-dependent conductivity of the kernel is not currently modified as a function of density change. The code keeps track of particles that undergo complete buffer densification. The code also tracks particles where gap closure occurs (i.e., when kernel swelling is sufficient to force the shrunken buffer against the IPyC).

An example of a fuel element temperature profile (as determined for step 1) as a function of particle power is shown in Figure 2-20. In this case, a prismatic block core was subjected to a constant irradiation temperature of 1273 K. Fuel compacts 12.46 mm in diameter were assumed to contain 171,260 fuel particles per meter of length. Diameter of the fuel kernels were 350 μm.
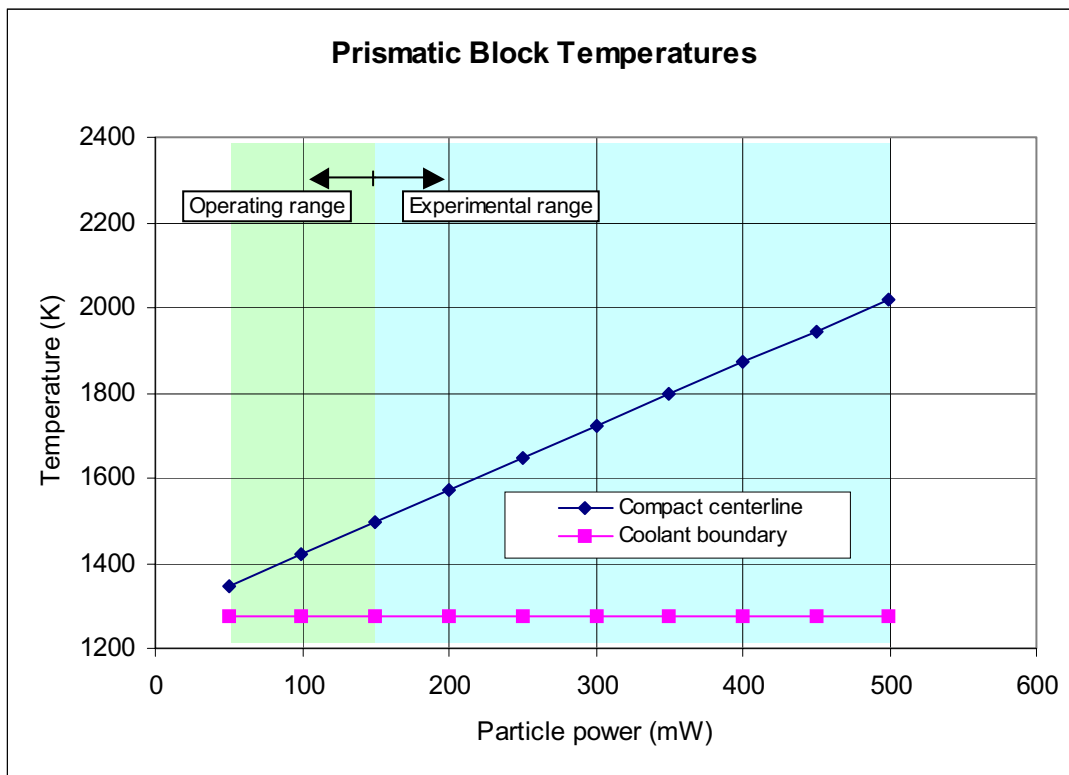
Figure 2-20. Temperature profile through a prismatic block core as a function of particle power.

The corresponding fuel particle temperature profile as a function of particle power is shown in Figure 2-21 as an example of the results from step 4. In this case, however, buffer creep, kernel/buffer contact pressure, and IPyC displacement were ignored to allow extension of the calculations to high power. If those effects are included, code numerical overflow failures can occur due to high pressure as the power increases.

Temperature gradients across the kernel, the buffer, and the balance of the particle are illustrated in Figure 2-21. However, temperature drops across the OPyC, SiC, and IPyC layers are negligible. Consequently, the gradient from the buffer outer surface to the OPyC outer surface as shown is effectively due to the presence of a gap between the buffer and the IPyC. Clearly, the gap ΔT can be a significant factor in the particle thermal response.
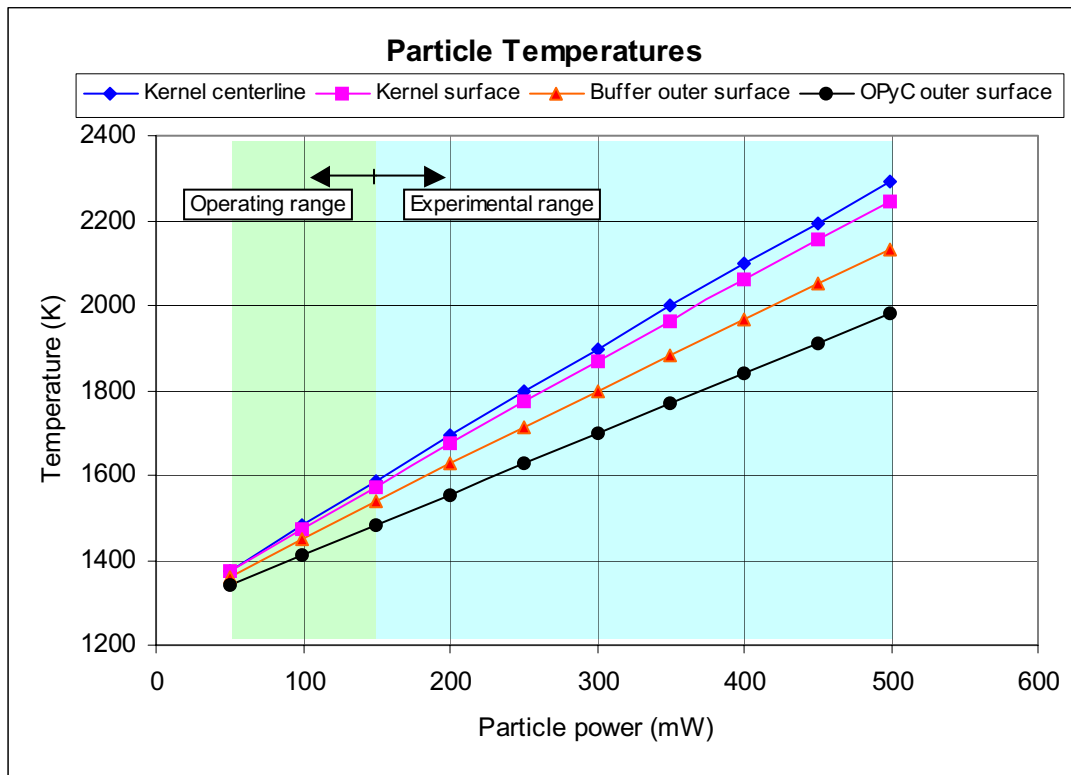
Figure 2-21. Fuel particle temperature profile in a prismatic block core as a function of particle power.

An example of gap development predicted by PARFUME as a function of burnup and particle power is shown in Figure 2-22. Fluence has a strong impact on gap growth (through buffer

shrinkage) and lower power particles accumulate the greatest fluence because of the longer time associated with accumulating the specified burnup. Consequently, gaps tend to decrease with particle power. Kernel centerline temperatures increase with gap growth as shown in Figure 2-23. High power, very accelerated irradiations can lead to large gaps and high kernel centerline temperatures even at relatively low burnups.
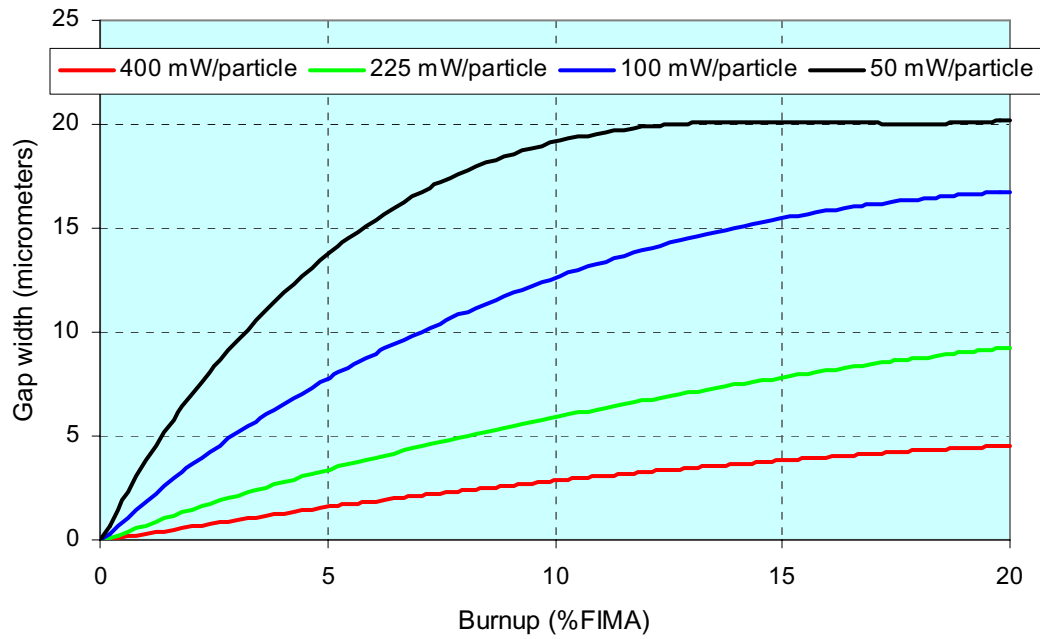
Figure 2-22. Gap development in a prismatic block core as a function of burnup and particle power.
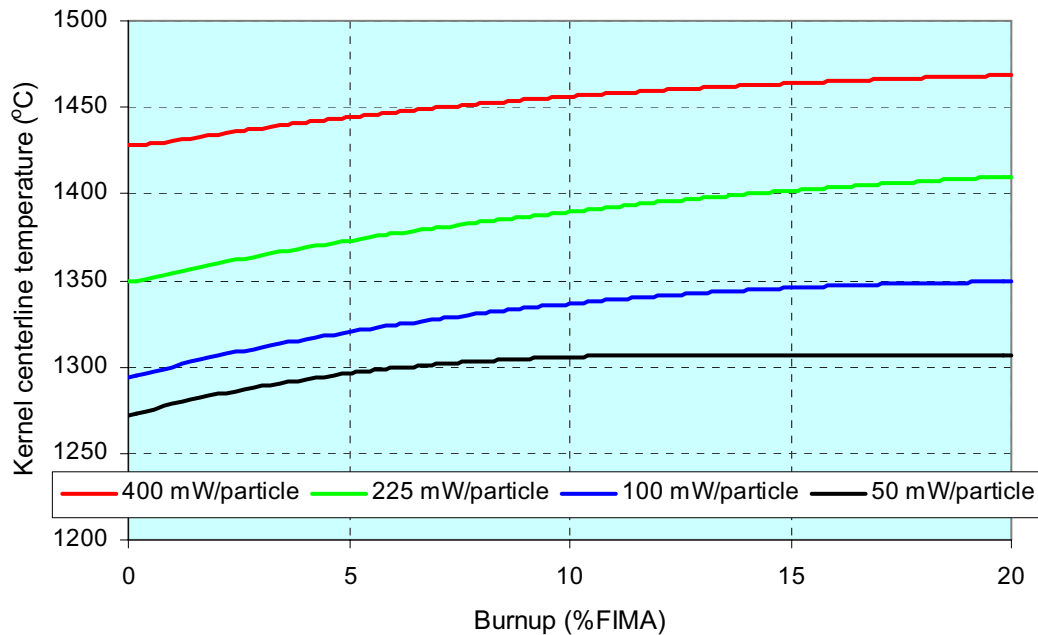
Figure 2-23. Kernel centerline temperatures in a prismatic block core as a function of burnup and particle power.

The capacity to calculate release rate to birth rate (R/B) of gaseous fission products are included in both the Monte Carlo and multiple integration routines of PARFUME. The calculation accounts for gas release from failed particles and uranium contamination in the fuel matrix. Connecting the R/B model to the integration routine requires that the differential failure probabilities computed in the routine be resolved into incremental probabilities over the time of irradiation. This enables the calculation of time histories for the R/B.

Figure 2-24 presents a comparison of time histories for R/B of Kr-85m as calculated by the Monte Carlo and integration routines, showing close agreement between the two methods. Particle parameters used in this calculation corresponded to those of an HFR-EU1 particle, with an irradiation temperature of 1223 K, end-of-life burnup of 20% FIMA, and end-of-life fluence of 5.4×10^{25} n/m^2. The Monte Carlo analysis was performed on a statistical sample of 200,000 particles. The agreement between the two methods improves as the size of the Monte Carlo sample increases.
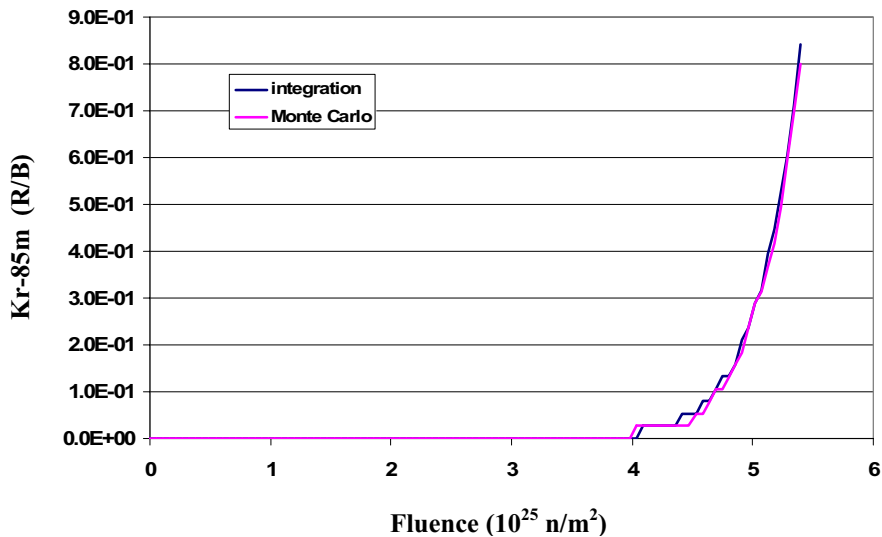
Figure 3-24. Comparison of (R/B) time histories, integration vs. Monte Carlo.

2.2 Task Technical Overview – CEA:

The simulation code, called ATLAS (Advanced Thermal mechanicaL Analysis Softfware) was developed with the following objectives:

- To quantify, by a statistical approach, the failed particle fraction of a loading (experiment, core) at a given time step for normal and accident conditions. Results can be directly used to verify safety analysis failure fraction requirements.

- To evaluate, by a statistical approach, the fission product release fraction of a loading (experiment, core) at a given time step for normal and accident conditions. Results can be used as input data for fission products transport codes.

The methodology is made up of three steps:

- deterministic calculations of different types of free particles, using a finite element method. The models are one-dimensional for intact particles or particles with fully debonded layers and are two-dimensional for cracked, partially debonded or irregular shaped particles. Temperatures, displacements, stresses, strains and fission product concentrations are calculated for each node of the model,

- deterministic calculations of a fuel element,

- statistical processing of the above results taking into account ceramic failure mode, but also fabrication, material property and core data uncertainties.

Thermal and mechanical models

A particle and an additional layer around the particle simulating the particle environment are modeled. A finite element method is used whereby a thermal calculation determines the temperature field in the meshing nodes and a mechanical calculation determines the displacements fields, stresses and strains in the meshing nodes.
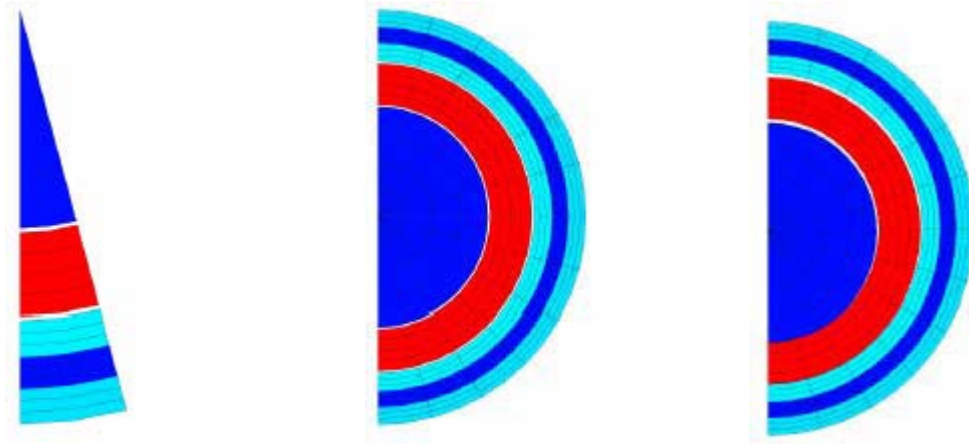
Figure 2-25. Finite element models (1D, centric 2D, excentric 2D).

Thermal models

The thermal models determine heat transfer in the particle. The layers can be bonded or not. In the TRISO models, the meshes between the kernel and the buffer and between the buffer and the IPyC simulate a gaseous joint. The size of this joint is determined by the mechanical computation and, in case of contact, this joint is low enough (0.1 µm) to have a negligible effect on the thermal computation. The boundary conditions of these models are twofold: a condition of nil flux on each side of the model and an imposed temperature on the particle external surface nodes. The conductivities of the layers, the kernel and the gaseous joints are re-calculated at each time step and depend on the temperature, the fluence and the porosities (fabrication and gaseous).

The thermal loading has two components:

- the power released by fission in the kernel, and
- the imposed temperature to the model. This is the temperature of the external surface of the outer PyC layer.
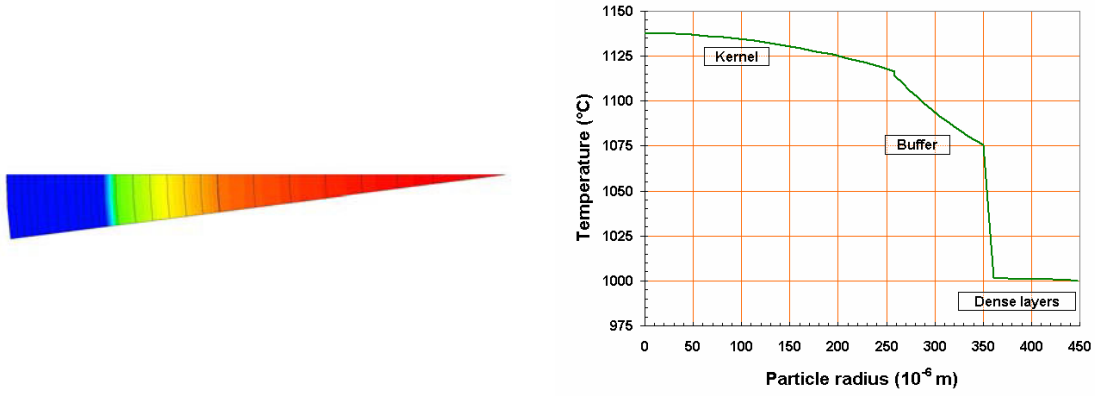
Figure 2-26. Temperature distribution in the particle.

Figure 2-26 presents an example of a thermal computation in which the pyrocarbon shrinkage creates a gap between the buffer and the IPyC layer. For this case, the gap involves a temperature step of a few tens of degrees.

Mechanical model

Consideration of irradiation-induced creep, the level of dimensional change during irradiation and formation of gaps between layers involve the use of nonlinear viscous elastic and large displacement resolutions. The non-linearities are of three types: first, the material non-linearity through irradiation creep laws, second, the geometrical non-linearity through a contact condition between each interface if needed (especially between kernel and buffer and between buffer and IPyC) and third, the large displacement resolution method. The dense layers can be connected to each other or not. The main characteristics of the model are as follows:

- the thermal load is the temperature field resulting from the thermal calculation,

- the pressure load is calculated at each time step from the free volume, the temperature and the quantity of gas present:

$$V_{free} = V_{\ker nel} \cdot P_{\ker nel} \cdot \xi_{\ker nel} + V_{buffer} \cdot P_{buffer} \cdot \xi_{buffer} + \sum V_{gap}$$

with V the volume of the deformed mesh, P the porosity and ξ the open porosity fraction. The Redlich-Kwong equation of state is used

82

$$RT = \left[P + \frac{a}{T^{1/2} \cdot V(V+B)} \right](V - b)$$

with P the pressure (Pa), V the volume (m^3), T the temperature (K), R the gas constant (8.3144 $J(K^{-1})(mol^{-1})$), and "a" and "b" are gas constants depending on the gas species (Xe, Kr, CO, CO_2).

- the loads imposed by the swelling of the kernel and the irradiation-induced dimensional change (IIDC) of the layers are considered as loads of imposed deformation type. These are taken into account by making an analogy between swelling and thermal expansion.

Diffusion model

The model for migration of long-lived fission products in the coated particle and more generally in the fuel element (pellet or compact) , is intended for aims at estimating the source term of the fission products released in normal operation or in accident conditions. All the transport mechanisms are simplified in a single transport law using effective diffusion coefficients for the fusion product (FP) species in the different constitutive materials.

The modelling consists of solving numerically the 2nd Fickian equation which is expressed in spherical geometry by the three term expression:

$$\frac{\partial c_i}{\partial t} = D_i^{eff} \left[\frac{\partial^2 c_i}{\partial r^2} + \frac{2}{r} \frac{\partial c_i}{\partial r} \right] - \lambda_i c_i + \dot{q}_i$$

where D_i^{eff} represents the effective diffusion coefficient of the specie i, generally given as an Arrhénius type equation as a function of temperature and globalizing the mechanisms of transport in each of the represented layers ; $\dot{q}_i$ and λ_i represent respectively the fission generation rate and the radioactive constant for the considered isotope.

The generation of the main fission product isotopes (^{137}Cs, ^{134}Cs, ^{90}Sr, ^{110m}Ag, ^{85}Kr, …) are expressed in ATLAS by analytical equations which were determined by APOLLO2 and DARWIN/PEPIN calculations representing a HTR core loaded with LEU fuel for ^{235}U enrichments between 10 and 20%.
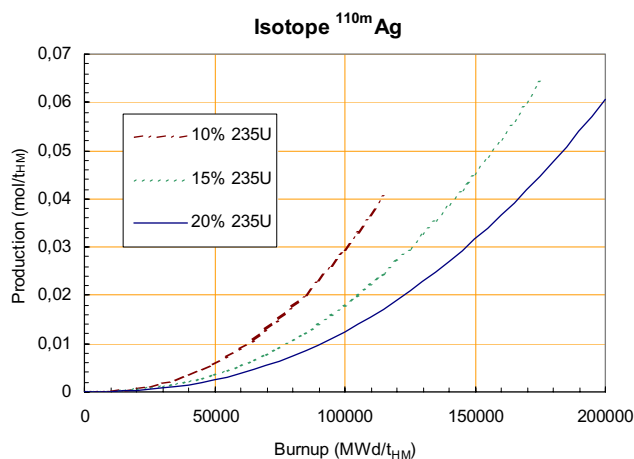
Figure 2-27. ^{110m}Ag production.

Diffusion coefficients have been chosen based upon an evaluation performed under the frame of the HTR-F project. A common assumption is the neglect of any effects of sorption or trapping within a coating layer or any preferential retention in a specific layer. As a consequence, in spite of the observation in microprobe analysis of certain discontinuities in concentration of caesium in the buffer / IPyC interface and of palladium in the IPyC / SiC interface, the partition coefficients are assumed to be one.

The simulation of fission product migration considers three types of particles in the fuel element: intact particles at the beginning of the irradiation which are modelled in one dimension, particles with broken SiC layers where the diffusion coefficient is multiplied by an adjustable factor and finally, particles with exposed kernels.

This preliminary model may evolve as new information becomes available from future irradiations and subsequent post- irradiation examinations.

Statistical approach

Particle failure probability analysis is supported by:

- a probabilistic model,

- one or more failure criteria, which include stress-loading limit, existence of a failed layer, existence of separation of dense layers…,

- fabrication, material property, and core data uncertainties.

Probabilistic modelling, used by the CEA for coated particles, is based on the "Monte-Carlo" method. This method has the advantage of including probability error control, yet requires a large number of calculations (10^5 to 10^6). The complexity of the thermal and mechanical models used by ATLAS make the application of this method difficult.

Different probabilistic approaches based on the same mechanical models, but that are more efficient in terms of the number of calculations to be performed have been studied by the CEA. . The importance sampling technique, which is one of the variance-reducing techniques in Monte Carlo methods, is notable.

The ATLAS code is being integrated with a unique Pleiades "platform", which can be used for all types of reactor fuels. Pleiades is a software platform under construction which will allow all available fuel models, independent of the reactor type (fuel geometry, irradiation conditions…) to be used. After this integration, code development will continue allowing multi scale simulation (from particle to compact) and statistical calculations to be performed.

The ATLAS code includes German, UK and CEGA layer properties. Currently, the code uses a deterministic approach for the calculations of stresses and strains in the coated fuel particle. The main investigations, which have been carried out during the I-NERI collaboration, are as follows:

- Tests and comparison with analytical solutions
- HFR-P4 calculations
- HFR-EU1 calculations
- CRP6 benchmark calculations.

Tests and comparison with analytical solutions

Comparison between analytical solutions from INEEL (analytical solution for stresses in TRISO-coated particles (Miller 1993)) and ATLAS calculations have been performed. The considered cases take into account irradiation-induced creep, irradiation-induced dimensional change rate (see Figure 2-28) and linear increase in pressure.

Table 2-13. Five comparison cases.

	Test 1	Test 2	Test 3	Test 4a	Test 4b
Layers (+buffer)	1	3	3	3	3
Creep	No	No	Yes	Yes	Yes
Dimensional change	No	No	No	Yes	Yes
Pressure	Yes	Yes	Yes	Yes	No

Layer 1 (i=1): IPyC

Layer 3 (i=3): OPyC

Layer 2 (i=2) : SiC
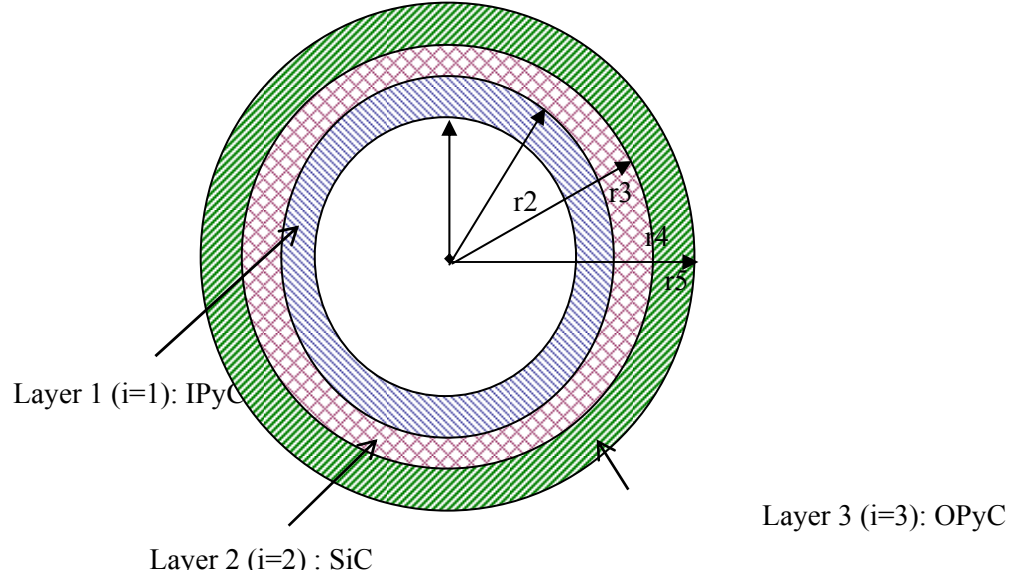
Figure 2-28. Geometry for comparison cases.

Boundary and continuity conditions between layers are:

$$\sigma_{r\_IPyC}(r_2) = P_{Interne}$$

$$\sigma_{r\_IPyC}(r_3) = \sigma_{r\_SiC}(r_3) \; ; \; U_{r\_IPyC}(r_3) = U_{r\_SiC}(r_3)$$

$$\sigma_{r\_SiC}(r_4) = \sigma_{r\_OPyC}(r_4) \; ; \; U_{r\_SiC}(r_4) = U_{r\_OPyC}(r_4)$$

$$\sigma_{r\_OPyC}(r_5) = P_{Externe}$$

Taking into account these boundary conditions leads to a differential system:

$$\frac{d(\sigma_{rI})}{dt} = h(t) + A_1 \cdot \sigma_{rI} + B_1 \cdot \sigma_{rO}$$

$$\frac{d(\sigma_{rO})}{dt} = g(t) + A_2 \cdot \sigma_{rI} + B_2 \cdot \sigma_{rO}$$

In order to solve these equations, the pressure history and the irradiation-induced dimensional change rates must be known. Moreover, h(t) and g(t) are third degree polynomials.
Finally:

$$\sigma_{rI} = C_1 \cdot e^{m_1 \cdot t} + C_2 \cdot e^{m_2 \cdot t} + k_0 + k_1 \cdot t + k_2 \cdot t^2 + k_3 \cdot t^3$$

$$\sigma_{rO} = D_1 \cdot e^{m \cdot t} + D_2 \cdot e^{m_2 \cdot t} + l_0 + l_1 \cdot t + l_2 \cdot t^2 + l_3 \cdot t^3$$

$$\sigma_{tO} = \sigma_{rO} + \frac{3 \cdot r_4^{-3}}{2 \cdot (r_5^{-3} - r_4^{-3})} \cdot [P_{Externe} + \sigma_{rO} - \frac{2}{3} \cdot F \cdot \ln(\frac{r_4}{r_5})] + \frac{F}{3}$$

In order to calculate the PyC inner surface tangential stress, a hypothesis of elastic thick shell is assumed and stresses are as follows:

$$\sigma_T = \sigma_{rI} \cdot \frac{r_3^3 \cdot (2 \cdot r_3^3 + r_4^3)}{2 \cdot r_3^3 \cdot (r_4^3 - r_3^3)} - \sigma_{rO} \cdot \frac{r_4^3 \cdot (2 \cdot r_3^3 + r_3^3)}{2 \cdot r_3^3 \cdot (r_4^3 - r_3^3)}$$

Results of the calculation are shown in the table and figures below.
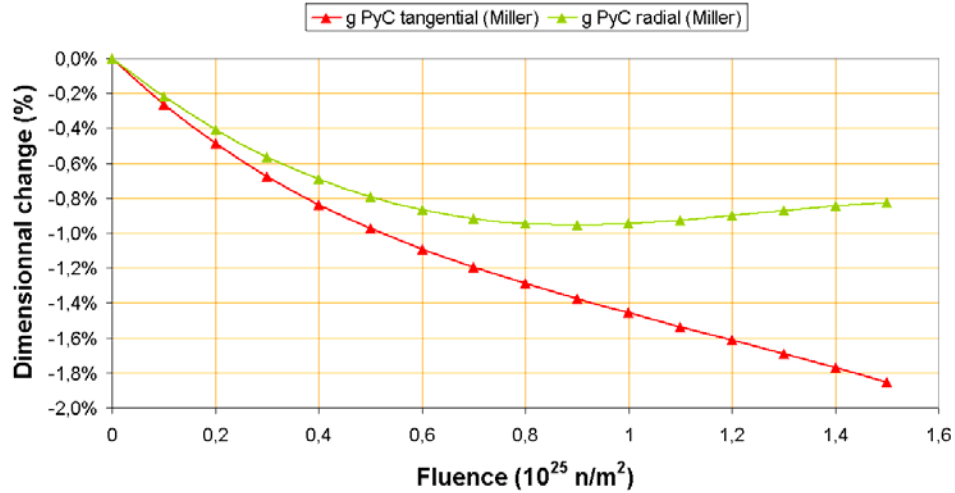
Figure 2-29. Dimensional change.

Table 2-14. Comparison between ATLAS, ABAQUS (Miller) and Miller's solution (EOI).

	Analytical solution	ATLAS solution	ABAQUS (INEEL)
Inner surface tangential stresses (MPa)			
OPyC	51.36	52	51.35
SiC	-47.7	-38.3	-47.51
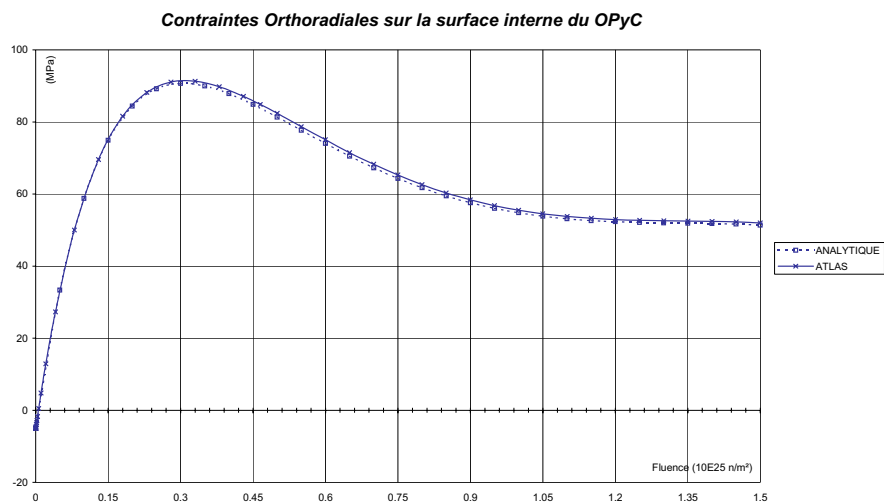
Figure 2-30. OPyC inner surface tangential stresses.
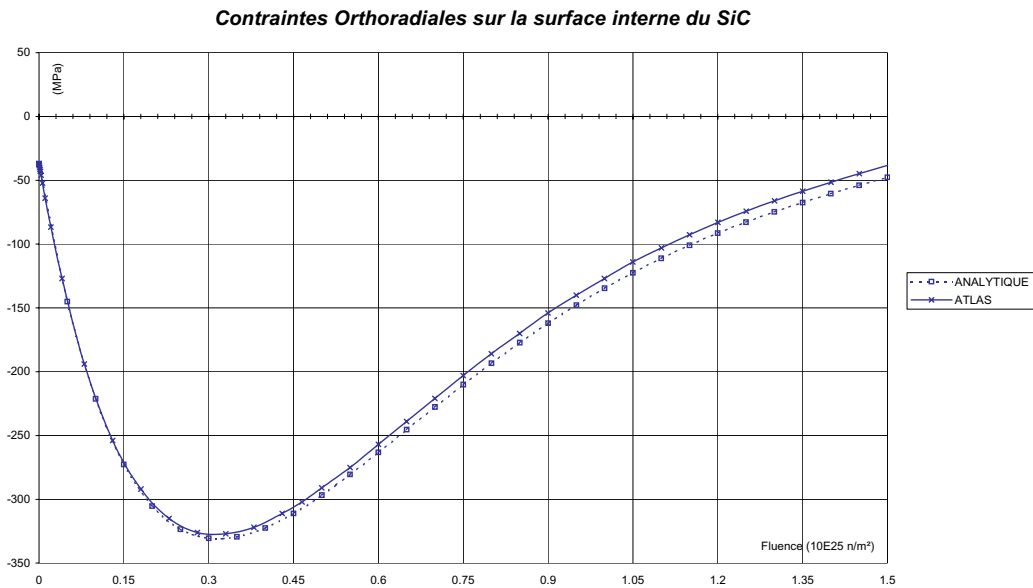
Figure 2-31. SiC inner surface tangential stresses.

HFR-P4 calculation

The document issued under of the 5°FP presents the first deterministic thermal and mechanical calculations on a free particle using the ATLAS.V1.0 code. These calculations were based on the HFR-P4 experimental irradiation of little pebbles in the HFR reactor. Two material property sets, from Germany and the UK, were used. The thermal and mechanical behavior of the particle under irradiation is a complex phenomenon with many parameters. The different property sets led to rather different results, from both a thermal and mechanical point of view.

These calculations helped identify the following important parameters:

- The deformation kinetics under rapid change of the pyrocarbon layers particularly at the beginning of irradiation.

- The irradiation creep coefficient of the PyC layers, and also that of the SiC,

- The layer failure mode

- The behavior of the buffer. Here it would be useful to know its structural evolution as well as its conductivity under rapid dimensional change

Knowledge of these properties would be an important step in the design and understanding of the in pile behavior of future fuels. This may entail the re-interpretation of past experiments as well as conducting new irradiation experiments specially for measuring material properties.
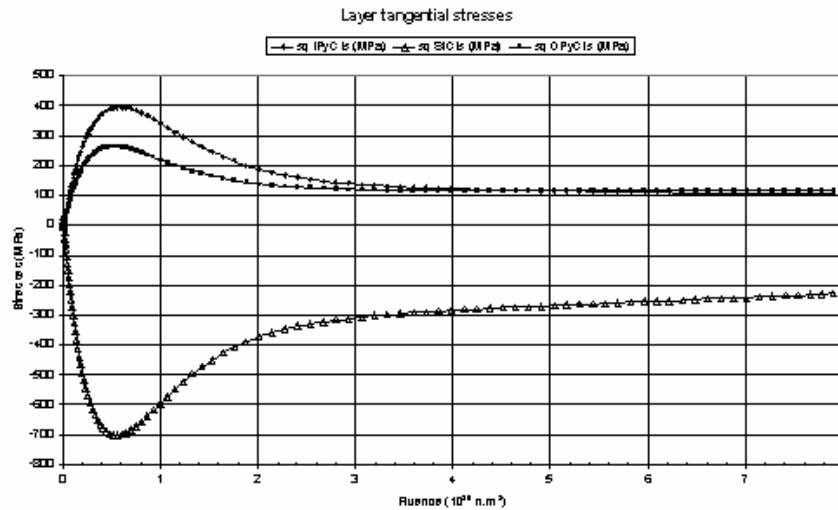
Figure 2-32. Layer tangential stresses with German set of data..

HFR-EU1 calculations, including first considerations on statistics

HFR-EU1 will be irradiated in the High Flux Reactor (HFR) at Petten, Netherlands for the European project HTR-F. The purpose of this experiment is to explore the fuel performance potential up to 20 %FIMA. The ATLAS code has been used to make fuel particle failure probability predictions. The irradiation conditions and particle parameters used in these calculations are summarized in the table below. Kernel properties, German layer properties and the models described previously were used for the calculations.

Table 2-15. Input parameters for HFR-EU1experiment.

Parameter	Units	Value	Standard Deviation
General particle data			
O/U ratio	atom ratio	2	
C/U ratio	atom ratio	0	
U-235 enrichment	weight %	16.7	
Kernel diameter	μm	501	10.8
Buffer thickness	μm	92	14.3
IPyC-SiC-OPyC thickness	μm	38 33 -41	3.4 1.9 3.8
Kernel density	g/cm^3	10.85	
Buffer density	g/cm^3	1.01	
IPyC/SiC/OPyC density	g/cm^3	1.9 3.2 1.87	
IPyC- OPyC BAF		1.02-1.02	
Irradiation conditions			
Irradiation duration	effective full power days	600	
End-of-life burn-up	% FIMA	21	
End-of-life fluence	10^{25} n/m^{-2} (E > 0.18 MeV)	5.4	
Ambient pressure	MPa	0.1	
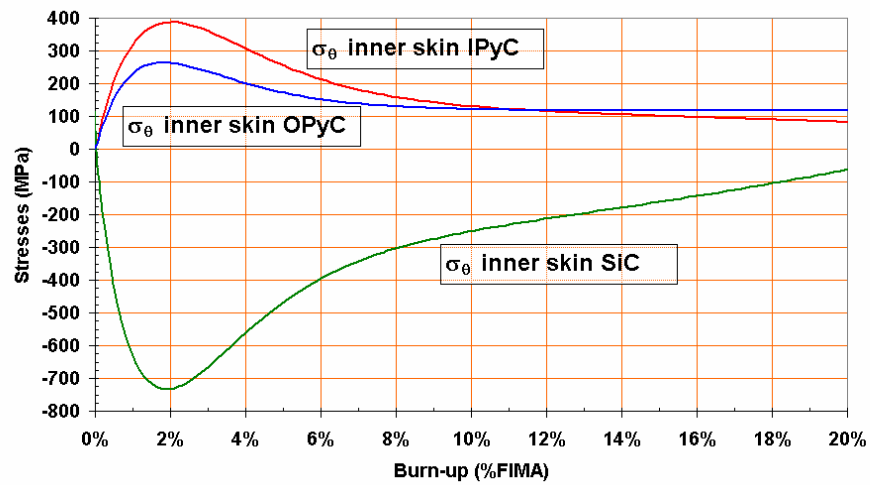
Figure 2-33. Tangential stress history for the mean particle.

Figure 2-33 presents the tangential stress history for the mean particle. A statistical approach taking into account the kernel diameter and layer thickness variation has been made. Only one mode of failure corresponding to SiC layer failure is considered(with the PyC layers staying intact until the SiC layer fails). The failure probability, F, of the SiC layer is given by a Weibull distribution, which is a function of the maximum tangential stress σ in the layer:

$$F(\sigma) = 1 - e^{-\ln(2).\left(\frac{\sigma}{\sigma_m}\right)^m}$$

at 1100°C: $\sigma_m = 834 - 57.1\Phi$ (MPa), $m = 8.02 - 0.425\ \Phi$, Φ fast neutron fluence (10^{25} n/m^{-2}).

To evaluate the mean failure probability, a Monte-Carlo method has been used:

$$E(F(A(X))) \underset{n\to\infty}{=} \frac{1}{n}\sum_n F(A(X_n))$$

where A is the ATLAS code response giving the maximum stress as a function of the particle layer thickness X ($\sigma = A(X)$). As the structure of the ATLAS model is not adapted for direct Monte-Carlo analysis, a response surface method has been used instead. This response surface is formed by two third-order polynomials.

$$\sigma = \sum_{i,j,k=0}^{5} a_{ijk} \frac{1}{e_i e_j e_k}$$

with $e_0 = 1$, $e_1 = R_{kernel}$, $e_2 = e_{buffer}$, $e_3 = e_{IPyC}$, $e_4 = e_{SiC}$ and $e_5 = e_{OPyC}$. The fitting of each polynomial is carried out by regression on 500 ATLAS simulations (Figure 2-34).
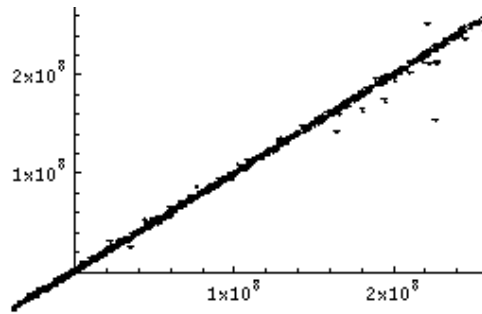
Figure 2-34. SiC tangential stresses (Pa) – ATLAS runs versus polynomial approximation.
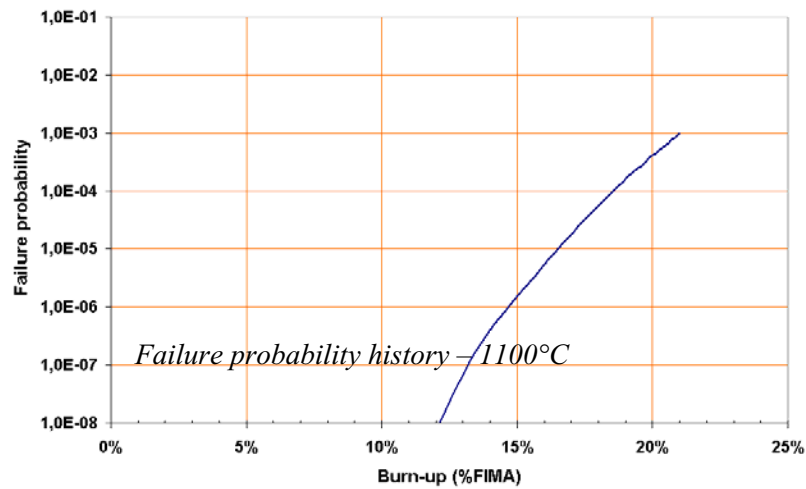
Figure 2-35. Failure probability history - 1100˚C.

Using this method, the mean failure probability of 10^7 random particles has been computed. With this set of data for three pebbles of 9560 particles, the prediction indicates the first particle failure near 18 %FIMA.

6th Co-ordinated Research Program (CRP6) benchmark

The case presented below is derived from Case 4 of the CRP6 coated particle fuel performance code benchmark (normal operation). This case simulates the behavior of a pressurized PyC/ SiC two-layer single particle under fast fluence without burn-up. This calculation, in which all the parameters needed by the codes are fixed (see Table 2-16), is useful to check the strength of the visco-elastic mechanical particle model.

Table 2-16. Parameters for IAEA CRP Benchmark Calculation.

Parameter	Unit	Value
General particle data		
Kernel diameter	μm	500
Buffer/IPyC/SiC thicknesses	μm	100/40/35
Kernel density	Mg/m^3	10.8
Buffer/IPyC/SiC densities	Mg/m^3	0.95/1.9/3.20
Irradiation conditions		
Irradiation duration	Effective Full Power Days	500
End of life burnup	%FIMA	0
End of life fluence	10^{25} n/m^2 (E > 0.18 MeV)	5
Constant temperature	K	1273
Internal pressure	MPa	25
Ambient pressure	MPa	0.1
PyC and SiC properties		
PyC - SiC Young Modulus	MPa	$3 \times 10^4 - 4 \times 10^5$
PyC - SiC Poisson's ratio	/	0.2 – 0.33
PyC creep coefficient	(MPa.10^{25} n/m^{-2} (E>0.18 MeV))$^{-1}$	4.0×10^{-29}
PyC IDC //, (η_θ)	(10^{25} n/m^{-2})$^{-1}$ (E>0.18 MeV)	-0.03
PyC IDC ⊥, (η_r)	(10^{25} n/m^{-2})$^{-1}$ (E>0.18 MeV)	-0.01
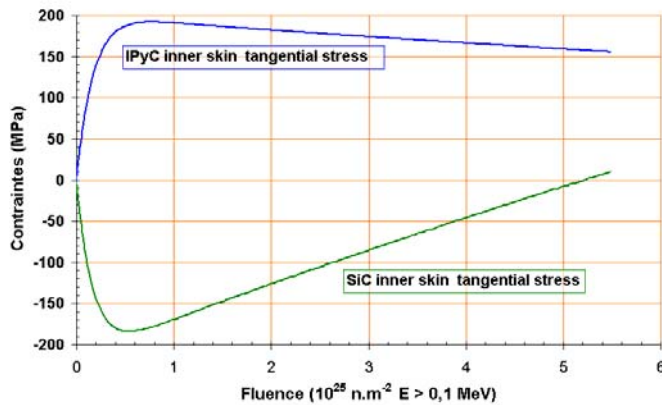
Figure 2-36. Benchmark case results: PyC and SiC tangential stress history.

Figure 2-36 above presents the tangential stress history. For this case, the IIDC leads to a very high value of dimensional change which corresponds to a high BAF value, about 15% in the tangential direction for $\Phi = 5 \times 10^{25}$ n/m^{-2} E > 0.18 MeV (10% would be perhaps more realistic). Nevertheless, to quantify the effect of the large displacement hypothesis, which is largely justified in this case, a parametrical study has been made with the same case but with the pressure equal to zero. Three set of results have been compared: two ATLAS options (large and small displacements) and an analytical solution from INEEL. The Figure 2-37 below presents the tangential SiC stress history for the three cases. Analytical solutions and small displacement ATLAS calculations are very close (stress goes up to an equilibrium which corresponds to an equilibrium between dimensional change and irradiation-induced creep). The large displacement hypothesis takes into account the particle geometry history in the stiffness matrix computation. This result must be consistent with the material property history and will be discussed elsewhere (under the CRP benchmark effort).
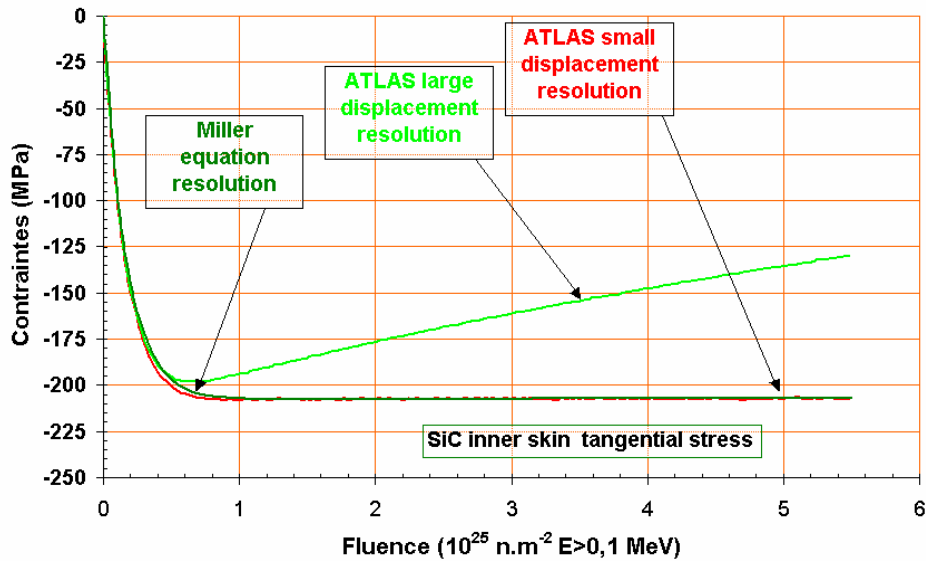
Figure 2-37. Parametrical study without pressure.

Filename: 3. INERI Task 2.doc
Directory: C:\Documents and Settings\talbhd\Desktop\FINAL INERI JAN3
Template: C:\Documents and Settings\talbhd\Application
    Data\Microsoft\Templates\Normal.dot
Title: TASK 2: DEVELOPMENT OF AN INTEGRATED MODEL TO
    EVALUATE THE MECHANISMS OF FAILURE FOR CLASSICAL TRISO PARTICLES
    IN THERMAL GAS REACTOR SPECTRUM
Subject:
Author: test
Keywords:
Comments:
Creation Date: 1/3/2005 10:21:00 AM
Change Number: 21
Last Saved On: 1/5/2005 12:07:00 PM
Last Saved By: test
Total Editing Time: 39 Minutes
Last Printed On: 1/18/2005 10:49:00 AM
As of Last Complete Printing
    Number of Pages: 58
    Number of Words: 12,773 (approx.)
    Number of Characters: 66,807 (approx.)

3. TASK 3: CONCEPT IMPROVEMENTS

Responsible Lead: MIT

Brief Description of Objectives:

In order to evaluate the ability of the classical TRISO fuel form to reach extended burnups (20% FIMA and higher), deterministic fuel performance calculations were performed using the models developed in Task 2. As a consequence of these extended fuel life calculations, requirements for fuel materials are illuminated. These requirements include that the fuel particles be able to withstand the developed stress levels and the internal chemical environment of the particle. Of particular concern to extended burnup fuel with pure oxide kernels is the production of CO. At high burnup, CO/CO_2 levels will increase significantly ($2\times$) compared to the current burnup levels. In addition, and perhaps more importantly, with high burnup fuel and/or fuel with large quantities of Pu, there will be a factor of 10 to 50 increase in the fission yields of Ag and Pd. These fission products have been shown to have a propensity to be released from the particle (Ag) or to attack the SiC barrier layer (Pd). It is also possible that these fission products act to weaken the SiC by their presence on the grain boundaries. Additionally, there is recent evidence to indicate that the transport mechanism for Ag in graphite is not by classical diffusion but by a vapor transport mechanism. However, the exact mechanism of Ag transport has been subject to much debate and the information with regard to Ag transport in graphite is new. MIT explores the fundamental interaction of Pd and Ag with SiC and ZrC. INEEL explores fission product interactions with particle layer materials. CEA explores the potential use of ZrC as the pressure barrier material for particle fuel.

3.1   Task Technical Overview: MIT

Ion Implantation

As discussed in Appendix A, silver release has been observed from SiC-coated fuel particles during irradiation and out-of-pile testing. In most cases, however, silver release was reported only for batches of fuel particles or entire fuel elements, leaving uncertainties about individual particle performance. To date, silver concentration profiles, characteristic of diffusion in silicon carbide, have not been reported. To address this topic and to study silver transport mechanisms directly, ion implantation experiments were performed to observe silver transport within CVD

SiC from a known initial concentration profile. These experiments were designed to obtain direct measurements of silver migration.

In previous work, Nabielek et al. implanted low energy silver ions into SiC disk samples and measured the concentration profile before and after heating (Nabielek, Brown, and Offermann 1977). There was no change in the silver concentration profile after 30 min at 1180°C. Nabielek et al. attributed this result to silver ions being trapped in silicon carbide grains during implantation and not being able to diffuse along grain boundaries.

In this previous ion implantation experiment samples were heated at a fairly low temperature for a very short time. The goals of the current ion implantation experiment were to investigate silver behavior in SiC at higher temperatures, those more likely to facilitate silver transport, and to witness silver migration in silicon carbide starting with a known and measurable concentration. A lack of silver migration, however, in silicon carbide during heating, as described below, provides evidence that implanted silver was deeply trapped and does not diffuse in silicon carbide via either a grain boundary or trans-granular mechanism.

Experimental Setup

Materials

Flat plate SiC, 0.3 cm thick, was the starting material for the ion implantation experiments. Chemically vapor deposited (CVD) by Coorstek, the reported density was 3.21 g/cm^3 with grain sizes on the order of 3-10 μm, preferentially oriented in the direction perpendicular to the SiC surface(CoorsTek 2003). XRD (X-ray diffraction) analysis on a polished SiC sample, shown in Figure 3-1, confirmed that the Coorstek CVD SiC contained crystalline β-SiC with a strong preferred orientation such that the (111) planes were parallel to the surface. Long, dendritic SiC grains, perpendicular to the surface, are evident in AEM analysis, show in the inset in Figure 3-1.
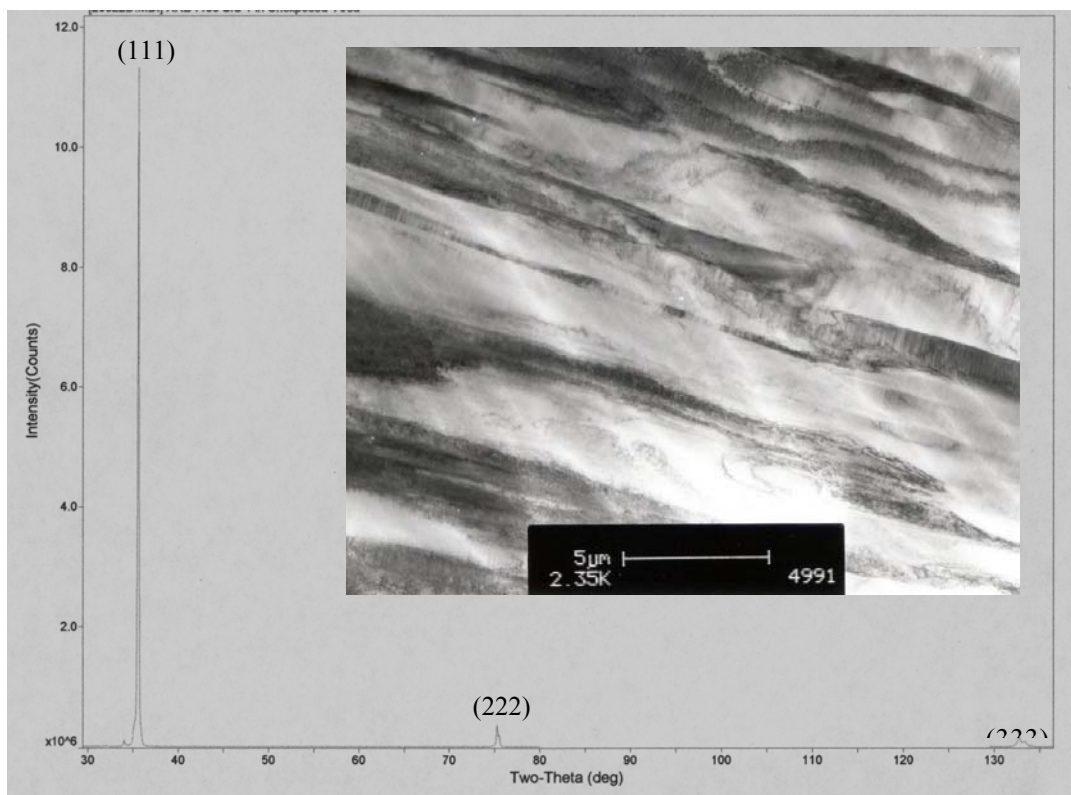
Figure 3-1. XRD analysis of an unexposed SiC sample shows β-SiC with a preferred orientation with (111) planes parallel to the surface. Long, dendritic grains are evident in AEM analysis (inset).

Each ion implantation sample was cut to 5 × 5 × 0.3 cm. One 5 × 5 cm face of each sample was polished to a mirror finish with a mean surface roughness, Ra, of 0.005 μm as measured by a Zygo interference microscope. A flat and uniform initial SiC surface ensured the best possible implanted silver profile. The silver ions began to slow down as soon as they hit the SiC surface during implantation. Excessive surface roughness across the implantation area would have caused variations in the silver implantation profile from the expected distribution which was predicted by the free-ware package SRIM (Stopping and Range of Ions in Matter) (Ziegler and Beirscak 2003).

Ion Implantation

The goals of the ion implantation were to implant a measurable quantity of silver in silicon carbide and also to implant the silver deep enough that it would not migrate out of the sample during heating. Based on silver diffusion coefficients reported in the literature by Amian and Stöver, it was expected that without accounting for trapping, the silver could diffuse greater than 10 μm in just 10 h at 1500°C with the peak concentration dropping to less than 1% of its original

value (Amian and Stöver 1983) To prevent possible silver loss during annealing and to avoid the region of surface anomalies resulting from the mechanical polishing process, the silver needed to be implanted approximately 9-15 μm into the silicon carbide. Calculations using the SRIM code indicated that ion beam energies on the order of 90-161 MeV were necessary to achieve implantation depths in the desired range.

The silver ions were implanted at the ATLAS facility at the Argonne National Laboratory using the positive-ion injector (PII) to create the silver beam. PII consists of three major subsystems: an electron cyclotron resonance (ECR) ion source and high-voltage platform, a 12-MHz beam bunching system, and a 12-MV super-conducting LINAC accelerator. The PII ECR source is a 10-GHz electron cyclotron resonance ion source mounted on a high-voltage platform. The beam bunching system compresses the beam into narrow time packets, allowing the linac to accelerate the ion beam without introducing significant energy spread. The super-conducting resonators in the PII linac accelerate the ion beam from the low velocity provided by the PII ECR to the higher velocity required for injection into the remainder of ATLAS (Argonne National Laboratory 2004). Figure 3-2 shows a floor plan of the ATLAS facility. All of the silver implantations were conducted upstream of the booster linac.
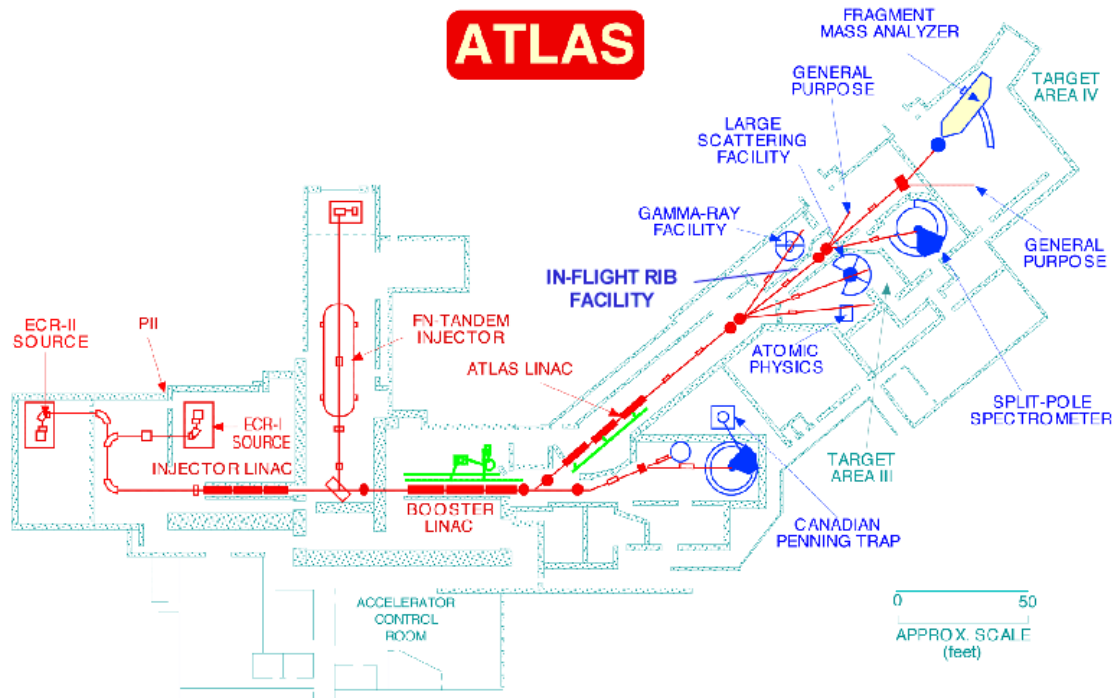
Figure 3-2. ATLAS floor plant (courtesy Argonne National Laboratory).

Two batches of samples were irradiated at ATLAS. The first batch contained samples designated 1, 2a, and 2b. Silver ions with a total energy of 161 MeV and charge state of +18 were implanted at a mean range of 12.8 μm with a peak at 13.0 μm. The second batch of samples (designated 4a-7b) were implanted with 93 MeV silver ions with charge state +19 at a mean range of 9.05 μm with a peak at 9.66 μm. A copper braid connected from the back of the sample holder to a water-cooled copper block cooled the silicon carbide samples during implantation. Type K thermocouples were used to measure the temperature at the back of the SiC samples. Average temperatures during implantation varied from 120°C to 240°C. The ion beam consisted of an irregular area approximately 10 mm in diameter with a 4 mm diameter central area where the ion concentration was the greatest and nearly uniform. The beam area can be seen on the surface of the SiC samples after implantation in Figure 3-3. The region outside the central beam area was much less uniform which resulted in variations in the as-implanted silver concentration profile. The entire ion beam was implanted directly in samples 1, 2a, and 2b. The depth profiles measured in sample 2b were taken from the center, high concentration area of the silver implantation. Silicon carbide plates with 4 mm diameter holes placed over samples 4a-7b provided masks, limiting silver implantation to only the high concentration, central beam area in the polished SiC samples. Figure 3-4*a* shows a SiC mask and 4-4*b* shows a SiC sample after implantation with a mask.
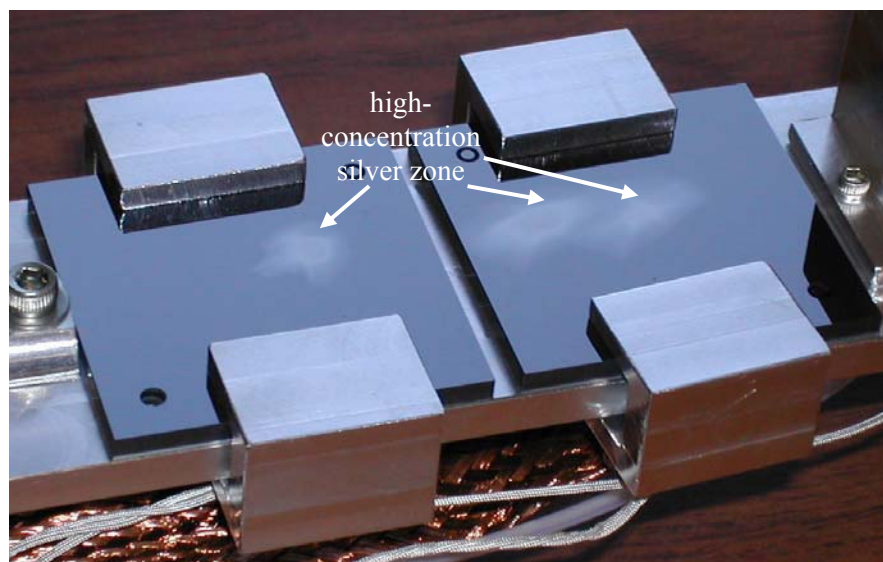
Figure 3-3. The silver implantation consists of a high-concentration center and low-concentration halo as seen on samples 1 (left) and 2 (right) after ion implantation.
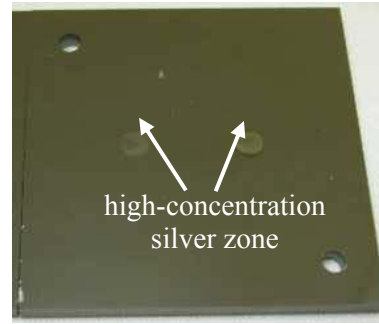
4-4a) The mask on sample 5 after implantation shows low-concentration silver region.　　*4-4b*) The silver implantation zone is well defined beneath the mask on sample 6.

Figure 3-4. SiC masks in front of the SiC samples restrict silver implantation to well-defined areas.

Table 3-1 lists the silver ion implantation conditions for all of the implanted SiC samples. The total irradiation times were selected to achieve implanted doses on the order of 10^{16} to 10^{17} atoms given the actual current during each implantation run. The calculated cumulative doses in the high silver concentration volume (4 mm diameter $\times$ 1 μm depth) ranged from 2.4×10^{16} silver atoms to 1.4×10^{17} silver atoms.

Table 3-1. Silver ion implantation conditions for all of the SiC samples.

Sample ID	Beam Energy (MeV)	Silver Charge State	Irradiat. Time (h:min)	Time Averaged Current (eμA)	Minimum Current (eμA)	Maximum current (eμA)	Cumulative dose (atoms)
1	161	+18	11:43	1.7	1.4	2.2	2.5 E16
2a	161	+18	7:54	2.4	2.3	2.8	2.4 E16
2b	161	+18	22:17	3.2	1.5	4.8	9.3 E16
4a	93	+19	18:31	3.6	2.7	5.1	8.5 E16
4b	93	+19	20:09	5.1	4.1	8.2	1.3 E17
5a	93	+19	10:10	6.9	7.9	9.8	1.0 E17
5b	93	+19	9:21	7.6	7.0	9.0	8.7 E16
6a	93	+19	6:27	13.1	12.0	14.0	1.3 E17
6b	93	+19	6:33	12.4	12.0	13.5	1.2 E17
7a	93	+19	7:34	10.7	9.8	12.0	1.3 E17
7b	93	+19	13:21	8.7	7.2	9.8	1.4 E17

Expected Implantation Effects on SiC Microstructure

The silver implantation resulted in extensive radiation damage in the SiC due to the energy loss and displacement cascades associated with the slowing down of the silver ions. Questions related to the possible interaction between the SiC damage and silver transport processes are important and must be addressed. Slowing down of the high-energy silver ions produces radiation damage that can be grouped into two general categories: 1) electronic energy loss, and 2) displacement production. The slowing down process is, as a rule of thumb, dominated by coulombic interactions (electronic energy loss) until the energy of the ion is reduced to a value in keV approximately equal to its atomic weight. For silver ions, therefore, electronic energy loss will dominate until the energy has decreased to approximately 100 keV. Roughly 99% of the silver energy loss, therefore, will be in the form of heat which will be deposited, spatially, in front of the displacement damage. The remaining energy loss will result in the production of displacement cascades. The displacement cascades will produce damage in the form of displacements, dislocation loops, and, if the dose and dose rate are high enough, amorphization and/or recrystallization of the SiC.

For the implantation conditions in this work, SRIM calculations indicate that significant displacement damage begins at a depth of 5 μm and 7 μm for the 93 MeV and 161 MeV cases, respectively, with the peak in displacement damage occurring at about 9 μm and 13 μm, respectively. Figure 3-5 shows the results of the SRIM calculations for 93 MeV and 161 MeV silver ions in SiC. Although the SRIM code calculates damage using a simple Kinchen-Pease displacement model, the results are instructive on a relative basis when comparing the number of displacements and subsequent vacancy production and will be quite accurate when predicting the energy loss and spatial distribution of damage.

93 MeV Silver Implantation

161 MeV Silver Implantation
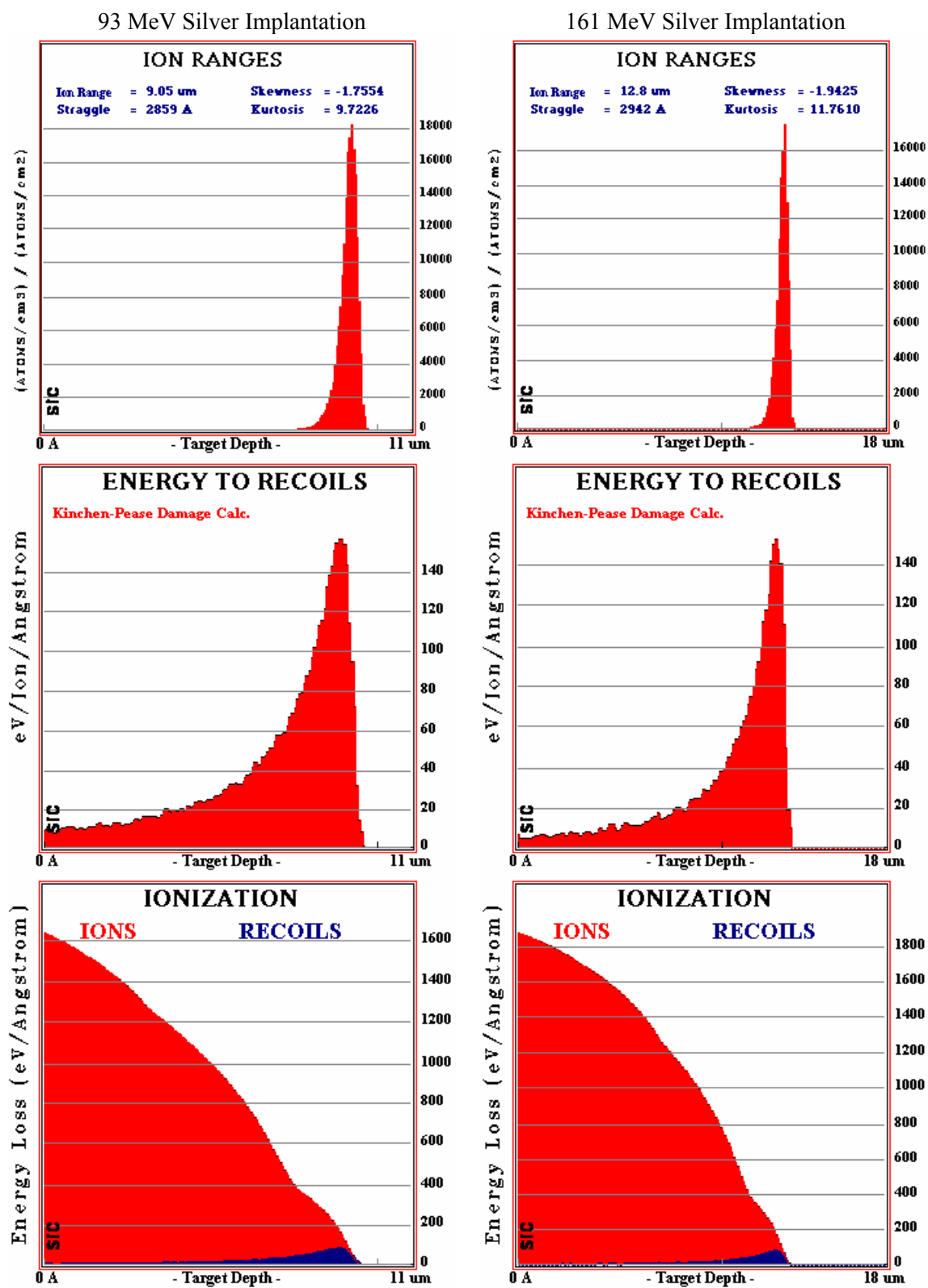
Figure 3-5. Results of SRIM calculations for silver implantation at 161 MeV and 93 MeV.

With respect to amorphization, Wendler et al. have shown that for high-energy ion damage, SiC amorphization becomes impossible at temperatures above approximately 250°C (Wendler, Heft, and Wesch 1998). Heera et al. have discussed the dynamic relationship between the damage rate, ion characteristics, and the location of the ion-beam induced epitaxial/amorphized region boundary (Heera et al. 1995). Also, Pacaud et al. have reported that the crystallization temperature for ion implanted SiC is approximately 950°C (Pacaud et al. 1996).

Based on the above discussion, the implantation process was expected to result in a multi-zone damage region consisting of the following zones when proceeding from the beam entry point: 1) a region of unaltered SiC where, while the electronic loss energy deposition is very high, the displacement damage will be essentially zero; 2) a region where the displacement damage begins to accumulate and in which the SiC will be severely disrupted and probably dynamically recrystallized; 3) a region where amorphization has occurred since the irradiation temperature was not expected to exceed 250°C; and 4) a region of undamaged SiC beyond which may have a diffuse boundary due to straggling of the ion slowing down process. The silver is expected to be in the rear of amorphous SiC region.

With respect to the effect of the radiation damage on the morphology of the silver, as it may affect migration during subsequent annealing, the damage process will result in complete mixing of the SiC and silver in the amorphous region. The silver, implanted at a peak concentration of approximately 20 atomic percent, is expected to precipitate, as elemental silver, within the damage zone since the solubility of silver in SiC is negligible. This arrangement should provide an almost ideal situation in which silver is in intimate contact, if not actually mixed, with the SiC matrix. Additionally, the recrystallized SiC region can be expected to provide grain boundary area for possible transport. Lastly, the annealing process will result in recrystallization of the damaged, amorphous region, producing grain boundaries in exactly the same location as the silver. Such conditions should be ideal for silver migration through the SiC as predicted in the literature.

Annealing Conditions

The goal of the ion implantation experiment was to observe silver migration in SiC from a known and measurable initial concentration. Implantation of a high silver concentration, on the order of 10 atomic percent averaged over the entire implantation volume, ensured that the silver

concentration profile would be measurable, above the detection limits of the analysis techniques, both before and after annealing.

All of the heat treatments were conducted in a Webb graphite furnace at 1500°C ± 15°C. A heat treatment temperature higher than typical operating temperatures was selected in an effort to encourage migration. A review of the literature indicated that grain boundary diffusion was a dominant silver transport mechanism with a representative diffusion coefficient of $2 \times 10^{-15} m^2/s$. The heat treatment conditions were selected to observe measurable silver transport after the test, based on the literature values. At 1500°C, measurable silver transport was predicted, given representative diffusion coefficients, in fewer than 10 h. Heat treatments as long as 480 h were conducted to allow ample time for silver transport in the SiC samples. The Webb furnace operates under low vacuum at 1500°C with typical vacuum readings in the range of 4-15 mTorr. Each sample was sandwiched between two blocks of silicon carbide, approximately $5 \times 5 \times 1.3$ cm, to limit interaction between the surface of the implanted SiC and any contaminants in the furnace atmosphere.

The silver concentration profile was measured in sample 2b before and after annealing at 1500°C for 210 h. AEM (analytical electron microscopy) of sample 6a after implantation and sample 5a after 480 h at 1500°C compared the effects of annealing on the silver distribution. Table 3-2 shows the heating data for the samples analyzed; details of the analyses are discussed below.

Table 3-2. Annealing conditions for selected samples.

Sample ID	Implanted Dose (atoms/cm^3)	Temperature (°C)	Time (h)	Analysis
2b	1.9 E+21	1500 ± 15	210 ± 0.25	XPS profiles
5a	2.1 E+21	1500 ± 15	480 ± 0.25	AEM
6a	2.6 E+21	n/a	n/a	AEM

Results and Discussion

Before and after heating, the ion implantation samples were analyzed using XPS (X-ray photoelectron spectroscopy) to measure the silver concentration profile, and SEM (scanning electron microscopy) and AEM to examine the silver distribution within the SiC. XPS detected no measurable change in the bulk silver concentration profiles after heating. SEM and AEM analyses showed a change in the microscopic distribution of the silver, with a diffuse silver

distribution after implantation transforming to discrete silver precipitates after heating. Additionally, the AEM analysis showed the diffuse silver residing in amorphous SiC after implantation and silver precipitates between recrystallized SiC grains after heating. Both the SEM and AEM analyses showed that the silver did not migrate out of its original deposition zone.

Silver Concentration Profiles

Measurements of the silver concentration profiles before and after heating were expected to show silver migration away from the initial implanted profile. Calculations based on previously reported diffusion coefficients predicted complete depletion of the silver concentration profile after 210 h at 1500°C. Figure 3-6, however, shows that there was no change in the silver concentration profile in sample 2b after heating at 1500°C for 210 h. The expected silver concentration profile, based on the diffusion coefficient reported by Amian et al., after just 1 h at 1500°C is also shown in Figure 3-6 (Amian and Stöver 1983). Diffusion of the magnitude previously reported clearly did not occur, if at all.

XPS, also known as ESCA (electron spectroscopy for chemical analysis), measures concentration profiles by alternating spectral data collection with sputter cycles. The spectral data collection includes the identification of the elements present along with bonding information while the sputter cycles remove material and expose successively deeper layers of the sample. One advantage of XPS analysis is the ability to distinguish not just the elements, but also the chemical bonds present; with this technique, for example, free silicon can be distinguished from silicon bound in silicon carbide. In the sample analyzed, XPS detected no free silicon above the detection limit of approximately 1 atomic percent.
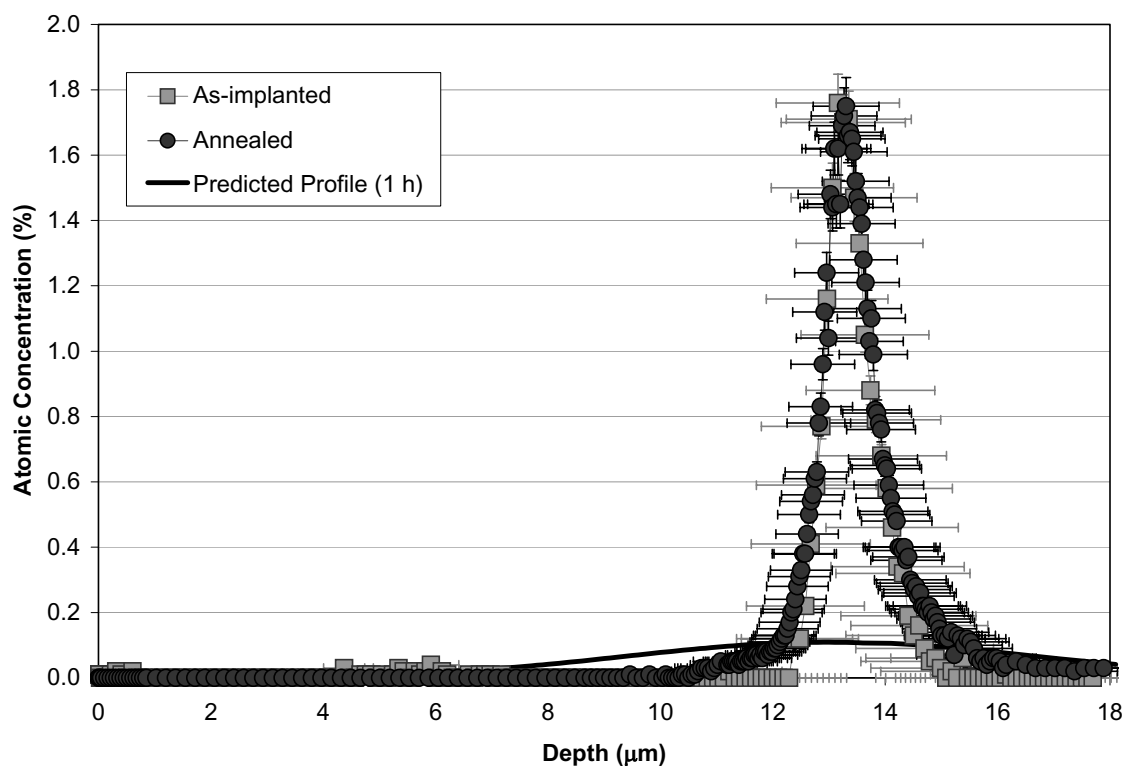
Figure 3-6. Silver concentration profiles before and after heating at 1500°C for 210 h are the same (sample 2b).

To achieve the best comparison between silver concentration profiles before and after heating, it was necessary to use the same sample. A 1.3 mm hole punched in a thin gold foil provided a mask over the 4 mm silver implantation area, preserving the small silver spot from the normally large XPS sputter area, usually a few millimeters in diameter. A schematic of the gold-foil mask over the SiC sample is shown in Figure 3-7. Use of the small gold mask increased uncertainties in the final XPS concentration profiles due to self-shielding during sputtering leading to edge rounding of the sputter crater. An uneven and sloped crater bottom also increased the uncertainty of the total depth of the crater.
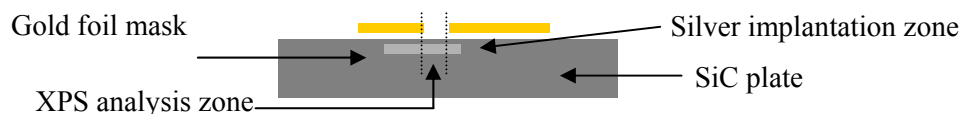
Figure 3-7. A gold-foil mask limited the XPS analysis area (schematic not to scale).

A tight fit between the size of the sputter area and the size of the XPS analysis beam increased uncertainty in the final concentration profile. The bottom of the sputter crater was about the same size as the analysis beam. When the analysis beam measured the concentration at a certain depth, up to 10% of the data signal actually came from the rounded edges of the sputter crater and even from the sides of the crater walls. At any depth, therefore, the detected signal was actually coming from a range of depths, not just the bottom of the crater. Although these uncertainties in the silver concentration profile tended to artificially widen the measured concentration profile, they were present in both analyses, still allowing for a direct comparison between the two profiles before and after heating.

A silicon carbide sputter standard was not available to determine the sputter rate during the XPS analysis. A Zygo interference microscope was used to measure the depth and shape of the sputter craters. Figure 3-8 shows the sputter crater after XPS analysis of the silver concentration profile after at 210 h, 1500°C heat treatment. The depth of the sputter craters was used to calculate the sputter rate during XPS analysis and generate a concentration depth profile from the spectral data. The sputter rate was assumed constant throughout the silicon carbide and equal to the total crater depth divided by the total sputter time. However, an uneven and sloped crater bottom created uncertainty in the total depth of the sputter crater and the sputter rate.
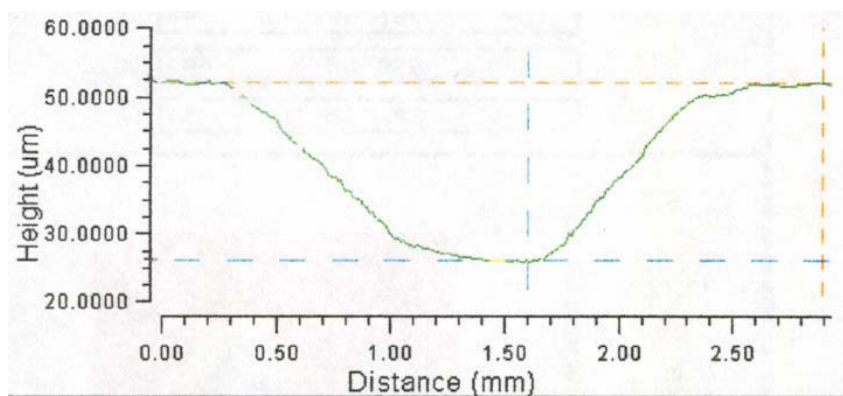
Figure 3-8. The sloped walls and narrow bottom of the XPS crater contribute to the measurement uncertainty.

These uncertainties are shown as error bars in Figure 3-6, but it is still clear that, within the uncertainty of the XPS analysis, there was no silver migration during heating, a significant departure from the expected results. If silver migration were governed by typical diffusion coefficients reported in the literature, the silver concentration after heating for 210 h at 1500°C would be completely depleted. However, there was no macroscopic silver concentration change during heating. Within the spatial resolution of XPS the silver concentration profiles before and after heating were the same and silver did not diffuse during the 210 h anneal at 1500°C. Based on the lack of change in the silver concentration profile after heating and the uncertainty of the measurement, the diffusion coefficient for silver in SiC must be less than $5\times10^{-21}m^2$/s at 1500°C. XPS results average the spectral data collected over a fairly large area, approximately 800 μm × 800 μm. Techniques with finer spatial resolution, such as SEM and AEM, were needed to investigate the detailed silver behavior and the effects of ion implantation in silicon carbide.

Electron Microscopy

Background

Although it is significant that no macroscopic silver concentration changes occurred during heating for 210 h at 1500°C, the details of silver behavior in silicon carbide were of interest. Both SEM and AEM examinations of the SiC samples revealed details of the silver distribution and the SiC microstructure. The goals of the SEM analysis were to observe the distribution of the silver in the SiC samples and to compare the width, if possible, of the silver zone before and after heating. Higher magnification AEM analyses provide details of the SiC microstructure and the silver distribution and orientation with the SiC zones.

AEM was used to analyze thin cross-sectional slices of two ion implantation samples, one before annealing and one after. The goals of the AEM analysis of the ion implantation samples were to observe and identify the silver location in the implanted region, both before and after heating. An additional goal was to characterize the silicon carbide grain structure both within and outside the implantation region and also to characterize, if possible, the damage in the implanted region. The AEM analyses were performed on a Philips CM300 equipped with an EDAX X-ray detector for elemental analyses.

Scanning Electron Microscopy

SEM analysis of polished cross-sectional surfaces of the SiC ion implantation samples, both before and after annealing, highlights contrast in atomic number at the sample surface, with higher Z materials appearing brighter in the images (e.g., silver appears brighter than silicon). The SEM analysis was performed on a FEI/Philips XL30 FEG Environmental SEM with energy-dispersive X-ray capability. The SEM was operated under H_2O vacuum mode.

The silver distribution after implantation is seen in *b* and *c* at low and high magnification, respectively. The implanted silver zone is approximately 9 μm below the front edge of the SiC sample and approximately 1 μm wide, in good agreement with the predicted silver profile calculated using SRIM and shown in *a*. The silver location is also consistent with the calculated displacement damage morphology shown in Figure 3-5 (93 MeV). Chemical analysis by EDS (energy dispersive spectroscopy) indicates that silver is located only in the bright area. The EDS spectra associated with the locations identified in Figure 3-9*b* are shown in Figure 3-10; the locations identified as 1 and 3 are SiC and location 2, in the bright region, contains silver.
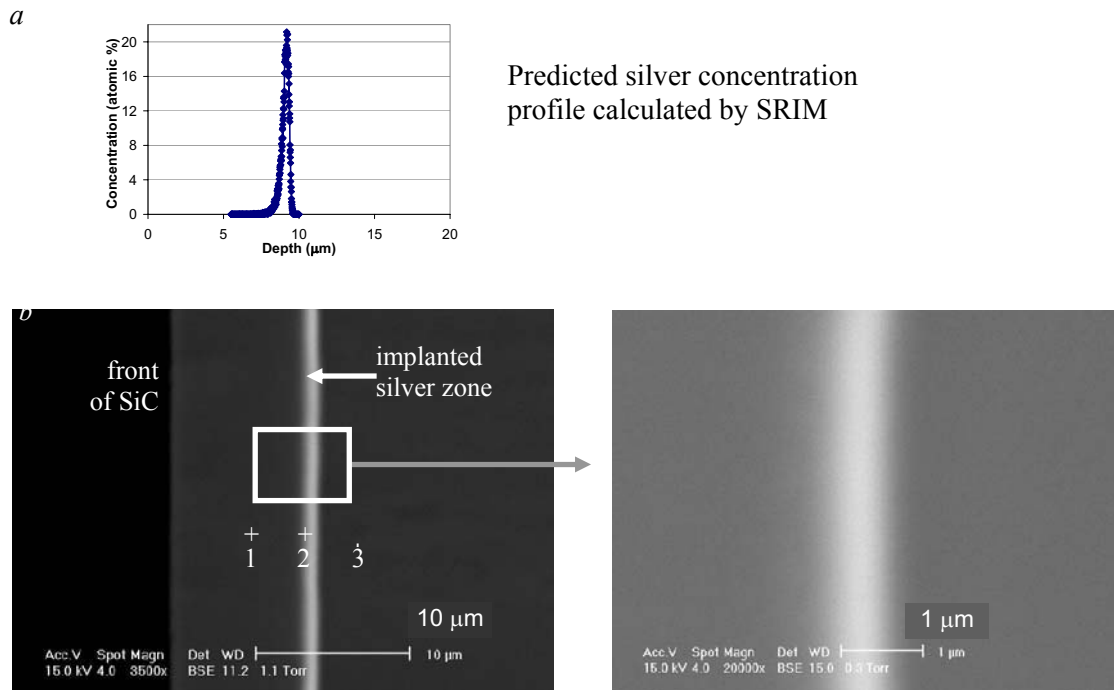
Figure 3-9. The as-implanted silver distribution matches the a) predicted profile from SRIM and appears bright in SEM backscatter imaging and is diffuse (homogeneous) in sample 6a at b) low magnification and c) high magnification.
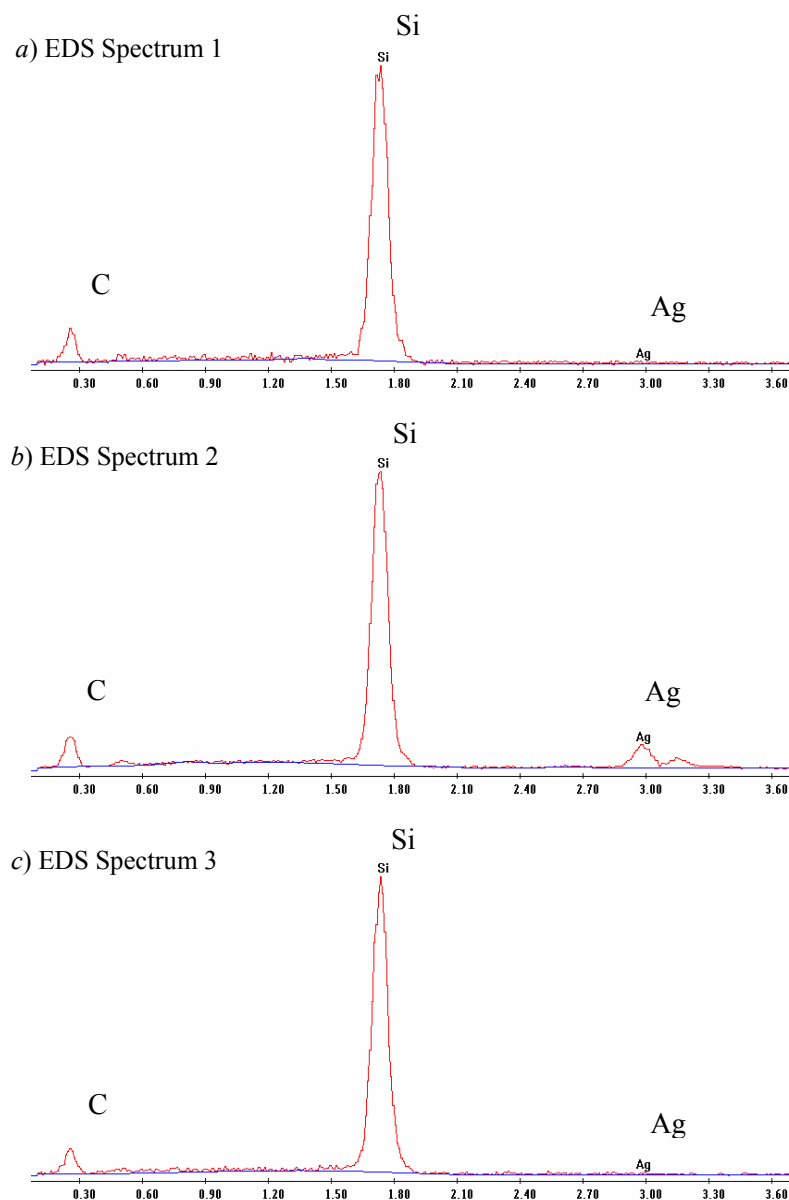
Figure 3-10. EDS spectra from points a) 1, b) 2, and c) 3 in Figure 3-9. Silver is only present in the bright area; no silver is detected on either side of the implantation zone.

After heating for 480 h at 1500°C, the silver appears discrete and individual silver particles are evident, as seen in Figure 3-11. While the arrangement of silver appears coarser after heating, the width of the silver zone is still approximately 1 μm, unchanged during heating.

As mentioned earlier, atomic number contrast in the SEM causes heavier elements to appear brighter in basckscatter images. Thus, silver appears as bright spots in contrast to the gray

silicon carbide in the SEM images. Some bright spots appear in front of the implanted silver zone in Figure 3-11 (towards the left in the image). Although EDS confirmed that the composition of the bright spots in the implanted silver zone was silver, the bright spots in front of the main implanted silver zone were not analyzed. These spots are likely silver that has precipitated in a defect structure in the SiC.
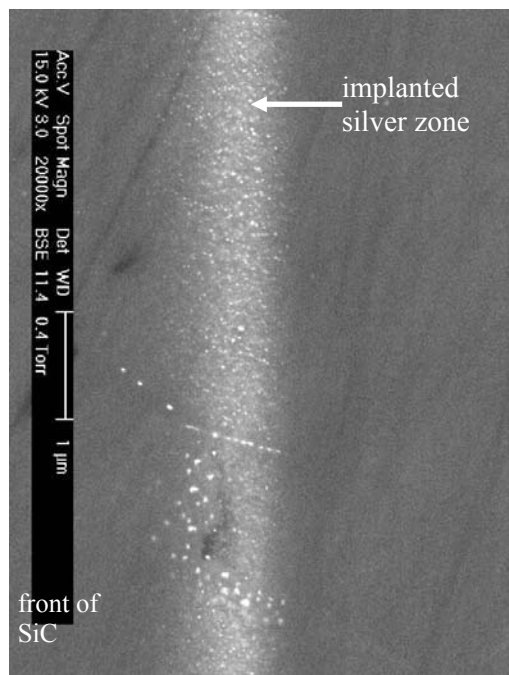
Figure 3-11. The silver distribution is discrete after heating at 1500°C for 480 h (sample 5a).

As-implanted SiC Microstructure

A recrystallized zone of silicon carbide defines the front of the silver implantation zone in sample 6a, before annealing, as seen in Figure 3-12. The original silicon carbide columnar grain structure is visible to the left and right of the implantation zone. The altered zone consists of three main regions. In the front-most region of the implantation zone, on the left in Figure 3-12, the SiC has already recrystallized. The middle of the altered zone contains amorphous SiC. Towards the back, the SiC is still mostly amorphous, but small SiC crystallites have nucleated. While all of the SiC grains in the recrystallized zone at the front of the implantation zone are fine-grain equiaxed, there appears to be a further distinction between smaller, more equiaxed grains at the front and slightly larger, more elongated grains at the back. The smaller equiaxed

grains are approximately 50-150 nm and the larger grains are about 100-200 nm wide by 250-400 nm long.

The back 1.1 μm of the altered zone is largely amorphous, but also contains some small equiaxed SiC crystallites ranging in size from less than 4 nm to about 30 nm. Silicon carbide grains have nucleated and started to grow in the back of the amorphous region during implantation, but have not been able to incorporate all of the SiC. A thin band of the original SiC behind the altered zone, about 80 nm wide, appears damaged with increased faulting, though the damage was not great enough to cause amorphization or recrystallization.

Predicted silver concentration profile from SRIM calculations
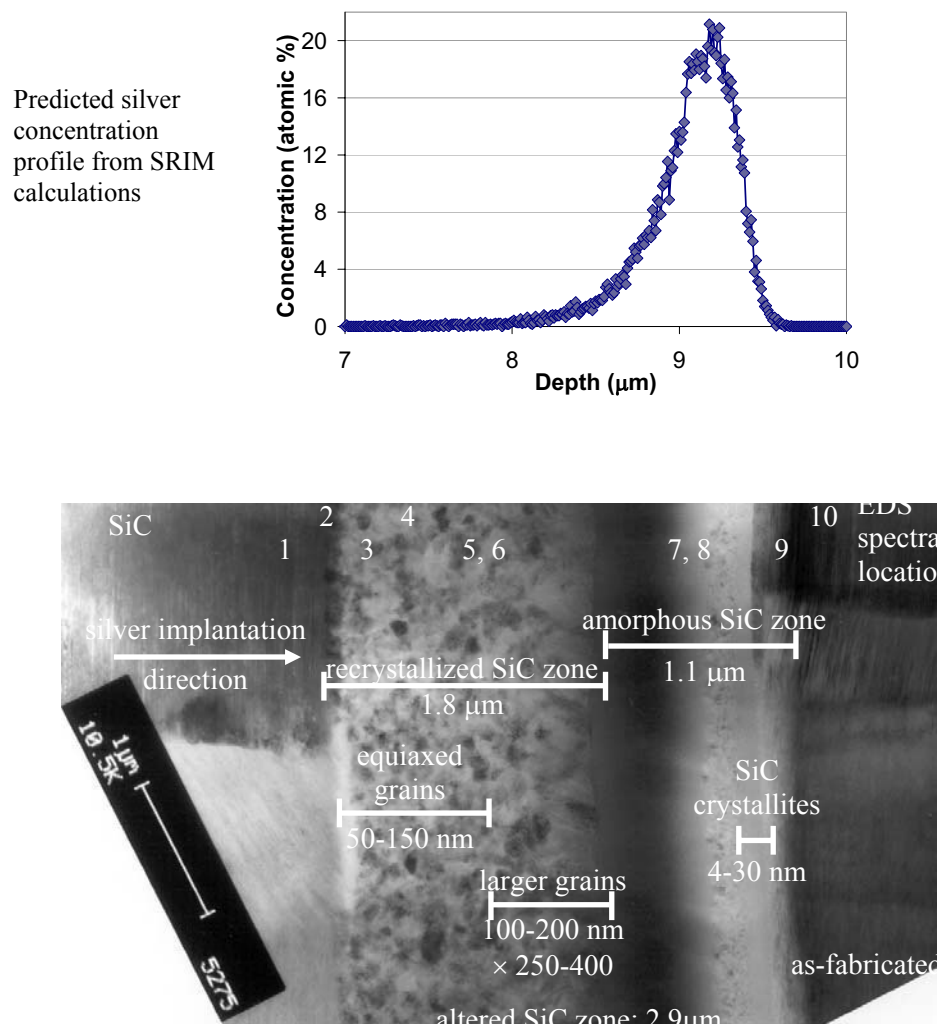
Figure 3-12. The as-implanted silver profile measured by EDS matches the predicted profile from SRIM calculations; numbers indicate EDS spectra locations.

113

EDS (energy dispersive spectrometry) measurements taken during the AEM analysis along the cross-section of the implanted sample provide a qualitative assessment of the silver concentration in the silicon carbide. The locations of EDS measurements are shown in Figure 3-12 and the silver concentrations are listed in Table 3-3. No silver was observed in the original SiC in front of the altered zone or in the front portion of the recrystallized zone. Silver just above the detection limit of approximately 1000 ppm (0.1 atomic percent) was measured in the recrystallized zone at the boundary between the equiaxed and slightly dendritic SiC grains. EDS detected peak silver concentrations in the amorphous SiC region. A small amount of silver was detected at the boundary between the amorphous region and the original SiC and just a trace of silver was measured in the damaged layer of the original SiC just behind the altered zone. The silver profile, measured by EDS, agrees with the predicted silver implantation profile, as seen in Figure 3-12, with the peak concentration occurring in the amorphous SiC.

Table 3-3. Most of the silver, detected by EDS, is located in the amorphous SiC region.

Spot #*	Location	Silver Concentration (%)
1	as-fabricated SiC, front	none detected
2	interface between front SiC and recrystallized SiC	none detected
3	~0.2 μm into recrystallized SiC	none detected
4	in the middle of the recrystallized, equiaxed SiC	1.1 (trace)
5	between the equiaxed and	2.8
6	dendritic recrystallized SiC	5.1
7	amorphous damaged region	26.3
8		25.1
9	interface between amorphous SiC and as-fabricated SiC	4.0
10	damage zone of as-fabricated SiC	1.2 (trace)

* EDS spot locations are shown in Figure 3-12.

Additional analysis using a VG HB603 STEM (scanning transmission electron microscopy) operated at an acceleration voltage of 250 kV highlights the presence of silver in the amorphous SiC zone and decorating the first row of grains in the recrystallized zone, as seen in Figure 3-13. The images displayed in Figure 3-13 correspond to the middle of Figure 3-12, the interface between the recrystallized and amorphous SiC zones. The small bright dots in the STEM images are silver-rich while the dark areas are silicon-rich. The spatial resolution of the chemical analysis in the STEM was on the order of the size of the bright features, so the quantitative

composition of the bright features and dark areas cannot be determined. No silver was detected in the undecorated recrystallized SiC grains below about the first row next to the amorphous SiC zone, as seen in Figure 3-13*a*.

At this resolution it is clear that the silver morphology depends on the SiC region in question. In the amorphous region, seen in Figure 3-13*b*, the silver is separated into small, approximately 5 nm in diameter, regions. The distribution of these silver-rich regions is random, in keeping with the amorphous nature of the region. In the recrystallized SiC material, seen in Figure 3-13*c*, the silver regions are slightly larger, but the morphology now appears oriented within the SiC crystal structure. The β-SiC (3C-SiC) crystallizes in the zinc blende structure, which can be visualized as two interpenetrating (carbon and silicon) face-centered cubic lattices offset by ¼ cubic diagonal. The morphology of the silver suggests a preference for precipitation on the close packed planes in this structure, i.e., the (111) body diagonals.
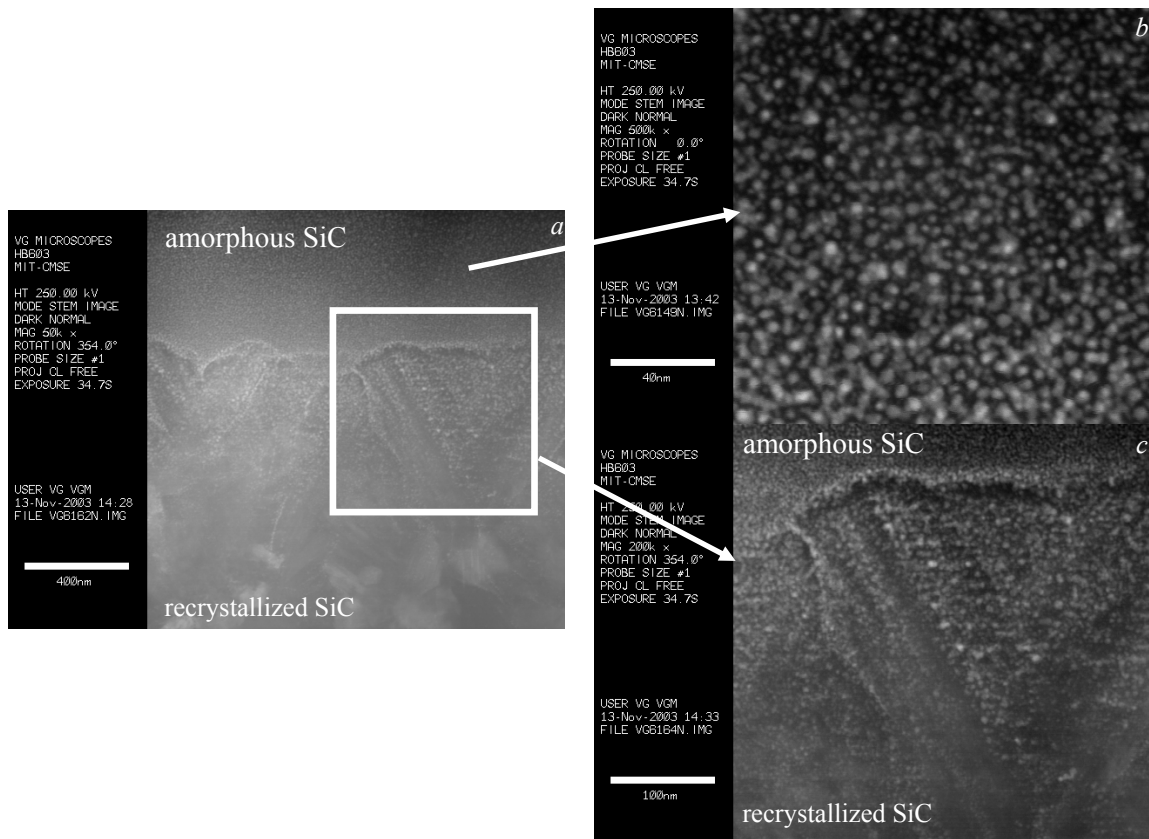
Figure 3-13. Silver is detected in the amorphous region and into the first rows of grains by STEM of the as-implanted sample 6a.

An elemental line scan collected during STEM analysis, shown in Figure 3-14, also confirms the implanted silver distribution as measured during AEM analysis and seen in Figure 3-12 and Table 3-3. The results, though qualitative, confirm that silver is located predominantly within the amorphous region and extends just into the recrystallized SiC zone.
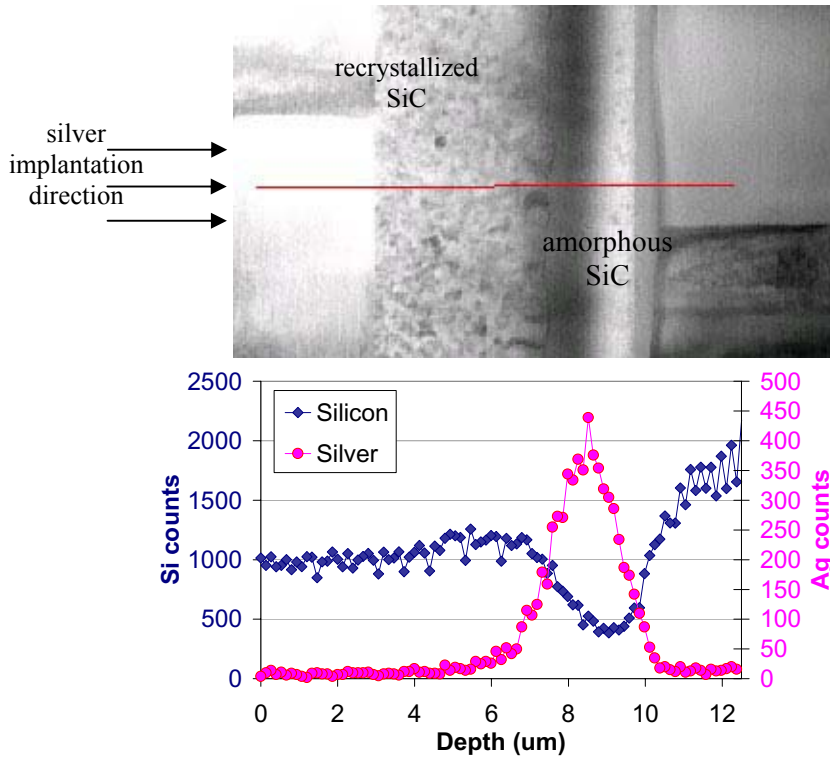
Figure 3-14. A line scan in STEM shows the silver concentration peak in the amorphous SiC zone of an as-implanted sample (6a).

Annealed SiC Microstructure

The amorphous implantation zone completely recrystallized, as expected, during a 480 h anneal at 1500°C (sample 5b), as seen in Figure 3-15. The amorphous SiC was completely eliminated from the altered zone during annealing. The recrystallized zone is approximately 2.1 μm wide and is characterized by two regions. The front region, which closely corresponds to the region that was dynamically recrystallized during implantation, has been transformed into an epitaxial, columnar region. The rear region, formally amorphous, has crystallized and is characterized by a fine, equiaxed structure. This region also contains precipitated silver, phase-separated from the SiC. Figure 3-16 shows a silver elemental map, taken during STEM analysis in the annealed material. The silver has clearly remained segregated within the implanted region. The crystallized SiC, after annealing, is shown in more detail in Figure 3-17. The silver appears

116

darker than the SiC in the AEM images due to its higher atomic number. The silver is segregated from the SiC and has accumulated on grain boundaries.

While all of the recrystallized SiC grains are small and generally equiaxed, the front of the recrystallized zone features elongated grains, oriented along the implantation direction with widths approximately 30 nm to 100 nm and lengths ranging from 300 nm to 800 nm. The back half of the recrystallized zone contains smaller, more equiaxed SiC grains, on the order of 40 nm to 100 nm.
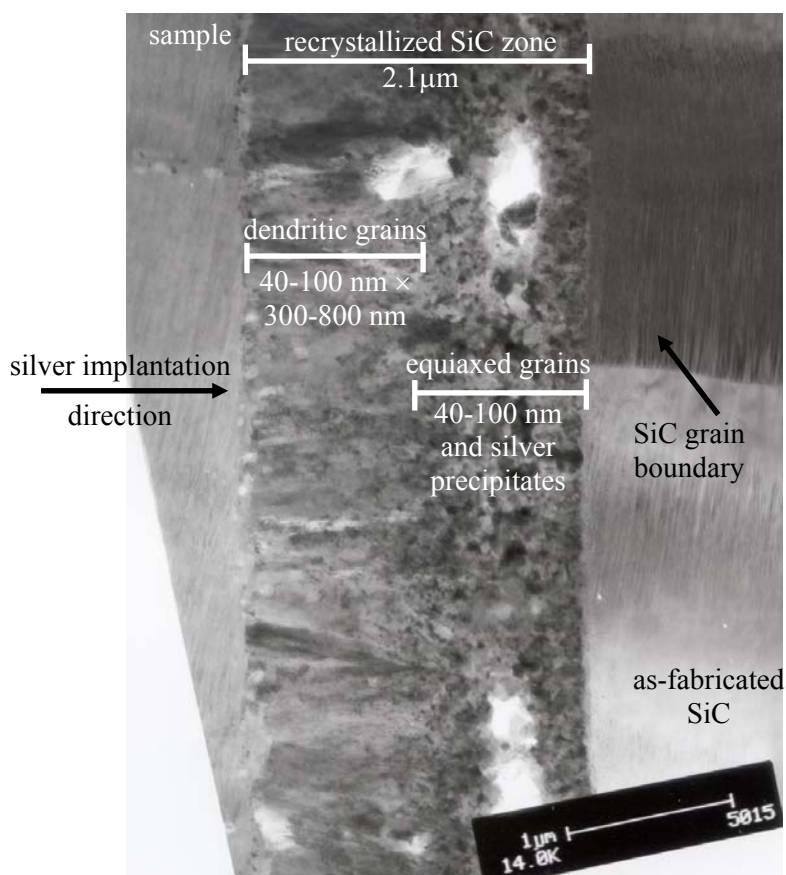
Figure 3-15. The SiC completely recrystallized in sample 5a after heating for 480 h at 1500°C.
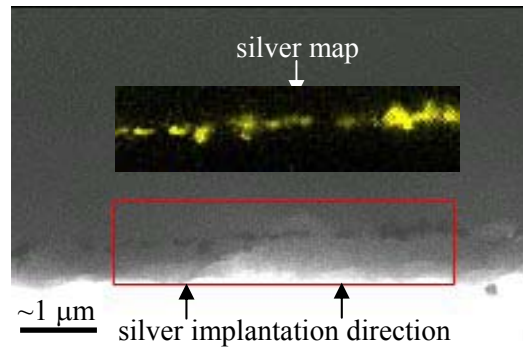
Figure 3-16. STEM micrograph and silver dot map shows discrete silver morphology in the SiC after heating for 480 h at 1500°C (sample 5a).
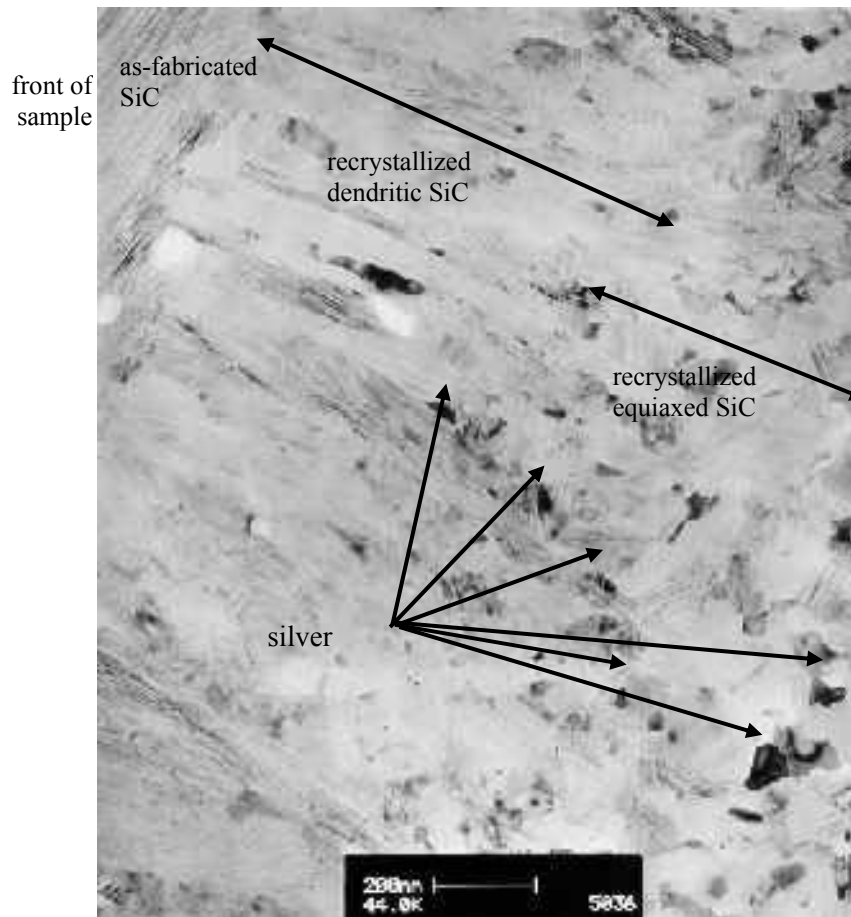
Figure 3-17. Detail of crystallized SiC after annealing for 480 h at 1500°C shows typical silver precipitates (sample 5a).

Just behind the recrystallized zone, there is a zone, approximately 0.5 μm wide, of heavily damaged, original silicon carbide, as seen in Figure 3-18*a*. In this region, the implantation damage was not sufficient to cause recrystallization or amorphization of the original SiC. The radiation damage calculations, however, indicate that a significant amount of displacement damage should have been present. Small precipitates of silver decorate the silicon carbide behind the recrystallized zone, shown in Figure 3-18*b*. These silver regions are approximately 4-20 nm in size. The damaged layer is approximately 300-400 nm wide. As seen by comparing Figure 3-18 a and *b*, silver is only present in the heavily damaged SiC zone. The low concentration of silver in the damaged SiC just behind the recrystallized zone is consistent with the tails of the silver concentration profile predicted using the SRIM code and the EDS spectra collected during AEM, as shown in Figure 3-12 and Table 3-3. Silver has not migrated into the undamaged SiC regions.

Silver appears only in the rear portion of the altered SiC zone, the same region where it appeared in the as-implanted sample, as seen in Figure 3-12. After implantation, but before heating, silver was detected in the amorphous zone. This zone recrystallized during heating, forming equiaxed grains where the silver was detected. No silver was implanted in the front portion of the altered SiC, where the grains recrystallized during heating and grew slightly during annealing, and none is detected after heating.
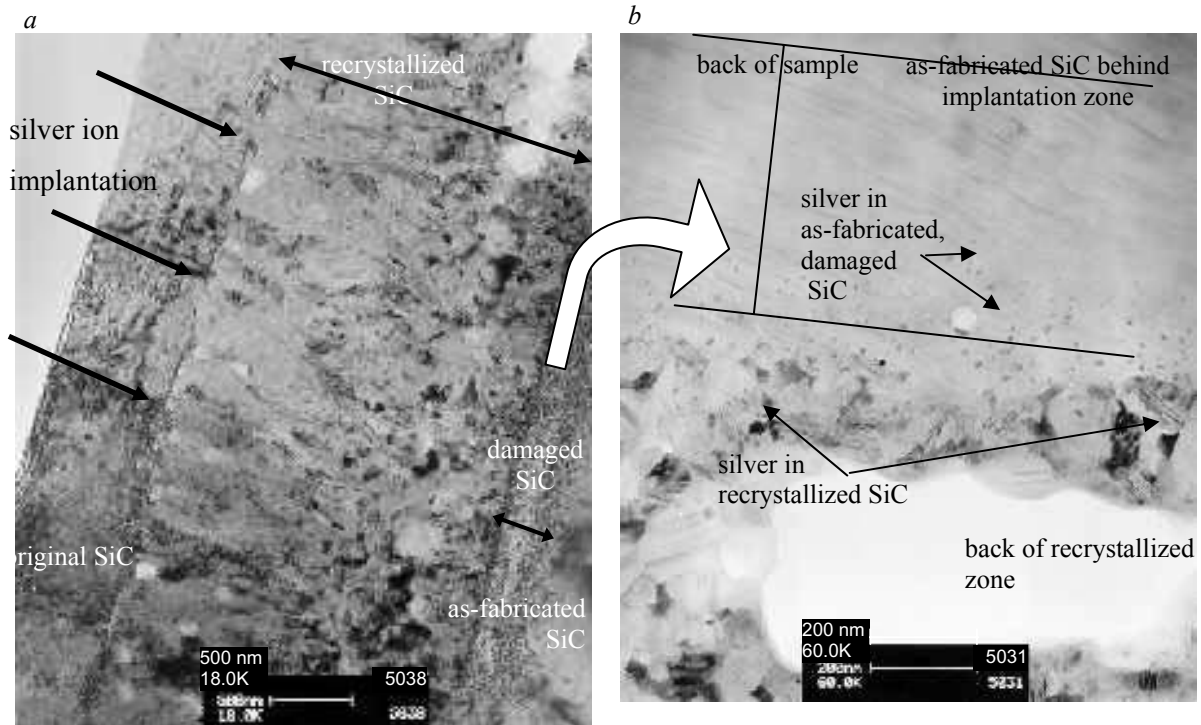
Figure 3-18. After 480 h at 1500°C, silver is only detected in the recrystallized SiC and in the heavily damaged SiC behind the recrystallized zone.

Figure 3-19 shows the details of a typical grain boundary region. Analysis of the grain boundaries in the region immediately behind the damaged region, where grain boundaries from the undamaged region intersect the damaged, silver-containing region, did not detect the presence of silver. Silver has not migrated into the undamaged SiC regions in spite of the fact that optimal conditions existed for migration to occur.
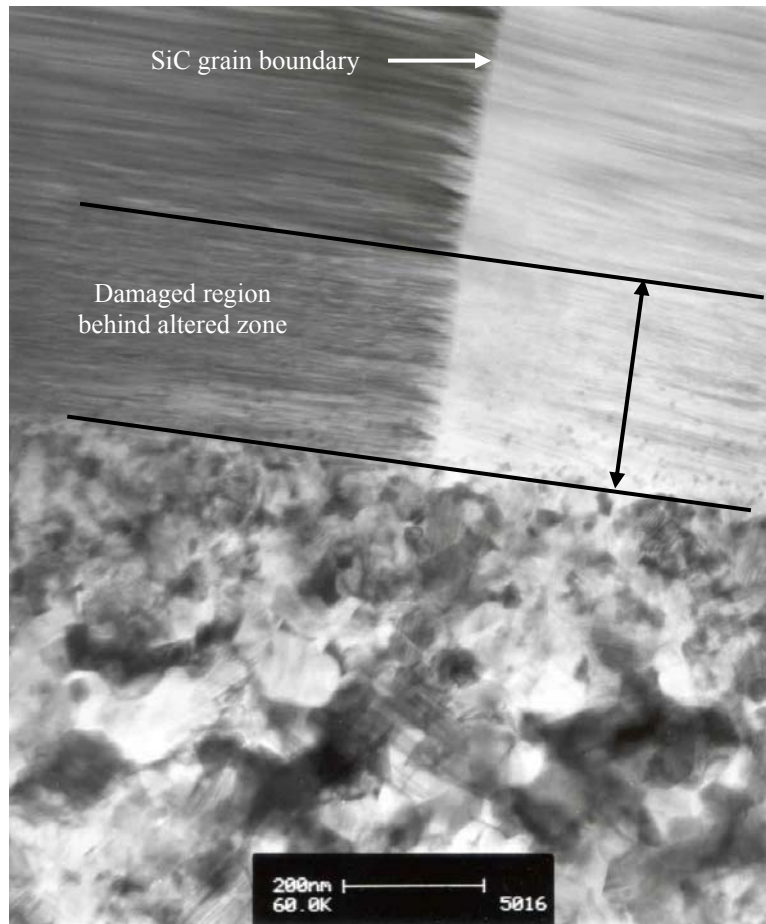
Figure 3-19. No silver was detected on grain boundaries at the interface between the damaged and undamaged regions after annealing for 480 h at 1500°C (sample 5a).

The recrystallization process created new grain boundaries as well as a significant increase in grain boundary area compared to the original CVD SiC microstructure. As the amorphous SiC crystallized and formed β-phase grains, impurity silver atoms were rejected due to their low solubility. The silver atoms, segregated from the recrystallized SiC grains, appear as phase separated precipitates in the SiC recrystallized zone, as seen in Figure 3-20. During annealing, silver was in intimate contact with SiC grain boundaries, but no silver migration was observed either by XPS or AEM analyses. A region of low concentration silver exists just behind the recrystallized SiC in the heavily faulted original SiC microstructure. There is no evidence, however, of silver migration along grain boundaries present in the original SiC, as shown in Figure 3-19 and in the lower right corner of Figure 3-20.
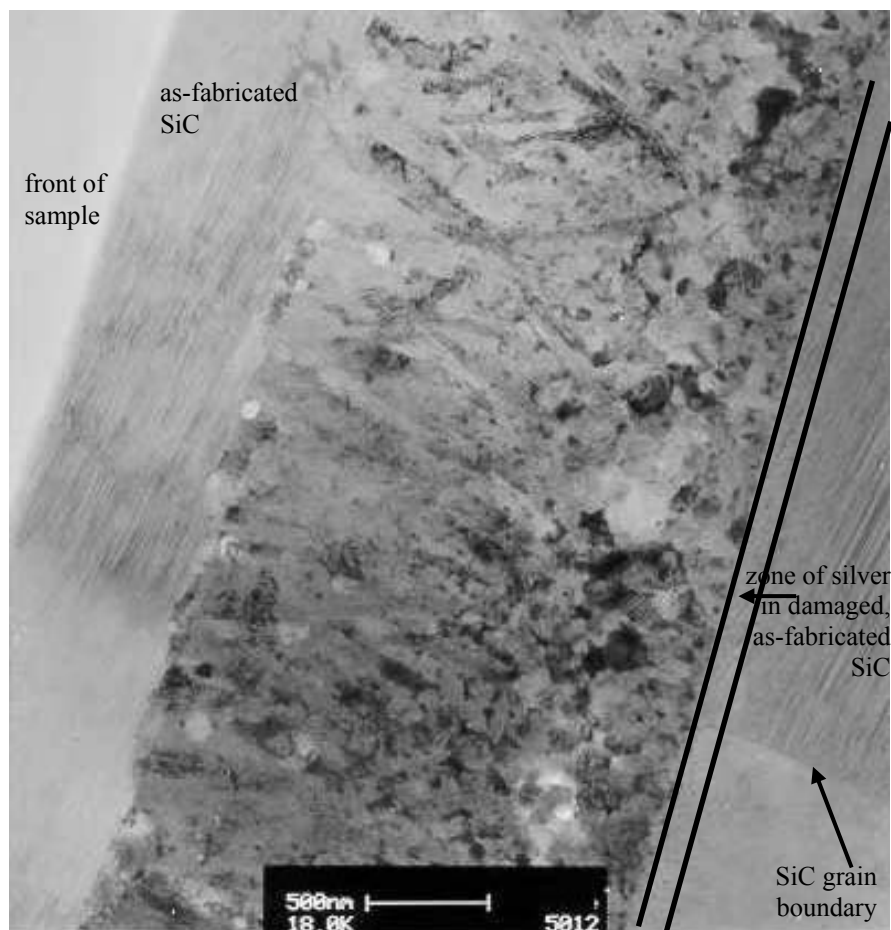
Figure 3-20. No silver was detected on grain boundaries at the interface between the damaged and undamaged regions after annealing for 480 h at 1500°C (sample 5a).

The recrystallized zone in sample 5a after heating is narrower than the recrystallized plus amorphous zone in sample 6a before heating. Sample swelling measured after implantation is proportional to the implanted dose. Sample 6a had a higher implantation dose than 5a and, therefore, increased swelling, consistent with a wider implantation zone. The implantation zone in sample 5a is also narrower after heating due to the transition from the disordered and lower density amorphous SiC to the more compact β-SiC.

A comparison of the AEM analyses before and after annealing makes it clear that the amorphous SiC region observed before annealing has recrystallized during heating. After annealing, the altered zone contains all crystalline silicon carbide with phase-separated silver. The silver concentration profile after heating matches the profile before heating. EDS did not detect any

silver in the front half of the recrystallized zone after heating. Discrete precipitates of silver lie between the SiC grains in the back half of the recrystallized zone. Lower concentrations of silver are present in the damaged layer of the original SiC, behind the recrystallized zone. The relative amounts and position of silver in the silicon carbide match before and after heating, showing that the silver did not move the distances expected based on previously published grain boundary diffusion coefficients.

The silver redistributed during heating as the amorphous silicon carbide recrystallized and the SiC grains grew. Silver, in intimate contact with SiC in the amorphous region before heating, phase separated during heating as the SiC recrystallized. As the SiC grains grew they rejected the silver, which appears to have negligible solubility in SiC, to the grain boundaries. Recrystallization created new grains and new grain boundaries, which advanced as SiC grains grew.   Yet, no large-scale silver migration occurred.   Silver rejected from SiC during recrystallization and grain growth had access to SiC grain boundaries, but no grain boundary diffusion was observed. Even silver at grain boundaries in the heavily faulted region of the original SiC just behind the recrystallized zone did not migrate, an observation in contradiction with the assumptions found in the previous literature.

Summary of Electron Microscopy Observations

The silver implantation resulted in a region of dynamically recrystallized SiC and a region of amorphous SiC. The amorphous SiC zone contained most of the deposited silver along with the peak of the silver concentration profile. The amorphous SiC recrystallized during heating and the grains that recrystallized during implantation also grew slightly during heating. There was no macroscopic change in the silver distribution in the SiC after heating for 480 h at 1500°C. The implanted silver appeared as randomly distributed, small, discrete regions in the amorphous SiC zone after implantation and as larger precipitates between crystalline SiC grains after heating. No silver migration was observed into the dynamically recrystallized SiC zone, in front of the amorphous zone, or into the original SiC behind the implantation zone either during implantation or heating. Additionally, no silver was detected along the grain boundaries, either in the recrystallized SiC or in the original SiC. These results are not consistent with diffusive behavior. Had the silver diffused according to the values reported in the literature, the silver would have diffused many micrometers away from the initial concentration profile and dropped to undetectable levels in the peak implantation zone.

Comparison to Literature

No silver migration was measured in a previously reported ion implantation experiment. Nabielek et al. implanted lower energy silver ions into silicon carbide, just below the surface, and annealed the sample for only 30 min at 1180°C (Carter, Davis, and Bentley 1984). Rutherford backscattering measurements before and after heating showed no change in the silver concentration profile. The authors concluded that silver had most likely been trapped in SiC grains and, therefore, silver diffusion was not observed because matrix diffusion of silver in SiC is much, much slower than grain boundary diffusion.

The current experiments show that massive SiC recrystallization occurred during both implantation and heating. The solubility of silver in silicon carbide is extremely low and silver was swept out of SiC grains during SiC recrystallization. This evidence shows that silver is not trapped in SiC grains during recrystallization and that trapping, therefore, does not prevent silver migration in ion implantation experiments. Silver, however, can be immobilized at SiC grain boundaries; silver, in intimate contact with SiC grain boundaries, did not migrate.

The silver concentration in this work was far above that which would be expected to exist in typical TRISO-coated particle fuel. The annealing temperature, however, was in the same range as the post-irradiation annealing studies used to derive diffusion coefficients for coated particle fuel. Also important to note is that the final recrystallized SiC grain structure is similar to that fabricated in typical SiC layers in tested TRISO-coated particle fuel. While there are variations in some of the coating parameters, the SiC used in the current experiments and the SiC from previous fuel tests were coated using a high temperature CVD process resulting in high-density β-SiC with a fine-grain structure. The results from this experiment are, therefore, applicable to silver migration in CVD SiC in typical TRISO-coated particle fuel. A comparison of the recrystallized SiC from the current experiments and a typical CVD SiC coating is shown in Figure 3-21.
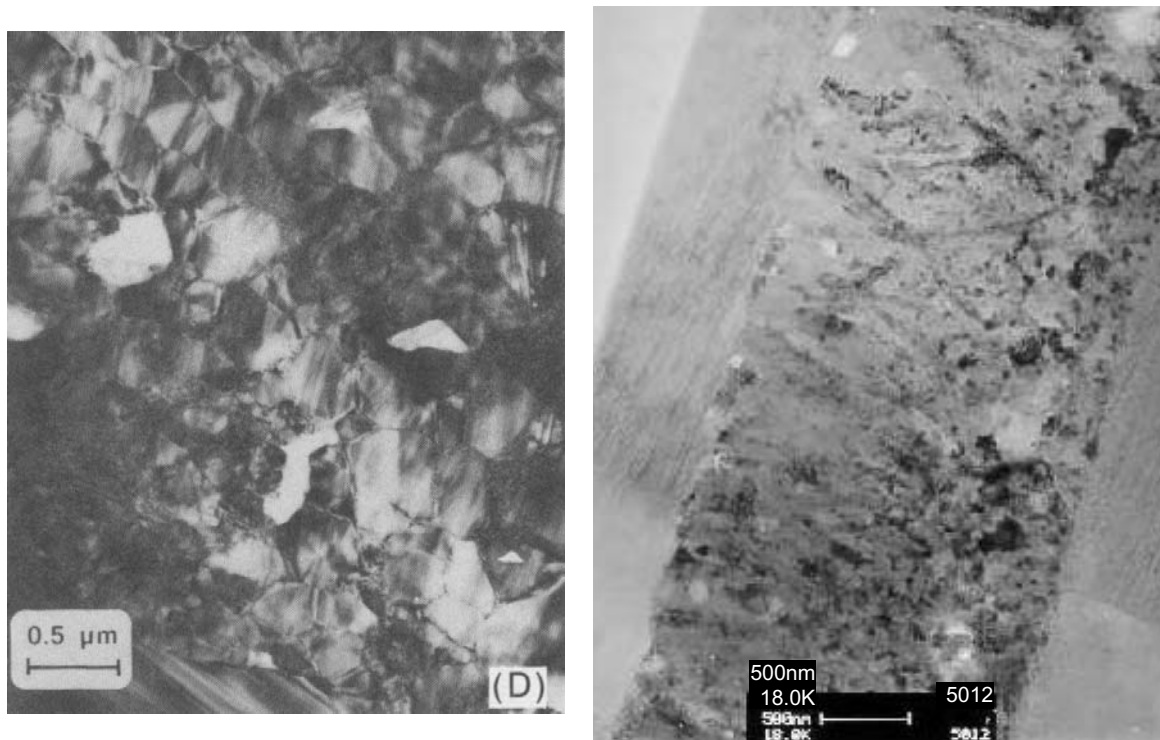
Figure 3-21. Comparison of typical SiC microstructures from a) a typical SiC coating and b) the current ion implantation experiments (Carter, Davis, and Bentley 1984).

Conclusions

The results of this work clearly show that silver does not move by diffusion, either in the matrix or along the grain boundaries, in CVD SiC for the conditions studied. Even silver near grain boundaries in the original SiC material, observed just behind the recrystallized zone in Figure 3-18*a* and Figure 3-20 did not migrate. There is considerable grain boundary area in the recrystallized portion of the SiC, but no silver was detected outside of its original deposition area. Recrystallization of the silicon carbide grains during annealing and the high vacancy concentration resulting from implantation damage could have provided many pathways for silver diffusion and migration during annealing, but no silver movement was measured.

Typical SiC coatings for fission product barriers in TRISO fuel consist of fine-grained SiC, usually slightly columnar, with grain sizes on the order of a few micrometers. The desired grain length is small enough such that the total width of the SiC layer consists of many grains and the probability of one grain extending through the total thickness is very small. The SiC grains in the recrystallized portion of the silicon carbide, where most of the silver remains, are fine

grained, slightly columnar, and have grains sizes less than 1 μm. This silicon carbide exhibits characteristics very similar to the desired characteristics of silicon carbide coatings in typical TRISO fuel for high-temperature gas reactors and silver migration did not occur. Additional work is required to identify the exact release path for silver in silicon carbide and to understand its cause and how to mitigate its effects.

Spherical Diffusion Couples
Goals and Background

The goals of the experimental program were to directly witness silver diffusion and measure silver concentration profiles in silicon carbide. Two types of experiments attempted to directly measure silver concentration profiles in silicon carbide as a result of diffusion or migration. The former section discussed the ion implantation results and this section reviews the results of spherical diffusion couple tests.

The aim of the spherical diffusion couple tests was to observe silver diffusion in silicon carbide by measuring silver concentration profiles in either a thin SiC coating over a hollow graphite shell or in a thick SiC shell. A lack of evidence, however, of silver migration in the silicon carbide layer resulted in a proposed change in the assumed mechanisms and a change in the goals of the experimental program. The new goals were to understand the causes of silver migration in silicon carbide and to determine what mechanisms govern silver release from silicon carbide.

As discussed in detail in this section, silver, although released in measurable quantities, did not diffuse through silicon carbide. Vapor migration is proposed as an alternative mechanism to solid-state diffusion to explain silver release in the current diffusion couples and in typical coated fuel particles.

Experimental Setup and Fabrication

A standard diffusion couple consisting of a diffusing substance plated on a substrate is not sufficient for silver experiments because of silver's low melting temperature and high vapor pressure. Silver plated on silicon carbide will evaporate from the surface or escape through any open edges rather than diffuse into the substrate material at temperatures near or above 960°C, silver's melting temperature (Lide 1990). A spherical diffusion couple design attempted to resolve this problem by enclosing silver within a silicon carbide coated sphere.

Diffusion Couple Design

Hollow shells, fabricated from either graphite or silicon carbide, formed the basis of the spherical diffusion couple. Two half shells, fabricated with an overlapping seam, mated together to form a 1.9 cm hollow sphere with 0.076 cm thick walls. Silver powder (99.9995% purity, -22 mesh) placed inside one half shell was completely enclosed inside the diffusion couple after a silicon carbide coating was deposited on the outside of two joined half shells. Figure 3-22 shows two open half shells, Figure 3-23*a* shows one half shell with silver powder, and Figure 3-23*b* displays a complete diffusion couple with a silicon carbide outer coating.

Graphite shells, selected for the best coefficient of thermal expansion matching to silicon carbide, were used in the first and second sets of diffusion couples, types SiC-1 and SiC-2. The graphite shells were fabricated from machined graphite with approximately 13%-15% porosity. A third set of diffusion couples, type SiC-3, were fabricated with chemical vapor deposited silicon carbide as the substrate shell. An outer coating of CVD SiC sealed the silver inside all of the substrate shells.

Figure 3-22. Graphite shell substrate for the diffusion couples. Silver powder is placed inside the shell then SiC is coated on the outside.

a) Silver powder in graphite half shell   *b)* SiC coating over graphite shell

Figure 3-23. Diffusion couple fabrication steps including a) loading with silver powder and b) coating with SiC.

The graphite shell of the diffusion couple types SiC-1 and SiC-2 created some challenges for silver migration analysis but also added some potential benefits. Among the challenges were the numerous literature summaries which indicate that there is no holdup of silver in PyC or any graphite material (Nabielek, Brown, and Offermann 1977). Over a long heating period a range of fast silver diffusion coefficients in graphite adds only minimal uncertainty, but for short heat treatments, the finite silver diffusion rate in the graphite shell needs to be considered. A more significant challenge, however, appeared to be the lack of silver wetting on graphite. If silver doesn't wet graphite then molten silver at the bottom of the diffusion couple during heating will not be able to penetrate the graphite surface and, hence, will not come into contact with the SiC layer. A major difference between the diffusion couples and typical coated particle fuel is the size of the diffusion couples. Typical diameters are on the order of 1 mm for coated fuel particles and 2 cm for the diffusion couples. In addition, the thickness of the SiC layer is greater on the diffusion couples (60-150 μm) than in typical coated fuel particles (35-40 μm). This significant difference in size affects the stress state of the silicon carbide layer and is also important when calculating the probability of a critical flaw occurring in a given volume of SiC.

Even though the uncertainties of silver transport through the graphite layer introduce challenges for analysis of these diffusion couples, advantages of this design include eliminating edge effects by trapping the silver inside the diffusion couple and a chemical similarity to fuel particles. Coated fuel particles generally contain a porous graphite buffer layer around the kernel and a high-density pyrocarbon layer surrounding the buffer, before the SiC layer. Although the diffusion couple shells consist of machined graphite and not pyrocarbon, the environment is

128

chemically similar to that existing for silver in coated particles. Even though the exact diffusion rate of silver in graphite materials is not known, the porosity in the graphite shells is within the range of connected porosity, suggesting that silver in the graphite layer can move quickly through the connected porosity by vapor transport and be transported to the SiC inner surface rather easily.

Replacing the graphite shell in favor of a silicon carbide shell provided a more direct investigation of silver migration in SiC and eliminated the uncertainties associated with silver migration through the graphite layer. In the SiC-3 type diffusion couples, silver was in direct contact with the silicon carbide, providing access to direct measurements on the SiC shell.

SiC Fabrication

The silicon carbide outer coating on the diffusion couples was formed by chemical vapor deposition using MTS (methyltrichlorosilane, CH_3SiCl_3) as the feed gas with a hydrogen carrier gas. The standard SiC coating used on diffusion couple types SiC-1 and SiC-3 was deposited at 1200°C and 0.1 atm (75 torr) with a total flow rate of $75cm^3/min$ and an H_2/MTS ratio of 7.5. The standard coating run lasted 6 h. Raising the deposition temperature to 1300°C and increasing the H_2/MTS ratio to 12.5 created a modified SiC coating deposited on diffusion couple type SiC-2. Each coating run for the SiC-2 samples lasted 9.25 h. All of the diffusion couples consist of two hemispheres, both either graphite or silicon carbide, loaded with silver and coated with silicon carbide. The three types of diffusion couples are referred to as SiC-1, SiC-2, and SiC-3 and are briefly summarized in Table 3-4. A modified SiC coat was deposited on some of the graphite-shell diffusion couples to permit a comparison of silver diffusion in SiC with different grain structures, one of the original objectives of the experimental program.

Table 3-4. Summary of diffusion couple set parameters.

	SiC-1	SiC-2	SiC-3
Shell Substrate	graphite	graphite	SiC
SiC Coating	standard	modified	standard
Microstructure	β-SiC	β- with α-SiC	β-SiC

The silicon carbide coating on diffusion couple types SiC-1 and SiC-3 consisted of columnar grains radially oriented, growing from the inner surface towards the outer. The grain sizes, as estimated from optical and transmission electron micrographs seen in Figure 3-24, range from

small equiaxed grains near the inner surface, on the order of 0.5 µm to 1 µm, to long columnar grains on the order of a couple micrometers wide by tens of micrometers long.

a) Optical micrograph of Ag12, unheated

b) AEM of Ag21 after heating at 1400°C for 240 h
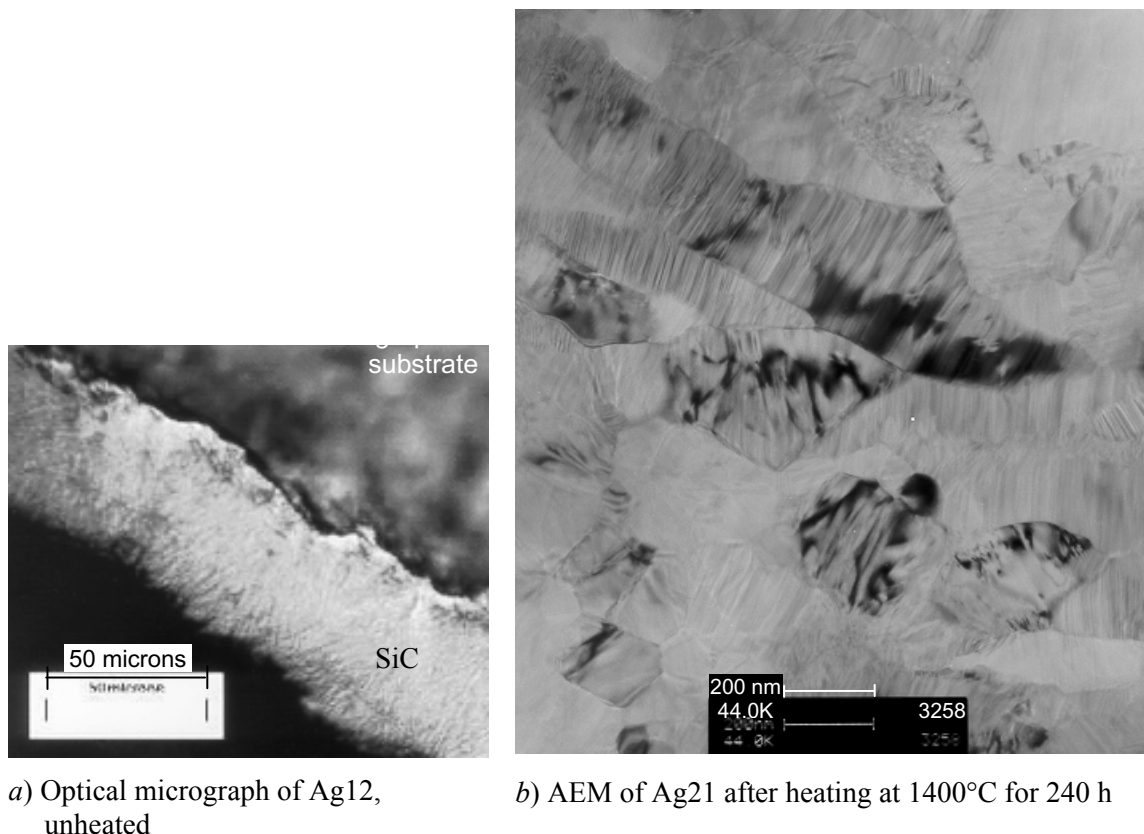
Figure 3-24. SiC coatings consist of columnar grains with some small equiaxed grains near the substrate interface; a) an optical micrograph of unheated sample Ag12 shows typical fan patterns and b) a transmission electron micrograph of sample Ag21 after heating shows small equiaxed grains near the inner surface.

Heat Treatments

The heat treatment temperatures were selected to cover the higher range of typical fuel operating temperatures, between 1050°C and 1600°C, a temperature range also applicable to some accident analyses. Many of the heat treatments focused on the higher end of the temperature range, around 1500°C, to accelerate silver migration. Based on silver diffusion coefficients reported in the literature, the heat treatments conducted around 1500°C should have produced measurable silver concentration profiles.

Two high-temperature graphite-based furnaces were used for the diffusion couple heat treatments. Each was a Red Devil™ vacuum furnace, seen in Figure 3-25*a*, from the R.D. Webb company, heated by a carbon-carbon heating element inside fibrous graphite insulation block. A solid graphite retort, shown in Figure 3-25*b*, sits above the heating element and defines a work zone 9 cm in diameter and 5 cm tall (R.D. Webb Company 2004). A solid graphite lid covers the retort during operation. The furnaces were maintained under medium vacuum (on the order of millitorr) during the diffusion couple heat treatments.

a) furnace and controller   *b)* solid graphite retort

Figure 3-25. R.D. Webb Company Red Devil™ furnace used for the diffusion couple heat treatments: a) furnace and controller, b) solid graphite retort.

In the Webb furnace, the heating element is situated beneath the solid graphite retort. This arrangement results in a thermal gradient inside the working zone during heating with the bottom of the graphite cup hotter than the top. During the heat treatments, 0.6 cm thick graphite plates with approximately 0.6 cm holes held the spherical diffusion couples in a secure position and also provided adequate physical contact between the retort and the sample, likely ensuring good heat transfer from the retort to the bottom of the diffusion couple. In this arrangement, the top of the diffusion couple was not in contact with any surface of the furnace and radiated heat from the diffusion couple to the cooler graphite lid on the retort, leading to an approximately 10°C-15°C temperature drop from the bottom to the top of the diffusion couple (R.D. Webb Company 2004). Heat treatments covered temperatures from 1050°C to 1700°C for cumulative times ranging between 2 h and 1760 h. Twenty-seven samples were annealed in all and seven of those samples were heated twice to obtain intermediate, nondestructive data, such as mass measurements, leak rates, and X-ray images, while accumulating longer anneal times. The uncertainty in heating temperature is ±15°C due to the hot zone geometry and thermocouple location and the uncertainty in heating duration is ±5 min. Heating rates varied from 4°C/min to

25°C/min with most of the diffusion couples heated at rates between 4°C/min and 10°C/min. Cooling rates were controlled by the natural cooling of the furnaces, typically about 5°C/min.
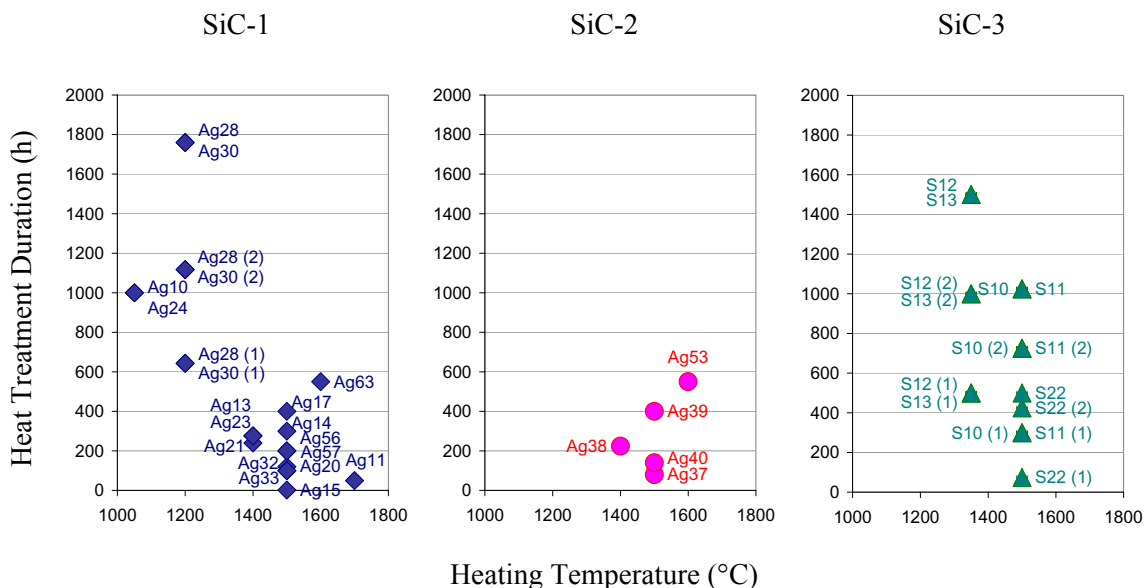
Figure 3-26. Heat treatment conditions for SiC-1, SiC-2, and SiC-3 diffusion couples.

Results and Discussion

Silver Distribution in Silicon Carbide

Various techniques aimed at detecting and analyzing the silver distribution in the diffusion couples were employed. None of the techniques used detected any silver in the silicon carbide layer below a detection limit of approximately 100 ppm.

X-ray Analysis

X-ray analysis and CT-scanning provide images highlighting atomic number contrast in the diffusion couples. Since silver has a much higher atomic number (Z=47) than either silicon (Z=14) or carbon (Z=6), these techniques provide a qualitative picture of the silver location in the diffusion couple. Both X-ray and CT imaging show solid, excess silver in the bottom of the SiC-1 diffusion couples and dispersed silver in the upper portion of the couples. Both X-ray radiography and CT-scanning are non-destructive techniques that take advantage of atomic number differences to distinguish between silver and silicon carbide in the diffusion couples. Additionally, CT-scanning is capable of rendering digital cross-sections of a sample.

Unfortunately, due to the limited resolution of X-ray radiography and CT-scanning and the thin SiC layer (relative to the overall size of the diffusion couple), the SiC coating could barely be distinguished using these techniques. The images and digital reconstruction of cross-sectional slices do, however, clearly show that silver has penetrated the graphite shell in the upper portion of the SiC-1 diffusion couples where the vapor existed (and was coolest), but not in the bottom underneath the molten silver pool.

Figure 3-27 shows an X-ray image from the CT-scan of sample Ag32 after heating for 100 h at 1500°C. Excess solid silver remains in the bottom of the diffusion couple after heating, a clear indication that sufficient silver was present during heating to maintain equilibrium between the liquid and vapor phases. A halo of silver exists in the upper portion of the couple, but silver is only detected in the graphite shell, not in the SiC coating, as seen in an optical micrograph cross-section of the upper portion of a typical diffusion couple in Figure 3-28.

Silver particles can be seen at the seam location using X-ray techniques. Further investigation of the inner surface of the diffusion couple near the seam area using optical stereo microscopy shows discrete silver particles in the open spaces of the seam, between the overlapping lips of the two half shells.
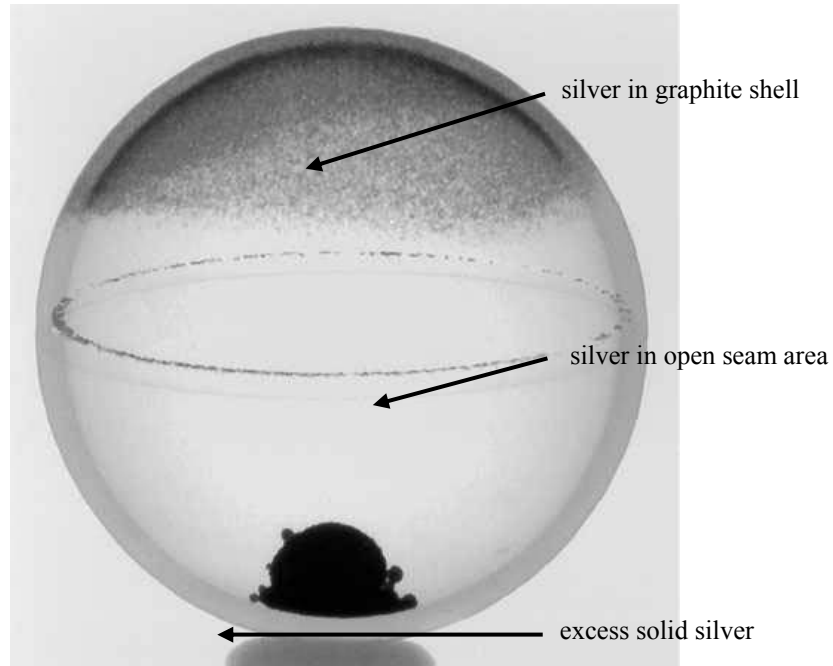
Figure 3-27. CT-scan image of a graphite-shell diffusion couple (sample Ag32) shows silver dispersed in the graphite in the upper region, silver particles in the seam, and excess silver at the bottom of the couple.
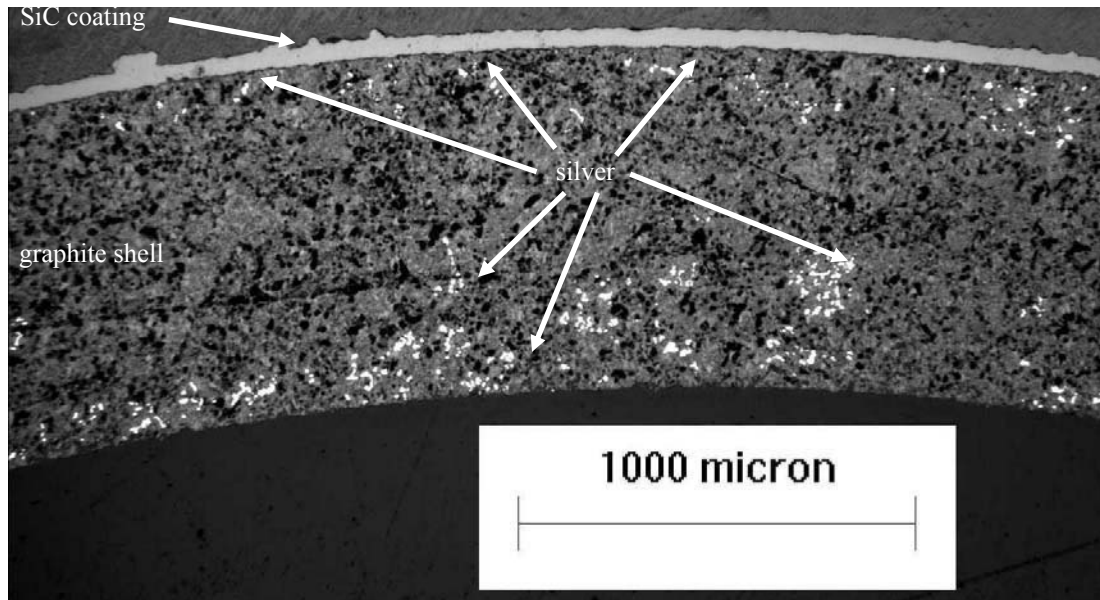
Figure 3-28. Optical micrograph of the cross-section of the top of sample Ag23 shows condensed silver in graphite pores but not in the SiC coating.

X-ray analysis and CT-scans of the SiC-3 diffusion couples with SiC substrate shells show a spattering of silver at the inner surface of the half shell, but no silver penetration into the SiC shell or outer coating. There was no evidence of silver diffusion into the SiC substrate shell either below the high-concentration molten pool or above the low-concentration vapor phase.

X-ray images and CT-scans show silver in the upper potions of the SiC-1 and SiC-2 diffusion couples after heating. This silver appears finely distributed around the upper third of the diffusion couples, but no silver was identified in the SiC coatings during digital reconstructions of the cross-section planes. No silver was identified in the SiC substrate shell or SiC coating in the SiC-3 diffusion couples. Discrete silver precipitates were identified in the free space of the seams of the diffusion couples. The excess silver remaining after heating is clearly visible in X-ray images and CT-scans, but there is no evidence of silver transport into the graphite or SiC substrate shells at the bottom of the diffusion couples.

Although the X-ray and CT techniques provide good qualitative, non-destructive images of the silver location in the diffusion couples, they require a fairly high concentration of silver in SiC to be detectable and are not readily applicable for quantitative analysis. Additional techniques were required to look for lower silver concentrations in the SiC shells and coatings.

XPS Depth Profiles

To achieve the goal of observing silver diffusion by measuring characteristic concentration profiles after heating, XPS (X-ray photoelectron spectroscopy) was employed. XPS measures not only elemental components of a sample, but also determines bonding information, distinguishing, for example, between free silicon and silicon bound as silicon carbide. XPS measures concentrations at the surface of a sample and by alternating measurements with sputtering to remove material obtains a depth profile. XPS profiling through the diffusion

couples attempted to measure the concentration profile due to diffusion and observe signs of silver migration through silicon carbide.

The detection limit for silver in the XPS analyses was approximately 100 ppm (atoms silver per total atoms measured). Silver may have been present in the SiC layers in concentrations less than 100 ppm, but anything greater than 100 ppm would have been detected during XPS concentration depth profiles. The highest silver concentrations existed in the bottom of the diffusion couples where solid silver formed a molten pool during heating.

The graphite substrate shell was removed by oxidation to reveal the inner surface of the SiC coating for XPS analysis in the SiC-1 and SiC-2 diffusion couples. For the SiC-3 diffusion couples, XPS measurements were obtained starting at the inner surface of the SiC substrate shell. Sample areas from both the top and bottom of selected diffusion couples were analyzed using XPS. No silver was detected, above the detection limit of 100 ppm (atoms of silver per total atoms measured) in the silicon carbide coating of and of the samples and no silver was detected in the SiC shell of the SiC-3 samples.

The density of the molten silver at the bottom of the diffusion couples is given by Equation (3-1) (Lide, 1990). At 1500°C, the density of molten silver in contact with the SiC shell in the SiC-3 diffusion couples was 8.8 g/cm^3. The expected concentration profile through the SiC shell using the diffusion coefficient recommended by Amian and Stöver is shown in Figure 3-29. Concentrations of this magnitude are easily detectable by XPS.

$$\rho_{liq} = \left(9.320 - 9 \cdot 10^{-4} \tfrac{1}{K}\left(T - T_m\right)\right)\frac{gm}{cm^3}$$ (3-1)

where ρ_{liq} = density of liquid silver at temperature T (gm/cm^3),
       T = Temperature (K), and
       T_m = melting temperature (962°C, 1235 K).
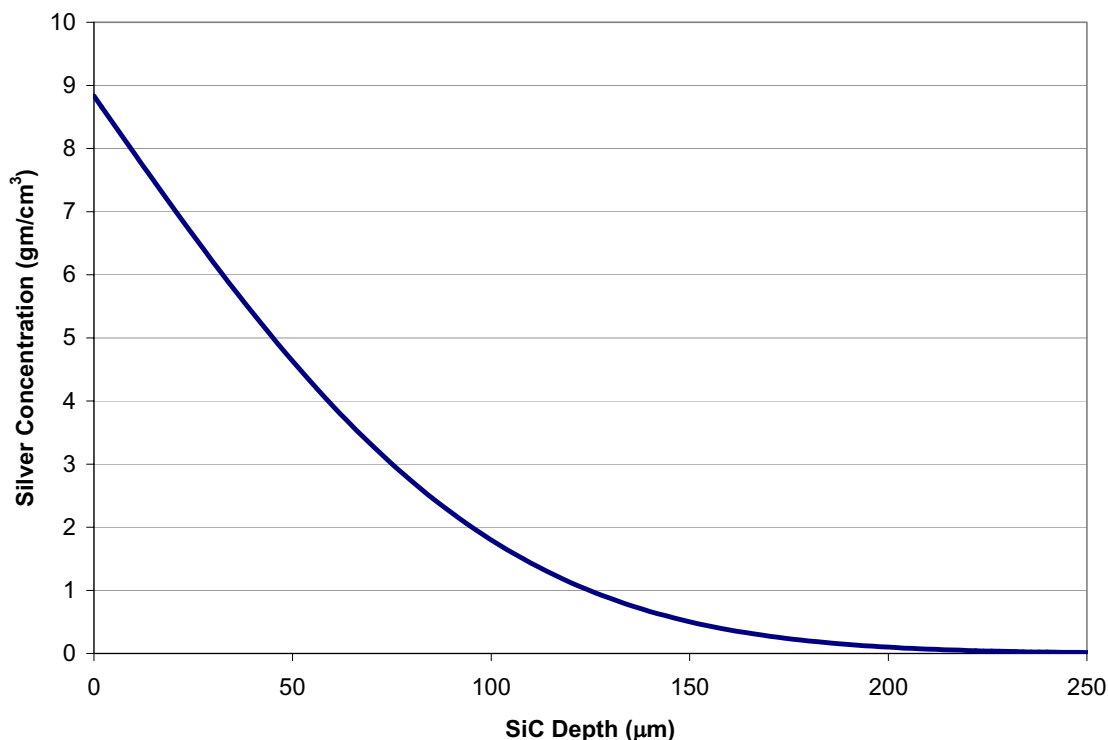
Figure 3-29. The expected silver concentration profile in the SiC shell after 500 h at 1500°C should have been easily detectable.

Incompatibility of the molten silver with the graphite shell may have prevented silver access to the SiC coating in the SiC-1 diffusion couples, but this should not have been a problem in the SiC-3 couples with SiC shells. Even after heating for 500 h at 1500°C, no silver was detected in the silicon carbide shell, at concentrations greater than 100 ppm, at the top or bottom of the diffusion couple. If silver diffused at rates in the range reported in the literature, XPS should have been able to measure characteristic concentration profiles. The lack of any silver detection in the SiC coatings or shells was an unexpected result and runs counter to the presumed diffusive mechanism.

XPS analysis provides quantitative chemical analysis over a fairly large area of the diffusion couple. The analysis area used for the XPS analysis measured approximately 800 μm in diameter. The concentration profiles collected during XPS analysis average the constituents in an area very large compared to the typical SiC grain size. To investigate these couples on a finer scale, higher magnification techniques were required.

137

Electron Microscopy Analysis

SEM (scanning electron microscopy) and EMPA (electron microprobe analysis) both clearly show silver penetration in the upper portions only of the SiC-1 and SiC-2 diffusion couple graphite shells. Neither analysis tool detected any silver in the SiC coating. Silver was observed near the graphite-SiC interface, as seen in Figure 3-30, but no penetration into the SiC coating was found.
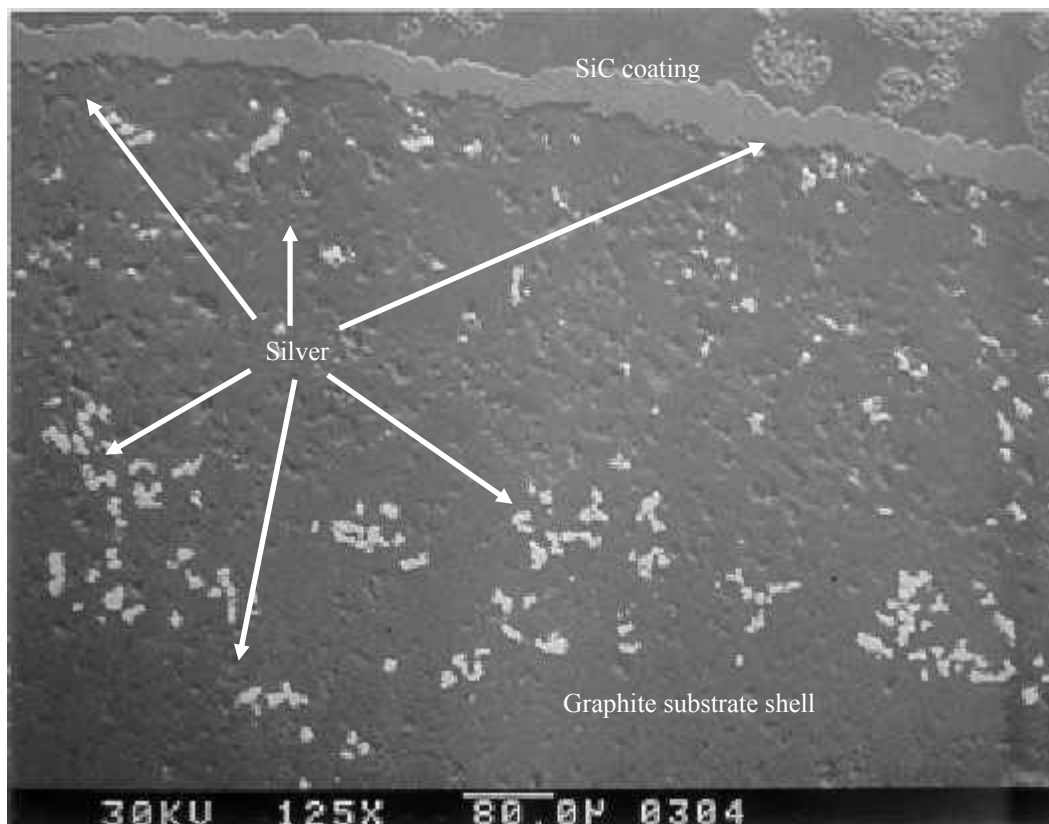
Figure 3-30. Scanning electron microscopy reveals silver as bright white areas in the upper portion of sample Ag20 after 120 h at 1500°C.

Silver was easily detected in AEM (analytical electron microscopy) analysis of the graphite shells of SiC-1 sample Ag21 after 240 h at 1400°C and SiC-2 sample Ag39 after 400 h at 1500°C. The AEM analyses were performed on a Philips CM300 equipped with an EDAX X-ray detector for elemental analyses. Silver fills many of the graphite pores near the graphite-SiC interface. In sample Ag21 (SiC-1 diffusion couple), AEM clearly reveals silver at the graphite-SiC interface, as seen in Figure 3-31*a*, but not in the SiC coating. AEM provides high

magnification images of the SiC grains and shows details of the fine-grained β-SiC structure, as seen in Figure 3-31*b*.

a) Large silver accumulations at the graphite-SiC interface

b) The SiC coating contains small, equiaxed grains, but no silver
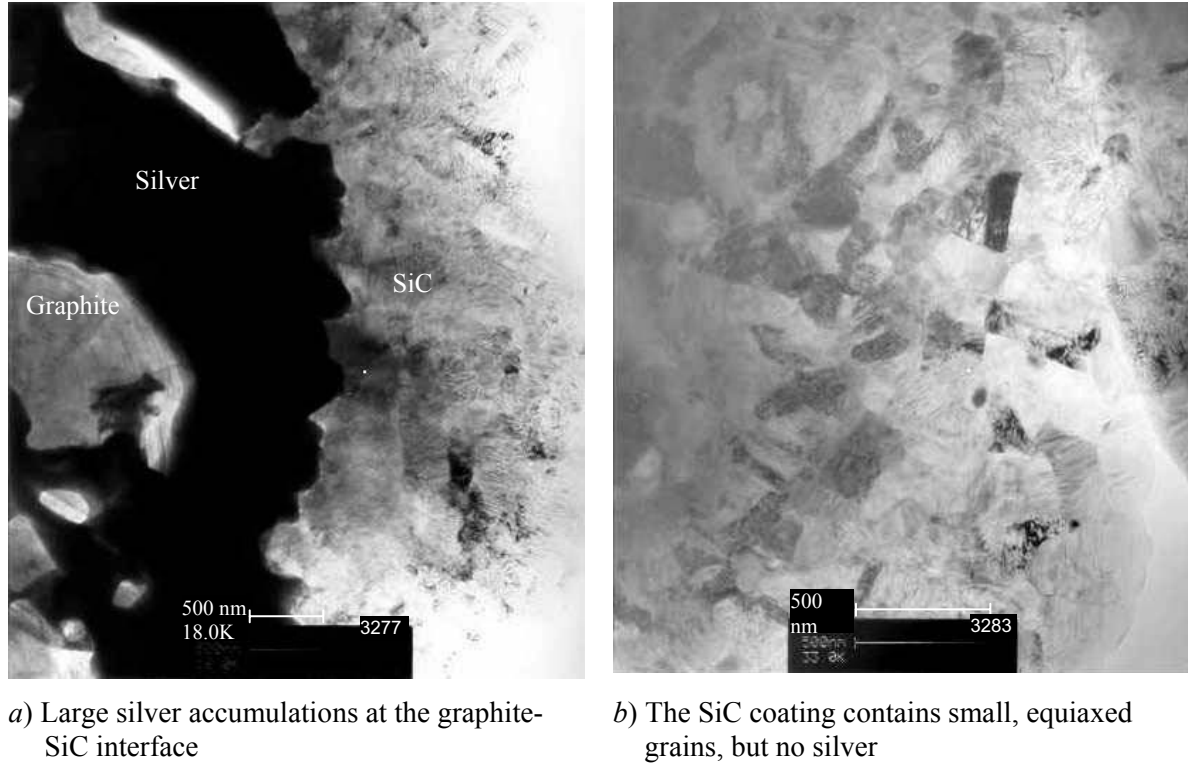
Figure 3-31. AEM of SiC-1 sample Ag21 after 240 h at 1400°C shows a) silver at the graphite-SiC interface and b) small SiC grains.

Sample Ag39, a SiC-2 diffusion couple fabricated according to the modified CVD conditions discussed in Section 0, consisted of large, blocky SiC grains near the graphite-SiC interface and thin dendritic grains further out into the SiC coating, oriented in the radial direction. AEM analysis detected silver decorating and bracketing the large SiC grains, as seen in Figure 3-32 and Figure 3-33, but there was no silver in the dendritic SiC grains. The diffraction patterns for both the large, single crystals and the polycrystalline dendritic regions index to β-SiC, as seen in the diffraction patterns in Figure 3-32.
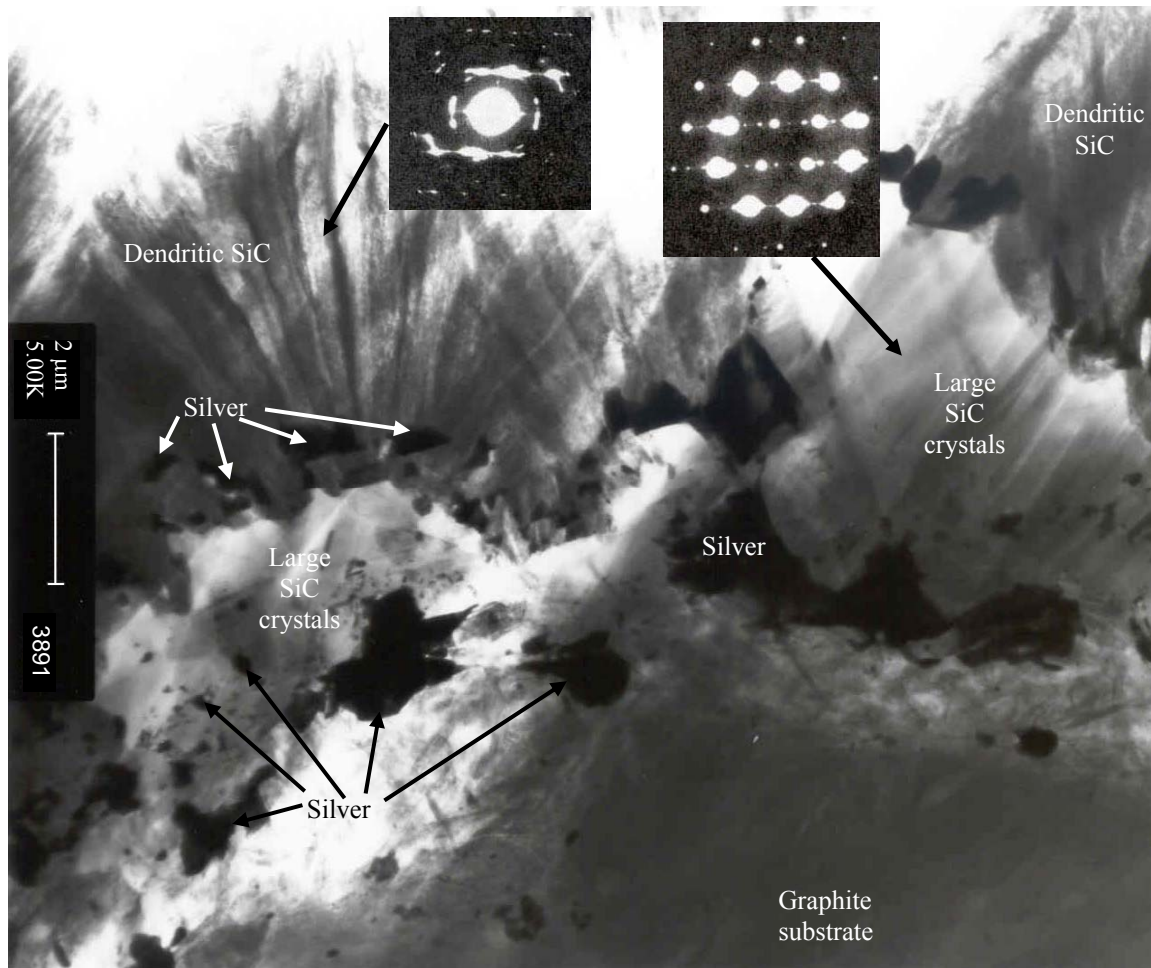
Figure 3-32. AEM of SiC-2 sample Ag39 after 400 h at 1500°C shows dendritic SiC grains along with large SiC crystals.

The large SiC crystals appear somewhat misaligned with each other, the surrounding graphite, and the dendritic SiC grains, providing room for silver migration around the large, blocky SiC grains. No silver, however, was observed in the dendritic SiC grains beyond the interface between the large, blocky crystals and the dendritic grains, as seen in Figure 3-32 and Figure 3-33*a*. These observations suggest that large SiC grains, present in the modified SiC-2 coating, and the mismatch between the different types of SiC grains provide pathways for silver transport not observed in fine-grain equiaxed or dendritic structures in the standard SiC coating used in these experiments and seen in the AEM of sample Ag21 in Figure 3-31.

The mismatch between poorly aligned SiC crystals likely increases residual stresses and may lead to localized cracking within the SiC coating which could provide open, direct pathways for silver escape. Although the SiC microstructure observed in the AEM analysis of SiC-2 sample

140

Ag39 is not likely to be present in typical coated fuel particle SiC coatings, the ability of silver to migrate around poorly aligned crystals emphasizes the importance of silver transport along short-circuit paths through SiC. Typical SiC coatings in coated fuel particles consist of many individual grains and how well those grains fit and grow together during deposition may be important for silver retention. The PyC and SiC coatings for typical TRISO fuel particles are fabricated in fluidized beds and, although the overall deposition parameters are closely controlled, a range of conditions exists within the fluidized bed. These variations could lead to variations in the microstructure of the SiC coating within individual particles, possibly creating regions or poorly aligned grains. Although the SiC microstructure seen in sample Ag39 is not desired for typical SiC coatings, the apparent ease of silver transport around ill-fitted SiC grains emphasizes the importance of localized SiC microstructure.
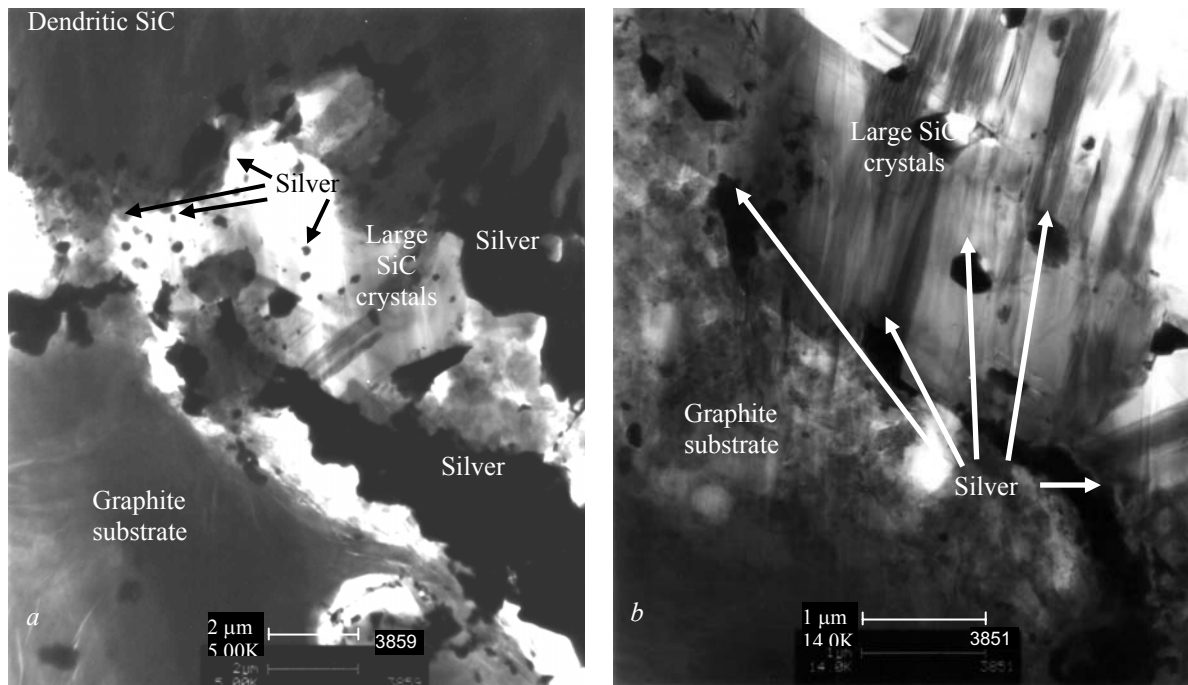
Figure 3-33. AEM of SiC-2 sample Ag39 after 400 h at 1500°C shows a) silver at the graphite-SiC interface and at the interface between large SiC crystals and dendritic SiC and b) silver bracketing and decorating the large SiC crystals.

Leak Testing

Standard helium leak testing of the diffusion couples showed an increase in leak rates for all samples after heating. These leak rates indicate a change in the diffusion couples during heating,

possibly providing a silver escape route other than grain boundary diffusion, as previously assumed. Silver release due to grain boundary diffusion would not show an increase in leak rate, however, a leak rate does indicate an open mechanical path.

In direct-read leak testing, the diffusion couple was soaked in a pressure chamber under 75 psi of helium for 20 min. During the soak period, helium entered the diffusion couple through any open mechanical paths. After 20 min, the sample was quickly transferred to a leak detector. This chamber was held under vacuum and a spectrometer was tuned to detect helium in the sample chamber. Any helium that leaked into the diffusion couple leaked out in the vacuum chamber and was detected by the spectrometer. The measured leak rate was recorded at 60 s and 120 s. An analytical fit, shown in Equation (3-2), was used to determine the predicted actual leak rate of the samples (DOD, 1996).

$$Q_{meas} = Q_{eq} \cdot \frac{P_{over}}{P_{ref}} \cdot \left(1 - \exp\left(-\frac{Q_{eq}\, t_{soak}}{V_{sp}\, P_{ref}} \sqrt{\frac{M_{air}}{M_{He}}} \right) \right) \cdot \exp\left(-\frac{Q_{eq}\, t_{dwell}}{V_{sp}\, P_{ref}} \sqrt{\frac{M_{air}}{M_{He}}} \right) \qquad (3\text{-}2)$$

where
Q_{meas} = measured leak rate of the tracer gas (He) (atm·cm^3/s),
Q_{eq} = equivalent leak rate in air (atm·cm^3/s),
P_{over} = over pressure applied to sample (5.1 atm = 75 psi),
P_{ref} = reference pressure (1 atm),
t_{soak} = soak time at pressure (1200 s),
t_{dwell} = dwell time between pressure release and spectrometer inspection (measurements recorded at 60 s and 120 s),
M_{air} = molecular mass of air (29 g/mol),
M_{He} = molecular mass of helium (4 g/mol), and
V_{sp} = volume of the specimen (cm^3).

The results of helium leak testing, shown in Figure 3-34, show that the leak rates for all types of samples were greater after heating than before. In general, the SiC-1 samples had low leak rates before heating, but high measured leak rates after heating. The SiC-2 samples had high leak rates before heating and even higher leak rates after. The SiC-3 samples received at least two coatings of SiC to achieve low leak rates in the as-fabricated samples. The leak rates for the SiC-3 samples increased after heating, but not as much as the increase for the SiC-1 samples. These qualitative results are listed in
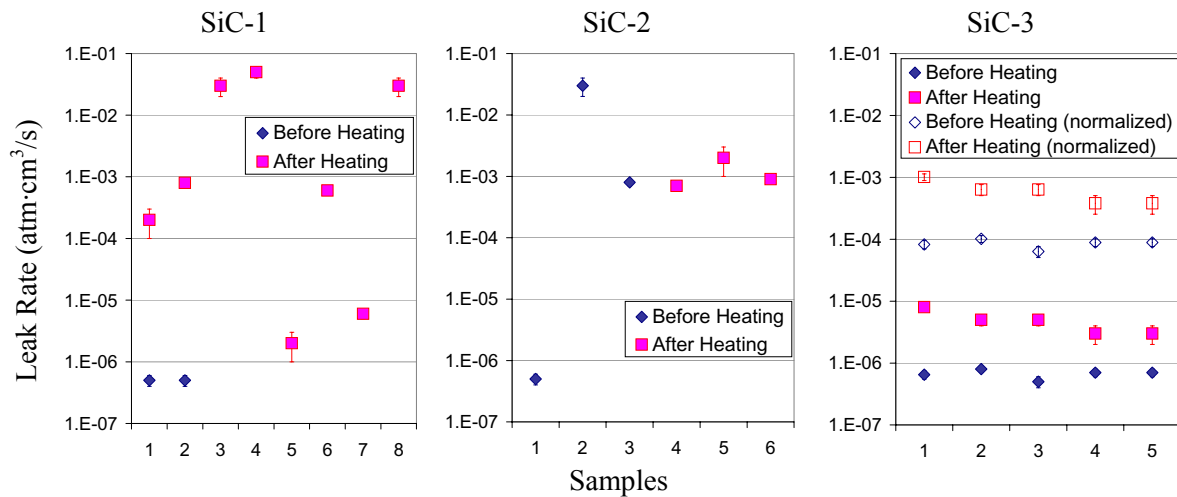
Figure 3-34. Helium leak testing on all types of samples. Leak rates increase after heating for all samples, with SiC-3 samples having the lowest increase.

Table 3-5. Qualitative assessment of leak rates. All samples measured higher leak rates after heating.

Sample Type	Substrate Shell	SiC Coating	Measured Leak Rates[1]	
			Before Anneal	After Anneal
SiC-1	graphite	standard	low[2]	high[3]
SiC-2	graphite	modified	high	higher
SiC-3	SiC	standard	low	medium

[1]low = 1 E-7 to 1 E-6 atm·cc / s
medium = 2 E-6 to 1 E-4 atm·cc / s
high = 2 E-4 to 8 E-2 atm·cc / s
[2]exception: sample Ag62 had a medium leak rate
[3]exception: sample Ag30 had a medium leak rate

Since helium can only leak through mechanical paths (helium does not diffuse through SiC) the leak testing results indicate increases in crack paths after heating compared to before heating. A review of the results for the three types of samples shows that the SiC-1 diffusion couples had mostly low leak rates before heating with generally large increases after heating. The SiC-2 samples had mostly large leak rates before heating, indicating poor quality of the modified SiC coating. The SiC-3 diffusion couples started with low leak rates and experienced modest increases after heating. Overall, the SiC-1 and SiC-3 couples had the best leak rates before heating while the SiC-3 samples had the lowest leak rates after heating. Leak testing measures the infiltration of helium into the sample under pressure and helium leaking out of the sample under vacuum. In the SiC-1 and SiC-2 diffusion couples, the SiC coating surrounds a porous graphite substrate shell; in the SiC-3 couples the SiC coating surrounds a fully dense SiC substrate shell. A crack anywhere in the SiC coating in SiC-1 and SiC-2 diffusion couples

143

would allow helium infiltration into the interior of the diffusion couple. Helium is impermeable through solid, intact SiC, so in the SiC-3 diffusion couples, only cracks in the SiC coating near the seam between the two SiC half shells would give helium access to the couple's interior volume.

Leak testing after heat treatment does not identify when leaks become active. There is no information on the time dependence for this data. No correlation between the duration of the heat treatment and leak rate appears. When a leak path opened during the heating and cooldown process cannot be determined from leak testing. Leak paths created near the end of a heat treatment or during the cooldown process would result in large measured leak rates after heating but may result in very little mass loss.

Mass Loss

Mass measurements of the samples before and after heat treatment on a Mettler AG245 scale with 0.0001 g resolution show that the diffusion couples lost weight during annealing. Contributors to mass change may include silver loss, oxidation of silicon carbide from the diffusion couple's surface, interactions between SiC and other contaminants in the furnace, and evaporation of water vapor adsorbed to the diffusion couple.

Since the furnace operated under medium vacuum, there should have been little oxygen available to oxidize the surface SiC. Any oxidation, however, of SiC to the volatile SiO would result in a net mass loss. A control sample without any silver was heated to estimate this effect along with any other mass effects. Reporting mass loss as a fraction of the initial silver inventory attempts to normalize all of the diffusion couple test results since varying amounts of silver were loaded into the samples. Even though the total amount of silver varied among the diffusion couples, in all but two cases (samples Ag53 and Ag63) there was excess silver available during the entire heat treatment to maintain equilibrium between the molten silver pool and the silver vapor.

Graphite-Shell Diffusion Couples

Sample Ag56, an SiC-1 type diffusion couple, was fabricated as a control sample with no silver to estimate any contribution to mass change from surface effects, contamination in the furnace, or oxidation of the silicon carbide. After heating for 200 h at 1500°C, control sample Ag56 exhibited a mass loss of 0.0061 g. Cutting a slice off sample Ag17, another SiC-1 type diffusion couple, created a second control sample. Sample Ag17 recorded a mass loss of 0.0071 g after

heating for 400 h at 1500°C. With one end of the diffusion couple removed, the inner graphite surface of sample Ag17 was exposed. This additional exposed surface area could influence the total amount of mass change based on any oxidation of the graphite layer during heating. Based on the mass loss of the two SiC-1 control samples, a possible threshold appears around 0.006 g; any mass loss below this level is most likely due to surface effects, not silver loss.

In the population of SiC-1 diffusion couples, mass loss ranged from 0.0013 g to 0.3297 g, equivalent to a range of 0.5% to 101% fractional release. The SiC-2 diffusion couples suffered mass loss between 0.0110 g and 0.3009 g, equivalent to fractional releases between 43% and 115%. Reported fractional release values greater than 100% are due to uncertainties in the measurement and from other possible interactions, such as oxidation at the surface, resulting in additional mass loss beyond silver escape. As can be seen in Figure 3-38 *a* and *b*, the different diffusion couples cover a wide range of fractional loss values with some samples retaining nearly all of their silver inventory while others suffer complete loss. This range of results does not support the assumption of diffusion as the controlling mechanism for silver release.   The diffusion couples were all fabricated using the same silicon carbide deposition method. Some variation occurs between coating batches when making these diffusion couples, but this is probably on the same order as variations within a single coating batch due to fluctuations between the top and bottom and between the center and outside edges in the fluidized bed. For similar diffusion couples with high-density SiC with similar microstructure, a diffusion mechanism does not explain the 0 to 100% range of fractional release.   As discussed in Appendix A, variations in grain structure could account for roughly a factor of 2 variation in the diffusion coefficient, but cannot account for the difference of 1-2 orders of magnitude or for the variation between 0% and 100% release.

SiC-Shell Diffusion Couples

SiC-shell diffusion couples (SiC-3) all had small mass losses recorded after heating. The mass loss ranged from 0.0007 g to 0.0037 g for heat treatments at 1350°C and 1500°C for 200 h to 1500 h. These values for mass loss are measurable, but may be within the limits of uncertainty for both the measurement and due to other mass loss phenomena in the furnace including water vapor loss from the couple surface and oxidation of SiC from any oxygen in the furnace.

The SiC outer coating on the SiC-3 couples was deposited using the same procedure under the same conditions as the SiC coating on the SiC-1 couples so changes in the diffusion couple

performance are not due to drastic variations in the SiC coating. The SiC-1 and SiC-3 diffusion couples, however, differ in the substrate material used as the basis of the diffusion couple. The SiC-1 and SiC-2 diffusion couples consist of a porous graphite shell and the SiC-3 couples contain fully dense SiC as the substrate shell. Silver vapor can migrate through the porous graphite shell and, therefore, has access to the entire inner surface of the SiC outer coating in the SiC-1 and SiC-2 diffusion couples, but in the SiC-3 diffusion couples silver has access only to the outer SiC coating in the vicinity of the gap at the SiC shell seam. This difference in silver access in shown schematically in Figure 3-35.

a) Silver has access to entire SiC inner surface in SiC-1 and SiC-2 couples with porous graphite shells

b) Silver only has access to SiC near the seam in SiC-3 couples with dense SiC shells
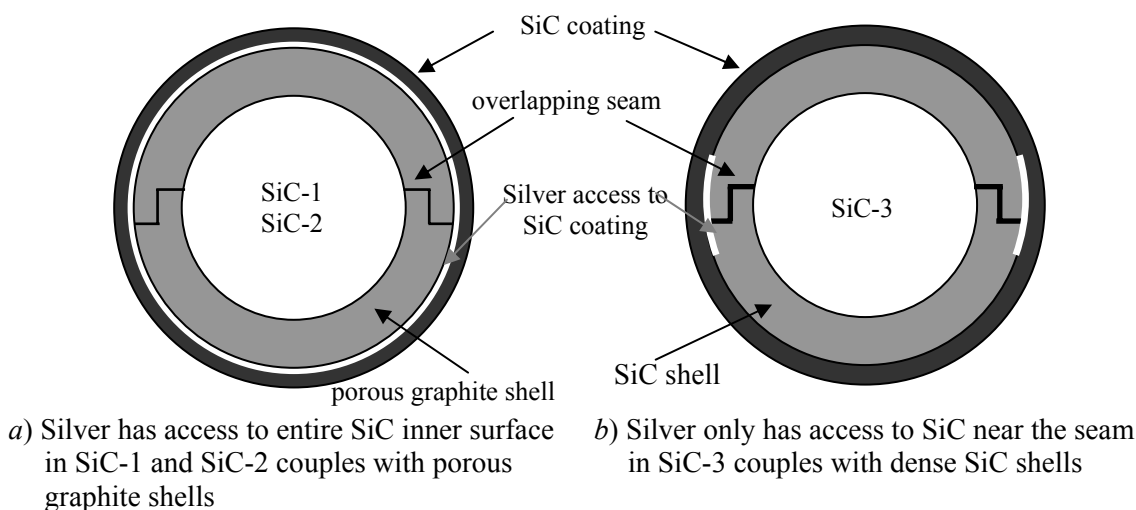
Figure 3-35. Schematic of diffusion couple cross-section showing the silver access to the SiC inner surface as white bands (not to scale).

The gap between the overlapping rim of the two SiC half shells forms the basis of the area normalization for the SiC-3 diffusion couples. This gap, shown in Figure 3-36, provides a direct pathway for silver vapor to reach the SiC outer coating. Any flaws in the SiC coating in the region near the seam in the SiC-3 diffusion couples will allow silver release during heating. Based on the gap observed in Figure 3-36, a band of SiC coating with a 150 μm width around the entire diameter of the diffusion couple is assumed to be accessible to the silver vapor during heating. The ratio of the area of the band surrounding the seam in the SiC-3 couples to the total SiC coating area in the SiC-1 couples provides the area normalization factor of 0.0079. The gap at the seam in a graphite-substrate diffusion couple is shown in Figure 3-37. The gap at the seam

146

is not considered in the graphite-substrate diffusion couples because the graphite shell itself is porous, allowing silver access to the SiC coating.
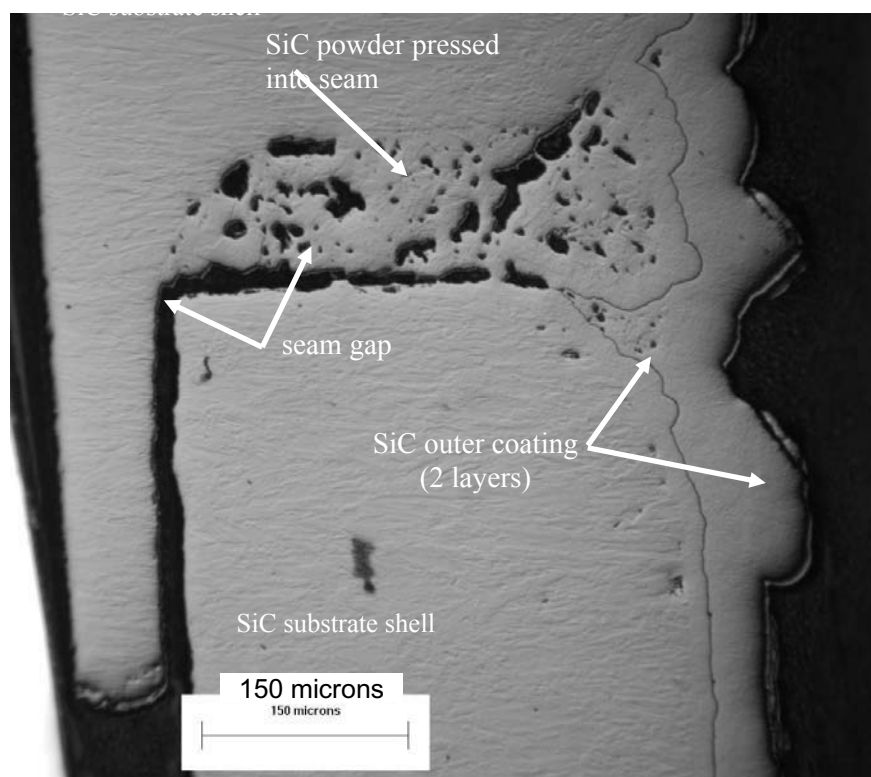
Figure 3-36. Optical micrograph of sample S09 shows the gap at the SiC shell seam.
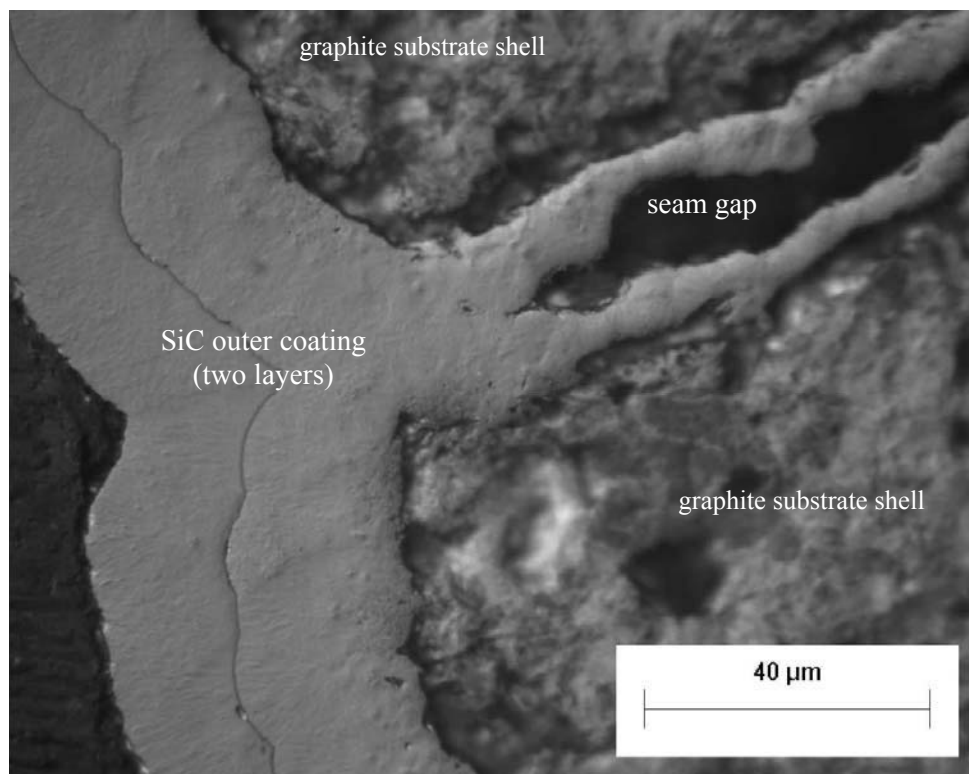
Figure 3-37. Seam between the graphite substrate shells in sample Ag29.

Initially, it appears that the SiC-3 diffusion couples have much lower mass losses than the SiC-1 and SiC-2 type diffusion couples. Adjusting the SiC-3 mass loss results for the fraction of the SiC area actually accessible to the silver, however, produces values in the same range as the SiC-1 and SiC-2 diffusion couples as seen in Figure 3-38.
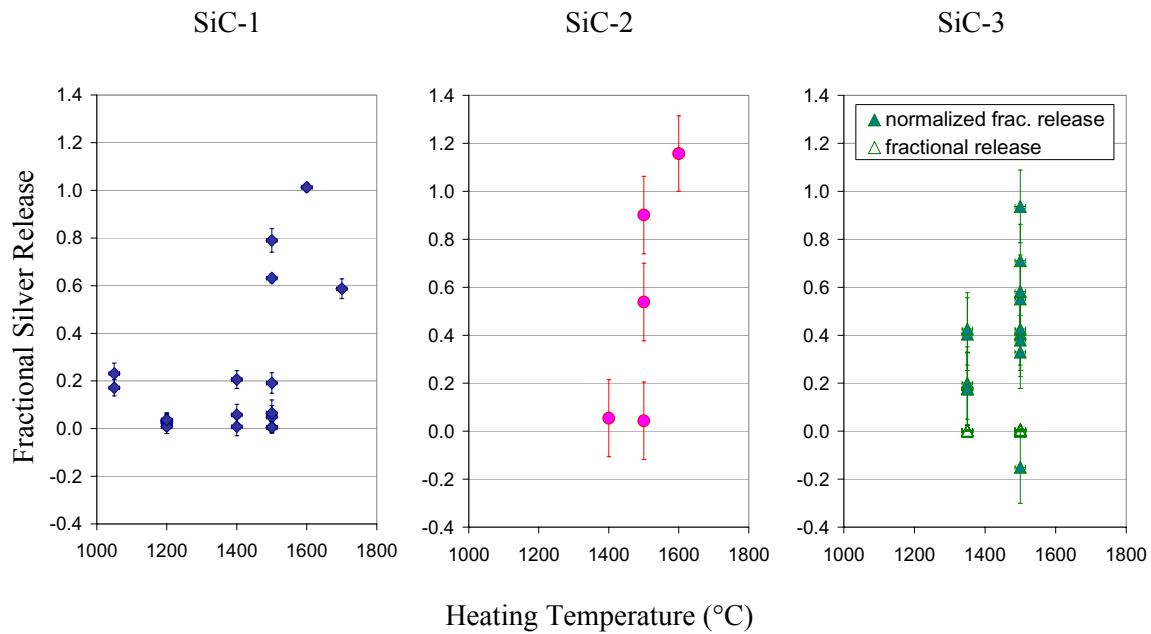
Figure 3-38. Fractional silver loss spans the range from 0% to 100% in the diffusion couples with large variations in each type of diffusion couple design.

No direct correlation between the mass loss and leak testing results is evident, as shown in shown in Figure 3-39. In general, the leak rates associated with the samples with high fractional release are very high, but all the leak rates greater than 1E-4 atm·cc/s are large leak rates. Unfortunately, when a leak path becomes active during testing is not known for these diffusion couple experiments. Leak paths that occur either during fabrication or handling or early during heating would be expected to result in large mass losses. However, paths that develop near the end of heating or during cool down would result in only small mass losses. Due to the variation between individual samples and the lack of time-specific data, further conclusions cannot be drawn from the mass loss vs. leak rate plot in Figure 3-39.
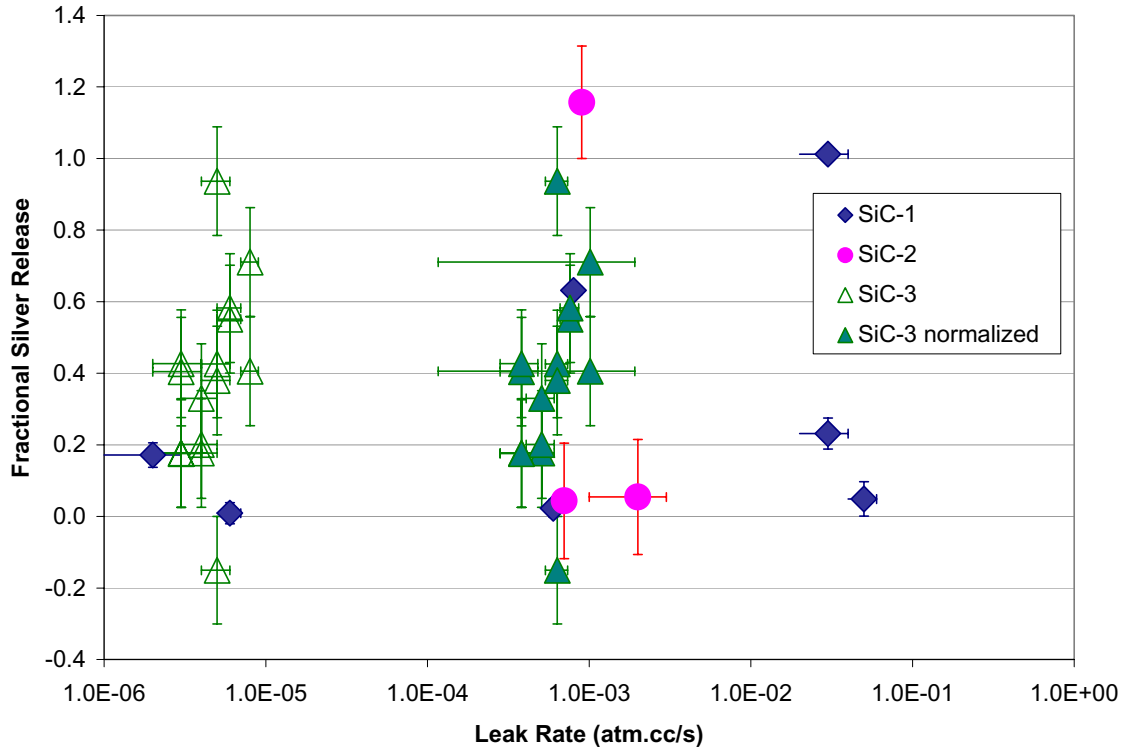
Figure 3-39. Fractional silver mass loss shows no direct correlation with leak rate measurements. In general, all of the leak rates measured after heating were very large and would allow significant mass loss during heating.

Effective Diffusion Coefficient Calculations

Even though the analysis techniques aimed at observing silver diffusion found no direct evidence of silver diffusion in silicon carbide, it is still instructive to evaluate diffusion coefficients from the spherical diffusion couple mass loss data. The mass loss from the current experiments was converted to effective diffusion coefficients using an analytical expression for release through a thin spherical shell, similar to the procedure used to calculate effective diffusion coefficients in the literature. The diffusion couples have a range of SiC coatings approximately 40-120 μm thick with overall radii on the order of 0.95 cm and qualify as thin spherical shells for the purposes of this analysis. The graphite shell in the SiC-1 and SiC-2 and the SiC shell in the SiC-3 diffusion couples were neglected for this calculation. Considering only the CVD SiC coating on the outside of the diffusion couples, an effective diffusion coefficient was calculated, using Equation 3-3 for different limits of the source silver concentration. The results are shown in Figure 3-40.

150

Equation 3-3 is the analytical solution for mass release from a thin spherical shell (Crank 1975). The diffusion coefficient necessary to produce the observed mass loss can be calculated from the difference in mass as measured before and after the diffusion couple heat treatments (Q_r), the known dimensions for each diffusion couple, and the silver concentration level at different areas in the couple. Three different values of the silver concentration have been considered: the first is the concentration of silver in the molten pool in contact with the silicon carbide at the bottom of the diffusion couples; the second is the limit of detection of XPS, the technique used to measure concentration profiles in the silicon carbide coatings and shells; and the third is the silver concentration in the vapor phase in contact with the silicon carbide in the upper portion of the diffusion couple.

$$Q_r = 4\pi\,a\,b(b-a)C_1 \cdot \left[\frac{D\cdot t}{(b-a)^2} - \frac{1}{6} - \frac{2}{\pi^2}\cdot\sum_{n=1}^{\infty} \frac{(-1)^n}{n^2}\exp\left[-\frac{D n^2\pi^2 t}{(b-a)^2}\right] \right]$$ (Eq. 3-3)

where Q_r = mass released (g),
  a = inner radius of spherical shell (m),
  b = outer radius of spherical shell (m),
  C_1 = source concentration of silver at $r = a$ (g/m^3),
  D = diffusion coefficient of silver in SiC (m^2/s), and
  t = duration of heat treatment (s).

Figure 3-40 shows the band of effective diffusion coefficients reported in the literature and discussed in Appendix A for comparison to the current data. Diffusion coefficients in the range of 10^{-16} m^2/s to 10^{-14} m^2/s at 1500°C are calculated from the silver concentration at the interface between the molten pool and the SiC at the bottom of the diffusion couple. These values are in the same range as those reported in the literature, but as discussed in the section on silver distribution, no silver was observed in the SiC coating at the bottom of the diffusion couple. Therefore, silver release by diffusion according to the rates reported in the literature did not occur in these experiments.

If the silver concentration, however, were just below the XPS detection limit of 100 ppm, XPS would not have measured silver concentration profiles in the SiC coating. If silver diffused through the SiC coating with a source concentration of 100 ppm diffusion coefficients would have had to be in the range of 10^{-14} m^2/s to 2×10^{-10} m^2/s at 1500°C, significantly higher than those previously reported for silver in SiC. If silver diffused through the SiC at the top of the diffusion couples where the source concentration was approximately 1 ppm, the diffusion

coefficients necessary to accommodate the observed mass loss would generally be in the range of 10^{-10} m^2/s to 10^{-7} m^2/s at 1500°C. The source concentration of the silver vapor in the upper portion of the diffusion couple, used as C_1 in Equation 3-3, was derived from the equilibrium silver vapor pressure during each experiment.

The calculated diffusion coefficients from the current tests using the silver source concentration values derived from the XPS detection limit of the vapor phase during heating are not consistent with the previously derived diffusion coefficients and the assumptions of grain boundary diffusion. Although the concentration profile measurements using XPS had a detection limit of 100 ppm, it is likely that any silver concentrations near that limit would have been detected either during XPS analysis or during AEM or other measurement techniques. If silver diffused through the SiC coating from the vapor source, the diffusion coefficients would have had to have been between 6 and 7 orders of magnitude greater than those previously accepted to support the observed mass loss. While the results collected so far cannot disprove silver diffusion from the low-concentration vapor source in the upper portion of the diffusion couple, typical diffusion coefficients reported previously in the literature do not support the total amount of silver released during the current experiments. Silver may diffuse in low concentrations, but another mechanism must be active to provide a pathway for the amount of silver loss measured. It is more likely, especially when considered together with the leak testing results discussed earlier, that silver vapor migrated through cracks in the SiC coating.
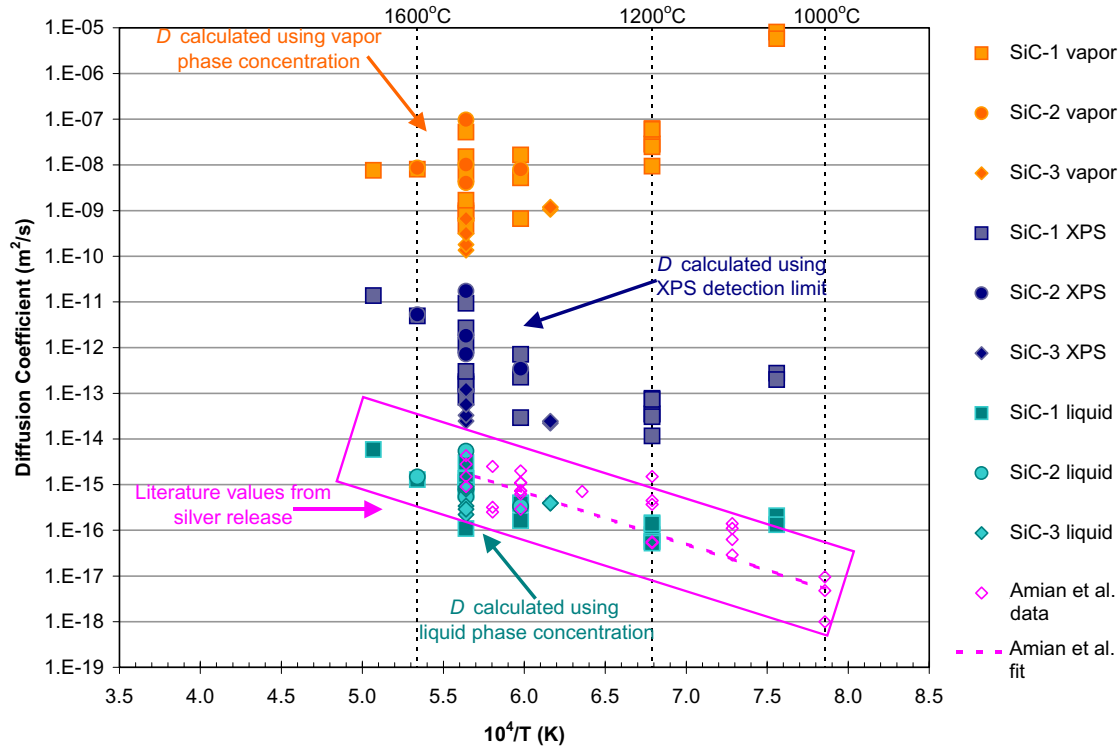
Figure 3-40. Effective diffusion coefficients calculated from diffusion couple mass loss are much greater than those previously reported in the literature.

Stress Analysis

Silver clearly escaped from some of the diffusion couples in the current experiments, but no signs of classical diffusion were identified. Silver release via vapor migration through cracks in the SiC coating fits the experimental observations, but a specific crack development sequence has not yet been identified. One possible scenario is that one or more cracks developed during the thermal cycling between fabrication, heating, and cool down due to the mismatch in the coefficients of thermal expansion between the graphite shell and the SiC coating.

A preliminary finite element stress analysis completed at the Idaho National Engineering and Environmental Laboratory indicates that stresses in the diffusion couple can exceed the fracture strength of the silicon carbide coating (Miller 2003). The selection of the graphite shells aimed at achieving the best possible match of the coefficient of thermal expansion (CTE) for both the graphite and SiC. Ibiden ET-10 graphite, with approximately 15% porosity, has a CTE equal to $3.8 \times 10^{-6}/°C$ and the CTE for SiC is $2.9 \times 10^{-6}/°C$ between room temperature and 100°C and $5.1 \times 10^{-6}/°C$ at 1200°C. Figure 3-41 shows the stress state for a perfectly spherical diffusion

couple, assuming a zero initial stress state during SiC deposition at 1200°C, cooling to room temperature, a heat treatment at 1500°C for 200 h, and a final cool down. The thermal cycling as shown in Figure 3-41 would cause stresses greater than the fracture strength of 480 MPa and could lead to SiC cracking during cooling (Ho 1993).
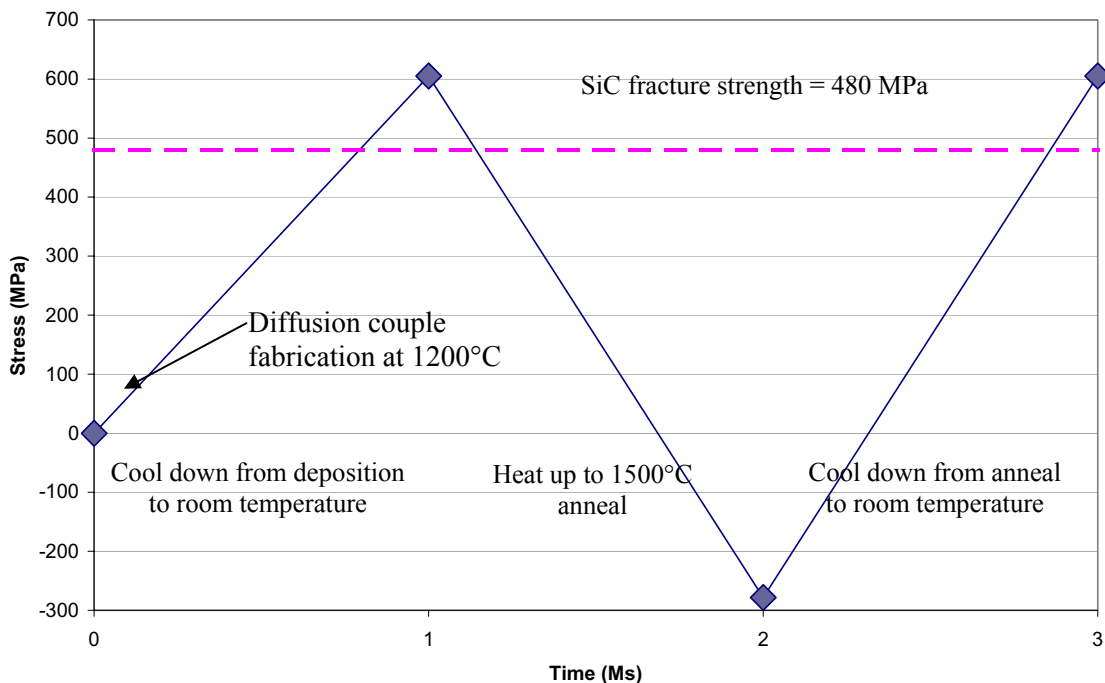
Figure 3-41. Stresses in SiC coating during thermal cycling due to differential thermal expansion between the SiC coating and the graphite shell exceed SiC's yield strength.

Preliminary analysis, though still inconclusive, indicates possible crack development in the SiC coating. AFM (atomic force microscopy) analysis detected no signs of silver in the SiC shell or coatings of two SiC-3 diffusion couples: S09, an unheated sample; and S22 after 500 h at 1500°C. Indications of "nano-cracks", however, were found in the heated sample, S22. Between grains, at a level of detail on the order of nanometers, indications of cracks appear on the order of angstroms wide, as shown in Figure 3-42. Additional AFM work is needed to verify the presence of nano-scale cracks in the SiC coatings, but features such as these may offer a silver transport pathway through SiC.
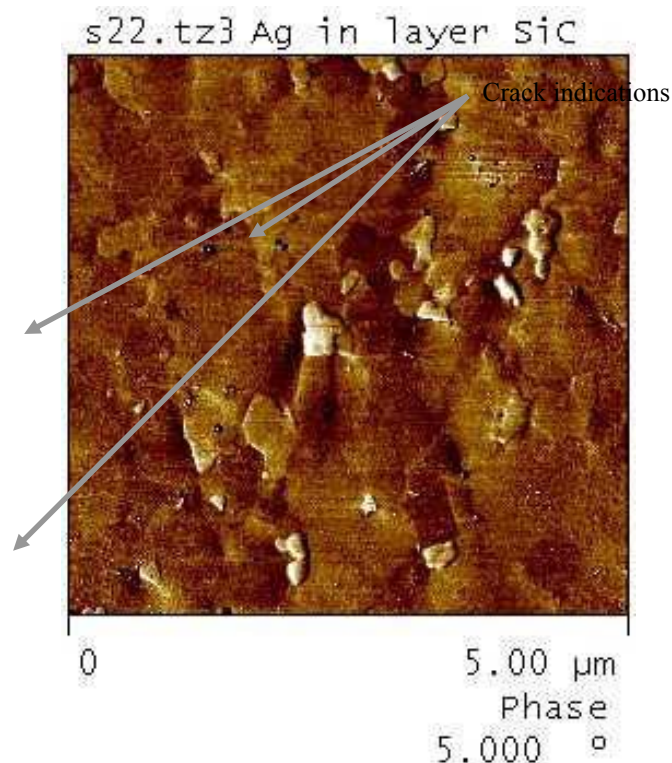
Figure 3-42. AFM analysis reveals nano-crack features in the SiC coating of SiC-3 sample S22 after 500 h at 1500°C.

Vapor Migration and Literature Data

Results from the current experiments lead to the conclusion that silver release from the silicon carbide coated diffusion couples is likely dominated by vapor migration through cracks in the SiC coating, not classical diffusion as previously thought. If silver cannot diffuse through SiC in the current spherical diffusion couples, then it cannot diffuse through similar SiC coatings in typical coated particle fuel. While this may at first appear contradictory to the results from previous literature reports, a reinterpretation of the literature data suggests some similarity.

As discussed in greater detail in Appendix A, silver diffusion coefficients have frequently been derived from batch-averaged silver release measurements. When silver release is collected for a large batch of particles during annealing, it is impossible to know individual particle silver release. Gamma counting of individual particles attempts to evaluate fission product inventory of each particle, but this process is time-consuming and has only been completed on small batches (Bullock 1984). In previous tests, the total amount of silver release from a batch of

particles was averaged over all of the particles to arrive at the average release per particle. From these data, diffusion coefficients were calculated assuming identical behavior within the batch. Moreover, the activation energies for this data fell within the range characteristic of grain boundary diffusion processes, lending support to the conclusions of silver diffusion in SiC coatings.

If all of the particles, however, are not assumed to behave identically, as seen by the large variation of fission product inventory measurements in the JAERI tests, other conclusions seem viable (Minato et al. 1998). Reported silver mass loss from annealed particle batches varied from about 0.4% to 29% of the total batch inventory (Amian and Stöver 1983). Although these data were equally attributed to all of the particles in order to calculate diffusion coefficients, the same total mass loss could have been obtained from large vapor migration from just a few particles in each batch. The example using the data reported by Amian and Stöver, discussed in Appendix A, illustrates that complete silver release from just a few particles in a batch could produce the same results that were interpreted as diffusion.

Summary of Silver Migration

Measurements before and after heat treatments show significant silver mass loss from the diffusion couples, but measurements aimed at recording silver concentration profiles in the silicon carbide coatings detected no silver. Leak rate increases after heating strongly suggest mechanical paths for non-diffusive release. Taken together these results lead to the conclusion that silver must have escaped from the diffusion couples through a vapor migration path. Silver diffusion, if it occurs at all in intact silicon carbide, is extremely slow, much slower than previously reported in the literature. Silver release from silicon carbide is controlled by vapor migration through cracks in the silicon carbide. Had silver diffused from the source of molten silver at the bottom of the diffusion couples, it would have been detected during concentration profile measurements. Silver diffusion from the low-concentration vapor source cannot be ruled out, but diffusion cannot account for the total amount of silver loss measured using the range of diffusion coefficients reported in the literature. Vapor migration through mechanical pathways accounts for the amount of mass loss, the extreme variation between samples, and the increase in leak rates after heating.

As discussed in Appendix A, a reinterpretation of historic literature data indicates that it is possible that silver releases in previous experiments likely resulted from large inventory losses

from a few individual particles rather than small fractional releases assumed due to grain boundary diffusion. Silver release values governed by vapor migration can still exhibit a temperature dependence, not unlike those presented in the literature, due to the vapor pressure driving force. The silver vapor pressure increases with temperature, increasing the driving force for silver release during higher temperature tests. A weak trend between the current experimental data and the product of the vapor pressure and duration of each test is seen in Figure 3-43, but this temperature dependence may account for the temperature trends observed in the literature.
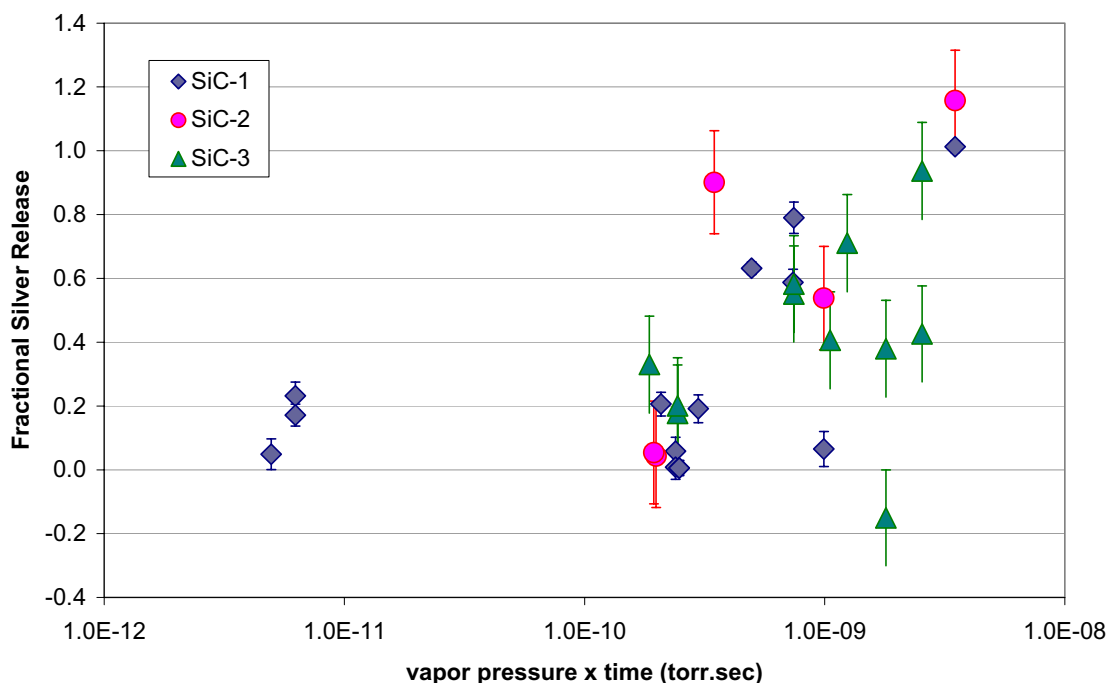
Figure 3-43. Silver fractional release displays a weak trend with the product of vapor pressure and time during anneal.

Conclusions and Significance

Contrary to previous assumptions in the literature, silver does not diffuse, but rather likely leaks through intact silicon carbide via vapor migration through cracks or flaws. The importance of this new finding is that silver release in high-temperature gas reactors may be reduced by improving silicon carbide quality. Only some of the diffusion couples released silver and it appears that only some of the coated fuel particles reported in the literature released silver, indicating that vapor migration is not endemic to all silicon carbide, but affects only certain

157

particles. Preliminary findings from the current experiments suggest silicon carbide cracking due to thermal cycling and a possible network of nanometer-sized cracks. If particles afflicted with or prone to crack networks can be removed from the population to be irradiated, silver release may be reduced.

The results of the current experiments that additional work is required to identify the exact pathway for silver vapor release and that the test methods used to evaluate silver migration need to be carefully reviewed. Care must be taken when applying large batch behavior to individual particles. Particle variation is a natural consequence of the fluidized bed fabrication process and the use of ceramic materials. Ignoring the variation in individual particle properties and behavior and assuming identical behavior among all particles can produce misleading results. Although large population tests are necessary and provide effective batch data, information on specific transport mechanisms can be missed.

Assessment of Silver Transport in SiC

As discussed previously, the results of this research strongly suggest that classical diffusion does not govern silver transport in apparently intact SiC. Although the bulk of the previous literature on silver migration in silicon carbide presents results based on the assumption of diffusion, there are still uncertainties in the data and some alternative explanations have been hinted at by other authors, as discussed in Appendix A. There is no question that coated fuel particles release silver under certain conditions; however, a new description is needed for silver release from fuel particles since silver does not diffuse through intact SiC via classical diffusion.

Data collected during the current experimental program clearly demonstrate that silver does not diffuse through intact silicon carbide. However, silver release does occur in both the current spherical diffusion couple and previous coated fuel particle tests. As discussed previously, this release is most likely due to vapor transport through mechanical cracks in the SiC layer.

The results of previous experiments, reported in the literature, characterize silver release from coated fuel particles as the result of diffusion. For more than three decades, authors have presented silver release data in the form of Arrhenius diffusion relationships. As discussed in Appendix A, there have been doubts about the accuracy of solid-state diffusion as the actual

mechanism controlling silver migration in SiC with some authors suggesting a "short-circuit" path.

Leak testing results of this work provide evidence that cracks exist in the SiC coating of the current diffusion couples. Although there is very little time data available to evince when cracks developed, the cracks provide a plausible pathway for silver release in the current diffusion couple experiments. Although the exact SiC crack formation scenario may be unique to these diffusion couples due to the large volume of SiC present and the presence of a large discontinuity at the seam of the diffusion couple, the existence of cracks in the SiC layer of the diffusion couples suggests that silver escapes by means of vapor transport through cracks.

The interaction of all of the layers in the coated fuel particle and the retention of other fission products in those layers, even when the SiC contains cracks, will be discussed in this section.

Uncertainty in the Literature

A detailed review of the state of knowledge in the literature regarding silver migration in silicon carbide was presented in Appendix A. In general, silver release has been discussed in terms of diffusion, but that representation is a useful tool rather than an exact description of the specific mechanism itself. Numerous authors, while presenting silver release results in the form of Arrhenius diffusion relationships, have suggested that silver release does not follow classical diffusion. Nabielek presented silver release results from fuel particles that did not follow the expected diffusive release and hypothesized rather that the SiC becomes progressively transparent to silver due to traces of free silicon on the SiC grain boundaries (Nabielek 1976). After a thorough review of the state of knowledge of silver release from coated fuel particles in 1992, McCardell et al. pointed out that "the technical community is not in complete agreement on the exact mechanism for silver transport through SiC (McCardell et al. 1992)".

Furthermore, a review of the overall literature data highlights the uncertainty of the silver release mechanism. Within tests containing a single batch of particles that were all manufactured under the same conditions, often in the same batch, silver release values vary from 0% to 100%. Some variations in total release would be expected for a diffusive process due to variations in total SiC thickness in each sample and variations in the specific microstructure and grain orientation within the SiC layers, but those variations would not produce fractional release values spanning

the entire possible range from 0% to 100%. Differences in SiC thickness or grain orientation (i.e., total path length) could cause a change in total silver release of a few percent, but clearly do not account for the large variation in release between samples within individual tests or the overall range of diffusion coefficients reported.

Unresolved questions also remain regarding the method of data collection from silver release experiments. In many of the experiments silver release was measured for a batch of particles. In many cases, individual fission product inventories were not measured and the silver released was assumed to have been distributed evenly among the particles in the test batches. This assumption has worked reasonably well to characterize batch performance and has provided a convenient tool for comparing test results between different types of fuel and between different researchers at different labs.

In cases where individual fuel particles were measured, the silver release varied widely, in some cases from 0% to 100% in the same batch and test. These types of results run counter to a diffusive release mechanism and suggest that another mechanism is responsible for silver release in some of the samples while the rest retain most of their silver inventories.

Diffusion Couple Leak Testing Review

There are some doubts expressed in the literature and uncertainties as to the exact mechanism or mechanisms responsible for silver release from coated fuel particles. Classical diffusion does not explain the current experimental results or the results previously reported in the literature. Silver doesn't diffuse through intact SiC, but clearly escaped from the diffusion couples in the current experiments.

Silver did not diffuse through the spherical diffusion couples but silver release did occur. Leak testing of the diffusion couples clearly indicates the presence of cracks (mechanical paths) in the SiC coating of many of the diffusion couples. Although leak rates are not available for all of the diffusion couples, these mechanical paths would certainly provide a pathway for silver vapor migration through the diffusion couples during heating. Additionally, where leak rates are available both before and after heating, they show that some of the samples definitely undergo a transition from low to high leak rates during heating.

These leak rates are proof of available mechanical pathways open to vapor transport. Leak testing was performed with helium gas, a gas with atoms much smaller than silver's, but the results clearly identify mechanical, not chemical, paths through the SiC coating that would allow vapor migration and release. Therefore, the next step in the study of silver migration through SiC is to consider vapor flow as the mechanism for silver release. Vapor flow modeling, discussed in the following section, can be used to estimate crack sizes in the current diffusion couples and also in typical coated fuel particles.

Vapor Flow Modeling

Background

Basic vapor flow modeling and some simplifying assumptions can be used to estimate the crack size required to accommodate the observed silver loss in the current diffusion couple experiments and in previous coated fuel particle tests. All cracks were assumed to be straight tubes with circular cross-sections such that the length of the crack was equal to the SiC coating thickness. In reality, the crack paths will likely follow tortuous routes and will not have perfectly circular cross-sections. Using these assumptions, however, allows an initial estimate of the size of the crack paths with minimal introduction of unknown quantities (e.g., tortuosity factors) and allows a comparison of the crack sizes between different sets of experiments.

Different regimes govern vapor flow depending on the system pressure and channel size. At very low pressures, the mean free path of the gas molecules is much larger than dimensions of the vacuum enclosure. Under these conditions, the gas molecules undergo collisions primarily with the walls of the enclosure rather than with other molecules; this is known as molecular flow. At atmospheric pressures, the mean free path of gas molecules is very small relative to the structure through which they're flowing. In this case, known as viscous flow, the gas molecules undergo collisions primarily with other gas molecules rather than with the walls and the gas viscosity limits the flow. At pressures in between, both viscous and molecular phenomena contribute to gas flow in the transition flow regime. For the data sets analyzed here, only molecular flow was encountered.

Since silver did not diffuse out of the diffusion couples, the silver release and leak rate results were reexamined using vapor flow theory. In addition, the results of a typical coated fuel particle experiment were reevaluated using vapor flow theory. Results of these calculations,

shown in the following sections, indicate that silver vapor flow through SiC cracks is a plausible migration mechanism. During molecular flow, the mean free path of the gas molecules is much larger than the diameter of the tube in which they're flowing; the movement of the molecules is dominated by collisions with the tube walls rather than with other molecules. The conductance of a gas governed by molecular flow is defined as: (Alcatel Vacuum Tech. 2004)

$$C_{molecular} = \frac{1}{6}\sqrt{\frac{2\pi R T}{aw}}\frac{d^3}{L}$$

(Eq. 3-4)

where
$C_{molecular}$ = conductance (liter/sec),
R = gas constant (8.314 J/mol·K),
T = absolute temperature (K),
d = crack diameter (m),
aw = atomic weight of the gas (107.87 g/mol for silver), and
L = length of the crack tube (assumed equal to the thickness) (m).

To convert from conductance to mass loss, a value measured during the current diffusion couple experiments, the time of the experiment and the molar volume are also needed. The molar volume is calculated from the ideal gas law and is given by:

$$v_{molar} = \frac{R T}{P}$$

(Eq. 3-5)

where
v_{molar} = molar volume (m^3/mol),
R = gas constant (8.314 J/mol·K),
T = absolute temperature (K), and
P = pressure (Pa).

For the molar volume as defined by Equation (3-5), the mass loss over a specified time, t, due to molecular flow is given by:

$$Q_{molecular} = \frac{C_{molecular}\ t}{v_{molar}}\ aw$$

(Eq. 3-6)

where
$Q_{molecular}$ = mass loss (g),
$C_{molecular}$ = laminar flow conductance (liter/sec),
t = time (sec),
v_{molar} = molar volume (m^3/mol), and
aw = atomic weight of the gas (g/mol).

The molecular flow equation attributed to Knudsen applies to pipes of circular cross-section. For pipes of equal cross-sectional areas, pipes with non-circular cross-sections will experience lower conduction than those with circular cross-sections (Varian Proceedings 1976). More details of vapor flow modeling are presented in Appendix C.

Silver Mass Loss from Diffusion Couples

There was no evidence of silver diffusion in the silicon carbide shells or outer coatings in the spherical diffusion couples. Silver did, however, escape from the diffusion couples. There were no signs of any interaction between the diffusion couples and the pools of molten silver at the bottom of the couples during heating. Vapor migration of silver through openings in the SiC layer, therefore, is the only plausible mechanism resulting in silver release.

The crack diameter necessary to account for the mass of silver released can be calculated from the equations presented previously and the temperatures, times, and pressures of the diffusion couple experiments. This procedure was also applied to the helium leak testing results on the diffusion couples, and also to mass loss data from the JAERI (Japanese Atomic Energy Research Institute) HRB-22 capsule irradiation and heating test.

The graphite substrate shell is ignored for the calculations on the SiC-1 and SiC-2 diffusion couples. The graphite layer consists of interconnected porosity, providing a direct path for silver vapor to reach the inner surface of the SiC coating in the diffusion couples. The pressure inside the SiC layers is simply the equilibrium vapor pressure of silver at the heat treatment temperature.

At all heating temperatures, there is plenty of excess silver available; only 2×10^{-5} g of silver is required to maintain vapor/liquid equilibrium inside the diffusion couples and approximately 0.12 g to 0.50 g of silver was loaded into each diffusion couple. One SiC-1 sample and one SiC-2 sample experienced fractional releases greater than 100% and did not maintain silver equilibrium throughout the heat treatment. All calculations assumed a single, straight crack with circular cross-section and a length equal to the thickness of the SiC layer. The SiC thickness was calculated from the measured weight gain of the diffusion couples after CVD deposition of the SiC layer.

The same assumptions were used for calculations on the SiC-3 diffusion couples with SiC substrate shells with an outer CVD SiC coating. The SiC substrate shell, however, was not porous like the graphite shell in the SiC-1 and SiC-2 diffusion couples and it was less likely that a crack would develop through the entire 800 μm thickness of the SiC substrate shell. The only release path, therefore, for the silver vapor was through the outer SiC coating.

There was a significant gap between the two SiC substrate shells, as previously shown. In this area, around the entire diffusion couple, silver vapor had direct access to the outer SiC coating. Any cracks or connected mechanical paths in the SiC outer coating near the seam would result in silver release. In the SiC-3 couples, only silver vapor near the seam in the inner shell could easily get to the outer SiC coating. Only cracks in the outer SiC coating near the seam area produced silver release, resulting in lower overall mass loss compared to the SiC-1 and SiC-2 diffusion couples.

The seam in the SiC-1 and SiC-2 diffusion couples between the graphite substrate shells did not significantly contribute to the overall silver release because the graphite shells were porous and allowed unimpeded silver migration to the SiC coating. The graphite substrate shells also formed a closer fit with each other, presenting only a small gap at the seam. In the SiC-1 and SiC-2 diffusion couples with SiC coatings over a graphite hollow shell, the silver vapor had ample access to the SiC coating through the porous graphite shell. At the seam location silver vapor had direct access to the SiC coating, but since the graphite shell did not significantly impede silver vapor migration the presence of a gap between the graphite substrate shells did not change the calculations.

The conductance and mass loss equations require the silver vapor pressure inside the spherical diffusion couple. At the heating temperatures used for the diffusion couple experiments, the silver existed as a vapor in equilibrium above its liquid. In all but two cases, there was sufficient silver inside the diffusion couple to maintain equilibrium between the gas and the liquid during the entire heat treatment. The equilibrium pressure for silver vapor above its liquid is given by (Barin, Knacke, and Kubaschewski 1977):

$$p_{silver} = 2.131 \times 10^8 \ \exp\left(-3.054 x 10^4 \ \frac{1}{T}\right) \qquad \text{(Eq. 3-7)}$$

where p_{silver} =   equilibrium silver vapor pressure (torr), and
             T =   absolute temperature (K).

As mentioned in Appendix A, graphitic materials do not act as barriers to silver migration. The graphite layer in the diffusion couples (types SiC-1 and SiC-2) had 13% porosity and was easily penetrated by the silver vapor. One heating experiment with a diffusion couple with a spot of exposed graphite approximately 0.16 cm in diameter, sample Ag15, resulted in significant mass loss in just 2 h at 1500°C. If the silver loss occurred primarily through the bare graphite location, then the effective transport coefficient for silver vapor through the graphite shells in the diffusion couples was roughly 0.5 cm^2/ s, resulting in nearly instantaneous transport of silver across the graphite shell. Therefore, the graphite shell is ignored during the crack size calculations and only transport through the SiC outer coating is considered.

The crack size calculations include the assumptions that the crack path is a straight tube with a circular cross-section such that the length of the crack path is equal to the SiC coating thickness. Additional assumptions include an active and accessible crack path during the entire heat treatment (i.e., silver is uniformly released during the heat treatment).

The molecular flow model was used to calculate the crack diameters for all of the spherical diffusion couples, then the Knudsen number of the resulting crack diameter and silver mean free path was checked. For all of the cases, the Knudsen number was well above the limit for molecular flow, confirming the use of the molecular flow model. Appendix C includes further details for calculating the Knudsen number and the flow regime.

Tables 3-6 through 3-8 list the relevant heating parameters and the calculated crack diameters from the three sets of spherical diffusion couple tests. The calculated crack diameters mostly fall in the range from 3 μm to 20 μm with one sample near 30 μm and two samples near 50 μm. These crack diameters may seem rather large and easy to detect, but if multiple cracks are present in the sample, a likely event given the large surface area of the diffusion couples, then the average crack diameter will be smaller. The crack diameter calculated for 20 identical cracks is also listed in Tables 3-6 through 3-8. These crack diameters vary from about 1μm to 4 μm with one sample near 7 μm and two greater than 10 μm. Although these dimensions are detectable under optical microscopy cracks may not be noticed if they are not perfectly aligned with the cross-section that is being viewed. It is possible, therefore, that cracks of the order of those listed in Tables 3-6 through 3-8 would not have been detected during investigation with optical microscopy.

Table 3-6. SiC-1 heating parameters and calculated crack diameters.

Sample ID	Heating Temperature (°C)	Heating Time (h)	SiC Thickness (μm)	Mass Loss (g)	Calculated Crack Diameter (μm)	Calculated Crack Diameter for 20 Equal Cracks (μm)
10	1050	1000	65.1	0.0319	54.8	12.1
24	1050	1000	49.6	0.0300	49.0	11.0
28	1200	1760	55.4	0.0083	12.8	2.7
30	1200	1760	53.7	0.0075	12.2	2.7
56*	1500	200	74.6	0.0060	8.4	1.8
57	1500	500	73.2	0.1913	19.4	4.2
63**	1600	550	61.9	0.3297	15.8	3.3

* 0.0000 g initial silver loading (control sample)
** 101% mass loss (of initial silver load)

Table 3-7. SiC-2 heating parameters and calculated crack diameters.

Sample ID	Heating Temperature (°C)	Heating Time (h)	SiC Thickness (μm)	Mass Loss (g)	Calculated Crack Diameter (μm)	Calculated Crack Diameter for 20 Equal Cracks (μm)
37	1500	80	39.4	0.0110	11.2	2.5
38	1400	224	41.9	0.0138	12.2	2.7
39	1500	400	39.9	0.1360	15.3	3.4
40	1500	140	79.4	0.2280	32.3	7.2
53*	1600	550	72.2	0.3009	16.2	3.6

* Significant mass loss (116% of initial silver load) violates the equilibrium assumption

Table 3-8. SiC-3 heating parameters and calculated crack diameters.

Sample ID*	Heating Temperature (°C)	Heating Time (h)	SiC Thickness (μm)	Mass Loss (g)	Calculated Crack Diameter (μm)	Calculated Crack Diameter for 20 Equal Cracks (μm)
S10-1	1500	300	110.2	0.0022	6.0	1.3
S10-2	1500	725	110.2	0.0000	0.0	0.0
S10	1500	1025	110.2	0.0017	3.6	0.7
S11-1	1500	300	116.7	0.0023	6.2	1.3
S11-2	1500	725	116.7	0.0015	4.0	0.9
S11	1500	1025	116.7	0.0037	4.8	1.1
S12-1	1350	500	112.3	0.0007	5.8	1.3
S12-2	1350	1000	112.3	0.0007	4.6	0.9
S12	1350	1500	112.3	0.0016	5.3	1.1
S13-1	1350	500	109.7	0.0008	6.0	1.3
S13-2	1350	1000	109.7	0.0007	4.6	0.9
S13	1350	1500	109.7	0.0017	5.3	1.1
S22-1	1500	75	63.0	0.0013	6.6	1.3
S22-2	1500	425	63.0	0.0016	4.0	0.7
S22	1500	500	63.0	0.0028	4.5	0.9

* Each sample was heated twice. For example, S10-1 represents the first heat treatment, S10-2 represents the second, and S10 is the combined heating and mass loss data for sample S10.

Helium Leak Testing of Diffusion Couples

Helium leak testing, performed on many of the spherical diffusion couples provides additional information on the presence of cracks in the silicon carbide coating. Leak testing techniques measure the presence of mechanical cracks. Since silicon carbide is not permeable to helium, this type of testing detects mechanical cracks present in the diffusion couples.

A procedure similar to the one described above can be used to calculate the crack diameter from helium leak testing results on the diffusion couples after heating. Since the leak testing results are in the form of leak rates for each sample, the leak rate model for transition flow can be used directly to determine the crack diameter. Again, assumptions of a straight crack with a circular cross-section and a length equal to the SiC coating thickness were employed.

As shown in Tables 3-9 through 3-12, the crack diameters as calculated from the helium leak testing data on the spherical diffusion couples are roughly one order of magnitude smaller than those calculated from the silver mass loss.

Table 3-9. SiC-1 calculated crack diameters from leak testing.

Sample ID	Mass Loss (g)	Crack Diameter from Silver Mass Loss(μm)	Crack Diameter from Helium Leak Testing (μm)
10	0.0319	54.8	5.3
15	0.0061	37.1	6.1
24	0.0300	49.0	0.34
28	0.0083	12.8	1.8
30	0.0075	12.2	0.49
56*	0.0060	8.4	1.5
57	0.1913	19.4	2.1
63**	0.3297	15.8	5.3

    * 0.0000 g initial silver loading (control sample)
    ** 101% mass loss (of initial silver load)

Table 3-10. SiC-2 calculated crack diameters from leak testing.

Sample ID	Mass Loss (g)	Crack Diameter from Silver Mass Loss(μm)	Crack Diameter from Helium Leak Testing (μm)
37	0.0110	11.2	1.7
38	0.0138	12.2	2.3
39	0.1360	15.3	N/A
40	0.2280	32.3	N/A
53*	0.3009	16.2	2.2

    * significant mass loss (116% of initial silver load) violates silver vapor equilibrium assumption
    ** No leak testing data available for samples Ag39 and Ag40

Table 3-11. SiC-3 calculated crack diameters from leak testing.

Sample ID	Mass Loss (g)	Crack Diameter from Silver Mass Loss(µm)	Crack Diameter from Helium Leak Testing (µm)
S10-1	0.0022	6.0	0.60
S10-2	0.0000	0.0	0.57
S10	0.0017	3.6	0.57
S11-1	0.0023	6.2	0.61
S11-2	0.0015	4.0	0.58
S11	0.0037	4.8	0.58
S12-1	0.0007	5.8	0.54
S12-2	0.0007	4.6	0.49
S12	0.0016	5.2	0.49
S13-1	0.0008	6.0	0.53
S13-2	0.0007	4.6	0.49
S13	0.0017	5.3	0.49
S22-1	0.0013	6.6	0.45
S22-2	0.0016	4.0	0.56
S22	0.0028	4.5	0.56

* Each sample was heated twice. For example, S10-1 represents the first heat treatment, S10-2 represents the second, and S10 is the combined heating and mass loss data for sample S10.

In all but two cases, the Knudsen number for helium flow through the calculated crack diameter at room temperature and 80 psi (the soaking over-pressure) was in the intermediate regime. For two cases, the Knudsen number was very close to the limit between intermediate and laminar flow.

Silver Mass Loss from Coated Fuel Particles

JAERI irradiated fuel elements with typical coated fuel particles in the HRB-22 capsule at ORNL (Oak Ridge National Laboratory). Some of the fuel elements were deconsolidated after heating and individual particles were removed and heated. The third accident condition test (ACT-3) was heated at 1700°C for 270 h. The activity of each particle was measured before and after heating. In addition, deposition cups inserted in the furnace were removed and counted periodically during heating to monitor fission product release.

The initial mean silver activity per particle was 1.04 µCi before the ACT-3 heating test. The mean mass of silver per particle before the heating test can be calculated from the initial mean activity and the decay constant for [110m]Ag. The relative change in activity per particle was

reported after the test. Therefore, the final activity and the final mass of silver per particle can be calculated by Equation 3-8.

$$m_{Ag} = \frac{A}{\lambda_{Ag-110m}} \frac{aw_{Ag}}{N_A}$$ (Eq. 3-8)

where
m_{Ag} = silver mass (g),
A = silver activity (Bq),
λ = ^{110m}Ag decay constant (s^{-1}),
aw_{Ag}= silver atomic weight (110 g/mol), and
N_A = Avogadro's number (6.02×10^{23} atom/mol).

The mass loss for each particle during the heat treatment can then be derived from the change in activity as shown in Equation 3-9. The fractional mass loss for each of the 25 particles in ACT-3 is shown in Figure 3-44.

$$\Delta m_{Ag} = \frac{A_{initial} - A_{final}}{\lambda_{Ag-110m}} \frac{aw_{Ag}}{N_A}$$ (Eq. 3-9)
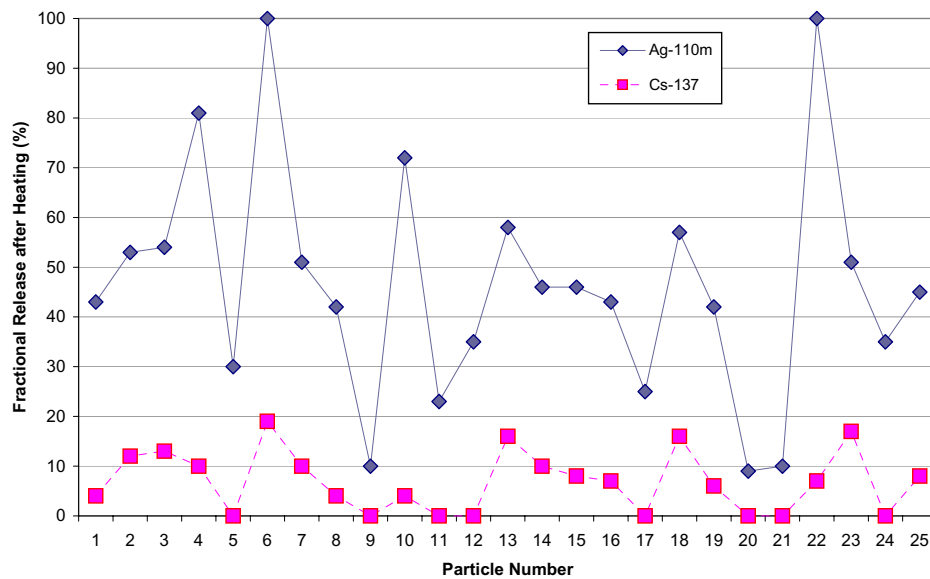
Figure 3-44. Significant variation in fission product fractional release occurs among the 25 heated particles in ACT-3.

The crack diameter in the coated fuel particles was calculated using the same procedure used to calculate the crack diameters from silver mass loss in the diffusion couples. The silver mass loss

was calculated from the change in activity, as shown in Equation (3-9), using the equilibrium silver vapor pressure at the heating temperature and assuming the length of the crack path equal to the SiC thickness. The calculated crack diameters are about 0.2 μm.

The calculated crack diameters for the JAERI ACT-3 coated fuel particles are extremely small. Features of this size would not have been visible during normal post-irradiation examination. Optical microscopy or scanning electron microscopy would likely not have revealed cracks of this order, especially if the crack was not aligned with the cross-sectional plane being viewed.

Crack Size Conclusions

A simple calculation of crack sizes in the silicon carbide layers of the current diffusion couples and typical coated fuel particles using the observed mass loss show that vapor transport through cracks can account for silver release. This explanation allows for some diffusion couples or some fuel particles to lose significant fractions of their silver inventory through cracks while other samples remain intact and retain their inventory. Due to the relatively small size of the estimated cracks, they would be difficult to detect by standard optical microscopy of polished cross-sections.

Other Fission Product Behavior

The previous sections have shown that vapor migration through small cracks in the SiC coating provides a viable mechanism for silver release from both the current diffusion couple experiments and previous typical coated fuel particle tests. The SiC coating, however, also acts as a barrier for other fission products and cracks existing through the SiC coating might also be expected to release some of the other fission products as well. The summary of fission product interactions in the layers of coated fuel particles and the surrounding fuel element materials provides evidence that cracks in the SiC resulting in silver release would not necessarily increase the release of other fission products. Silver vapor migration through SiC cracks is, therefore, a viable explanation for silver release.

Catastrophic failure of the TRISO coatings or through-coating cracks that extend through the IPyC-SiC-OPyC system will certainly result in significant fission product release of both gases and metallic fission products. Minor flaws in a single layer, however, may allow preferential release of only certain fission products. Retention of fission products in layers other than the

SiC layer may prevent release even if cracks are present in the SiC. The role of all of the layers in the coated fuel particle needs to be examined to understand the effect cracks in the SiC layer would have on the overall fission product release.

The key fission products of interest for release and the ones most frequently measured during testing include the fission gases krypton and xenon and the solid fission product cesium. These fission products are discussed below.

Fission Gases

Intact pyrocarbon layers are effectively impermeable to fission gases during normal operating conditions McCardell 1992). The SiC layers also provide holdup of the fission gases, but as long as at least one of the PyC layers remains intact, the particle will retain the fission gases. Therefore, small cracks in the SiC layer that permit the escape of silver will not result in an increased krypton or xenon release as long as the PyC layers remain intact.

Cesium

Many of the layers in a typical coated fuel particle retain cesium better than silver. Therefore, even if cracks are present in the SiC layer, allowing silver release, cesium release may be decreased or delayed due to increased retention in the particle relative to silver.

In general, cesium has been reported to diffuse more slowly than silver out of UO_2 fuel kernels (Martin 1993; IAEA 1997). This increased retention of cesium in the fuel kernel will decrease the amount of fractional release of cesium relative to silver and will also delay the time to breakthrough of cesium relative to silver. Also aiding retention of cesium is the formation of stable compounds in the kernel such as CsMoO (McFarlane 2002).

Although the pyrocarbon layers do not do a great job of retaining the solid fission products compared to the SiC layer, they do provide more retention for cesium than for silver (Martin 1993; IAEA 1997) Additionally, cesium experiences some sorption in the matrix graphite in fuel elements (McCardell et al. 1992;Schenk, Pitzer, and Nabielek 198). Therefore, cesium released from fuel particles into the matrix will be, at least partially, adsorbed onto the graphite. Silver is not retained by any of the PyC layers or the matrix graphite. Where reported, the diffusion coefficients for silver in PyC and matrix graphite are all lower for cesium than for silver, indicating greater cesium retention in those materials.

Greater retention of cesium by PyC layers also means that if cesium does migrate through the SiC layer, even if through cracks as proposed for silver release, additional holdup by the OPyC layer will decrease the amount of cesium released from the fuel particle and will also delay the breakthrough time for cesium relative to that for silver (McCardell et al. 1992).

Concentration profiles measured through fuel particles typically show cesium mainly in the kernel and buffer with steep concentration gradients through the IPyC layer indicating retention in that layer (McCardell et al. 1992). A crack in the SiC will result in silver release, but retention in the PyC layers and matrix graphite will lessen the amount of cesium that escapes.

Crack Formation Possibilities

Although cracks in the SiC coating provide a good explanation for the wide variations in silver release, cracks have not yet been positively identified or observed and remain a hypothesis at this time. However, the formation of microscopic-scale cracks in the SiC coating may not be surprising given the residual stresses remaining in SiC after fabrication and the individual grain behavior during thermal cycling. For the current diffusion couples, an additional stress factor not present in typical coated fuel particles is the seam. The seam is an asymmetrical feature and may promote crack growth around the circumference of the diffusion couples. Additionally, the differential thermal expansion between the graphite substrate shell and the SiC coatings can lead to cracking. Finite element calculations of a typical diffusion couple, neglecting the discontinuity of the seam, indicate that the stress in the diffusion couple could exceed the fracture strength of the SiC due to differential thermal expansion after fabrication, as shown in Figure 3-41.

With the variation in the fission product release data, diffusion does not explain the range of silver release. Further, it is unlikely that one mechanism can describe all observed results. Within a single batch, some particles appear to undergo catastrophic failure, releasing most of their fission product inventories in a short time, while others lose only small fractions, if any at all, over long heat treatments. Crack sizes based on observed silver mass loss from both the current diffusion couples and typical coated fuel particles and from leak testing results on the diffusion couples offer a reasonable and plausible explanation of silver release. Furthermore, this proposed mechanism is also consistent with other fission product behavior in coated fuel particles.

Conclusions

Although silver release from various coated fuel particle designs has been observed for decades, its exact transport path has yet to be identified. One of the goals of the work described in this task was to observe silver diffusion, the assumed mechanism governing silver transport through and release from silicon carbide by measuring characteristic concentration profiles.

Many authors have reported diffusion coefficients to explain silver release observations. These values represent average batch behavior, but do not address the variability within batch populations. Identifying the exact path and cause of silver transport in silicon carbide is hampered by the small feature size of the potential cracks or flaws and the relatively small number of flawed particles.

Key Findings

As stated earlier, the goals of this work were to observe silver diffusion in silicon carbide and to measure the resulting silver concentration profiles. Two different types of experiments with different silver concentration ranges showed no evidence of silver diffusion through silicon carbide. The results of the experiments described in this work indicate that silver release from silicon carbide is dominated by vapor migration through physical cracks.

(1) A reassessment of the literature, detailed in Appendix A, highlights variations in silver release and reported diffusion coefficients in excess of that expected for a grain boundary diffusion mechanism. Although variations in silver release would be expected from a grain boundary diffusive process, diffusion does not account for the variations observed in individual particles and even between batches. The range of diffusion coefficients reported in the literature spans almost 2 orders of magnitude. If the size of that range were the result of differences in exact path length between particles, due to SiC thickness and microstructure, the total path length would have to change by a factor of roughly 13 for an effective path length of 470 μm through a 35 μm thick coating. Silver traveling along SiC grain boundaries, as suggested in the literature, would follow a meandering path through a 35 μm thick SiC layer, but total path lengths on the order of 400-500 μm are not plausible. The population of silver release results reported in the literature is not consistent with solid-state diffusion, either grain boundary or trans-granular.

173

(2) Silver did not diffuse in silicon carbide in ion-implanted samples, even along the abundant grain boundary area in the recrystallized and original SiC. If ion-implanted silver were controlled by a diffusion mechanism, the silver concentration profile would have been completely depleted during heating. No change in the silver concentration profile, however, was observed. Based on the measured silver concentration profiles, the diffusion coefficient for silver in SiC must be less than 5×10^{-21} m^2/ s at 1500°C. The microscopic distribution of silver changed from a fairly homogeneous mixture in amorphous silicon carbide after implantation to discrete precipitates between recrystallized SiC grains after heating. Pockets of unit-activity silver provided ideal sources for diffusion along grain boundaries, but no silver diffusion was observed.

(3) Diffusion did not govern silver release from the spherical diffusion couples. The diffusion couple experiments resulted in a range of silver release from 0% to 100%. Although the silicon carbide coating thickness varied significantly in the diffusion couples (from approximately 40 μm to greater than 100 μm), the release results are not explained by a diffusive mechanism. Furthermore, the diffusion coefficients necessary to account for the silver mass loss from the silver vapor source at the top of the diffusion couples would have had to be about 6 orders of magnitude greater than those reported in the literature. Although the diffusion couple experiments did indeed produce silver mass loss, silver migration was not controlled by diffusion on the scale of that reported in the literature.

(4) Increased helium leak rates after heating prove the presence of cracks in the SiC coating on the diffusion couples. Cracks in the silicon carbide coating could have provided a pathway for silver vapor escape. Crack sizes in the diffusion couples calculated from simplified vapor flow models are on the order of 1-10 μm. Features of this dimension would not likely have been observed during analysis due to their small size and random orientation within the sample.

(5) Vapor migration through cracks is proposed to dominate silver release from silicon carbide. Only silver vapor had access to the SiC coating, via migration through the graphite porosity, during heating. Molten silver, at the bottom of the diffusion couples, did not penetrate the graphite shell and, therefore, could not have resulted in silver release. A vapor migration mechanism is consistent with the results and observations of the current experimental program and is also consistent with results and observations reported in the literature. Vapor

migration through mechanical cracks explains why some particles, those with cracks, release large fractions of their silver inventories while other particles, those without cracks, retain all of their silver. Diffusion cannot account for this broad variation in fractional release results. Given the properties of the other coated fuel particle layers, vapor migration is also consistent with other observed fission product behavior. The presence of small cracks in the SiC layer will not result in large releases for other fission products, for example cesium and krypton, due to their retention in the other layers. The PyC layers retain krypton, xenon, and the noble fission gases; as long as either the IPyC or the OPyC is intact, the noble fission gases will be retained in the particle, even if the SiC layer is damaged. Although the SiC improves cesium retention (relative to the PyC layers), the graphite materials, both within and surrounding the fuel particles, aid in retention. Therefore, cesium release through SiC cracks will be lower than silver release.

3.2 Task Technical Overview- INEEL

Introduction

The purpose of this section is to document INEEL's work to date on fission product modeling in TRISO coated particle fuel. An understanding of fission product transport in the coated particle is a key component of the ultimate source term for the very high temperature gas cooled reactor. In addition, modeling fission product transport in the fuel element matrix and reactor graphite will eventually be needed.

The classical gas reactor coated-particle fuel is a spherical layered composite of microscopic dimensions. It has a fissile fuel kernel, generally made of UO_2 or UC_2, or UCO, that is surrounded by a porous graphite buffer layer that absorbs radiation damage, allows space for fission gases produced during irradiation, and resists kernel migration at high temperature. Surrounding the buffer layer is a layer of dense pyrolytic carbon, a SiC layer, and a dense outer pyrolytic carbon layers. The pyrolytic carbon layers act to protect the SiC layer, which is the primary pressure boundary for the micro-sphere. The inner pyrolytic carbon layer also protects the kernel from corrosive gases that are present during the deposition of the SiC layer. This layer arrangement is known as the TRISO coating system. Each micro-sphere acts as a mini pressure vessel, a feature that is intended to impart robustness to the gas reactor fuel system.

The TRISO-coated particle fuel is a complicated fuel form from the perspective of fission product modeling. The multiple layers, the chemical state of the fission products, the different transport mechanisms responsible for gaseous and metallic fission product transport in each layer, and the projected high burnups and fast neutron fluences make the modeling of fission product transport challenging. The following sections will discuss fission product transport in the TRISO-coated particle fuel layer by layer. Each section includes a review of the existing database for transport in the layer, discusses potential mechanisms responsible for the transport, and presents results of preliminary scoping calculations for the transport in the layer. A simplified integrated transport model is presented and some simple sensitivity results are discussed. Preliminary benchmarking of a more sophisticated fission product transport model is also discussed. This is followed by a summary of the findings.

The Kernel

Fission product transport in the kernel is complicated. Important mechanisms include recoil, diffusion of fission products to grain boundaries, vaporization and transport through the

interconnected porosity of the kernel to the surface of the kernel and chemical reaction at the boundary of the fissile kernel. These processes are functions of burnup and temperature and thus change over the life of the fuel.

Recoil

Recoil from the kernel can be estimated using the following equation:

$$(RF)_{recoil} = 0.25 \, [r_k^3 - (r_k - d)^3]/r_k^3$$

where r_k is the radius of the fuel kernel and d is the average fission fragment range. The average fission fragment ranges are calculated for a given fuel composition from compiled experimental data [1]. Based on fission energies of 107 MeV for krypton and 72 MeV for xenon, the average krypton range is 5.8 microns and the average xenon range is 4.1 microns in UO_2 with a density of 10.5 g/cm^3. Thus, for a 500 micron kernel, the recoil release fraction is ~ 1.5%. For a 350 micron kernel, the recoil release fraction is ~2%.

Short-lived Fission Gas Release Rate to Birth Rate (R/B) Ratio

A model has been developed to account for the release rate to birth rate (R/B) of short-lived gaseous fission products from failed particles and from uranium contamination in the fuel element matrix (compact or sphere). This is expressed for gas specie i as:

$$(R/B)_i = f_{fail} \, (R/B)_{fail,i} + f_{U-contamination} \, (R/B)_{U-contamination,i}$$

where

       f_{fail} = particle failure fraction
       $(R/B)_{fail,i}$ = release rate to birth rate ratio per particle failure for gas specie i
       $f_{U-contamination}$ = uranium contamination fraction
       $(R/B)_{U-contamination,i}$ = release to birth rate for gas specie i due to U contamination.

The (R/B) correlations are based upon the widely used Booth equivalent sphere gas release model. These correlations may be generally expressed as[2]:

$$(R/B) = (3/x) \, [\, coth(x) - (1/x) \,]$$

U. Littmark and J. F. Ziegler, "Handbook of Range Distributions for Energetic Ions in All Elements," Pergamon Press, 1980.

D.R. Olander, "Fundamental Aspects of Nuclear Recator Fuel Elements", ERDA, TID-26711-P1, 1976.

where

$$x = [(\lambda a^2) / D]^{1/2}$$

λ = decay constant = $\ln 2 / T_{1/2}$ (s^{-1})

$T_{1/2}$ = isotope half life (s)

$D/a^2 = D' $ = reduced diffusion coefficient (s^{-1})

a = radius of equivalent sphere (m)

$$coth(x) = [exp(x) + exp(-x)] / [exp(x) - exp(-x)].$$

The equivalent sphere radius, a, is equal to the kernel radius when considering (R/B) for failed particles and is proportional to the raw graphite grain size of the matrix when considering (R/B) from uranium contamination.

Several correlations for reduced diffusion coefficients to be used in (R/B) calculations exist in the literature (IAEA 1997). A few of the more prominent correlations were selected for evaluation before incorporation into the PARFUME code. These included:The U.S. Model (Martin 1993) which contains a unique reduced diffusion coefficient correlation and also differs from the classic Booth Equivalent Sphere formalism presented above in that it contains a diffusion parameter, multiplicative temperature and burnup functions and empirical factor. The British Model (IAEA 1997) that incorporates intrinsic diffusion, vacancy diffusion and athermal diffusion (a function of fission rate density) terms in its reduced diffusion coefficient. The German I and II Models (Nabielek 1991, 2002) that incorporate two separate sets of reduced diffusion coefficients dependent upon temperature only.

A comparison of the four models for Kr-85m (R/B) per failed particle is presented in Figure 3-45. Input parameters for this comparative calculation are representative of fuel irradiated in the NPR-1A experiment. On-line gas release measurements from the experiment indicated that Kr-85m (R/B) per failed particle was 0.028 at a time-average volume-average temperature of 977 ºC (Maki et al. 2002). This experimental value compares almost exactly with the calculated German II value of 0.029.
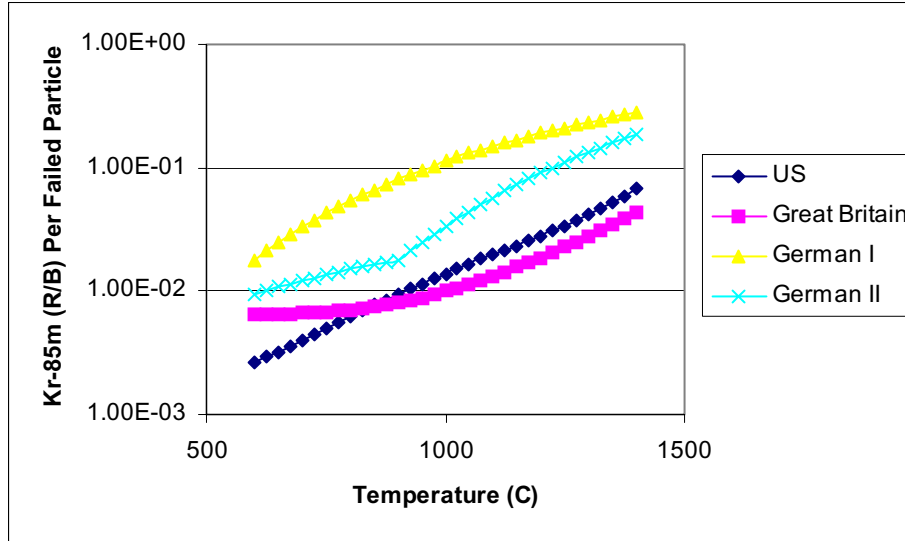
Figure 3-45. Comparison of (R/B) model results.

Considering its adherence to first principals, lack of ad hoc data fitting "fixes", and agreement to experimental data, the German II reduced diffusion coefficient correlation was chosen for use in the PARFUME code. Thus, the following reduced diffusion coefficients are currently used in PARFUME:

When considering $(R/B)_{\text{U-contamination,I}}$ (Röllig 2001).

$$D' = 3.0 \times 10^{-5} \exp[-1.06 \times 10^{5} / (8.314) \, T \,] \; (s^{-1}) \; \text{ for krypton isotopes}$$
$$D' = 1.7 \times 10^{-7} \exp[-7.86 \times 10^{4} / (8.314) \, T \,] \; (s^{-1}) \; \text{ for xenon isotopes}$$

where

$\quad$ T = temperature in degrees K.

When considering $(R/B)_{\text{fail,i}}$ for krypton and xenon isotopes (Nabielek 1991, 2002),

$$D' = (500/d)^{2} \, 10^{[-7.97 - (1920 / T)]} \quad \text{for } T < 1173 \text{ K}$$
$$D' = (500/d)^{2} \, 10^{[-2.60 - (8220 / T)]} \quad \text{for } T \geq 1173 \text{ K}$$

where

$\quad$ d = kernel diameter in μm.

Decay constants, with the corresponding half lives, for the isotopes considered in PARFUME are presented in Table 3-12.

Table 3-12. Decay constants used in PARFUME.

Isotope	Half Life	Decay Constant (s^{-1})
Kr-85m	4.48 h	4.298 x 10^{-5}
Kr-87	76 m	1.520 x 10^{-4}
Kr-88	2.84 h	6.780 x 10^{-5}
Kr-89	3.16 m	3.656 x 10^{-3}
Kr-90	32.3 s	2.146 x 10^{-2}
Xe-131m	11.92 d	6.730 x 10^{-7}
Xe-133	5.25 d	1.528 x 10^{-6}
Xe-135m	15.3 m	7.551 x 10^{-4}
Xe-135	9.10 h	2.116 x 10^{-5}
Xe-137	3.84 m	3.008 x 10^{-3}
Xe-138	14.1 m	8.193 x 10^{-4}
Xe-139	40 s	1.733 x 10^{-2}

Booth Equivalent Sphere Diffusion

The conventional release process of long-lived fission product diffusion through grains to the grain boundaries and subsequent transport through the interconnected porosity is a mechanism that has been studied extensively in the context of light water reactor fuel behavior. The Booth equivalent sphere diffusion model has been used to estimate the release of fission gases via these mechanisms and has been used in the gas reactor community to describe fission product release from the kernel. The release fraction is given by (Booth 1957):

$$FR = 1-(\frac{6}{D't})\sum_{n=1}^{\infty}[1-\exp(-n^2\pi^2D't]/[n^4\pi^4]$$

where D' is the reduced diffusivity which is equal to D/a^2. The two key parameters in the model is a, the effective radius for diffusion, and D the diffusion coefficient. The formulation for diffusion coefficients by Turnbull, which accounts for intrinsic, athermal and radiation-enhanced diffusion, is believed to be the most accurate for UO$_2$ (Turnbull 1982). The definition of the effective radius is usually taken to be the grain size of the UO$_2$.

There are several limitations with the Booth model:

- The original Booth model was used to describe gas release from a fuel grain and not a fuel kernel or fuel pellet per se where the gas phase transport in the interconnected porosity is also important.

- The use of the Booth model makes it difficult to capture the effect of burnup on the microstructural changes in the kernel and the subsequent impact on release.

- The release of some of the metallic fission products, which tend to form nodules along grain boundaries in the fuel (e.g., Ru, Mo, Tc, Pd), is not governed by this classic diffusion mechanism.

Despite these shortcomings, many researchers have correlated or "force-fitted" release measurements to an effective Booth model. For coated particle fuels, effective diffusivities exist for the fission gases and some fission metals like cesium, silver and strontium. The effects of changes in the microstructure with burnup are not directly accounted for but are implicit in the values used for D and a. Figure 3-46 is a plot of the values of D measured on UO_2 coated particles by the Germans (assuming a = 250 μm) (IAEA 1997) and form the baseline to be used for scoping analysis presented here. No diffusivity data exist for the more noble fission metals like Ru, Mo, Tc, and Pd. Similar data do not exist for UCO and thus UO_2 values are used in the interim. Plans exist to measure these parameters in UCO fuel in the DOE Advanced Gas Reactor Fuel Development and Qualification Program (Oak Ridge National Laboratory 2003).
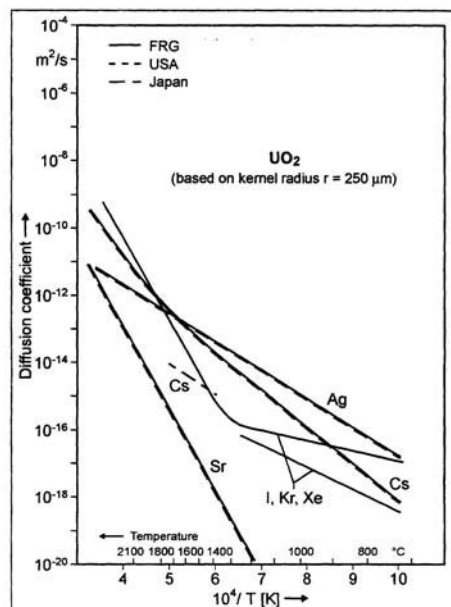
Fig. A-1: Diffusion coefficients of fission product species in UO_2 as function of temperature

438

Figure 3-46. Comparison of diffusivities of fission gases and some fission metals in UO_2 kernels of coated particle fuel (IAEA, 1997).

Scoping Calculations

This simple effective Booth model has been used with the measured diffusivities for UO_2 fuel to determine the impact of time and temperature on the release of fission gas, cesium, silver and strontium from a 500-μm UO_2 kernel. Three specific calculations have been performed:

- A three-year 900°C irradiation, typical of the average exposure of a UO_2 coated particle in a prismatic reactor
- A three-year 1200°C irradiation, typical of the peak exposure of a UO_2 coated particle in a prismatic reactor
- A ten-cycle three-year 600 to 1200°C cyclic exposure typical of peak exposure of a UO_2 coated particle in a pebble bed reactor.

The resultant fission product releases are shown in Figures 3-47, 3-48, and 3-49. The results indicate that the release is dominated by the time at high temperature.
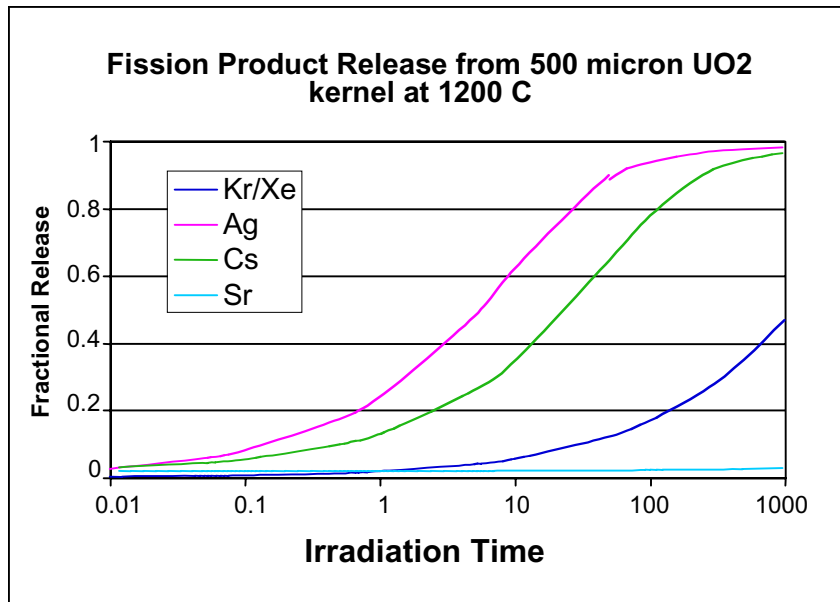
Figure 3-47. Fission product release from 500 μm UO_2 kernel at 900°C.
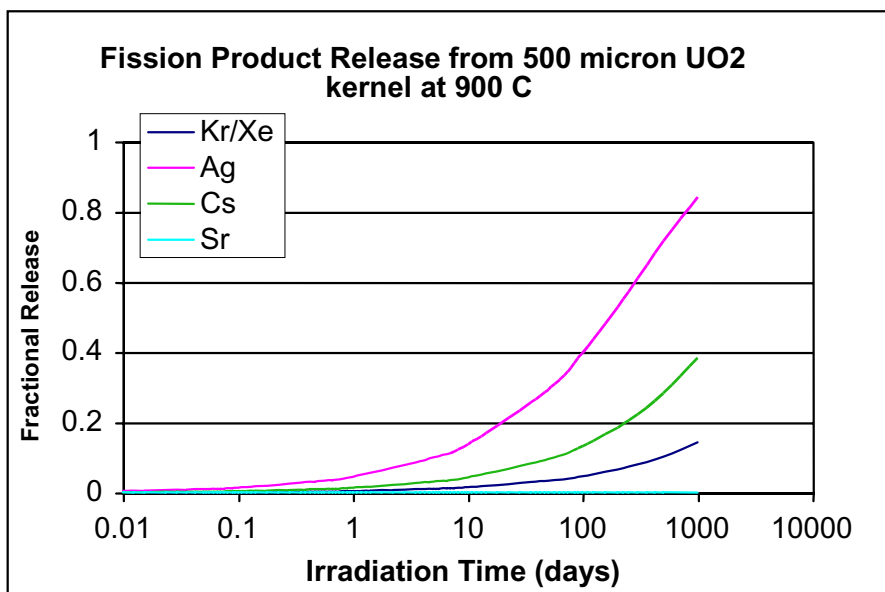
Figure 3-48. Fission product release from 500 μm UO_2 kernel at 1200°C.
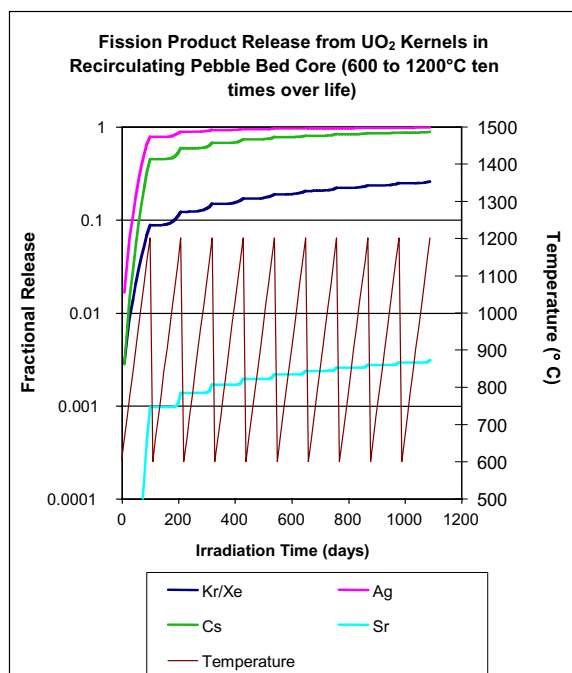
Figure 3-49. Influence of cyclic temperature in a pebble bed reactor on fission product release from a 500 μm UO_2 kernel.

The Buffer

The buffer plays an interesting role in the coated particle from the perspective of fission product transport. Depending on the specific irradiation conditions, the nature of the shrinkage and densification of the buffer establishes the initial condition for fission product transport during irradiation and under accident conditions. The buffer is a porous carbon layer (~50% dense initially) whose function is to serve as a void volume for fission gases and act a material to absorb fission recoils and swelling of the fuel kernel. Sometimes the buffer can crack because of tangential stresses developed under irradiation. Because of the high porosity of the layer, it has the lowest conductivity of any layer in the coated particle and thus the largest temperature drop. Depending on the power produced in the kernel, the temperature gradient in the buffer can be quite large, which may cause thermal (or Soret) diffusion in the layer.

Behavior of the buffer

For a first approximation we assume that the outer boundary temperature of the fuel particle is uniform and calculate the internal temperature distribution using a simple one-dimensional heat conduction model. In a spherical fuel kernel with uniform heat generation rate, q_f''' (W/m^3), the steady state temperature rise is given by

$$T_o - T_1 = - q_f''' \, r_1^2/6k_f,$$

where $T_o = T(0)$, $T_1 = T(r_1)$, r_1 = fuel kernel radius, and k_f = fuel kernel thermal conductivity. Ignoring heat generated in the buffer, the buffer temperature drop is given by:

$$T_1 - T_2 = q_f \, (r_2\text{-}r_1)/4\pi k_c r_1 r_2$$

where r_2 = buffer outer radius, k_c = thermal conductivity of the buffer, and $q_f = (4/3) \, \pi r_1^3 q_f''' =$ thermal power generated in the fuel kernel. Assuming no gaps develop between layers which can cause large temperature drops, similar equations apply to the temperature drops across other layers (IPyC, SiC, OPyC).

Table 3-13 presents the calculated temperature drop across each layer, and the layer's associated thermal properties for an average particle that generates ~ 62 mW of power, which is the average power per particle in a pebble bed modular reactor core (PBMR). Thus, for an average particle, the ~ 10 K temperature drop across the buffer translates into ~ 1000 K/cm gradient across the layer.

Figure 3-50 plots the thermal gradient and the temperature drop that can develop across the buffer as a function of the power per particle for a 500 micron UO_2 German coated particle. As the power increases, significant thermal gradients can develop. These thermal gradients lead to increasing thermal stresses in the layer. The resulting stresses in the buffer due to thermal gradients and densification, if high enough, could cause cracking of the buffer. Furthermore, high thermal gradients across the buffer ($> \sim 1000$ K/mm) can drive thermal diffusion (Soret effect) of fission products across the layer.

Table 3-13. Temperature drops across layers of a coated particle.

	Outer radius, μm	k, W/m-K	ρ, kg/m^3	C_p, J/kg-K	ΔT, K layer
UO_2	$r_1 = 250$	2.52	10960	332	3.92
Buffer (50% dense graphite)	$r_2 = 345$	0.5	1100	1.5	10.88
IPyC	$r_3 = 385$	4.0	1700	1.5	0.372
SiC	$r_4 = 420$	13.9	3200	0.50	0.077
OPyC	$r_5 = 460$	4.0	1700	1.5	0.261
				Total ΔT =	15.5
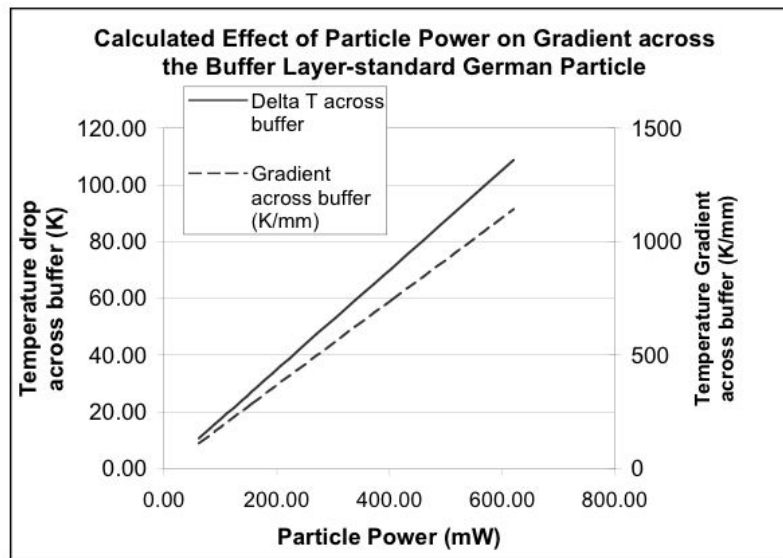
Figure 3-50. Effect of particle power on gradient across the buffer layer of a standard 500-μm UO_2 German particle.

Figure 3-51 is a photomontage of different fuel particles that have been irradiated under different power conditions. As shown in the figure, as the irradiation is accelerated the power being produced in the particle is increased and the state of the buffer changes. The German LEU UO$_2$ particle from AVR shows very little change in the buffer after irradiation probably because of the low power being produced (the exact power history is not well know given the nature of pebble bed refueling). The LEU UCO particle irradiated in the HRB-14 irradiation shows a typical cracked buffer. These cracks can act as fast paths for fission product transport. The particle in HRB-15A is an example of severe cracking of the buffer. The NPR-2 HEU UCO particle was accelerated a factor of 10 from that expected in a gas reactor. There is significant densification of the buffer on one side of the particle as the buffer shrank during the irradiation.
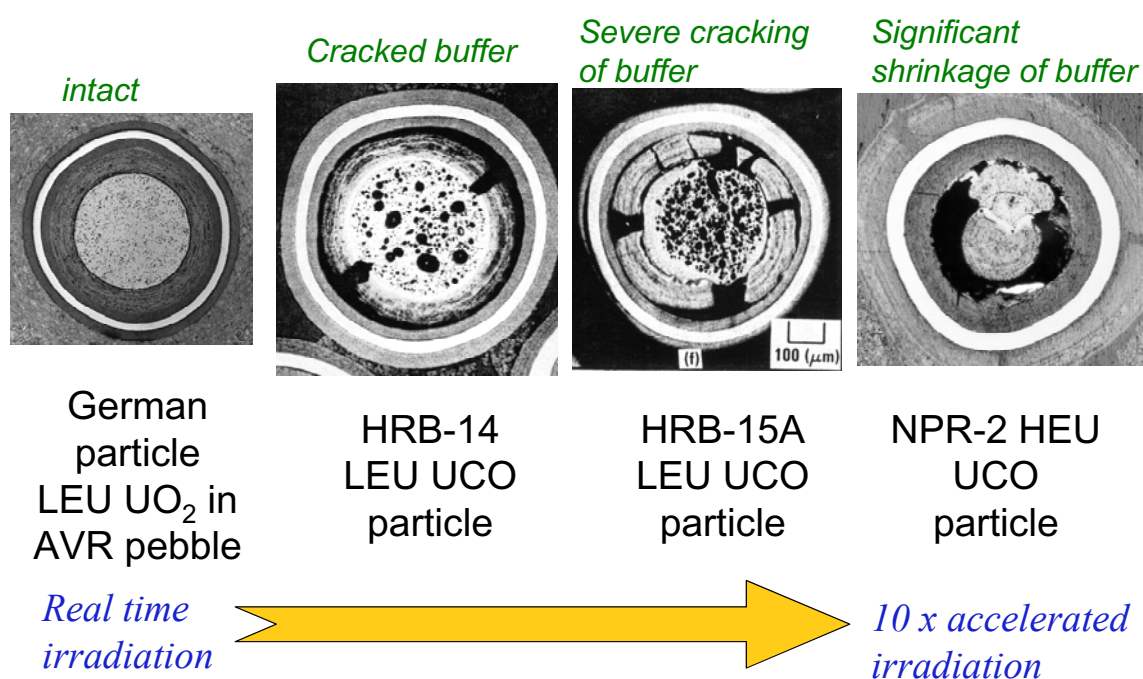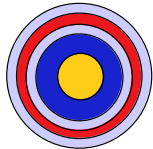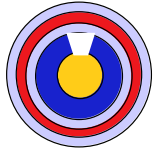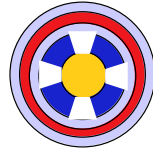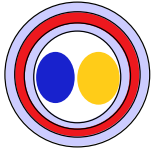
Figure 3-51. Different states of the buffer in coated particles following irradiation.

Table 3-14 schematically presents this evolution of the buffer as it scales with particle power. The table describes possible locations where such powers might be found in a pebble bed reactor, in a prismatic gas reactor core or in an irradiation. In addition, the thermal gradient that develops across the buffer of a 500-μm UO$_2$ kernel has been estimated and some comments about the condition of the buffer are provided. (Note that the thermal gradients for a 350-μm

kernel in a prismatic core would be about double that shown here for the same power level because of the smaller kernel size).

Table 3-14. Particle power considerations on the condition of the buffer in coated particle fuel.

Description or location	PBMR low flux region; GT-MHR average	PBMR average	PBMR pebble and prismatic compact peak	Current prismatic irradiation limit	Very accelerated irradiations
Particle Power	25 to 40 mW	60 mW	100 mW	400 mW	500 to 5000 mW
Thermal gradient Across buffer (for 500 micron)	< 50 K/mm	~ 100 K/mm	~ 250 K/mm	~ 750 K/mm	~ 900 to 9000 K/mm
Condition of buffer	Uniform shrinkage		Moderate tensile stress - some cracking	High tensile stress - many cracks	Excessive shrinkage; buffer and fuel side by side

Finite element studies have also been performed to evaluate the effects of a thermal gradient across the buffer, irradiation induced shrinkage and restraints on deformation of the buffer. The condition of the buffer is an important initial condition for fission product transport modeling. It was determined that a thermal gradient alone does not impose significant thermal stresses in the buffer. Calculations showed that any significant stresses in the buffer were caused by irradiation-induced shrinkage of the buffer while the buffer is bonded to the IPyC layer. These stresses are easily large enough to cause cracking of the buffer. Cracks would likely develop first at the inner surface of the buffer, since this is the location of maximum tensile stresses.

Deformation of the buffer is controlled primarily by the irradiation-induced shrinkage of the layer, and boundary conditions acting on the layer. As shown in Figure 3-9, the buffer shrinks away from the IPyC during irradiation when the buffer is free from any restraint. In this calculation, a temperature gradient of 500 °C was imposed across the thickness of the buffer (An

extreme case to determine any sensitivity). The presence of radial cracks at various locations along the inner surface (extending halfway through the thickness of the buffer) had essentially no effect on this deformation. However, when a restraint (in direction *1*) was imposed at the midsection of the buffer, the buffer kinked inward at the restraint location (Figure 3-52). Removing the 500 °C gradient across the buffer had little effect on this deformation (Figure 3-53), showing that the deformation of the buffer was controlled more by irradiation-induced shrinkage than the thermal gradient. The results suggest that lateral restraint imposed by the presence of the kernel and irradiation induced shrinkage of the buffer has the greatest effect on deformation of the buffer under irradiation.
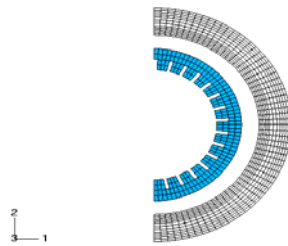
Figure 3-52. Deformation of buffer when radial cracks are present on its inner surface.
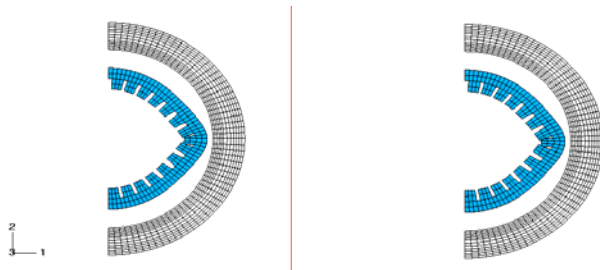
Figure 3-53. Deformation of buffer when lateral restraint is applied.

Transport in a porous medium

Given the large interconnected porosity in the buffer, we have examined the transport of gases in a porous medium to describe the behavior of fission gases and vapors in the layer. Pressure driven diffusion has been well studied in porous mediums and References (Kast and Hohenthanner 2000) and (Mason and Malinaukas 1983) provide a comprehensive overview of the subject. In all cases, the molar flux of material through the porous medium is a function of the pressure gradient across the material. Three different regimes are traditionally considered depending on the mean free path of the gas relative to the characteristic size in the medium, or the Knudsen number ($Kn = \lambda/d_{pore}$, where λ is the mean free path). Characteristic sizes could range from nanopores in a material like an as fabricated buffer to microcracks as might be typical of a cracked buffer.

For Kn >1, the mass transport behavior is described using free molecular flow and the molar flux is given by:

$$\dot{N}_{Kn} = -\frac{D_{Kn}}{RT}\frac{\varepsilon_p}{\mu_{p,Kn}}\nabla p$$

$$D_{Kn} = (4/3)\bar{d}_{pore}\sqrt{RT/2\pi M}$$

where:

D_{Kn} = the Knuden diffusivity,

d_{pore} = the average pore size in the medium,

ε_p = the porosity of the medium

$\mu_{p,Kn}$ = the tortuosity

M = the molecular weight of the gas

R = gas constant

T = absolute temperature.

In the transition region, $0.01 < Kn < 1$, both viscous flow and diffusive flow must be considered. They are summed to determine the overall molar flux. Hence:

$$\dot{N} = \dot{N}_{vis} + \dot{N}_{diff}$$

$$\dot{N}_{diff} = -\frac{D_{Eff}}{RT}\frac{\varepsilon_p}{\mu_{p,Kn}}\nabla p$$

$$D_{Eff} = \left[\frac{1}{D_{Kn}} + \frac{1}{D_{12,gas}}\right]^{-1}$$

$$D_{Kn} = (4/3)\bar{d}_{pore}\sqrt{RT/2\pi M}$$

$$D_{12,gas} = Chapman - Eskong - Theory$$

$$\dot{N}_{visc} = -\frac{k\bar{p}}{\eta RT}\nabla p$$

Note that the diffusive flux has the same form as in the free molecular flow regime but the diffusivity is an effective diffusivity that considers the effects of Knudsen flow and traditional gas phase mass transport as given by Chapman Eskong Theory (Bird, Stewart, and Lightfoot 1960) in series. The viscous diffusion term depends on the pressure gradient as well as the viscosity of the gas, η, the average pressure of the system, $\bar{p}$, and the apparent permeability of the material, k.

In the continuum region, where $Kn < 0.01$, the contribution from viscous flow and diffusive flow are summed to determine the overall molar flux. However in this case, molecular flow effects are very small and the diffusive term takes on traditional form with the diffusivity equal to the traditional gas phase mass transport value as given by Chapman-Eskong Theory. Thus:

$$\dot{N} = \dot{N}_{vis} + \dot{N}_{diff}$$

$$\dot{N}_{diff} = -\frac{D_{12,gas}}{RT}\frac{\varepsilon_p}{\mu_{p,Dif}}\nabla p$$

These equations have been used to estimate effective diffusivities as a function of pore or crack size. We have selected Kr gas at 1000 and 1600°C to be representative of normal operation and accidents. We have also considered the effect of pressure ranging from 0.5 MPa to 25 MPa,

values that are representative of the range of the internal pressure in a particle over its life. Figure 3-54 plots the effective diffusivities at 1000 and 1600°C respectively. The results suggest that gas pressure is only important for characteristic sizes greater than ~ 0.02 μm. Furthermore, comparison of the two figures suggests that the influence of temperature is moderate at best. The most important effect is that of the characteristic size of the transport path in the medium. For nanopores, effective diffusitivies are on the order of 3 to 5 x 10^{-7} m^2/s. By contrast, transport through micropores or micron sized cracks is much faster, with effective diffusivities ranging between 10^{-4} and 10^{-2} m^2/s depending on the pressure of the gas involved. Although the actual pore size in the buffer is not well known, these results suggest that rapid transport of fission gases and fission product vapors could be expected through the buffer layer in a coated particle. However, to use the model completely to calculate the molar flux, the porosity and tortuosity of the buffer need to be known or estimated. By way of comparison, the Germans assumed the diffusivity of all species in the buffer was 10^{-8} m^2/s and the U.S. used a value of 10^{-10} m^2/s in their evaluations.
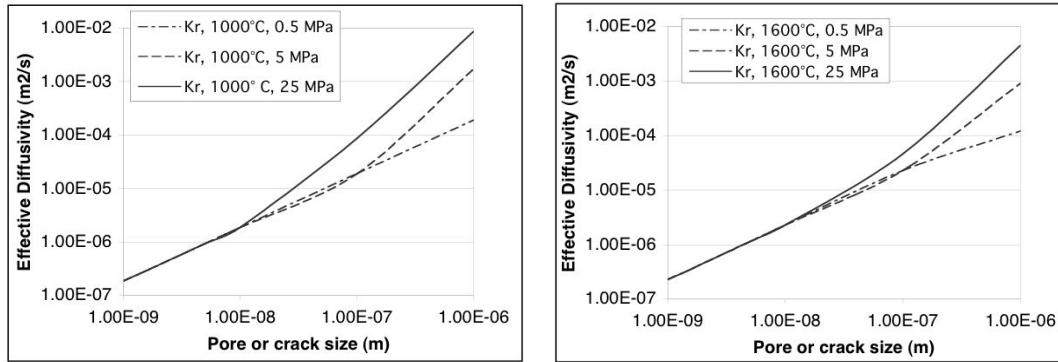
Figure 3-54. Effective diffusivities for Knudsen and viscous diffusion.

Thermal Diffusion

The large thermal gradients in the buffer can lead to thermal diffusion, which must be added to the traditional concentration driven Fickian diffusion across the layer. The diffusive flux can then be written as:

$$J = -D(\nabla C + \frac{C_s Q^*}{RT^2}\nabla T)$$

191

This second term on the right hand side of the equation is the thermal diffusion component, or Soret effect. Most of the literature dealing with thermal diffusion (the Soret effect) relates to gases or liquids. There are a few references dealing with solids. The heats of transport, Q*, for the buffer and condensable fission product material combinations are unknown but values of Q* range from about –210 kJ/mol to + 50 kJ/mol for various material combinations in the literature (Korte, Janek, and Tmm 1997; Hofman, Hayes, and Petri 1996; Kleykamp and Heiko 2001). This corresponds to values of Q*/R from –25,000 K to + 6,000 K. We have considered a value of + 20,000 K, to determine an upper bound on fission product transport through the buffer layer in the presence of a temperature gradient.

To scope out the influence of irradiation and thermal gradient diffusion on the potential release of fission products, we have modeled the kernel and each layer of the coated fuel particle using a one-dimensional diffusional transport code called TMAP4 (Longhurst et al. 1998). We have used cesium as the fission product but clearly we could have used any other fission product of interest. Given the power per particle and the irradiation temperature, the model calculates the temperature of each material constituent in the coated particle. Based on the power level and time (burnup), the fission product generation is input to the code. Using the diffusivity of cesium in the kernel and each of the layers in the TRISO coating from the German experience (IAEA 1997), a diffusivity of 10^{-7} m^2/s in the buffer layer and a value of Q*/R of 20000 K, we then calculate the transport of fission products from the kernel and into the coatings under a user specified irradiation history and a subsequent 500 hour heating at 1600°C to simulate a traditional German heating test. Figure 3-55 summarizes the result of these calculations. Plotted is the fraction of cesium in the OPyC layer at the end of the irradiation and the fraction of cesium released from the particle at both the end of irradiation and the end of the 500-hour high temperature heating for different particle powers. Two different irradiation conditions are considered: a three year constant irradiation at 1225°C and a 10-cycle 3-year pebble bed irradiation where the fuel experiences a change in temperature from 600 to 1200°C ten times over its three year life, as illustrated in Figure 3-55.
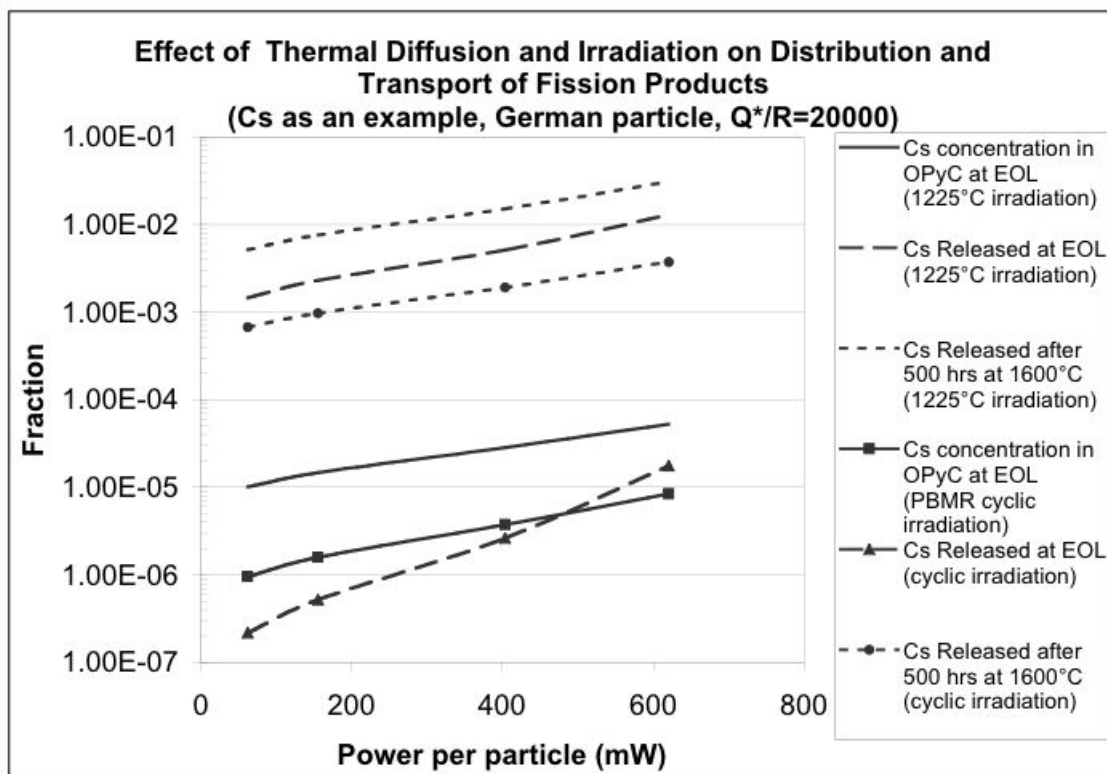
Figure 3-55. Effect of thermal diffusion and irradiation on the distribution and transport of fission products in the coated particle.

The results indicate that the cyclic irradiation has a strong influence on the distribution and transport of fission product cesium. The model predicts an order of magnitude more cesium reaching the OPyC layer in the case of the 3-year constant irradiation at 1225°C than in the case of cyclic irradiation, and three to fours orders of magnitude more cesium released from the particle at the end of irradiation in the case of constant irradiation at 1225°C than in the case of cyclic irradiation. After the 500-hour high temperature heating, the cesium release from the particle is an order of magnitude greater in the case of constant irradiation at 1225°C than in the case of cyclic irradiation. Given the diffusional transport and the strong effect of temperature on diffusivities this is hardly surprising.

The results also indicate that thermal diffusion (Soret effect) can have a moderate influence on the transport and distribution of fission products. A factor of ten increase in power per particle (from 60 mW to 600 mW) increases the concentration of cesium in the OPyC and the fraction of cesium released after irradiation and after high temperature heating by factors of 5 to 10.

193

These results illustrate the important role that irradiation history has on the distribution of fission products in the coated particle and the potential release under normal operation and accident conditions. The irradiation effects have a large impact on the fission product behavior in the accident because the initial conditions are different. However, given the low power/thermal gradients in German pebbles and the low level of acceleration in most German irradiations (Petti et al. 2003), thermal diffusion is not considered to be very important in modeling of fission product release, even with the potentially high value of Q*/R that was used in these calculations. Only in cases where the irradiations are very accelerated as has occurred in U.S. fuel in the past would thermal diffusion be important.

The Pyrocarbon Layers

Pyrocarbon is a dense layered carbon structure. The goal is to make the pyrocarbon as isotropic as possible during the deposition to ensure the best radiation stability of the layer. Some data exist on effective diffusivities in the PyC layers. Measured values from BISO particles (without SiC) have been collected and the results shown in Figure 3-56 (IAEA 1997). These data suggest that the dense pyrocarbon layer is a very good barrier to noble gas release with significant diffusional releases not observed until temperatures near 2000°C are reached. The PyC layers do not pose significant barriers to release of cesium, silver and strontium under normal or accident conditions.

The mechanism for the transport of gaseous and metallic fission products in the PyC layer has not been the subject of significant study in the world gas reactor community. A complete understanding of the mechanism responsible for noble gas transport in PyC is somewhat lacking. A comparison of different measurements and calculations are overlaid on the original diffusivity data in Figure 3-57.
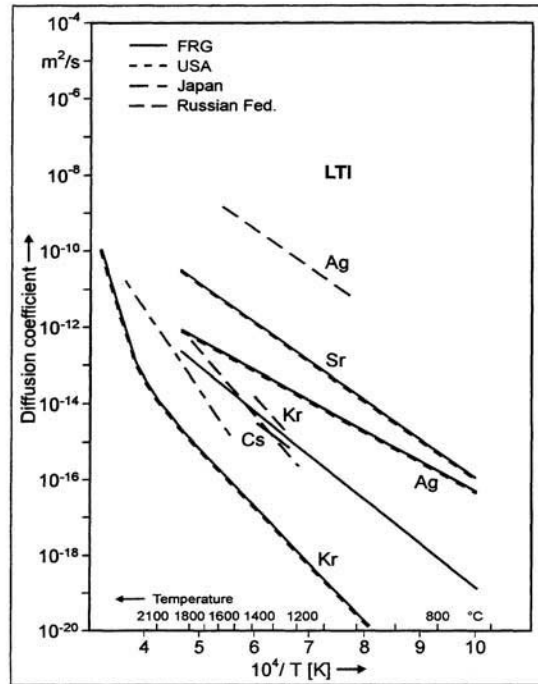
Fig. A-2: Diffusion coefficients of fission product species in LTI pyrocarbon as function of temperature

441

Figure 3-56. Fission product diffusivities in PyC.

Gas Phase Transport

The measured diffusion coefficients suggest very slow transport through the layer. Permeability measurements using He and CO (Braun et al. 1980) indicated by the red box in Figure 3-57, suggest very slow transport of these gases consistent with the measured fission product diffusivity. By contrast, diffusion predicted by the Knudsen diffusion model in for nano-porosity or viscous diffusion for micro-porosity (the yellow and blue boxes respectively) if applied to the PyC layer would predict transport rates that are 6 to 10 orders of magnitude faster than the measured data on BISO particles. These results suggest either (a) Knudsen diffusion of noble gases is extremely small in PyC perhaps because the interconnected porosity is very low or (b) that Knudsen diffusion is not the mechanism responsible for noble gas transport in PyC.

195

Figure 3-57. Fission product diffusivities in PyC compared with permeability data (red vertical box) and Knudsen (blue horizontal box) and viscous (yellow horizontal box) diffusion estimates.

Metallic Fission Product Transport and Trapping

For some of the fission metals like cesium and strontium and even iodine, it is valuable to examine literature related to battery storage where alkali and alkali earth elements and even bromine and carbon monoxide have been intercalated in graphitic materials (Mathur et al. 1996; Hollerman et al.1995; Palnichenko and Tanuma 1996; Levi and Aurbach 1999). Intercalation, the insertion of guest atoms into a host structure, has been studied extensively and a diffusion and trapping mechanism has been proposed as the mechanism responsible for the resultant transport behavior in the material (Bisquert and Bikhrenko 2002). Thus it is fair to expect

intercalation to be the mechanism responsible for the transport of Cs, Sr and perhaps even iodine and CO in the PyC. A classic diffusion and trapping model has been proposed for modeling the transport, with trapping occurring perhaps at the carbon crystallite edges and defects in the graphitic material.

Diffusion and trapping is modeled using a simple modification to classical Fickian diffusion as shown in the following equations (Longhurst et al. 1998).

$$\frac{\partial C}{\partial t} = D\nabla^2 C - \frac{\partial C_T}{\partial t}$$

$$\frac{\partial C_T}{\partial t} = w\frac{x_T}{N}C - rC_T$$

$$x_T = x_T^o - C_T$$

Trapping acts as impedance to diffusion. Many times a concentration dependence of diffusivity is observed, which is an indication that trapping is involved. As the traps get filled at high atom concentrations in the material, the observed transport increases. Thus, one can also write an expression for an apparent diffusivity as follows (Olander 1976):

$$D_{app} = \frac{D}{(1+\frac{wx_T}{rN})} = \frac{D}{(1+\frac{D_o}{\lambda^2 v_o}\exp(\frac{E_{trap}-E_{diff}}{kT})\frac{x_T}{N})}$$

Where:

D = diffusivity (m^2/s)

w = trapping rate(/s)

r = resolution or release rate from the trap(/s)

λ = jump distance (m)

v_o = Debye frequency (/s)

X_T = empty trap density (atoms/m^3)

E_{trap} = trap energy (ev)

E_{diff} = diffusion constant activation energy (ev)

N = number density of host material (atoms/m^3)

An initial concentration of traps is assumed to exist in the material and a mass balance on the traps is performed to determine when all of the trapping sites are occupied. To model the behavior in detail, the trap concentration or trap density is required as well as the energy of the trap, which is important to model release from the traps accurately. Irradiation is known to result in the production of traps via defect formation and thus can complicate this picture somewhat.

A few simple parametric and sensitivity calculations can be used to understand the magnitude and importance in PyC layers of TRISO-coated particle fuel. Figure 3-58 plots the diffusion coefficient of Cs in PyC[3] and SiC along with the apparent Cs diffusion coefficient in PyC for different trap concentration levels from 10 to 5000 ppm using the measured 4 ev trap energy for graphite.

The transport through the TRISO coating will then be controlled by the lowest diffusivity in the figure. Under accident conditions, the SiC diffusivity is the lowest suggesting it is the greatest barrier to cesium release. Under normal operating temperature, trapping can lower the apparent diffusion coefficient in PyC significantly. A comparison of the apparent diffusivities in the PyC with that of PyC with no traps suggests that the apparent diffusion coefficient can be four to five orders of magnitude lower than the intrinsic diffusivity depending on the trap concentration. At the higher temperatures, the release rate from the traps is so large that the effects of trapping is diminished somewhat.

---

[3] Existing German data were measured on BISO particles. Concentrations are probably high enough that trapping effects were small and thus the measured diffusion coefficients are representative of transport without trapping.
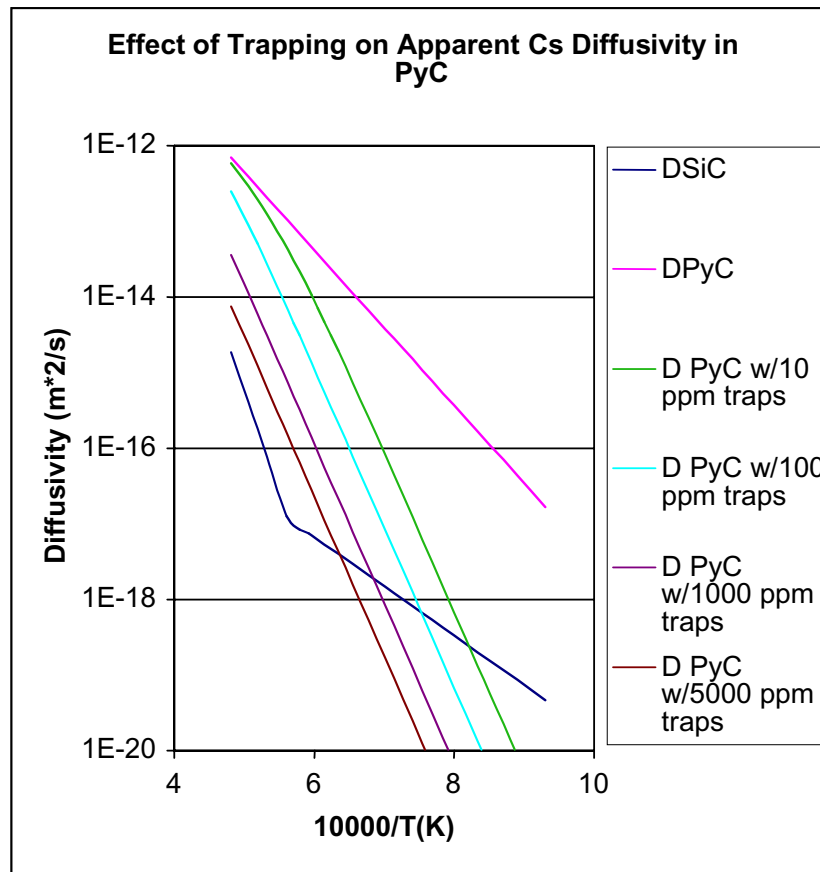
Figure 3-58. Effects of trapping on apparent Cs diffusivity in PyC.

However, it is important to remember that diffusion and trapping are dynamic phenomena. As atoms diffuse through the layer a certain fraction is trapped. As these traps are filled the apparent diffusivity increases. In fact, the magnitude of the intrinsic diffusion coefficient in PyC is high enough that significant diffusion of cesium into the PyC is expected during normal operation. The Cs concentration in IPyC is expected to be much greater than the trap density, perhaps at the level of 0.5 to 1% atom concentration, so the traps would fill quickly and not affect overall transport behavior. Thus, we conclude that trapping is not very important on the transport behavior in the IPyC layer. However, in the OPyC layer, the Cs concentration in OPyC is much smaller, on the order of the trap concentration expected in graphite. Thus, in the OPyC layer trapping could result in a much slower transport.

Similar analysis for Sr suggests that given the very low release of Sr from the kernel during operation, the Sr concentration in the IPyC would be at the high end of the trap concentration and thus may not be influenced by trapping. In the OPyC, the Sr concentration is much smaller and trapping effects could be very important.

The SiC Layer

SiC in TRISO-coated particle fuel is a high-density polycrystalline beta-SiC. It is the major fission product barrier in the fuel. As with the pyrocarbon layer, data on the effective diffusion coefficients of noble gases, cesium, strontium and silver have been inferred from integral release measurements (IAEA 1997). Figure 3-59 plots the effective diffusion coefficient for noble gases, cesium, strontium and silver.

Transport Mechanisms

The mechanism for the transport of gaseous and metallic fission products in the SiC layer has not been the subject of significant study in the world gas reactor community. A complete understanding of the mechanism(s) responsible for fission product transport in SiC is somewhat lacking. A Knudsen diffusion mechanism could be postulated for the transport of noble gases and Ag vapor through the SiC layer especially under normal operating conditions. The interconnected porosity of the SiC layer is expected to be quite small because the beta-SiC is very high density (3.21 to 3.23 g/cc is commonly fabricated). Under accident conditions, bulk diffusion may play an increasing role in the transport.

Fig. A-3: Diffusion coefficients of fission product species in silicon carbide as function of temperature

Figure 3-59. Diffusion coefficients of Xe, Cs, Sr and Ag in SiC.

For the other metallic fission products, a mixture of grain boundary and bulk diffusion has been postulated depending on temperature, with grain boundary diffusion most likely operable at low temperatures and bulk diffusion at high temperatures representative of accidents. The magnitudes of the activation energies in Figure 3-57 tend to support this theory. A comparison of the effective diffusion coefficients for fission gases, Cs, Sr and Ag in SiC with more recent measurements on other species in SiC can shed additional light on the underlying mechanisms. Figure 3-60 overlays the original data with self-diffusion data for C and Si in SiC (red box) and grain boundary diffusivities for Fe, Cr (blue box) (Fusamae 1996; Takano et al. 2001). The magnitude and slopes of the grain boundary diffusivities for Fe and Cr are similar to that for Cs and Sr perhaps indicating that grain boundary diffusion is the dominant mechanisms for Cs and

Sr transport through SiC. The slope of the C and Si self-diffusion coefficients are similar to that for Xe at high temperature suggesting that a vacancy mechanism may describe noble gas transport in SiC.
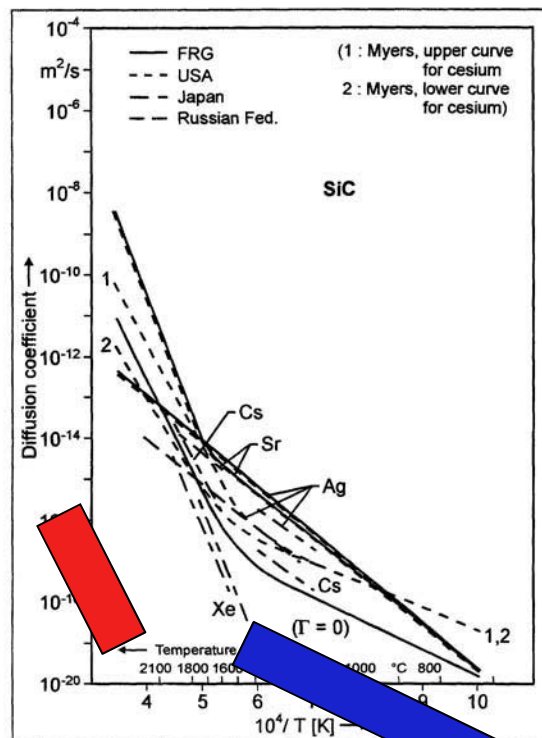
Fig. A-3: Diffusion coefficients of fission product species in silicon carbide as function of temperature

444

Figure 3-60. Comparison of C and Si self-diffusion coefficient (red box) and Fe and Cr grain boundary diffusivities (blue box) with fission product diffusivities inferred from integral release measurements on coated particles.

Grain Boundary Diffusion

It appears that both grain boundary and bulk diffusion may be important in describing fission product transport in coated particle fuel. The importance of each mechanism will depend on the temperature, the individual diffusivities in the bulk and along the grain boundaries, and the area fraction occupied by grains and boundaries. Grain boundary diffusion has been studied extensively in the literature. It can act as a fast diffusion channel in polycrystalline materials. This fast diffusion sometimes manifests itself as a very high pre-exponential factor, D_o, in the measured diffusion coefficients. The classic Arrhenius formalism suggests that D_o should be on the order of the product of the Debye frequency and the square of the lattice spacing for atomic diffusion. (For many materials this is $\sim 10^{-3}$ m^2/s). Experimentally observed values can be 10^7 greater than this value (Wang et al. 2002)and may be related to the presence of grain boundaries, defects and surface effects. The influence of grain boundaries has been studied extensively and three different kinetic regimes have been found: Type A, B and C (Mishini and Herzig 1999). Figure 3-61 sets up the analytic picture of a grain boundary of thickness, δ. The grains are of width d and a uniform concentration of the fission product, C_o, exists across the grains and grain boundary. A segregation coefficient, s, describes the ratio of the concentration in the grain and in the boundary at the surface interface. Solutions are then sought to the classic Fickian diffusion equations in two dimensions in both the grain, denoted by v in the figure, and the grain boundary, denoted by gb, in the figure.
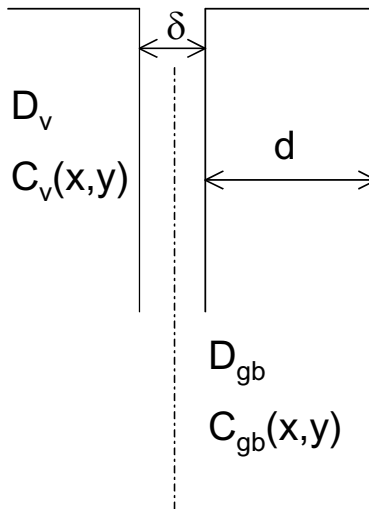
Figure 3-61. Schematic of grains and grain boundary**.**

In Type A grain boundary diffusion, the penetration distance into the grain is much greater than the grain boundary thickness. In this case, both grain boundary and bulk diffusion are operative as would be the case for high temperatures and long heating times as is the case in safety testing of fuel particles. In this case, an effective diffusion coefficient is measured which is a volume weighted average of the bulk and grain boundary diffusion coefficient. The concentration profile is given by a classic complementary error function using the effective diffusivity. For Type A kinetics, these conditions are summarized below.

$$(D_v t)^{1/2} >> d$$
$$c_b = s c_v$$
$$D_{eff} = f D_v + (1 - f) D_{gb}$$
$$\bar{c} = erfc(\frac{y}{2\sqrt{D_{eff}t}})$$

In Type B kinetics, there is much greater penetration down the boundary than into the grains. In this case, what is actually measured is an apparent diffusion coefficient sometimes denoted as P_{gb}, which is the product (s δ D_{gb}). This regime may be applicable at high irradiation temperatures. The analytic conditions for Type B kinetics and the resultant solution to the diffusion equations are given by:

$$s\delta << (D_v t)^{1/2} << d$$

$$P_{gb} = s\delta D_{gb} = 1.322\sqrt{\frac{D}{t}}(-\frac{\partial \ln \bar{c}}{\partial z^{6/5}})^{-5/3}$$

where the spacial derivative term is the measured concentration profile in the sample.

In Type C kinetics, bulk diffusion is "frozen out" and the transport is dominated by grain boundary diffusion $[(D_v t)^{1/2} << s\delta]$. This is probably applicable at very low temperatures, conditions that may be representative of average irradiation temperature experiments. In this case, the concentration is given by a Gaussian for a point source and an Error function for constant source with the effective diffusivity equal to the grain boundary diffusivity, D_{gb}. These idealized situations are useful to understand the concepts of grain boundary and bulk diffusion in

polycrystalline material. However, in practice the microstructure of the material is more complex and development of appropriate mixture rules to establish an effective diffusivity through the structure is an area of active research (Zhu et al. 2001). Figure 3-62 compares three different microstructures that may bound that expected in SiC. The large columnar structure, which is found in some SiC, is idealized in the left portion of the figure. In this case, the volume weighted mixture rule for the effective diffusivity is appropriate. At the other extreme is the case of SiC with an idealized laminar structure. In this case, a reciprocal series approach to establishing the effective diffusivity may be appropriate. In the middle of the figure is a schematic representation of small-grained SiC, which is the form most sought after in coated particle fuel. In this case there is no exact mixture rule to use, but the two extreme cases are expected to bound the actual behavior.

Idealized large columnar structure

Small grain structure

Idealized laminar structure

$$D_{eff} = D_v(1-f) + D_{gb}f$$

$$D_{eff} = \frac{D_v D_{gb}}{D_v(1-f) + D_{gb}f}$$
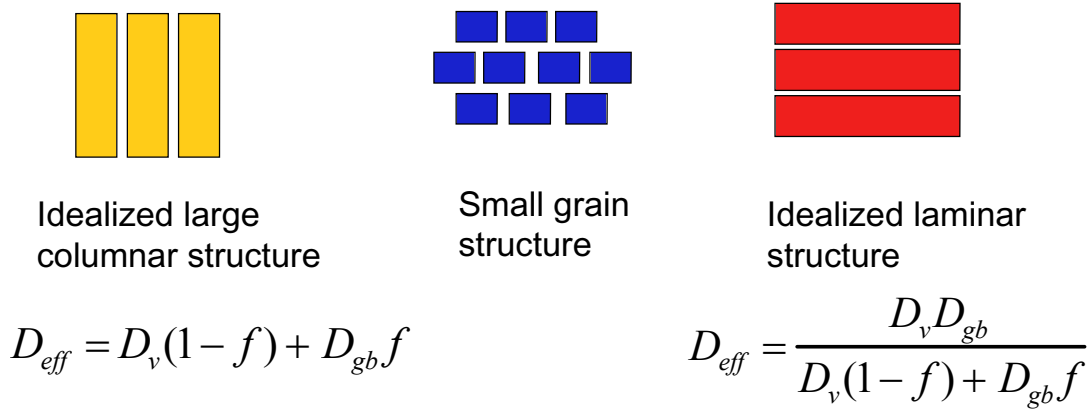
Figure 3-62. Influence of microstructure on apparent diffusivity.

Simple Integral Coating Model

In the previous sections, the transport mechanisms in each layer have been reviewed. In this section we develop a simplistic integral model of release from TRISO-coated particle fuel using some of the ideas and data in the previous sections and present some preliminary calculations using the model.

Morgan and Malinauskaus (1977) developed an analytic solution for depletion of a fission product through a single coating layer given by:

$$FR = 1 - \frac{Ka}{b} \sum_{n=1}^{\infty} \frac{\exp(-D^* t \alpha_n^2 / \delta^2) \sin(\alpha_n)}{\left[2K\alpha_n + (4b\alpha_n/\delta)\sin^2 \alpha_n \right] + K\sin(2\alpha_n)}$$

where

$$\cot(\alpha_n) = (b\alpha_n / K\delta) - (\delta / b\alpha_n)$$

$$K = (A/V)s$$

    a = the inner radius of the coating,
    b = the outer radius of the coating,
    A = the surface area of the inside of the coating,
    V = the volume inside the coating, and
    S = segregation factor (ratio of surface layer concentration to source concentration).

If we consider the TRISO coating as a composite layer then we can use the simple resistance concept to model all three layers as one layer and write the apparent diffusivity D* as

$$\frac{\delta}{D^*} = \frac{\delta_{IPyC}}{D_{IPyC}^{eff}} + \frac{\delta_{SiC}}{D_{SiC}^{eff}} + \frac{\delta_{OPyC}}{D_{OPyC}^{eff}}$$

This simple model uses effective diffusivities for each layer and can account for trapping if needed, transport through cracks or pores, and different microstructures with the level of detail available to the user. The model also accounts for the effects of a depleting source and can consider partitioning(s) between coating layer and kernel.

We have used this model in conjunction with the Booth release model from the kernel to perform some simple scoping calculations for diffusional releases from the particle expected during a constant 1600°C heating and a depressurized conduction cooldown. No thermal diffusion is included in the model. (Note that in the real event the matrix can absorb the metallic fission products and thus the results are not intended to represent an accurate model for the entire reactor, but instead, should be viewed as a scoping tool to understand what phenomena and factors are important in the particle.)

Figure 3-63 and Figure 3-64 plot the fractional release for various fission products during post-irradiation heating at 1600°C following a constant three year irradiation at 1200°C typical of a peak fuel particle in a prismatic gas reactor and a ten cycle three-year 600 to 1200°C cyclic irradiation expected in a pebble bed reactor. The results suggest that the irradiation temperature has at best a modest influence on the release at high temperature, given the long time at temperature in these calculations.
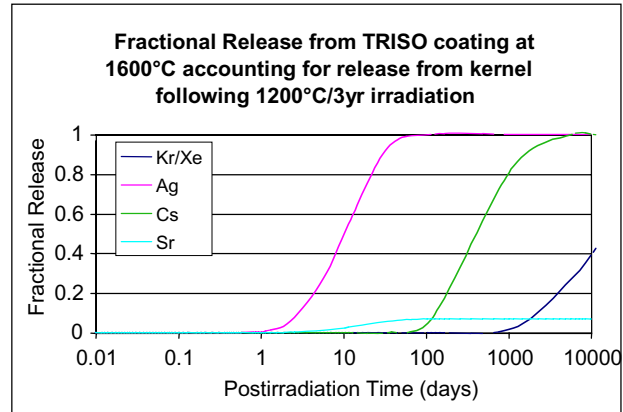
Figure 3-63. Fractional release from a coated fuel particle during 1600°C heating following a three year irradiation at 1200°C.
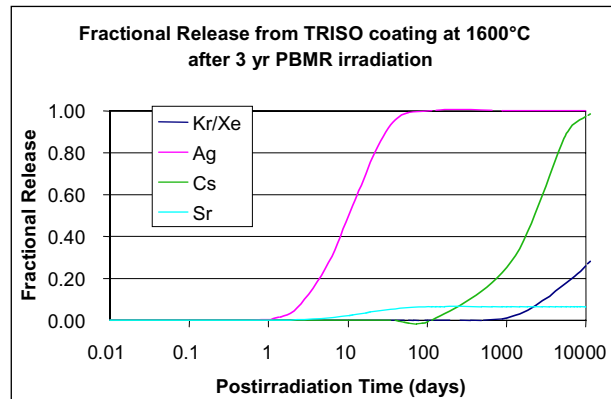
Figure 3-64. Fractional release from a coated fuel particle during 1600°C heating following a three-year ten-cycle PBMR irradiation between 600 and 1200°C.

The calculated diffusional releases from a conduction cooldown (see Figure 3-65) following a PBMR irradiation are shown in Figure 3-66. The conduction cooldown is characterized by a slow heatup to a peak temperature of ~ 1600°C followed by a gradual cooldown over the course of hundreds of hours.
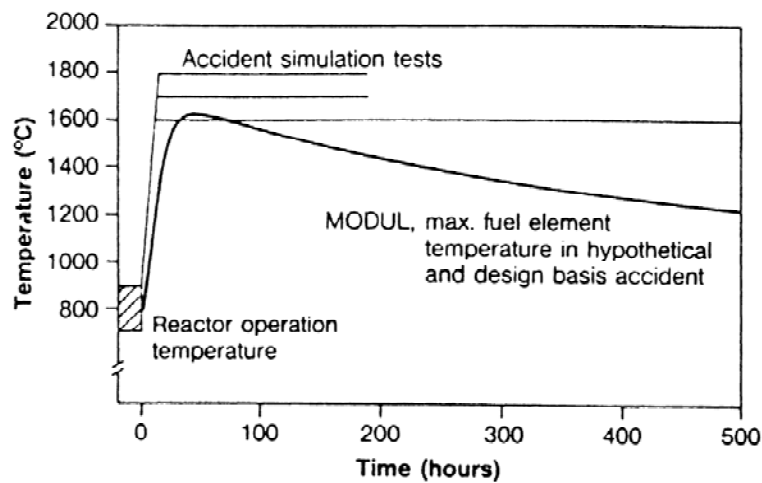
Figure 3-65. Thermal response during a conduction cooldown.

By comparison to the releases during a constant high temperature heating in Figures 4-63 and 4-64, only silver and strontium releases from the particle are calculated given the magnitude of the diffusivities in the layers and the time/temperature profile in the accident scenario given in Figure 3-65. These results illustrate the importance of time at temperature on the magnitude and timing of the calculated releases.
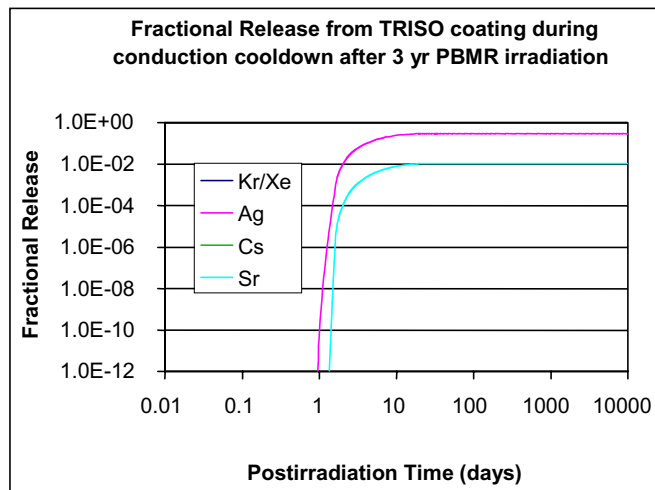
Figure 3-66. Calculated diffusional release from TRISO coated particle during a conduction cooldown following a three-year ten cycle PBMR cyclic irradiation.

Table 3-15 presents the results of two sensitivity studies: (a) a case where all temperatures are increased by 100°C and a case where the diffusivity in the SiC layer has been increased by a factor of 10 over the base value. The results show modest impact of between a factor of two and six on the overall release for silver and strontium and little impact on either noble gases or cesium.

Table 3-15. Effect of increased temperature and increased SiC diffusivity on diffusional releases from TRISO coated particles.

Cases Fission Product	Base	+100 °C	10X SiC Diff
Kr/Xe	0	0	0
Ag	0.27	0.59	0.98
Cs	0	0	2.54E-05
Sr	0.0098	0.026	0.06

As a final sensitivity study we examine the influence of the segregation factor on the overall diffusional release from the particle. The segregation factor can be used to account for the build up of fission products that may occur near cracks because of the fast diffusion. Figure 3-67 plots the fractional release versus dimensionless time for four different segregation factors (1, 5, 10, 50).
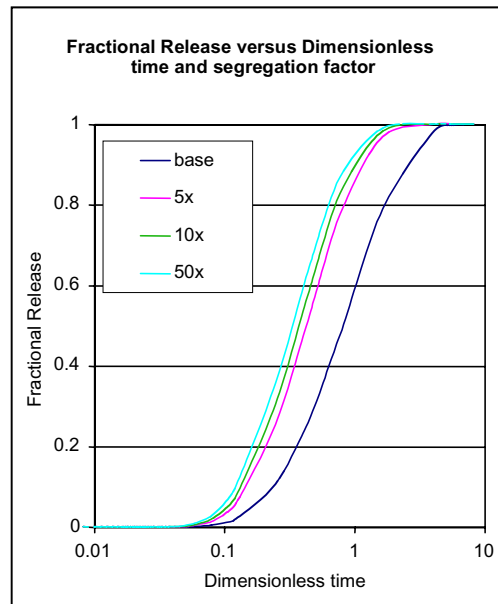
Figure 3-67. Effect of partition coefficient on fractional release during heating.

The results suggest that the fractional release at a given time can vary easily by a factor of 2 to 3 depending on the magnitude of the partitioning that exists at the interface. Reference (IAEA 1997) suggests that segregation factors between 0.3 and 3 have been measured. The simple calculation suggests that segregation or the build up of fission products at the interface between layers may explain some of the variability that has been observed in heating tests of coated particles irradiated to nominally the same conditions. The model presented here, although simple, can help scope out the importance of different reactor parameters on the source term from a gas reactor.

One-Dimensional Analysis in Coated Particle Fuel Using TMAP4

Based on the scoping assessment of fission product transport mechanisms in the previous sections, we have developed a one-dimensional fission product transport model for the TRISO-coated particle using the TMAP4 code (Longhurst et al. 1998). The TMAP4 code solves the one-dimensional diffusion equation with trapping (if needed) for an arbitrary number of user defined structures that can be linked together to model the kernel and each layer of the TRISO coated particle. The code can account for any arbitrary user defined fission product generation rate during the irradiation. TMAP4 also solves heat transfer through the particle based on any arbitrary user defined energy generation in the kernel and an imposed outside surface temperature of the particle. The code can handle both irradiation and accident conditions based on the needs of the user. It can account for both pebble cyclic heating and steady prismatic irradiation conditions and can model any conduction cooldown scenario or any temporal accident heating temperature profile. We have selected this code because of its ability to model the relevant fission product transport phenomena and its flexibility in input and output.

Input Model

We have developed this model and performed preliminary benchmarks against a series of German pebble irradiations and post-irradiation heatup experiments. The fuels consisted of both full size pebbles and reduced sized compacts used in the German fuel development effort. Some of the pebbles were irradiated in the AVR while others were irradiated in capsules in the FRJ and HFR reactors. Critical parameters for the irradiations and subsequent post-irradiation heatup are shown in Tables 3-16 and 3-17 compiled from Gontard and Nabielek (1990). Six specific fuel elements were selected for analysis: AVR 82/20, SL P1 6, HFR P4 1/8, HFR P4 1/12, HFR P4 3/7 and KFR K3/1. These pebbles were selected because they represented a good range of irradiation and post-irradiation heating conditions to benchmark against the model.

In the TMAP model, the kernel and each layer of the particle (buffer, IPyC, SiC, OPyC) are modeled as slabs with individual nodes representing interior locations in each layer. The geometries of the particles are based on particle batch measurements given in Petti et al 2003). (The use of Cartesian instead of spherical coordinates results in a very small error in comparison to other uncertainties in the analysis.) Note that the fuel matrix has not been included in this model to date.

The thermal conditions for the capsule irradiations and post-irradiation heatup testing were simulated in TMAP4 in the following way. For the irradiation, the average temperature of the irradiation was assumed to represent the outer surface of the OPyC layer of the particle. TMAP4 then calculated the thermal response of each layer using the heat conduction solution option in the code and the heat transfer properties for each layer presented earlier. The average energy generation in the kernel was determined from the burnup and irradiation duration. (This is important to calculate the thermal gradient across the buffer for Soret diffusion). This heat generation value was used for the entire irradiation duration. To simulate the high temperature heating, the energy generation was set to zero and the outside of the OPyC layer was set to follow the time-temperature heating exposure given in Table 3-16 and 3-17. The thermal response of the other layers in the model was calculated using the heat conduction solution option in the code. In general, the high temperature conductivity of the layers resulted in little temperature drop across the particle during the high temperature heating experiment. In a few cases because of uncertainties associated with temperature measurements during the irradiation sensitivity calculations were performed where the average temperature was increased by 50 and 100°C. In the case of the AVR pebble, the exact time temperature history is not known with certainty. The temporal response of a GL3 pebble in AVR from reference data (Gontard and Nabielek 1990) was used as the boundary condition for the outer surface of the OPyC layer in that case.

Noble gases, cesium, silver and strontium were modeled in TMAP4 but only cesium was used in the benchmarking to this point. (TMAP4 can handle up to 10 species.) The fission product generation rate in the kernel was based on ORIGEN calculations for a gas reactor reactor (Terry et al. 2001) scaled appropriately for burnup and irradiation duration in the actual experiment. Diffusion coefficients for the kernel, PyC and SiC layers were taken from German data (IAEA 1997). No segregation is assumed in these calculations; concentrations are continuous across all the interfaces of the different layers. For the buffer, since Knudsen diffusion was felt to be a good representation of the transport of vapors in that layer, a value of 10^{-7} m^2/s based on calculations presented earlier was used for all fission product species. Thermal diffusion was considered in the buffer layer only and a value of Q*/R of –20000 was used for this set of calculations.

Table 3-16. Accident tests with full size pebbles.

Fuel element	FRJ2-K13/2	FRJ2-K13/4	HFR-K3/1	AVR 71/22	AVR 82/20
Particle batch	EUO 2308	EUO 2308	EUO 2308	HT 232-245	HT 232-245
Burnup (%FIMA)	8.0	7.6	7.5	3.5	8.6
Fast fluence (10^{25} m^{-2}, E > 0.10 MeV)	0.2	0.2	4.0	0.9	2.2
Center temp. (°C)	1150	1120	1200	1250	1250
Surface temp. (°C)	990	980	1020	1050	1050
Irradiation duration (efpd)	396	396	359	481	1253
Heating test temp. (°C)	1600	1600	1600	1600	1600
Heating test duration (h)	160	138	500	500	100
Cs-137 fractional release at test end	3.9×10^{-5}	2.5×10^{-6}	1.1×10^{-4}	2.0×10^{-5}	6.5×10^{-5}

Note: AVR pebble temperatures are generic values and not actual temperatures.

Table 3-17. Accident tests with reduced size compacts.

Fuel element	SL-P1 6	HFR-P4 1/12	HFR-P4 1/8	HFR-P4 2/8	HFR-P4 3/7
Particle batch	EUO 2308	EUO 2308	EUO 2308	EUO 2309	EUO 2308
Burnup (% FIMA)	10.7	11.1	13.8	13.8	13.9
Fast fluence (10^{25} m^{-2}, E > 0.10 MeV)	6.7	5.5	7.2	7.2	7.5
Max temperature (°C)	800	940	940	945	1075
Min temperature (°C)	Not recorded	915	915	920	1050
Irradiation duration (efpd)	330	351	351	351	351
Heating test temperature (°C)	1600	1600	1600	1600	1600
Heating test duration (h)	304	304	304	304	304
Cs-137 fractional release at test end	3.9×10^{-4}	2.6×10^{-4}	2.0×10^{-3}	1.4×10^{-3}	3.9×10^{-3}

Results

Table 3-18 tabulates the measured and calculated cesium release results from the German fuel. Also included is a description of the fuel specimen, the irradiation conditions (temperature, burnup, power per particle, fast fluence, irradiation duration) and the high temperature heating conditions (time at 1600°C).

As expected, the calculated results show very little release of cesium during irradiation. Because no measurements were made of this parameter, comparisons are unavailable. A comparison of the releases following high temperature heating shows generally good agreement. The best

agreement is for pebble AVR 82/20; reasonably good agreement is seen for pebbles SL P1 6, HFR P4 1/12 and HFR K3. The largest discrepancy between measured and calculated results is for pebble HFR P4 1/8. Although this pebble received an irradiation exposure and high temperature heating that is not that different from HFR P4 1/12, the measured cesium release for HFR P4 1/8 is about ten times greater than that for HFR P4 1/12. The TMAP4 calculations suggest that the differences in the irradiation conditions translate into cesium releases that differ only by about 20%. Sensitivity calculations in which the irradiation temperature is increased by 50 and 100°C result in 10 to 20% more cesium calculated to be released under post-irradiation heating. Thus, even when accounting for temperature uncertainties during the irradiation, the calculated releases still are well below the measured data. The Germans (IAEA 1997; Gontard and Nabielek 1990) suggest that the higher release is not related to classic diffusion but instead is attributed to enhanced permability of the SiC perhaps due to chemical interaction between cesium and the SiC leading to greater releases under post-irradiation heating conditions. It is important to note that the TMAP4 model does not currently have a model for any fission product/SiCinteractions.

Table 3-18. Preliminary TMAP4 Benchmarking results.

Fuel Specimen	AVR 82/20	SL P1 6	HFR P4 1/8	HFR P4 1/12	HFR P4 3/7	HFR K3
	40 mw/particle 8.6% FIMA 2.2 nvt Cyclic	185 mW/particle 10.7% FIMA 6.7 nvt	225 mW/particle 13.8% FIMA 7.2 nvt	180 mW/particle 11.1% FIMA 5.5 nvt	225 mW/particle 13.9% FIMA 7.5 nvt	120 mW/particle 7.5% FIMA 4.0 nvt
Irradiation Conditions	600-1300°C 1253 day irradiation	800°C/ 330 day irradiation	925°C/351 day irradiation	925°C/351 day irradiation	1075°C/351 day irradiation	1110°C/359 day irradiation
High Temperature Heating conditions	1600°C/ 100 hours	1600°C 304 hours	1600°C 304 hours	1600°C 304 hours	1600°C 304 hours	1600°C 500 hours
Measured Fractional Cesium Release after Heating	6.5e-05	3.9e-04	2.0e-03	2.6e-04	3.9e-03	1.1e-04 from pebble 1.2e-03 from particle
Base Case: Calculated Fractional Cesium Release after Heating	7.4e-05	1.3e-04	2.0e-04	1.74e-04	4.6e-04	1.82e-03
+50 C Calculated Fractional Cesium Release after Heating	----	1.4e-04	2.5e-04	2.18e-04	6.6e-04	
+100 C Calculated Fractional Cesium Release after Heating		1.6e-04	3.4e-04			

215

This review suggests that knowledge of the spatial and temporal temperature distribution in the reactor is most important for understanding fission product release from gas reactors. Releases are probably dominated by particle failures during the accident, which have not been considered here. Particle failure and SiC corrosion by fission products need to be considered in additional to traditional mass transport.

Different mechanisms are likely responsible for the transport of gases and metals in different layers. Gaseous transport can be described using pressure driven diffusion models through porous media but the use of these models requires information on the connected porosity, the characteristic size of the porosity and the tortuosity of the porous media which are not well known for the layers of the TRISO coating. Metallic fission product transport is probably a combination of grain boundary and bulk diffusion depending on the temperature and specific fission product of interest.

Our preliminary assessment suggests that the power generated in the particle determines conditions in the buffer (cracked versus uncracked). This in turn defines the initial conditions for fission product transport. With the exception of cracking, multi-dimensional effects are probably less important. The calculations presented here suggest that Knudsen diffusion is consistent with rapid transport through the buffer and cracks but not intact PyC. Segregation/concentration of fission products at cracks can lead to greater releases and may explain some of the variability seen in accident heating tests. Thermal diffusion as a result of large thermal gradients (Soret effect) across the buffer would tend to only be important under the cases of high power generation in the particle corresponding to very accelerated irradiation conditions that are not typical of gas reactors.

Effective diffusivities have been obtained from previous German and U.S. work, but the research did not always focus on the mechanism involved and the researchers did not always reduce the data with a specific mechanism in mind (e.g. Knudsen diffusion parameters, trapping parameters). The measured effective diffusivities in PyC and SiC are consistent with both older and more recent transport coefficient measurements.

Furthermore, our assessment suggests that trapping is important in OPyC layers where concentration of fission products is on the same order as the trap density. Trapping is much less important in IPyC and SiC layers.

Sensitivity studies using currently available effective diffusivities and educated guesses on trapping parameters and the simple multi-layer diffusion and trapping model presented here can help scope out these issues in more detail.

Pd – SiC Interaction

The INEEL neared completion of a metallic Pd – SiC interaction model. All available in-reactor data for Pd penetration in SiC (Lauf 1984; Minato 1990; Montgomery 1981; Tiegs 1982) were mathematically fitted according to an Arrhenius temperature dependency.   Figure 3-68 presents the Pd penetration rate data with the corresponding least squares fit.
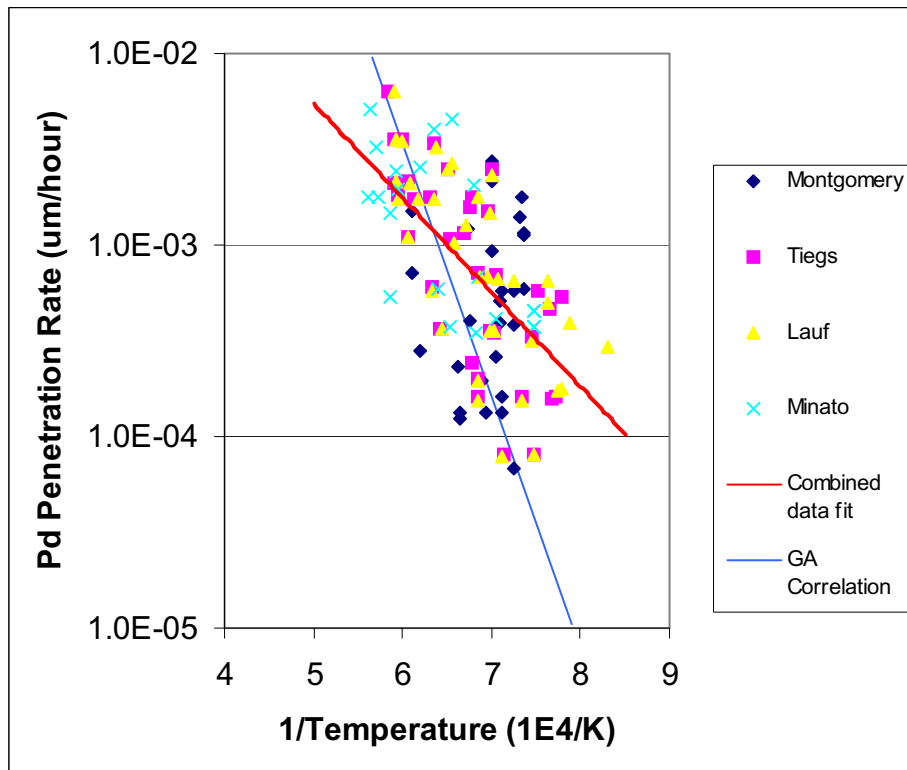
Figure 3-68. In-reactor data for Pd penetration in SiC.

The above combined data fit is used in the PAFUME model for Pd attack. Also shown in Figure 3-68 is GA's FDDM/E model (Saurwein 2004) for Pd penetration rate.   The PARFUME correlation predicts lower penetration rates, and hence, lower failure probabilities above about 1300 °C but higher penetration rates and failure probabilities below 1300 °C. This may be considered conservative relative to the GA model for temperatures of primary interest to gas

reactors. It should be noted that the GA correlation includes data from high temperature, out of reactor experiments using simulated fission products. These data and omission of low temperature results, which tend to show large scatter, may explain the difference between the two models.

Implementation of the Pd – SiC interaction model into the PARFUME code has begun. The model first evaluates the Pd penetration depth for a given time and temperature history using the penetration rate correlation described above (combined data fit). A preliminary particle failure model assumes failure to occur when the penetration depth exceeds one half the thickness of the SiC layer. For each time-temperature history, a failure probability due to Pd attack is then estimated by determining the fraction of particles, with an assumed normal distribution of SiC thickness, that meet the failure criterion. The overall failure probability is finally determined by weighting the individual failure fractions by the fraction of particles with the corresponding time-temperature history.

Preliminary failure probabilities as calculated by the PARFUME model and the GA model for a simple case of all particles at a constant temperature for 640 days are presented in Figure 3-69. (The calculations are based on a mean SiC thickness of 35 μm with a standard deviation of 3 μm.) This comparison clearly illustrates the conservative nature of the PARFUME model.

A more detailed time-temperature history was used to calculate the particle failure probability due to Pd attack in the Advanced Gas Reactor Fuel Development and Qualification Program experiment AGR-1. For this case, ABAQUS calculated temperatures for 4000 equal volume elements within a representative cell (individually sealed and controlled compartment) of the AGR-1 capsule at the lowest and highest expected power levels. Using MCNP physics calculations for power over 16 40-day reactor cycles, a thermal history was approximated by three cycles at high power (high temperature), four cycles at low power (low temperature), and nine cycles at average power (arithmetic average of high and low temperatures). Again, assuming a 50% SiC penetration depth failure criterion (and a mean SiC thickness of 35 μm with a standard deviation of 3 μm), the preliminary PARFUME model calculates a failure probability fraction of 5.3×10^{-4} and the GA model calculates a failure probability of 4.8×10^{-11}.

The final Pd- SiC interaction PARFUME model will combine the time-dependent Pd penetration correlation described above with a thinned SiC layer model described in the Task 2 section.
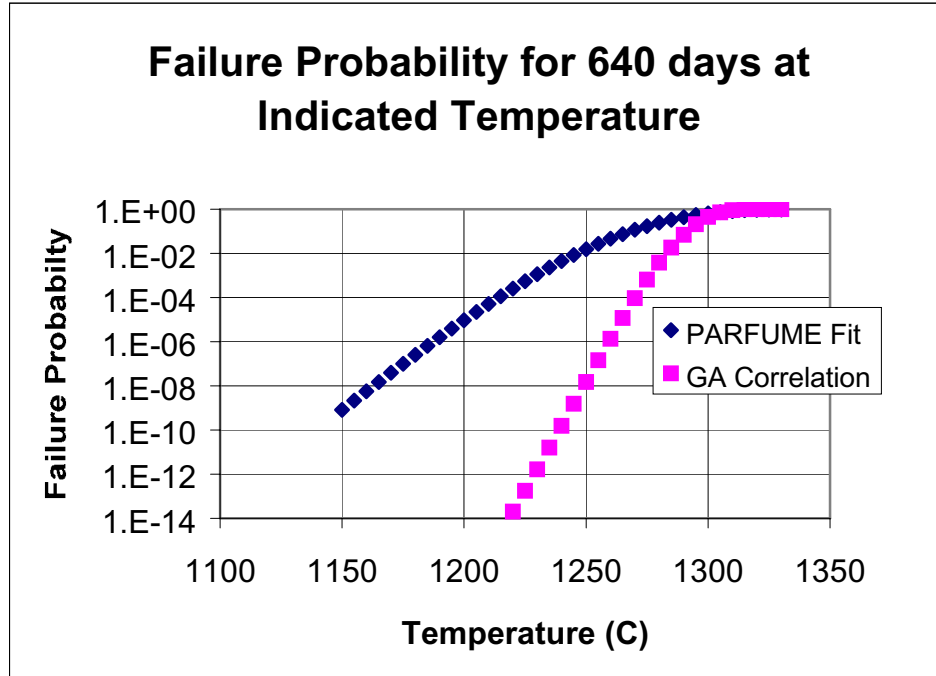
Figure 3-69. Failure probabilities due to Pd attack at constant temperature.

Kernel Migration (Amoeba Effect)

The INEEL has incorporated a model for particle failure due to kernel migration, or Amoeba effect, into the PARFUME code. Kernel migration occurs within the presence of a macroscopic temperature gradient where particle failure is assumed to occur when the kernel comes into contact with the SiC layer. The migration distance is calculated according to a standard formulation (Martin 1993) that utilizes kernel migration coefficients (K_{MC}) derived from experimental data. For UCO fuel where kernel migration is expected to be miniscule, a General Atomics derived correlation (Martin 1993) for K_{MC} is used. This correlation was actually derived from UC_2 data but is considered conservative for UCO. For UO_2 fuel where kernel migration can be significant, recent data from the U.S. (Ketterer 1985) and Germany (HBK 1984) were fitted to an Arrhenius function to derive a kernel migration coefficient correlation. These correlations for K_{MC} are presented in Figure 3-70.
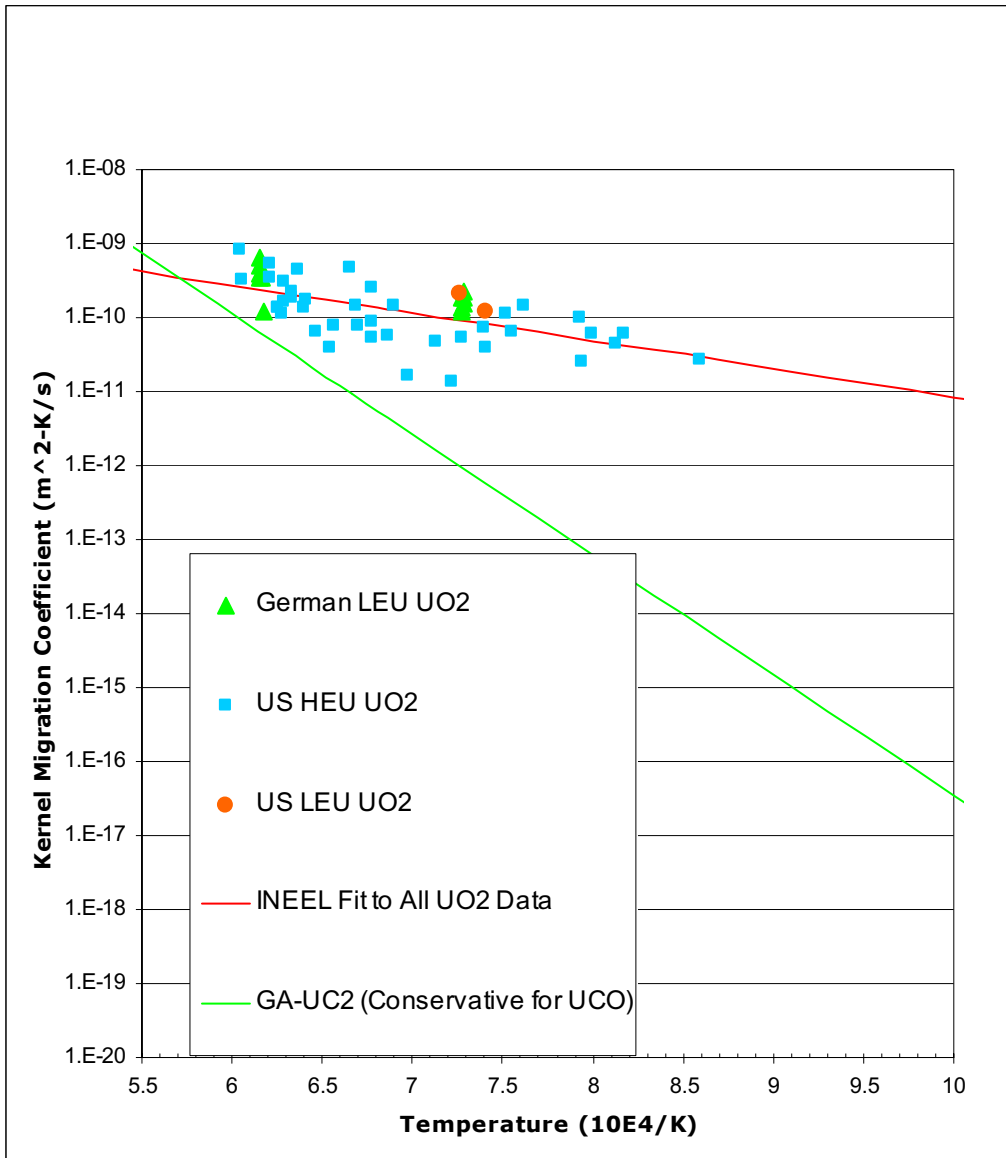
Figure 3-70. Kernel migration coefficients for UO$_2$ and UCO fuel.

SiC Thermal Decomposition

The INEEL has begun implementation of a SiC thermal decomposition model. This phenomenon becomes a significant fuel failure mechanism at high temperatures, generally above 1600 °C. Model development began by fitting all available SiC thermal decomposition data to an Arrhenius function. The data were developed by Benz and reported in (Martin 1993) for burned-back fuel particles from HOBEG, KFA, and General Atomics. Earlier data were reported (Ghoshtagore 1966) for SiC wafers. Each measurement series was conducted in an inert, non-

oxidizing atmosphere on exposed SiC. Figure 3-71 presents the SiC decomposition rate data with the combined data fit. Since SiC that is covered by a layer of pyrolitic carbon decomposes more slowly that exposed SiC (Price 1977), correlations based upon these data may be considered to be conservative. The final thermal decomposition PARFUME model will combine this decomposition rate correlation with a thinned SiC layer model described in the Task 2 section.
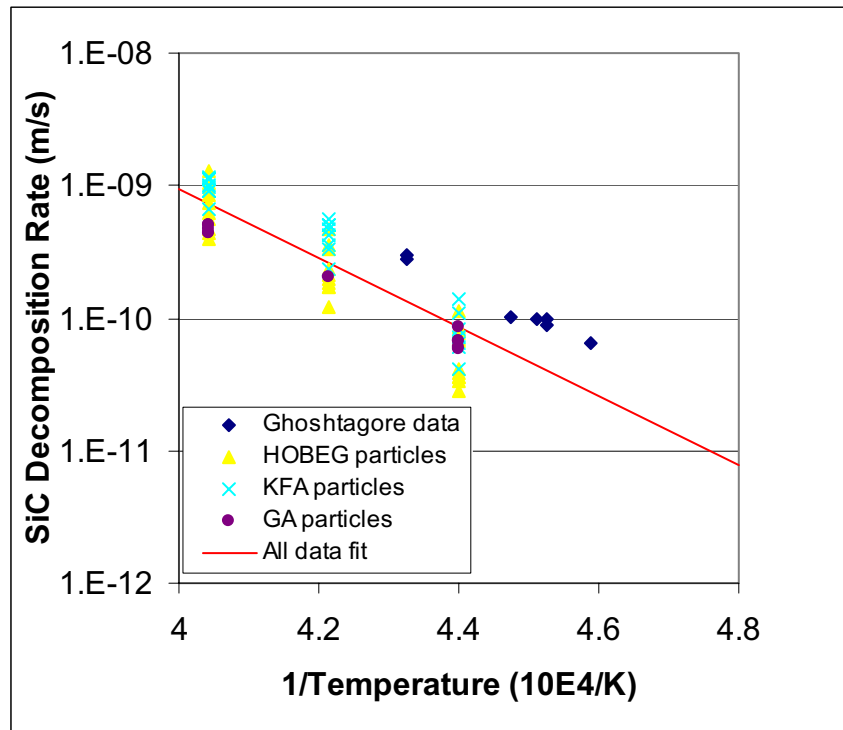
Figure 3-71. SiC thermal decomposition rate data.

3.3 Technical Task Overview- CEA

UCO Fuel

UCO fabrication, composition history under irradiation, behavior under irradiation and accident conditions have been reviewed. UCO seems to be better in comparison with UO_2 considering that particle pressure is lower by avoiding CO production and there is no risk of amoeba effect. Kernel swelling, fission gas release and diffusion of fission products would be nearly identical as for UO_2. Nevertheless, the CEA assumes that fabrication is not easy. Specifically, a good homogeneity of the microstructure seems difficult to obtain. Silver and palladium metallic fission

produced diffusion could be the worst. UO_2 has been tested in several countries on an industrial scale whereas UCO has been produced only in the U.S. on a laboratory scale. In conclusion, a comparison with identical irradiation and layer coating conditions would be useful for decision making.

Coatings

In the VHTR concept, ZrC is a candidate to replace SiC because of its physical properties. Zirconium carbide has a melting point at 3540°C and melts eutectically with carbon at 2850°C, whereas SiC begins to decompose above 2000°C. Irradiations of ZrC coated particles studied under normal or accidental conditions have shown good results. Zirconium carbide shows higher resistance to chemical attack by the fission product palladium than SiC, a good retention capability of cesium (and less for ruthenium). The method chosen for ZrC deposition is to mix Zr powder with HCl gas diluted in Ar to form $ZrCl_4$. Hydrocarbon gases such as C_3H_6 or methane (CH_4) are used to provide the carbon. A H_2 atmosphere is used to avoid formation of free chlorine.

Previous studies have shown that an increase in the ratio of the hydrocarbon gas to the $ZrCl_4$ in the coating gas results in a co-deposition of carbon (i.e., an increase if the C/Zr ratio in the deposit). In this case, increasing the H_2 concentration inhibits this effect and allows the ZrC to be deposited at higher hydrocarbon gas concentrations, which is effective in increasing the coating rate of ZrC.

Preliminary ZrC coating trials of about 35µm thick have been performed. During the deposition process, however, the $C_3H_6/ZrCl_4$ ratio varied due to an uncontrolled increase of temperature in the chlorinator vessel (the chlorination is a very exothermic reaction). Thus, it has been impossible to master the experimental coating conditions to date. Modifications of the chlorinator vessel are in progress to suppress these technical problems and to focus on the optimization of the ZrC deposition parameters.
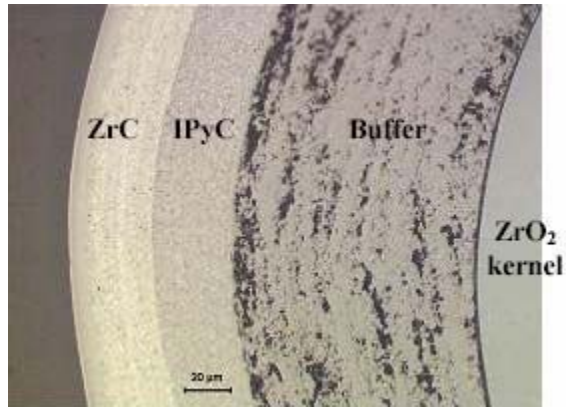
Figure 3-72. Cross-section of ZrC coated particle produced at CEA Grenoble.

In addition, the following data from the literature have been gathered for ZrC:

- Specific heat
- Coefficient of thermal expansion
- Thermal conductivity
- Young's modulus.

However, permeation, irradiation-induced creep, and swelling data are lacking.

Filename: 4. INERI Task 3.doc
Directory: C:\Documents and Settings\talbhd\Desktop\FINAL INERI JAN3
Template: C:\Documents and Settings\talbhd\Application
      Data\Microsoft\Templates\Normal.dot
Title: TASK 3: CONCEPT IMPROVEMENTS
Subject:
Author: test
Keywords:
Comments:
Creation Date: 1/3/2005 10:25:00 AM
Change Number: 107
Last Saved On: 1/6/2005 9:32:00 AM
Last Saved By: test
Total Editing Time: 1,483 Minutes
Last Printed On: 1/18/2005 10:51:00 AM
As of Last Complete Printing
      Number of Pages: 128
      Number of Words: 33,698 (approx.)
      Number of Characters: 177,590 (approx.)

4. TASK 4: FEASIBILITY OF THE CONCEPT IN HARD SPECTRUM

Responsible Lead: CEA

Brief Discussion of Objectives:

The feasibility of using particle fuel in a fast neutron environment was investigated. Service conditions for particle fuel operating in a fast reactor were determined from reactor physics calculations. Based upon these operating conditions, candidate fuel designs and materials were evaluated for suitability.

The traditional TRISO fuel particle has been designed for operation in a mild, thermal neutron spectrum. Of particular concern when this design is exposed to a hard spectrum is the influence of radiation damage to the coatings. Radiation damage in excess of 200 dpa can be expected in gas-cooled fast reactors. The influence of He generation (from n-alpha reactions) and void swelling in the SiC and their influence on SiC strength will be investigated. In addition, the shrinkage and swelling in the pyrocarbon layers (IPyC and OPyC) at high fast neutron fluences is significant and may limit the lifetime of the fuel. Material properties of other more radiation-resistant candidate materials at high neutron fluences will be investigated and incorporated into the fuel behavior models as needed.

Work on this task included assessing the limits of the TRISO particle concept with respect to fast fluence. The approach was to consider the particle as designed for a thermal spectrum and to calculate the stresses and strains generated in the layers by a kernel ($(U, Pu)O_2$) submitted to fast neutron fluence (coupling of the deterministic model with the GERMINAL code dedicated to oxide fuel for fast breeders). Nevertheless, the flux was adjusted to reflect the fact that the power density in gas cooled fast reactors is significantly reduced compared to liquid metal cooled for example. The results were obtained in terms of the maximum reasonably achievable burnup given known properties of SiC and their dependence on temperature and fast neutron damage based on data from the literature (e.g. fusion).

4.1 Task Technical Overview: CEA

The studies of Gas Cooled Fast Reactor cores in the range 600 to 2400 MWth, liable to be self generating without blankets or with limited blankets, reveals in any case the following inputs for fuel design:

- the need for a high density of heavy atoms,
- a Pu enrichment of 15 to 20%,
- the request for materials to sustain fast fluences (E>0.1 Mev) as high as 10^{27} n/m^2,
- the ability of the fuel to retain fission products with the same performance (R/B ratio in normal, upset and accident situations) as required for thermal reactors.

The fact that fission products are associated with a closed cycle of all the actinides requires in addition that the fuel should be able to incorporate an amount of minor actinides in dilution for a fraction of 2 to ~5%, and be reprocessable.

In order to cope first with the conditions above, the burnup value to start with, i.e. 5 at%, is targeted not to enhance the challenges in fuel design. On this basis different types of fuel are envisaged. Among them, is particle fuel for which pros, cons and unknowns can be stated as follows:

- pros: local containment of fission products, different materials ensuring separated functions
- cons: complex manufacturing,
- unknowns: ability to increase heavy metal content, possibility to find materials able to work under fast fluence, and burnup potential.

What seems clear at this stage is that particle concept should be associated with large cores only (with less neutron leakage), the use of dense actinides compounds in kernels (i.e. mixed mono carbide or nitride rather than di-oxide) and reduced particle layer thickness to kernel diameter ratios, typically half the current values in HTRs (0.15 instead of 0.3).

A first attempt was made to assess such a particle with the ATLAS code. The concept is BISO coating, both layers being made out of SiC (dense for the barrier layer, porous for the buffer

layer). The relative proportion of the two layers was a parameter of the calculation. The table below lists the main parameters for the final concept.

Table 4-1. Fuel concepts for gas coated fast reactor.

Kernel	
Composition	(U,Pu)C
C/M	1.00
Enrichment Pu(%)	20.0
Diameter (μm), D	3200*
Initial porosity (50% open)	15%
Coatings, total thickness T SiC(μm)	482*
Density high density SiC *(g/cm³)*	3.20
Density porous SiC) *(g/cm³)* (initial value)	1.6

* T/D=.15

Reactor parameters were assumed as follows, corresponding to a "low" power density core (~40 MW/m³):

- Peak particle temperature: 600-1200°C

- Power: 3.3 W/kernel

- Fast fluence: 10^{26} n/m² /at %

Materials behavior was modelled as:

- kernel: swelling, gas release, thermal/elastic behavior (no irradiation/thermal creep)

- dense SiC: swelling (see figure below: swelling vs. fluence and temperature), thermal/elasto-viscoplastic behavior (irradiation creep)

- buffer: thermal/elastic behavior, densification under irradiation (different hypothesis tested)

The internal gas pressure is calculated at each time step with updated void volumes and gas concentrations.
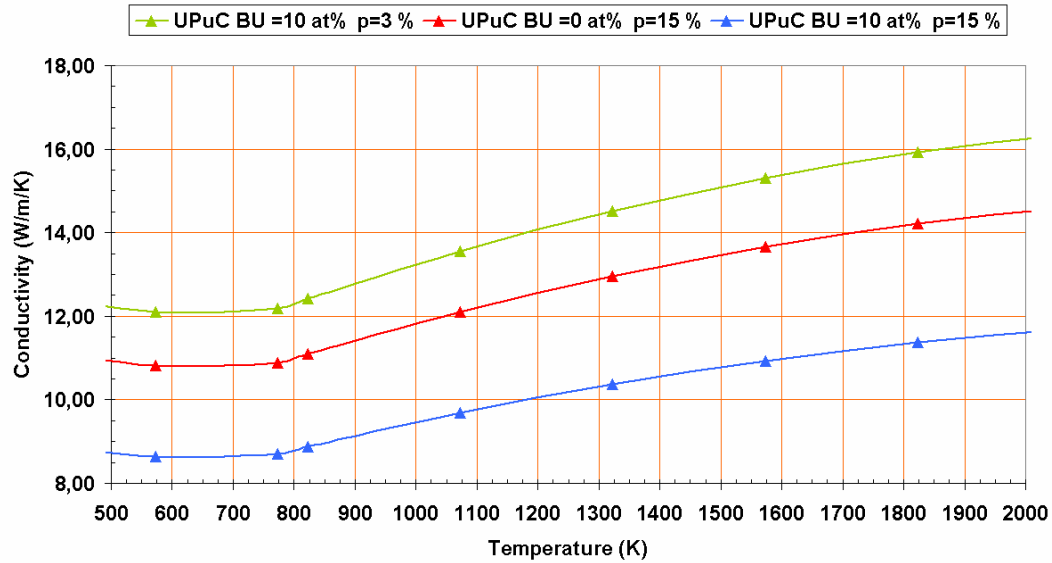
Figure 4-1. (UPu)C conductivity.

4.2   Task Technical Overview - INEEL

The concept of coated particle fuel embedded in a ceramic or metallic matrix has merit. However, with the high fast neutron fluence expected in gas cooled fast reactors, the effects of radiation damage from fast reactions, helium production from (n,α) reactions and hydrogen production from (n,p) reactions need to be considered. For the PyC layer, irradiation induced shrinkage and swelling limits the usefulness of this material to fast neutron fluences below 7-10 x 10^{25} n/m^2 (E>0.1 MeV). Fast neutron fluences in gas cooled fast reactors are expected to be 10 to 50 times greater than this value. The PyC layers would not survive in such radiation damage. For the SiC layer, data on radiation damage suggests that it is more resilient.

We have evaluated the use of traditional TRISO coatings for gas-cooled fast reactors. The hard neutron spectra will induce both displacement damage and cause threshold particle reactions that create an internal volumetric source of hydrogen and helium gases in the material. The resulting displacement damage and buildup of gases over time can in turn lead to degradation of the material's physical and chemical properties over time.

The fast gas-cooled reactor (GFR) spectrum is based on MCNP transport models developed for the pebble-bed GFR with metallic fuel spheres and supercritical CO_2 coolant. The GFR reactor is assumed to operate at a total core power of 600 MWt.

Computer Code

The neutronic analyses were performed with the MCNP (Monte Carlo N-Particle) code (Briesmeister 1997) version 4B (MCNP4B). This code is a general purpose, continuous energy, generalized geometry, coupled neutron-photon-electron Monte Carlo transport code and can be used to calculate reactor core eigenvalues, neutron spatial and spectral fluxes, nuclear reaction rates, and energy deposition. In our case, we are using MCNP4B to calculate threshold particle nuclear reaction rates in SiC that produce hydrogen and helium nuclei. The ENDF-VI cross-sections, 6000.60c and 14000.60c for natural carbon and silicon, respectively, were used in the calculation.

Nuclear Reactions

Although all of the following nuclear reactions were considered in the analysis, not all of them actually resulted in a production rate due to the relatively high threshold energy for some of these reactions. In fact, of the 13 reactions listed above in Table 4-1, only the following four nuclear reactions, (n,p), (n,d), (n,α), and (n,np) occurred for carbon for the GFR fission spectrum MCNP tallies. But all five listed nuclear reactions, (n,p), (n,d), (n,α), (n,nα), and (n,np) occurred for silicon.

Table 4-2. Hydrogen and helium production reactions considered in the analysis.

Element	Nuclear Reaction	MT Reaction
Carbon	(n,p)	103
	(n,d)	104
	(n,t)	105
	(n,α)	107
	(n,2p)	111
	(n,pα)	112
	(n,pd)	115
	(n,pt)	116
	(n,2nα)	24
	(n,np)	28
	(n,nd)	32
	(n,nt)	33
	(n,2np)	41
Silicon	(n,p)	103
	(n,d)	104
	(nα)	107
	(n,nα)	22
	(n,np)	28

Results

Based on the data in Table 4-3, the total hydrogen production rate would be 2.7674E+10 hydrogen atoms per cm^3 per second in the SiC material. The corresponding helium production rate would be 1.6851E+10 helium atoms per cm^3 per second in the SiC material. Therefore, from these production rates one can now estimate both the hydrogen and helium concentration (ppm) in SiC for a given irradiation time in the GFR (Table 4-4).

Table 4-3. GFR fission spectrum hydrogen and helium production rates by reaction.

Element	Nuclear Reaction	Production Rate (reactions/cm^3/sec)	Production Rate* (reactions/gm –SiC/sec)
Carbon	(n,p)	9.960E+05	3.113E+05
	(n,d)	2.398E+06	7.493E+10
	(n,α)	4.482E+09	1.401E+09
	(n,np)	1.082E+05	3.380E+04
Silicon	(n,p)	2.758E+10	8.617E+09
	(n,d)	2.885E+07	9.015E+06
	(n,α)	1.235E+10	3.861E+09
	(n,nα)	1.466E+07	4.582E+06
	(n,np)	6.632E+07	2.073E+07

* Density of SiC is assumed to be 3.2 g/cc.

Table 4-4. GFR fission spectrum hydrogen and helium concentrations (ppm) as a function of irradiation time.

Irradiation Time (days)	Hydrogen Concentration (ppm)	Helium Concentration (ppm)
30	0.04	0.09
60	0.08	0.18
100	0.13	0.30
150	0.19	0.45
200	0.25	0.60
250	0.31	0.76
300	0.38	0.91
400	0.50	1.21
500	0.63	1.51
600	0.75	1.81
700	0.88	2.12
800	1.00	2.42
1000	1.25	3.02

Displacement Damage

Atomic displacements are accepted as the principal underlying radiation damage mechanism for energetic neutron radiation in many materials. It is believed that accumulated displacements at the microscopic level (i.e., radiation damage) form the basis for the changes in material properties at the macroscopic level (i.e., radiation effects). Therefore, it is important to quantify the amount of displacements caused to such materials in the radiation field corresponding to their intended use. Dpa is a commonly accepted measure for radiation damage at the macroscopic level. The rational calculation of dpa requires the availability of displacement kerma cross sections for the materials of interest. The displacement kerma cross section has been a useful tool in calculating dpa because it allows the integration of the energy-dependent response of the material to the neutron radiation environment. Estimates for displacement kerma cross sections for silicon carbide and graphite have been developed and the results documented (Ougouag, Wemple, and Petti 2003).

Modifications have been made to the NJOY99 code to expand the capabilities of the displacement kerma cross section calculation method. These modifications include a method to calculate the contributions from generalized (multiple) particle emission, addition of the modified Kinchin-Pease (NRT) model, and other modifications to model non-monatomic solids more accurately. The results using the fast gas-cooled reactor spectrum mentioned above yields damage rates of

0.0403 dpa/day for C and 0.0470 dpa/day for SiC. For a 1000-day fuel lifetime this would result in about 40 dpa for C and 47 dpa for SiC.

Conclusions

For the fast fission environment of the GFR operating at 600 MWt, the total production rates for hydrogen and helium generation in SiC have been estimated. These production rates are readily converted to hydrogen and helium ppm concentrations for a given irradiation time in the reactor (Table 4-4). For a 1000-day fuel lifetime, 1.25 ppm hydrogen concentration and a 3.0 ppm helium could be expected to be generated in the SiC. Similar values would be expected in graphite. The seemingly small gas production rates can be attributed to the high threshold energies required to induce these reactions (7-16 MeV) and the small nuclear reaction cross sections (~0.1-0.3 barns) for both silicon and carbon. These gas concentrations are small enough not to be a first order concern from materials perspective.

In terms of displacement damage, 40 to 50 dpa could be expected in C and SiC of TRISO coated particles. This damage is based on the average neutron flux in the GFR. Peak damage could be twice this value if peaking factors are on the order of 2 in the system. These damage rates are high enough that radiation damage could influence the material properties. In particular the high radiation damage to the C layers would result in acceptable dimensional change. At this level of radiation damage, SiC would also see significant property changes in terms of strength, swelling and other material properties. The use of the traditional TRISO coating is not recommended for coated particle fuels in fast spectrum reactor applications.

Filename: 5. INERI Task 4.doc
Directory: C:\Documents and Settings\talbhd\Desktop\FINAL INERI JAN3
Template: C:\Documents and Settings\talbhd\Application
    Data\Microsoft\Templates\Normal.dot
Title: Task 4: FEASIBILITY OF THE CONCEPT IN HARD SPECTRUM
Subject:
Author: test
Keywords:
Comments:
Creation Date: 1/4/2005 12:21:00 PM
Change Number: 3
Last Saved On: 1/4/2005 12:22:00 PM
Last Saved By: test
Total Editing Time: 1 Minute
Last Printed On: 1/18/2005 10:59:00 AM
As of Last Complete Printing
    Number of Pages: 8
    Number of Words: 2,009 (approx.)
    Number of Characters: 10,811 (approx.)

5. TASK 5: IRRADIATION OF PROTOTYPE PARTICLES

Responsible Lead: INEEL

Brief Description of Objectives:

The logical follow on to the development and design of advanced prototype particle fuel is fabrication and irradiation testing. U.S. and French plans are discussed.

5.1   Task Technical Overview: INEEL

The Advanced Gas Reactor Fuel Development and Qualification Program is planning a series of irradiation experiments in the Advanced Test Reactor (ATR) at the INEEL. These experiments will irradiate TRISO-coated UCO fuel particles to (and perhaps beyond) maximum conditions envisioned for a next generation Very High Temperature Reactor (VHTR). To ensure prototypic conditions and limit potential deleterious interactions, the irradiation acceleration will be kept within three times that expected for real time in the reactor. The large B positions within the ATR are well suited for such irradiations. Full burnup and fast neutron fluence can both be achieved within a reasonable time yet not exceed the 3X acceleration factor. Figure 5-1 presents projections for 19.7% enriched UCO fuel at the test capsule mid-plane irradiated in a large B position of the ATR. The burnup projections show the effect of surrounding the test fuel with graphite holders containing 6 wt% boron carbide. Early in the irradiation, the boron carbide flattens the power generation within the fuel and allows for greater temperature control of the test. After 600 effective full power days of irradiation (about 2 calendar years), the fuel reaches a burnup of 19.4 %FIMA and a fast neutron fluence of 3.95×10^{25} n/m^2 (E>0.18 MeV). These peak conditions represent an acceleration factor of about 1.5 times that expected in the actual reactor. Such irradiation conditions would also be suitable for testing other prototype fuel particles developed in the future.
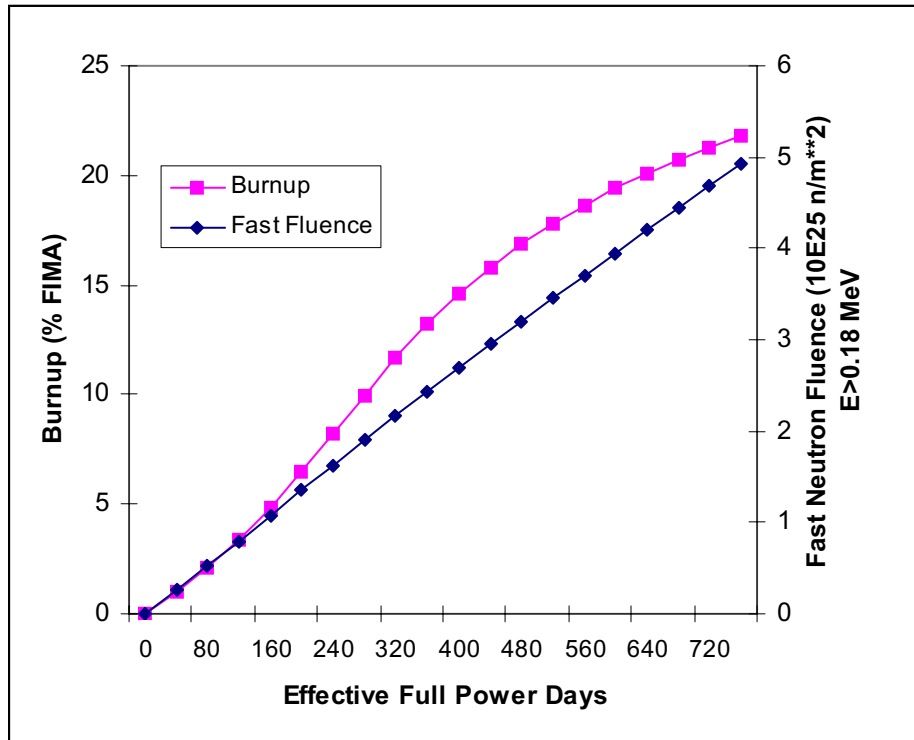
Figure 5-1. AGR-1 projections at capsule midplane in the ATR.

5.2 Task Technical Overview- CEA

An extensive HTR Fuel irradiation program (the SIROCCO program) is planned by CEA and AREVA:

- to provide data on fuel performance under irradiation
- to support fuel process development
- to qualify fuel under normal operating conditions, non operating conditions and accidental conditions
- to support development and validation of fuel performance and fission product transport models and codes.

This irradiation program will mainly be conducted at the French Material Testing Reactor OSIRIS (CEA, France, Saclay) with HTR fuel manufactured by the GAIA line (CEA, France, Cadarache).

Currently, the first two irradiations are well defined and under preparation. These irradiations address the first step in the qualification of UO_2/SiC reference industrial (German fuel). The objectives of the first irradiation are to verify the quality of the fuel in terms of integrity and fission product retention.

Table 5-1. Fuel description.

Type of particle	UO_2/Buffer/OPyC/SiC/IPyC
Particle geometry	German reference geometry (500/95/40/35/40 µ)
Matrix geometry	Compact
Enrichment (%)	9.2
Packing fraction (%)	~10 (about 1500 particles per compact)

Table 5-2. Irradiation conditions.

Fuel surface temperature (˚C)	~ 1000
Fluence (n/m^{-2})	$> 2 \times 10^{25}$
Power density (W/particle)	<0.2
Duration (EPFD)	~150

The fuel quality verification will consist of a direct comparison between new French particles and German particles. The best historical German particles will be compacted according to the same CERCA process, the same packing fraction, the same enrichment and irradiated in the same device (with a separate fission gas release measurement system) under the same irradiation conditions. This will allow the determination of the new French fuel quality in comparison to the German reference fuel with a high degree of confidence in terms of fission gas release, PIE and safety tests. In addition, these two set of particles will be characterized before and after irradiation with the same QC methods.

The objective of the second irradiation is to verify the ability of the reference particle to withstand VHTR conditions.

Table 5-3. Fuel description.

Type of particle	UO_2/Buffer/OPyC/SiC/IPyC
Particle geometry	German reference geometry (500/95/40/35/40 µ)
Matrix geometry	Compact
Enrichment (%)	9.2
Packing fraction (%)	~10 (about 1500 particles per compact)

Figure 5-4. Irradiation conditions.

Fuel surface temperature (°C)	~1100 and 1200
Burn up (%FIMA)	~15
Power density (W/particle)	< 0.2
Duration (EPFD)	~450

The continuous-on-line fission product release measurements and PIE will form the basis of the industrial fuel qualification program.

Following irradiations will allow for the licensing of the UO_2/SiC reference industrial fuel, and supply material properties for modelling codes, and finally qualify the fuel.In the future, the SIROCCO program will also deal with optimized HTR fuel (material, geometry…) to obtain high temperature and high burnup conditions.

In addition to the SIROCCO program, an irradiation of fuel material in HFR has been proposed in the European program FP6 and is under negotiation with the EC. In the WP3 of the HTR-F project, kernel and layer properties have been gathered and incorporated into the ATLAS code. Thermal and mechanical calculations by the code pointed out the most important parameters governing stresses in the layers as irradiation induced dimensional change rate and irradiation-induced creep of the PyC layers. Moreover, the properties of PyC can be extremely variable, being highly dependent on the exact details of the manufacturing procedure. In the past, major HTR projects have both manufactured coated particles and measured properties of their PyC. Among these were the Dragon Project, UKAEA and the U.S. Although the Dragon Project and UKAEA work occurred in the same country, the programs were quite distinct. Understandably, observed values of properties that are structure sensitive were not identical for materials manufactured by different organizations. Thus, it would be imprudent to assume that the properties of PyC deposited on particles manufactured nowadays will be identical to those of the past, even if attempts are made to reproduce closely previously manufacturing conditions.

In order to be able to obtain the required information, two irradiations are proposed. The design of the two experiments will be similar, but one irradiation will be relatively short in order to obtain a fluence of 1-2 x 10^{25} n/m^2 (E>0.1 MeV) and the other irradiation will be relatively long

in order to obtain a fluence of 3-6 x 10^{25}. These two irradiations are planned to start simultaneously:

Table 5-5. Proposed irradiation experiment conditions.

	Irradiation #1	Irradiation #2
Irradiation position	HFR-G3	HFR-G3
Temperature (^{o}C)	900, 1100, 1300	900, 1100, 1300
Irradiation time (Full Power days)	100	350
HFR cycles (~25 F.P. days/cycle)	4	14
Irradiation time (Calendar days)	120	425
Thermal fluence	0.7-1.2 x 10^{25}	2.7-4.2 x 10^{25}
Fast fluence (E>0.1 MeV)	1.0-1.7 x 10^{25}	3.8-6.0 x 10^{25}

Several types of fuel specimens, coating and graphite materials will be made. Batches of about 50-100 particles/kernels will be irradiated in order to be able to have access mean values.

Filename: 6.   TASK 5 .doc
Directory: C:\Documents and Settings\talbhd\Desktop\FINAL INERI JAN3
Template: C:\Documents and Settings\talbhd\Application
     Data\Microsoft\Templates\Normal.dot
Title: 5
Subject:
Author: test
Keywords:
Comments:
Creation Date: 1/18/2005 12:00:00 PM
Change Number: 2
Last Saved On: 1/18/2005 12:00:00 PM
Last Saved By: test
Total Editing Time: 0 Minutes
Last Printed On: 1/18/2005 12:01:00 PM
As of Last Complete Printing
     Number of Pages: 5
     Number of Words: 1,113 (approx.)
     Number of Characters: 6,200 (approx.)

Appendix A (MIT):
Silver Transport Literature Review and Assessment

Introduction

In many previous silver transport tests, coated fuel particles were irradiated, often at low temperatures to prevent fission product migration, and then heated, out-of-pile, to measure fission product release. Various measurement techniques were used to evaluate fission product migration and release including on-line gas measurement systems, gamma counting for fission product inventory, periodic analysis of fission product plate-out on cold traps, and electron microscopy.

Experimenters often selected heating temperatures to represent typical HTGR operating conditions. However, some experiments were conducted at elevated temperatures to either simulate accident conditions or to accelerate fission product release. Bullock selected annealing temperatures between 1200°C and 1500°C, above those expected during operation, in order to accelerate the diffusive release of fission products (Bullock 1984). While high-temperature testing may be more aggressive than typical operating temperatures during irradiation, it does allow experimenters the ability to obtain relative comparisons between different fuel types in a more efficient manner.

Fuel particles retain fission products either by forming chemically stable compounds in the fuel kernel or in one of the coating layers or by preventing diffusion through the coating layers. Fission products that do not form stable compounds in the fuel particle are thought to diffuse through the coating layers. If the diffusion rate is sufficiently slow, the fission products will remain in the fuel particle during operation. If the diffusion rates are fast enough, however, fission products may escape, depending on the temperature and duration of operation.

Diffusion is generally reported as an Arrhenius equation of the form:

$$D = D_o \cdot \exp\left(\frac{-Q}{R\,T}\right) \tag{A-1}$$

where
- D = diffusion coefficient (m^2/s),
- D_o = pre-exponential constant (m^2/s),
- Q = activation energy (J/mol),
- R = universal gas constant (8.314 J/mol·K), and
- T = absolute temperature (K).

The two most common types of silver experiments encountered in the literature are batch experiments in which the total fission product release from a population of particles is measured, and individual experiments in which the fission product inventory of each fuel particle is measured before and after heating.

In batch experiments, cold plates typically collect metallic fission products released from a large population of fuel particles or even whole fuel elements (pebbles or compacts). Periodic analysis, typically gamma-counting, of the cold plates reveals any condensed metallic fission products released from the entire population of particles. Sweep gas monitoring during these heating experiments detects catastrophic particle failure by detecting pulses in release in the sweep gas stream characteristic of fission gas release accompanying through-coating particle failure.

Although batch measurements during heating experiments can document the overall behavior of a large population of fuel particles, these measurements do not give any insight into individual particle behavior. Attempts to measure individual fuel particle inventories are reported in the literature, but are limited by the time and resources required to separately examine each individual particle. For this reason, individual fission product inventory measurements tend to only survey a limited number of fuel particles, on the order of 10-25 per test. While these individual measurements may supply more detailed information about particle performance, they are hampered by poor statistics, using only a small number of particles to characterize large batches of fuel with greater than 3×10^9 particles proposed for a single HTGR core. Similar to bulk measurements, individual particle inventory measurements also do not reveal the specific release pathway.

Batch Measurements

Many experiments have used fission product release measurements from a large batch of particles during post-irradiation heating to gather information on overall fuel performance. Common measurements include on-line monitoring of fission gas release in the sweep gas system and periodic gamma counting of the metallic fission products condensed on a cold plate assembly. In batch testing, large populations of fuel particles, either loose or bonded in fuel elements, are heated together and the total amount of released fission products is measured. Using analytical and numerical solutions for diffusion and release from spherical shells, researchers calculate effective diffusion coefficients in the different layers.

Assumptions

An inherent assumption when evaluating fuel performance from batch measurements is that all of the fuel particles within the batch behave the same. This would indeed be the case were a thermally activated process such as diffusion to be the operative phenomena where one would expect "average" behavior from similarly fabricated/processed material. Fission gas release values can be used to estimate the number of individual failed particles by comparing the amount of fission gas released to the estimated average particle inventory. In most cases, however, solid fission product collection on cold plates is attributed to all particles equally.

Silver Diffusion in UO₂

Silver release from fuel kernels in coated particles via diffusion largely determines the amount of silver available to escape through the rest of the coatings. Any silver retained in the fuel kernel itself will not be released from the fuel particle. Several studies have measured silver diffusion from UO₂ fuel kernels either from bare kernels or from BISO particles coated with a buffer and a single pyrocarbon layer. Nabielek et al. determined the diffusion coefficient of silver in UO₂ as:

$$D'_{UO_2} = 5.49 \times 10^{-2} \cdot \exp\left(\frac{-213 \frac{kJ}{mol}}{R\,T}\right) s^{-1}$$

$$D'_{UO_2}\left(1500^o C\right) = 2.68 \times 10^{-8}\ s^{-1}$$

(A-2)

where D' is the reduced diffusion coefficient, equal to the diffusion coefficient divided by the grain size, a, squared (Nabielek, Brown, and Offerman 1977).

$$D' = \frac{D}{a^2}$$

(A-3)

From a separate set of experiments, Nabielek et al. determined a slightly lower silver diffusion coefficient in UO₂ at 1500°C:

$$D'_{UO_2}\left(1500^o C\right) = 9.3 \times 10^{-9}\ s^{-1}$$

(A-4)

Brown and Faircloth also measured silver diffusion in UO₂ using radiochemical analysis to measure the silver content of fuel kernels after irradiation and comparison to the calculated inventory based on the irradiation conditions (Brown and Faircloth 1976). Testing fuel irradiated between 1000°C and 1400°C, Brown and Faircloth derived the following reduced diffusion coefficient for silver in UO₂ fuel:

$$D'_{UO_2} = 3.80 \cdot \exp\left(\frac{-269\,\frac{kJ}{mol}}{R\,T}\right) s^{-1} \tag{A-5}$$

Since the buffer and pyrocarbon layers do not retain silver, Förthmann et al. measured silver release from PyC-coated particles at 1400°C and determined the kernel release using the equivalent sphere model (Förthmann et al. 1982). In this model, also known as the Booth model, the fuel kernel is assumed to consist of spherical grains of equal radius. The equivalent sphere model also assumes that when diffusing atoms reach the surface of a spherical grain they are able to move rapidly along grain boundaries; only the spherical grains, not the grain boundaries, slow atom transport in this model.

$$D_{UO_2}(1400°C) = 6.9 \times 10^{-15}\,\frac{m^2}{s} \tag{A-6}$$

According to Förthmann et al., the time dependence of fractional release from SiC-coated particles contains two contributions: 1) spontaneous release described by the Booth model, and 2) diffusion-controlled release starting after a breakthrough time. No explanation is offered for the observation of spontaneous silver release.

No Silver Retention in PyC

It is well accepted in the literature that pyrocarbon layers do not retain silver. Nabielek et al. compared silver release from bare kernels and BISO particles, those containing a fuel kernel surrounded only by buffer and PyC layers. From these results Nabielek et al. concluded there is no silver holdup in low-density graphite buffers or in any type of pyrocarbon (Nabielek, Brown, and Offerman 1977). Additionally, Nabielek et al. found that graphite matrix materials also do not retard silver at temperatures above 850°C. Offermann derived the following diffusion coefficient for silver in pyrocarbon after implanting silver in flat pyrocarbon samples and heating at constant temperatures between 450°C and 800°C (Offerman 1977).

$$D_{PyC} = 1.00 \times 10^{-8} \cdot \exp\left(\frac{-164\,\frac{kJ}{mol}}{R\,T}\right) \frac{m^2}{s} \tag{A-7}$$

McCardell et al. extrapolated this fit to 1250°C, typical of fuel operating temperatures, and determined that breakthrough times for silver in pyrocarbon are on the order of hours (McCardell 1992). This indicates that PyC does not function as a barrier to silver release during normal operation.

Verfondern et al. summarized the diffusion coefficients reported from a variety of sources (Verfondern, Martin, and Moormann 1993). Two diffusion coefficients for silver in pyrocarbon are listed below with the source country (research program) in brackets:

$$D_{PyC} = 5.3 \times 10^{-9} \cdot \exp\left(\frac{-154 \frac{kJ}{mol}}{RT}\right) \frac{m^2}{s} \quad \text{[FRG, USA]} \tag{A-8}$$

$$D_{PyC} = 5.3 \times 10^{-4} \cdot \exp\left(\frac{-193 \frac{kJ}{mol}}{RT}\right) \frac{m^2}{s} \quad \text{[Russian Fed.]} \tag{A-9}$$

The three diffusion coefficients for silver in PyC discussed above are plotted as a function of temperature in Figure A-1.
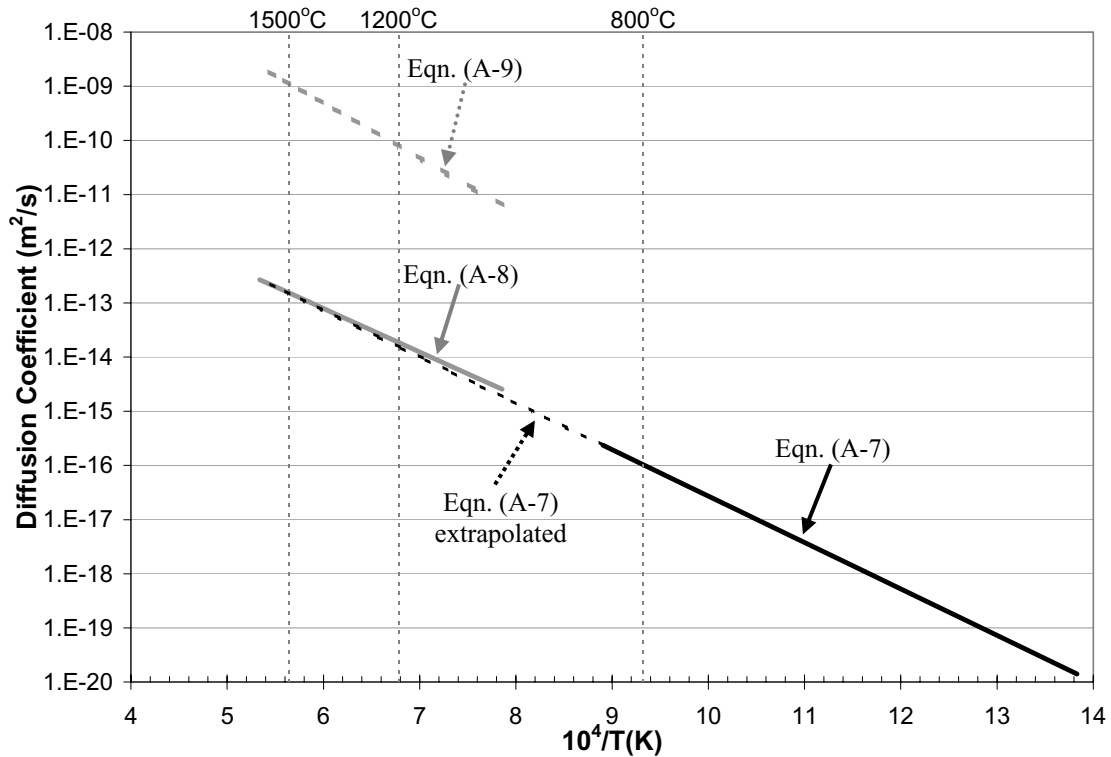
Figure A-1. Diffusion coefficients for silver in pyrocarbon.

The breakthrough time through a thin spherical shell can be approximated from the following relationship:

$$D = \frac{x^2}{6t_o} \qquad \text{(A-10)}$$

where D is the diffusion coefficient (m²/s), x is the shell thickness (m), and t_o is the breakthrough time (s) (the time when the diffusing atoms reach the outer surface of the shell). At 1500°C, the relationship shown in Equation (A-10) predicts silver breakthrough from a 40-μm thick PyC shell in approximately 30 min using the diffusion coefficients in Equations A-7 and A-8 and in less than 1 sec using the diffusion coefficient shown in Equation A-9. These estimated breakthrough times through PyC coatings are short enough that diffusion through PyC layers is usually neglected; any silver released from the fuel kernel is assumed to migrate directly to the inner surface of the SiC coating.

Silver Transport in Silicon Carbide

Observations recorded during previous testing have suggested that silver migration in coated fuel particles is governed by diffusion through intact silicon carbide layers. This conclusion has been driven by results of silver release from coated particles while the volatile fission gases and cesium are still retained. Through-coating failures, where both pyrocarbon layers and the silicon carbide layer have failed and the fuel kernel is exposed, result in the release of the fission gases and any other mobile fission product. At typical operating and testing temperatures, cesium and silver escape from fuel particles with through-coating failures.

To date, the literature data has been interpreted as representing diffusion-controlled release of silver through intact silicon carbide layers. Observations of silver release with cesium retention suggest rapid silver diffusion through intact silicon carbide layers. If the silicon carbide layer were not intact, both cesium and silver should escape. Additionally, activation energies calculated for silver diffusion coefficients in silicon carbide (derived from silver release measurements) fall in the same range as activation energies for grain boundary diffusion of other fission products (Amian and Stöver 1983). Thus, the current interpretation of silver migration data indicates that silver diffuses along grain boundaries in intact silicon carbide at typical operating temperatures. Variations in the diffusion coefficients reported, however, are not

consistent with grain boundary diffusion and other observations, described below, raise doubts about diffusion as the dominant silver transport mechanism.

Nabielek et al. measured silver release from a variety of fuel particles during irradiations and posit-irradiation anneals. Silver detected by gamma-ray spectrometric measurements in fuel tubes and other graphite components was interpreted as release due to diffusion. By measuring the fractional release of silver from a variety of coated particle types, in both loose and elemental form, between 850°C and 1500°C, Nabielek et al. derived an upper limit of the effective diffusion coefficient for silver in silicon carbide:

$$D_{SiC} = 6.76 \times 10^{-9} \cdot \exp\left(\frac{-213\frac{kJ}{mol}}{R\,T}\right)\frac{m^2}{s} \qquad \text{(A-11)}$$

Nabielek et al. also heated 170 previously irradiated TRISO fuel particles at 1500°C and measured the total fission product release every 10 days. While cesium and strontium were retained in the TRISO particles, silver release began after 10 days. According to the authors, however, the shape of the release curve with heating time is not consistent with silver diffusion in SiC. At the beginning of the heat treatment silver release matched the characteristic release curve corresponding to a diffusion coefficient of 10^{-16} m^2/s, but as the heat treatment progressed the silver release corresponded to a diffusion coefficient of 10^{-15} m^2/s. The authors suggested instead that the silicon carbide became gradually "transparent" during heating allowing increased silver release. Although a physical mechanism for this apparent change in the SiC properties during the heat treatment was not proposed, this finding suggests that silver release is not dominated by a classical diffusion mechanism

In other irradiation experiments performed by Nabielek et al. a very steep increase in silver release was noted between 1140°C and 1240°C in both the shorter and longer duration experiments (Nabielek, Brown, and Offerman). These results indicate that SiC may only perform as an effective barrier to silver release at temperatures below 1200°C.

Brown and Faircloth compared silver release behavior from BISO and TRISO particles. While the BISO particles exhibited rapid silver release starting at the beginning of the annealing period, the silicon carbide layer in the TRISO particles prevented silver breakthrough for 16 days at

1500°C (Brown and Faircloth 1976). Brown and Faircloth determined an effective diffusion coefficient for silver in SiC from the breakthrough time:

$$D_{SiC}(1500°C) = 1.5 \times 10^{-16} \frac{m^2}{s} \qquad \text{(A-12)}$$

Amian and Stöver measured silver and cesium release from loose particles that had been previously irradiated at temperatures varying from <<400°C to 1050°C. Other irradiation parameters included a burnup range between 2.3% and 12.1% FIMA and a fast fluence range from <0.5×10^{23} n/m^2 to 8.2×10^{23} n/m^2. Different particle types had different fuel kernel materials with slight variations in coating dimensions. Water-cooled cold plates in the furnace collected released silver and were removed and counted periodically during heat treatments. Fractional release results were interpreted using Fickian diffusion theory and evaluated with a simple diffusion model with multizone geometry to estimate diffusion coefficients for each heat treatment. Combining all of the results, Amian and Stöver derived a diffusion coefficient for silver in silicon carbide (Amian and Stöver 1983):

$$D_{SiC} = 4.5 \times 10^{-9} \cdot \exp\left(\frac{-218 \frac{kJ}{mole}}{R\,T}\right) \frac{m^2}{s} \qquad \text{(A-13)}$$

Figure A-2 shows this diffusion coefficient along with the diffusion coefficients listed for each batch test. The diffusion coefficients cover a span greater than one order of magnitude at any given temperature. At 1000°C, the 95% confidence region for this diffusion coefficient is between 2×10^{-18} m^2/s and 1.5× 10^{-17} m^2/s.
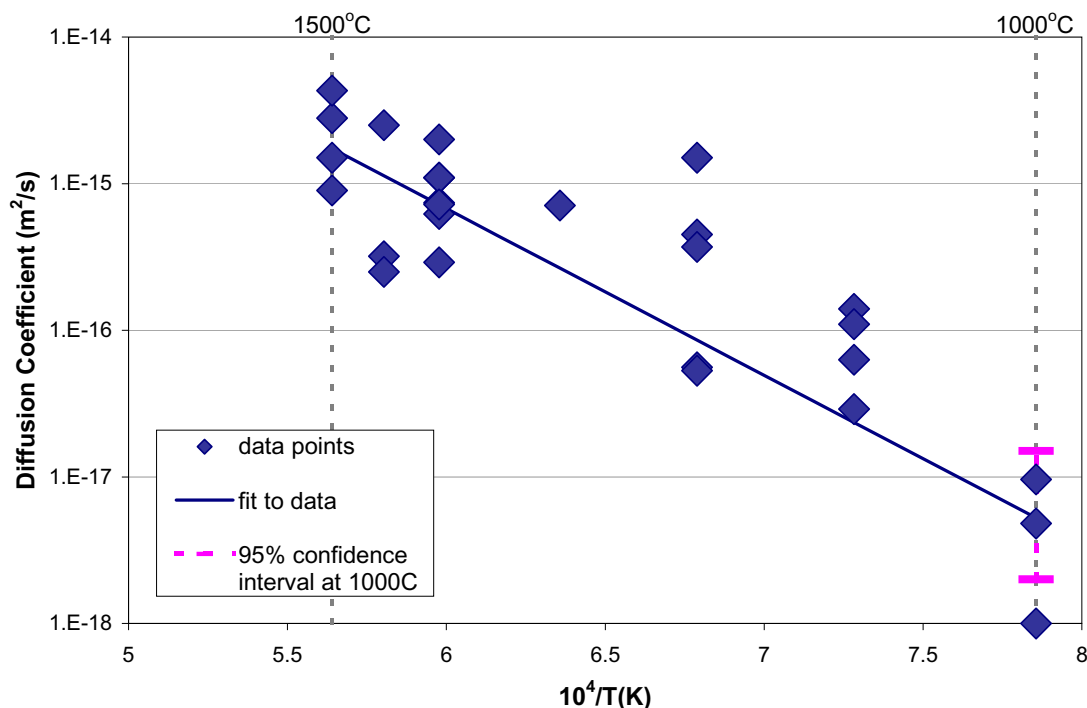
Figure A-2. The calculated diffusion coefficients from Amian and Stöver's post-irradiation annealing tests exhibit scatter up to a factor of 30.

Total silver release values were normalized to the estimated silver inventory before heating to calculate the fractional release. Amian and Stöver attribute scatter in the diffusion coefficient results to variations in the specific silicon carbide microstructure, which varies from coating to coating. Within the range of burnup and fast fluence of the tested fuels, the authors found no dependence of silver diffusion on those variables within the intrinsic scatter of the data (Amian and Stöver 1983).

According to Amian and Stöver, activation energies for diffusion in pyrolytically deposited SiC coatings are approximately 200 kJ/mol while the activation energies for diffusion in single crystals are about 450 kJ/mol (Amian and Stöver 1983). Given the results of the experiments performed by these authors, these data (and the diffusion coefficient proposed) suggest that the mechanism responsible for silver diffusion in SiC is grain boundary diffusion in the polycrystalline material, not volume diffusion through grains. A grain boundary diffusion mechanism also accounts for the large scatter in the data, according to the authors. Grain boundary diffusion depends on the exact microstructure of the sample, which varies from sample to sample. Grain boundary diffusion is a collection of "different elementary processes" with

different activation energies. Since each sample has a different microstructure, there will be scatter in the data reflecting the exact microstructure of each sample (the exact path of Ag transport through a given set of SiC grains). However, the scatter in the reported data exceeds the expected variations in SiC structure and the silver path length traveled through the SiC coatings.

Bullock measured the cumulative release of silver and other fission products at three temperatures from five types of previously irradiated fuel. TRISO coatings formed the basis of the five types of fuel, but three variations in the fuel kernel material and two variations to the TRISO coating constituted the experimental base. The five types of fuel denoted by their fuel kernel material include UO_2; UC_2; UCO, a mixture of UO_2 and UC_2; $UO_2^*(1)$, UO_2 with a solid ZrC overcoating on the kernel; and $UO_2^*(2)$, UO_2 with ZrC dispersed in the buffer layer. Three sets of ten particles of each fuel type were selected to be heated at three temperatures: 1200°C, 1350°C, and 1500°C. Fission products released during annealing condensed on the mullite sleeve or tantalum tube in the furnace. By periodically removing these components from the furnace and counting them with a gamma detector, Bullock collected fission product release data as a function of time during the greater than 10,000-hour tests (Bullock 1984).

These heating experiments revealed strong temperature dependence: as the temperature increased, the fission product breakthrough times decreased dramatically. The breakthrough times also appeared to depend on the type of fuel particle tested. The $UO_2^*(1)$ particles did not release any fission products during the annealing tests while the other particle types all released silver with breakthrough times varying from about 30 h to 8,000 h. Each batch, however, consisted of only ten particles and one must exercise caution when drawing conclusions about large population behavior from only a few particles.

The fairly long delay times, in general, before silver release do suggest that no silver escaped during irradiation. Silver escape during irradiation would have (most likely) required silver distribution throughout the particle. If that were the case, silver escape during heating would have occurred much sooner. This does raise concern about the knowledge of the silver distribution before heating began. The silver concentration at the beginning of heating must be assumed in order to accurately calculate the diffusion coefficients from release measurements. If these data are uncertain, however, the uncertainty of the diffusion coefficient will increase.

Schenk and Nabielek conducted post-irradiation annealing of 60 mm diameter spherical fuel elements, with 16,400 particles per element, between 1600°C and 1800°C. Seven fuel elements with low-enriched UO_2 with TRISO coatings were irradiated and heated. During irradiation these elements experienced a range of burnup from 3.5% to 10.6% FIMA, fast fluence from 0.2×10^{23} n/m^2 to 5.9×10^{23} n/m^2, a mean irradiation temperature of 700°C to less than 1280°C, and durations from 350 to 1200 full power days (Schenk and Nabielek 1991). The fission product content of each spherical element was measured before and after heating. In addition, electrolytic deconsolidation of the elements after heating exposed individual fuel particles, which could be selected from specific locations of the element and further analyzed.

During heating, a water-cooled cold finger with a removable condensation plate collected released fission products. Analysis of the condensation plate determined the quantities of ^{137}Cs, ^{90}Sr, and ^{110m}Ag. Analysis of the matrix graphite from the fuel elements after electrolytic deconsolidation also determined fission product release. All seven fuel elements released a greater fraction of their silver inventory than any other fission product. The high release of silver from these fuel elements was attributed to its high mobility in silicon carbide, but Schenk and Nabielek did not calculate any diffusion coefficients from these results.

Schenk and Nabielek derived the fractional release values by comparing the total amount of silver released during heating (as trapped on the cold plate) with the measured inventory before heating. If one looks, however, at the reported values from a different perspective, one can calculate the number of failed particles necessary to release the same amount of silver. With 16,400 particles per element, if one particle lost its entire silver inventory, the effective fractional release would be 6.1×10^{-5}. Using this base value, the fractional release values are converted to an equivalent number of failed particles as listed in Table A-1.

Table A-1. ^{110m}Ag fractional release increases with heating temperature.

Heating Temperature (°C)	Heating Time (h)	^{110m}Ag Fractional Release	Equivalent Failures
1600	138	2.8×10^{-3}	46
	500	9.0×10^{-4}	15
	500	2.7×10^{-2}	443
1700	185	4.8×10^{-2}	787
1800	100	0.17	2788
	100	0.67	10988
	200	0.62	10168

Although an increase in silver release would be expected to accompany an increase in temperature, according to the Arrhenius form of diffusion, seen in Equation A-1, other mechanisms may also produce these results. Measurements of silver release from the collection of coated fuel particles inside an element do not provide any insight to the mechanism controlling silver transport. The equivalent failures calculated from the fractional release values shown in Table A-1 indicate that a mechanism resulting in complete silver loss from a fraction of the particles in the element could produce the same observed quantities of silver release. As the temperature increases the number of particles releasing their entire silver inventory would also increase if silver transport were dominated by cracks in the SiC layer whose formation was exacerbated by higher temperatures.

Förthmann et al. also measured the fractional release of silver from UO$_2$ TRISO-coated fuel particles in post-irradiation heating at 1400°C, but they focused on the variation in the calculated diffusion coefficient with variations in SiC coating parameters (Förthmann et al. 1982) While such variables as the SiC density, grain size, microstructure, and light reflectivity had no apparent correlation with silver release the authors did report a range of diffusion coefficients corresponding to the range of deposition temperatures and carrier gas used during SiC deposition. Seven types of fuel, compressed with matrix graphite to form compacts, were heated at 1400°C after irradiation. A cold plate collected silver released from the fuel particles. Silver was leached off the cold plate and counted after different annealing periods.

In an effort to account for multiple contributions to silver release Förthmann et al. modeled the results with a spontaneous release portion, described by the Booth model for release from the kernel, along with the more complicated diffusion-controlled release after a breakthrough time (Förthmann et al. 1982). The spontaneous release portion of the silver release curve provides a

steady contribution of silver before the general breakthrough of silver and is most likely due to uranium contamination outside of the silicon carbide layer. Any silver born outside the silicon carbide layer will be released almost immediately and contribute to the overall silver deposition on the cold plate.
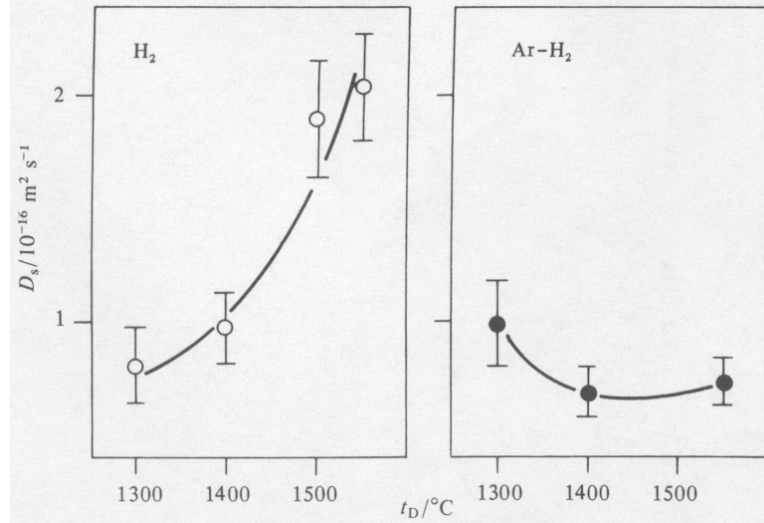
Figure A-3. Diffusion coefficients at 1400°C for ^{110m}Ag in SiC deposited by H_2 and Ar+H_2 have opposite trends with deposition temperature.

The diffusion coefficient increased from 8.0×10^{-17} m^2/s to 2.0×10^{-16} m^2/s as the deposition temperature increased from 1300°C to 1550°C for SiC deposited in pure hydrogen (Förthmann et al. 1982). Förthmann et al. also noted that the SiC microstructure consisted of striated structure with free silicon when the deposition temperature was 1300°C, crystalline structure with small crystallite sizes when the deposition temperature was 1400°C, and large columnar crystals when the deposition temperature was 1500°C. The presence of free silicon in the SiC deposited at 1300°C does not result in increased silver diffusion as suggested by Nabielek et al. (Nabielek, Brown, and Offermann 1977). For SiC deposited in pure hydrogen, it appears that the silver diffusion coefficient increases as the SiC microstructure becomes more columnar, but the total change in the diffusion coefficients with SiC deposition temperature is much smaller than the range observed in the literature that a definite trend cannot be verified. Additionally, the residual stress state within the SiC coatings is different for different SiC grain structures and those stresses may play a role in the ability of SiC to retain silver.

For SiC deposited in a mixture of argon and hydrogen, the diffusion coefficient decreased from $9.9 \times 10^{-17} m^2 /s$ to $7.3 \times 10^{-17} m^2/s$ as the deposition temperature increased from 1300°C to 1550°C. Förthmann et al. observed less variation in the SiC appearance with temperature for the SiC deposited in an argon-hydrogen mixture. The SiC consisted of crystalline structure with small crystallite sizes when the deposition temperature was 1300°C, small and uniformly distributed crystallites when the deposition temperature was 1400°C, and coarse-grained but not columnar grains when the deposition temperature was 1550°C. No correlation between the SiC microstructure and silver release could be determined from these data.

Although the trend of diffusion coefficient change with respect to deposition temperature appears fairly clear (at least for SiC deposited in pure hydrogen), as shown in Figure A-3, and the uncertainty bands are fairly small, the values reported here are all within the range of diffusion coefficient reported by other authors. Based on the small variation in Förthmann et al.'s data relative to the other data reported in the literature, one cannot conclude that the change in SiC microstructure associated with the change in SiC deposition temperature is a primary contributor to silver transport in SiC.

A collaboration between JAERI (Japanese Atomic Energy Research Institute) and ORNL (Oak Ridge National Laboratory) irradiated and heated UO_2 TRISO-coated particles. Capsule HRB-22 contained 12 annular fuel compacts composed of 32,200 UO_2 TRISO-coated particles dispersed in a graphite matrix. The irradiation of capsule HRB-22 lasted 88.8 effective full power days with a maximum burnup of 6.7% FIMA, maximum fast fluence of 2.8×10^{25} n/m^2, and the maximum fuel compact temperature maintained below 1300°C (Minato et al 1998).

The sweep gas monitoring system examined fission gas release during irradiation with coating failures causing a distinctive pulse in the ion chamber signal. Four pulses in the sweep gas monitoring system indicated single particle failures at 29.57, 32.52, 56.91, and 83.07 effective full power days. These through-coating failures suggest a failure fraction during irradiation of 1.2×10^{-4}. The release-to-birth ratio (R/B) was also monitored during irradiation. The R/B results suggest that there were two through-coating failures at the beginning of the irradiation. Silver release was not measured during irradiation, but further heating tests on this fuel are discussed below.

Accident condition testing on the irradiated fuel subjected one intact compact to 219 h at 1600°C. Krypton gas release was monitored continuously during the heating test and silver release was monitored periodically by measuring collection on a removable deposition cup in the furnace. High gas release measurements during the test indicate that there may have been two or three failed particles at the beginning of the heating test. The rapid krypton release indicative of an additional particle failure caused a spike in the gas monitoring system about 49 h into the test. According to the measurements of the deposition cup, the fuel particles in the element released 38% of their silver while only releasing 1% of their cesium inventory. Measurements of the remaining solution after deconsolidation suggested there were at least two failed particles in the compact. As in many other tests reported in the literature, silver release significantly exceeded cesium release. The release information, however, does not provide any insight regarding the mechanism governing silver transport in SiC.

Verfondern et al. summarized silver diffusion coefficients in SiC from a number of sources. The diffusion coefficients reported are listed below:

$$D_{SiC} = 3.6 \times 10^{-9} \cdot \exp\left(\frac{-215 \frac{kJ}{mole}}{R\,T}\right) \frac{m^2}{s} \tag{A-14}$$

$$D_{SiC} = 6.8 \times 10^{-11} \cdot \exp\left(\frac{-177 \frac{kJ}{mole}}{R\,T}\right) \frac{m^2}{s} \tag{A-15}$$

between 1200°C and 1400°C

$$D_{SiC} = 3.5 \times 10^{-10} \cdot \exp\left(\frac{-213 \frac{kJ}{mole}}{R\,T}\right) \frac{m^2}{s} \tag{A-16}$$

between 1200°C and 2300°C

$$D_{SiC} = 5.0 \times 10^{-10} \cdot \exp\left(\frac{-182 \frac{kJ}{mole}}{R\,T}\right) \frac{m^2}{s} \tag{A-17}$$

The diffusion coefficients calculated from the experiments described in this section are displayed in Figure A-4. The diffusion coefficients span more than an order of magnitude at most temperatures and more than 2 orders of magnitude at 1200°C.
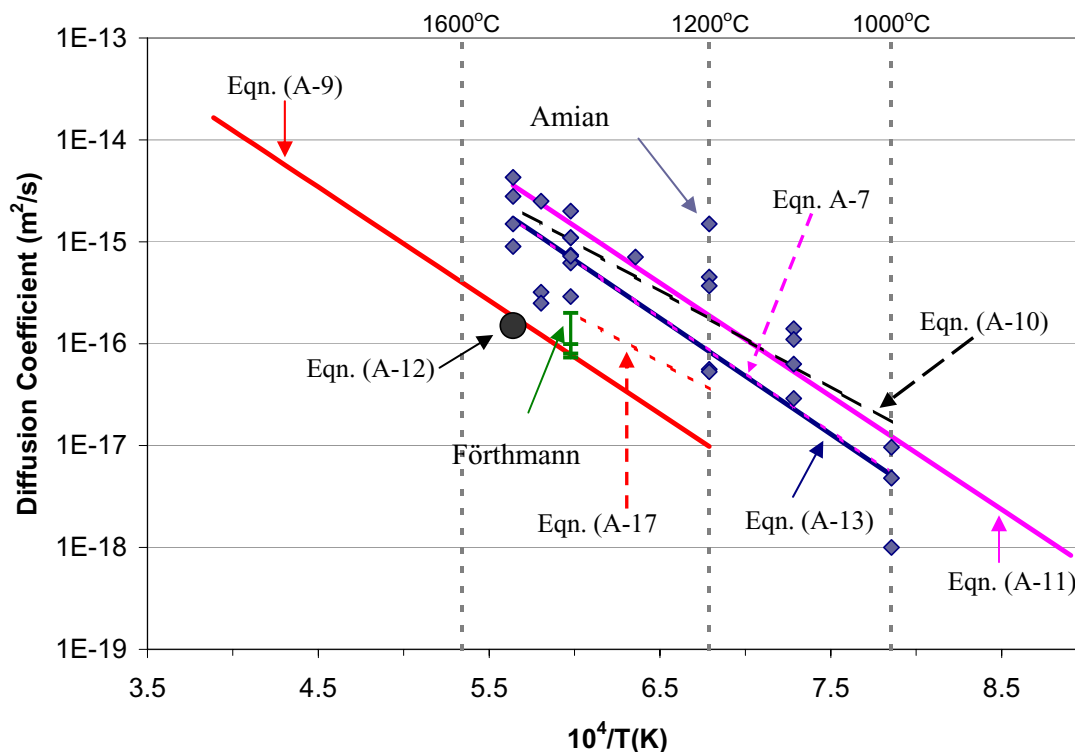
Figure A-4. Silver diffusion coefficients derived from irradiation and annealing experiments span more than an order of magnitude.

Individual Inventory

Whereas fission product release measurements on large batches of fuel provide useful information on overall performance, individual particle measurements attempt to develop a more detailed image of fission product transport. Individual particle measurements include techniques such as gamma counting of fission product inventory measurements and electron microscopy.

Assumptions

One of the primary challenges with conducting measurements on individual particles is the time required to count each particle. Counting times up to 8 h have been required to obtain reasonable counting statistics. This demand on resources limits the number of particles that can be individually counted to evaluate fission product release. Therefore, small populations of particles, sometimes just 10 to 25, are investigated and assumed to be representative of much larger batches, on the order of tens of thousands of particles.

Silver Migration in Silicon Carbide

In addition to batch testing, Nabielek et al. measured the individual silver content of particles. Although the particles selected appeared intact and had retained all of their cesium and other fission products, the authors noted "drastic variations" in silver content. They attributed the scatter in particle silver release to variations in availability and accessibility of free silicon on the silicon carbide grain boundaries as the presence of free silicon on the SiC grain boundaries facilitates silver migration.

After heating ten selected particles from the capsule HRB-15B irradiation, Bullock examined each particle individually and measured the silver, cesium, europium, and cerium contents. From each of the five different irradiated fuel types, Bullock selected ten particles for each of the three annealing experiments. Intermediate counting of mullite collector sleeves and tantalum tubes during heating measured fission product release during the test. In addition, the fission product inventory of each particle was counted using gamma spectrometry before and after heating.

The individual fission product inventories after irradiation but before heating were normalized to the ^{106}Ru inventory, a chemically stable fission product in the fuel particle, and the experimental and calculated values were compared. These measurements and calculations indicate whether any of the fission products were released during irradiation. Good matching between the experimental and theoretical values for the ^{134}Cs and ^{137}Cs inventories indicate no cesium release during irradiation. The experimental measurements showed about 25% less silver, 15% less cerium, and 25% more europium than predicted. However, uncertainties in the variables used to calculate these fission product inventories can account for the discrepancies.

The silver release per particle during heating was "highly nonuniform." Many of the heated particles released more than 50% of their silver, but in seven out of the eight batches experiencing silver release, at least one particle retained all of its silver. Cesium, on the other hand, appeared to be mostly retained with only three particles from two of the batches losing their entire cesium inventory. Partial cesium release was not observed in any particle. The range of observed silver release, from complete retention to complete release, casts doubt on diffusion as the governing mechanism. In identical particles in the same test, a diffusion process should have produced similar release results. The fact that some of particles retained their entire silver inventory while others experienced total release indicates that the release mechanism for silver is not intrinsic to

all SiC coatings; rather, SiC can be an effective barrier to silver even at temperatures up to 1500°C.

Silver release occurred in four of the particle types: UO_2, UC_2, UCO, and $UO_2^*(2)$ (ZrC dispersed in the buffer). No silver release was observed from the $UO_2^*(1)$ (ZrC coating around the fuel kernel) during the almost 3000-hour test. The SiC microstructures varied considerably from laminar to large columnar grains among these four fuel types. The UO_2 particles, suffering the greatest silver release, consisted of columnar, large-grained SiC. The $UO_2^*(1)$ particles retained all their silver and other fission products and had laminar structured SiC, but the presence of the solid ZrC coating on the fuel kernel may have also aided retention. The UCO particles also had laminar SiC and good silver retention. However, the UC_2 particles, also with laminar SiC, readily released silver indicating that laminar SiC is not the sole reason, if at all, for silver retention.

Silver breakthrough times increased significantly as the heating temperature decreased. Figure A-5 shows the silver fractional release curves for the $UO_2^*(2)$ particles during heat treatments at three temperatures. Measurements of the fission product inventory before the heat treatments provide the total amount of silver in each particle at the beginning of each test, but do not reveal the exact location or distribution of the silver. Any silver not already released from the fuel kernel into the coating layers must diffuse through at least part of the fuel kernel and the coatings before it reaches the silicon carbide. For particles irradiated under the same conditions the location and distribution of silver should be similar, but without knowing the exact initial condition it is impossible to know the contribution of silver retention due to holdup in the fuel kernel versus the silicon carbide layer.
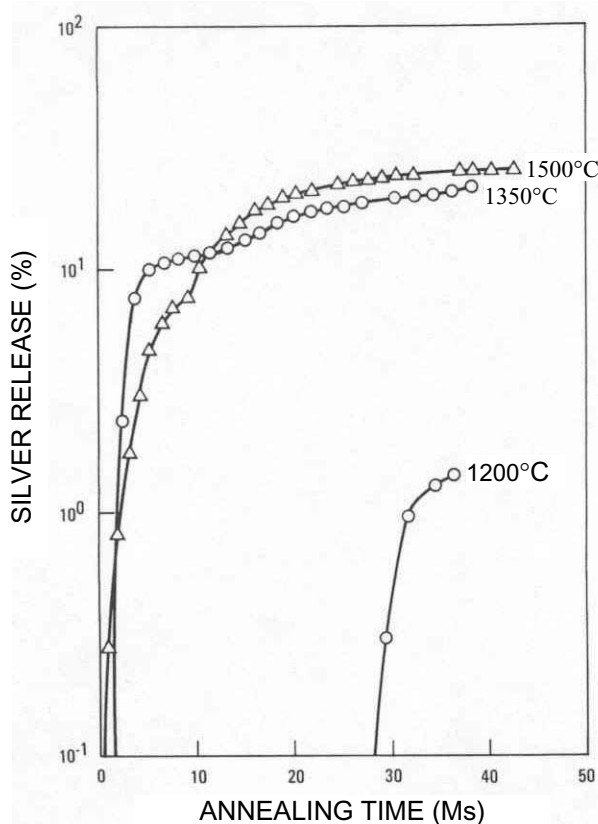
Figure A-5. Silver breakthrough times from TRISO-coated UO2*(2) particles increase as the heating temperature decreases.

Silicon carbide microstructures within a given batch of fuel appeared similar after etching, but silver release varied from particle to particle within a batch. While variations in SiC microstructure may appear to play a role in silver release between batches, SiC microstructure does not, by itself, explain the large variations in silver release within the batches. Short-circuit paths or cracks in the SiC layers, however, could explain the large variations in silver release with flawed particles losing silver while truly intact SiC coatings retain silver. Silver must diffuse through the fuel kernels within coated particles before release is observed. The time and temperature dependence of silver diffusion through fuel kernels contributes to the apparent time and temperature dependence of overall silver release.

Experiments conducted at the Oak Ridge National Laboratory studied the interaction of silver in UO_2 TRISO-coated particle in out-of-pile testing. Silver was mixed with UO_2 during fuel kernel fabrication and the standard TRISO coatings were applied (Pearson, Lindemer and Beahm, 1980; Pearson, Lauf and Lindemer 1982). The silver-doped fuel particles were not irradiated, but were

heated on a graphite wafer in a 27.8°C/mm temperature gradient so that the particles were exposed to a range of temperatures during each test.

The samples contained 3.3 wt % silver in the fuel kernel, about 100 times more silver than expected during normal operation of medium-enriched UO_2 to 20% FIMA. This increased silver concentration ensured detectability after heating while accounting for any silver loss from the fuel kernel during the coating process. The heating conditions for the first set of silver-doped tests are shown in Table A-2. Pearson et al. mounted the particles after heating and then polished them to the midplane. X-ray analysis in either an SEM (scanning electron microscopy) or an EMP (electron microprobe) identified several locations of silver interaction with the SiC in many of the particles. A distribution of silver in the SiC coatings consistent with a diffusion process was not reported. Additionally, the silver lay along the PyC-SiC interface on the cold side of the particles.

Table A-2. Heating temperature ranges silver-doped fuel heating tests.

Wafer #	Heating Temperature Range (°C)		Time (h)
	minimum	maximum	
1	1550	1900	25
2	1400	1750	260
3	1250	1500	3528

In further testing of silver interaction, Pearson et al. heated TRISO particles with 1.26 wt% silver mixed in with the UO_2 fuel kernel. These tests were conducted at a maximum temperature of 1500°C with particles on graphite wafers heated in a 27.8°C/mm temperature gradient. No silver penetration into the SiC layer could be observed during SEM examination. The authors did, however, note occasional large nodules in the SiC layer where silver had completely replaced the silicon carbide. If diffusion controlled silver transport in SiC, one would expect to observe silver distributed uniformly around the particle and a silver concentration gradient through the SiC layer. Pearson et al.'s observations continue to indicate that silver migration is not dominated by diffusion, but rather is dominated by localized interactions where discrete pockets of phase-separated silver are observed in the SiC coating.

Transmission electron microscopy after 2000 h of heating revealed no microstructural changes either on the hot or cold side of the particles, no second-phase nodules, and no obvious grain

boundary films. Particle silver inventories were not measured and no discussion of silver release was included. It is not clear whether the silver was retained or if release accompanied the findings.

Further work by the JAERI/ORNL collaboration examined particles that were deconsolidated from irradiated fuel elements. The IMGA (Irradiated Microsphere Gamma Activity) system measured the fission product inventory of the individual particles before and after heating. The predominant gamma rays after irradiation were from ^{95}Zr, ^{106}Ru, ^{134}Cs, ^{137}Cs, and ^{144}Ce. Activity ratios of mobile fission products, such as cesium, cerium, and silver, to chemically stable fission products, such as zirconium and ruthenium, allowed comparisons between fuel particle inventories while accounting for individual variations in fuel kernel size and burnup. During accident condition testing (ACT) solid fission products released from the fuel particles were collected on deposition cups, which were removed periodically and counted. Charcoal traps connected to the flowing helium monitored the amount of ^{85}Kr release as a sign of through-coating particle failure during heating.

ACT-1 heated 100 deconsolidated particles at 1600°C for 73.6 h. The test, initially planned for 1000 h, was stopped short due to the high number of particle failures and the contamination caused by fission product release. Online gas monitoring of ^{85}Kr during heating indicated four through-coating particle failures after 5 h, 28 h, 44 h, and 50 h at 1600°C. Based on the IMGA results, five particles lost significant cesium during heating. A total of 22 particles lost part of their OPyC layers. Three of the five particles that lost significant cesium also lost part of or had hair line cracks in their OPyC layers. Only six of the 100 particles were counted for silver; two of those six lost more silver than cesium. The fission product release curves evaluated from seven measurements of the deposition cups during heating have similar shapes for both silver and cesium indicating that silver and cesium were released within the same 5-20 h windows. Silver and cesium fractional release curves as measured by accumulation on the deposition cups are shown in Figures A-5a and b respectively. While suggesting that silver and cesium may have been released at the same time, presumably from the same particles, the long gap between deposition cup readings leaves uncertainty about the individual behavior of silver and cesium.

The goal of the following two tests, ACT-3 and ACT-4, was to measure silver diffusion through intact SiC layers. Each test was limited to 25 particles to accommodate the long counting times, 8 h, to measure silver inventories. Minato et al. selected a compact with a lower burnup,

4.79±0.11% FIMA, for deconsolidation to provide more safety margin during heating and avoid through-coating failures. Particle identities were maintained during heating so that fission product inventories measured by IMGA could be compared before and after heating. The fractional release curves for silver and cesium during ACT-3 and ACT-4 heating are shown in Figure A-5 a and b, respectively.

a) Fractional release of silver   b) Fractional release of cesium
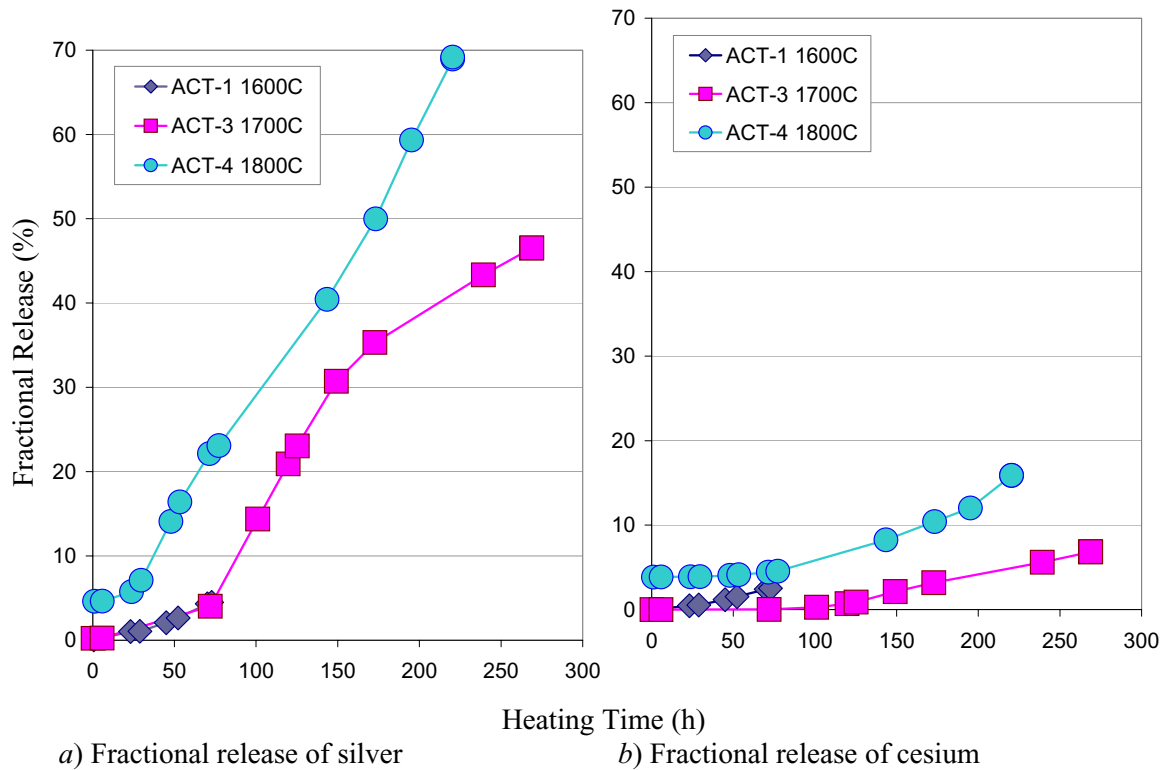
Figure A-5. Fractional release of silver is greater than cesium during accident condition testing.

The gas monitoring system detected no significant fission gas release indicating no through-coating failures during ACT-3 heating for 270 h at 1800°C. However, IMGA counting detected "considerable variation" in the retention of silver, cesium, and europium among the particles, as shown in Figure A-6. It appears that there was much more silver release than cesium, but the accuracy of the measurements and calculations is not known. Based on the total inventory measurements of the 25 particles before and after heating, the particles lost an average of about 47% of their silver and about 7% of their cesium during ACT-3.

The 25 particles heated in ACT-4 at 1800°C for 222 h again exhibited "considerable variation" in the retention of the fission products silver, cesium, and europium, as shown in Figure A-8. As

with ACT-3, the 25 particles together released more silver than cesium, losing about 69% of their silver and 16% of their cesium. Visual examination of the particles after heating revealed one particle with completely fragmented coatings and an exposed fuel kernel (noted as a failed particles in Figure A-8). The fractional release of cesium is, again, lower than the fractional release of silver. This feature has been interpreted to mean that silver diffuses faster than cesium through SiC. Although the pyrocarbon layers are generally not credited with retaining cesium, they do slow cesium transport more than they slow silver transport contributing to the lower observed releases. Again, the variation in fractional release among the 25 particles in each of the ACT-3 and ACT-4 tests argues against diffusion as the controlling silver transport mechanism.
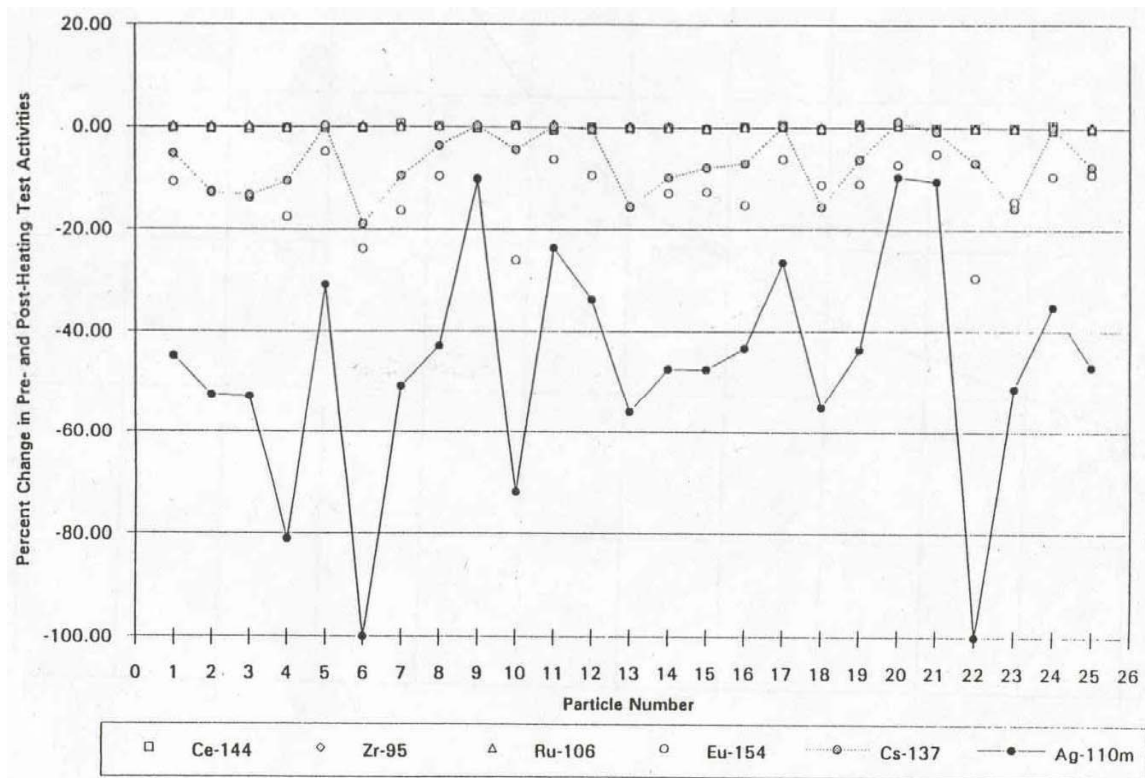
Figure A-6. Individual particle fission product retention varies significantly during ACT-3 heating at 1700°C.
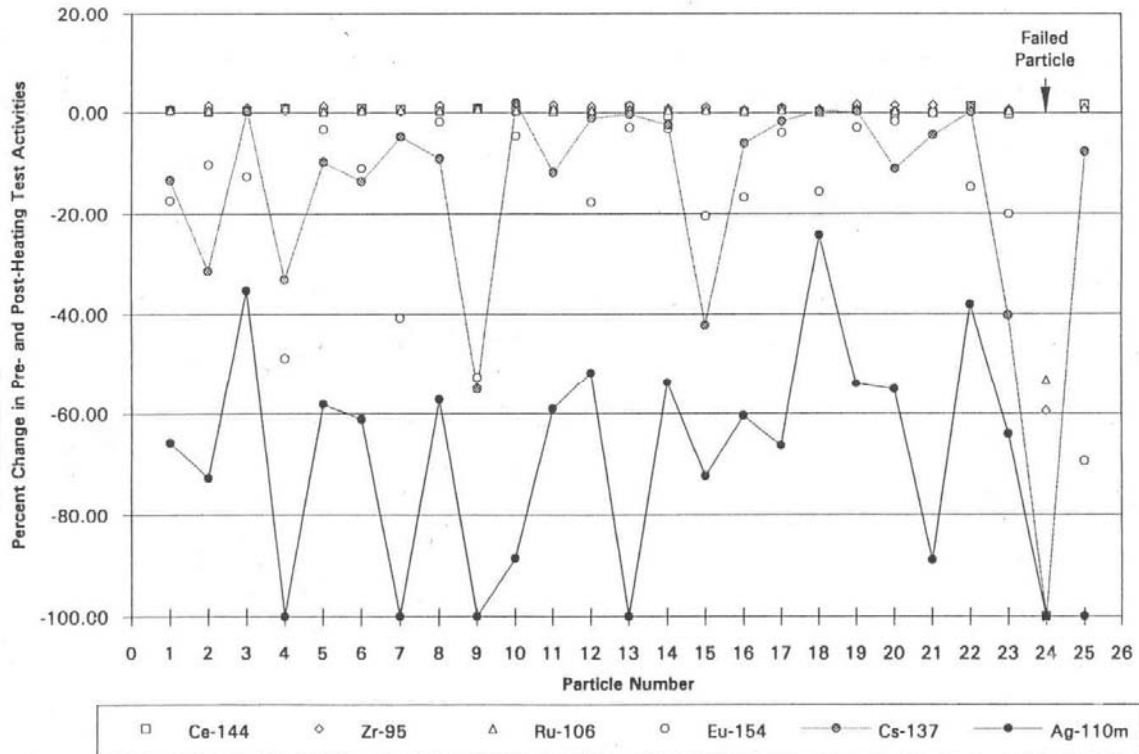
Figure A-7. Individual particle fission product retention varies significantly during ACT-4 heating at 1800°C.

Ketterer and Bullock examined loose particles for silver and cesium release after irradiation in capsule HRB-15B (Ketterer and Bullock 1981). During irradiation, the low-enriched fuel, approximately 19.5% ^{235}U, achieved a peak exposure of 6.6×10^{25} n/m^2 fast fluence and about 27% FIMA fissile burnup with nominal time average temperatures between 815°C and 915°C. The TRISO-coated particles retained all of their fission products except for small quantities of silver. Different fissile and fertile fuel types were tested. The TRISO-coated fissile fuels included UO_2, UC_2, UCO, and two types of UO_2[*] fuels with either ZrC dispersed in the buffer or a ZrC coating over the fuel kernel.

IMGA measurements of the particles after irradiation generally indicate complete retention of ^{137}Cs, but "significant loss" of ^{110m}Ag. Uncertainties for IMGA results are on the order of 9%-15% for the ^{137}Cs /^{106}Ru inventory ratio and 10%-16% for the ^{110m}Ag/^{106}Ru ratio. The 0%-8% ^{137}Cs release indicated by IMGA measurements falls within the uncertainty of the measurement and is, therefore, not sufficient evidence of cesium release during irradiation.

There is some confusion about the meaning of the silver release measurements. IMGA results and the ^{110m}Ag/^{106}Ru ratio indicate that, on average, 27% of the silver inventory was released during irradiation. Gamma-counting measurements on the empty graphite trays indicated only 2%-13% silver release. Even considering the uncertainties of both types of measurements, the release values from IMGA on particle and gamma-counting of empty trays do not agree. While this discrepancy was a source of concern for the authors, other work on silver migration in graphite materials indicate that they do not retain silver. Although silver is expected to condense on cold (significantly less than silver's melting temperature, 960°C) components in the system, it should not be surprising that silver was not detected on the graphite trays. IMGA measurements on particles after irradiation showed no cesium loss and unquantified silver release. However, gamma-counting of empty trays detected ^{134}Cs, ^{137}Cs, and ^{110m}Ag. Of the trays with significant autoradiograph patterns, two trays had silver but no cesium and two trays had cesium but no silver. While gamma scans of empty particle trays suggest that the particles released 2%-13% of their theoretical silver inventory, the uncertainty of approximately 13%-15.6% for ^{137}Cs and 21.6%-23.3% for ^{110m}Ag means that cesium and silver release cannot be confirmed.

The fuel temperatures were greater than the graphite tray temperatures. While the graphite tray mean temperatures were approximately 840°C, the actual temperatures were greater than the mean for a significant time during irradiation. Although even the mean fuel temperatures may have been relatively low during irradiation, fuel temperatures exceeded the melting temperature of silver, 960°C, for a significant portion of the irradiation. At these temperatures, any silver escaping the fuel particles would be a vapor and would not likely condense on the graphite trays.

The SiC layers of the TRISO-coated UC$_2$ and UCO fuels contained some flaws and porosity that may have degraded their performance. Short, lenticular flaws observed during metallography are purported to be associated with areas of free silicon in the SiC layer. Porosity found in the UCO particles was randomly dispersed in the silicon carbide and was observed both before and after irradiation.

In another irradiation test, fission gas release measurements and gamma-ray analysis of fuel particles and structural components provided means for Ketterer et al. to compare fuel performance of different fuel kernel materials and the effect of replacing SiC with ZrC in the TRISO coating. The irradiation at ORNL in capsule HRB-15A included fuel particles in fuel rods, bonded trays, and unbonded particle trays. Fission gas release measurements during

irradiation and end-of-life release-to-birth ratios indicated some fuel failure, about 2% average in-service particle failure (Ketterer et al. 1984). Fuel in capsule HRB-15A experienced burnup between 20% and 29% FIMA and fast fluence between 3.3 n/m^2 and 6.5×10^{25} n/m^2. Time-averaged temperatures for the fuel rods and bonded and unbonded particle wafers all fell in the 1000°C-1100°C range.

Two batches of fuel with $UC_{0.5}O_{1.5}$ kernels were the least retentive of silver and experienced severe SiC degradation by fission product (e.g. palladium) attack in 70% of those particles observed with ceramography. Degradation of the SiC coating by palladium or interactions with other fission products may provide pathways for silver release. Two batches of ZrC-TRISO (ZrC instead of SiC layer) exhibited better resistance to fission product attack, but the batch with UC_2 fuel still had poor silver retention. It is not yet clear whether ZrC retains silver better than SiC does.

Gamma counting of particles, particle trays, the graphite sleeve, and the stainless steel primary tube all provided data on fuel performance during the irradiation. The empty particle trays contained no silver after irradiation, but cesium, cerium, and europium were detected on some of the trays. Cobalt, cesium, silver, and europium were found on the graphite sleeve surrounding the fuel rods and trays with 60% of the silver detected occurring at the elevations of the $UC_{0.5}O_{1.5}$ fuels. Silver was also leached off the stainless steel primary containment tube indicating that silver passed through the graphite sleeve while the other fission products remained inside the sleeve.

Deconsolidation of the fuels rods provided fuel particles for gamma counting after irradiation. Analysis of the electrolytic solution after deconsolidation indicated a significant number of failed particles per rod. By measuring the amount of uranium contained in the solution after deconsolidation and comparing that to the calculated inventory per particle, Ketterer et al. calculated the number of failed particles per rod. Gamma analysis of the ^{134}Cs, ^{137}Cs, ^{110m}Ag, ^{95}Zr, and ^{106}Ru inventories per particle and the ratios of mobile (cesium and silver) to stable (zirconium and ruthenium) fission products provided insight into cesium and silver and, in some cases, cerium and europium release during irradiation.

Table A-3. Silver retention is less than cesium retention in HRB-15A fuels.

Fuel	Coating	Number of Particles	Failure Fraction	Silver Retention (%)		Cesium Retention (%)	
				Mean	Range	Mean	Range
UO_2	TRISO	467	6.5×10^{-3}	48	26-71	94	90-99
UO_2	TRISO	201	2.5×10^{-3}	44	0-69	91	75-95
UO_2^*	TRISO ZrC in buffer	365	1.5×10^{-2}	56	35-80	96	69-100
UC_2	ZrC-TRISO	342	6×10^{-2}	47	0-66	90	0-97
UC_2	TRISO	184	1.8×10^{-2}	55	40-73	92	89-96
UCO	TRISO	345	3×10^{-2}	15	0-72	91	24-98

As shown in Table A-3, silver is generally released more readily from all fuels from the HRB-15A irradiation than cesium. In the UO_2 TRISO fuels, high silver release was observed in some of the same particles with high cesium retention. The UC_2 fuel with ZrC-TRISO coating experienced poor silver retention with the best particle only retaining 62% of its silver. Release values, however, for both silver and cesium vary significantly within a single batch and single fuel rod. Ketterer et al. suggest that variations in the microstructures of the barrier layers (SiC and ZrC) within and between batches are responsible for the variations in fission product release. Differences in individual SiC grain structures, however, are not sufficient to account for the scatter in the release values.

Cesium releases were significantly greater than expected and Ketterer et al. suggest this is due to particles with failed SiC but intact OPyC layers. According to Ketterer et al., with lower average fuel temperatures during expected HTGR operation, cesium diffusion through OPyC layers would be hindered and holdup in the core graphite would limit cesium release even with failed SiC layers.

Particles with failed SiC coatings and intact OPyC coatings would release silver and cesium while retaining the noble fission gases krypton and xenon. An intact OPyC layer would retard cesium release, explaining lower observed releases of cesium relative to silver. Although path length variations due to individual SiC microstructures are insufficient to explain the range of release values, failed SiC layers in some of the particles does account for observations of silver release from some particles (the ones with failed SiC coatings) with silver retention in others (those with intact SiC coatings).

Ion Implantation

In addition to studying total silver release from fuel particles, Nabielek et al. examined the migration of silver implanted in a silicon carbide disk. Using SiC chemically vapor deposited on a plane graphite disk, silver was implanted with a peak concentration equivalent to 2×10^{-3} mole ^{109}Ag per mole SiC. After heating the sample at 1180°C for only 30 minutes, the authors reported that the "mobility of silver was too small to be detectable."

The silicon carbide contained some pores and had a density of 3.18 g/cm^3, within the range of typically characterized SiC and fairly close to the theoretical SiC density of 3.21 g/cm^3. The implanted silver concentration was in the range typical of in-pile concentrations reached at 12% FIMA of 2×10^{-4} to 4×10^{-3} mole ^{109}Ag per mole SiC. The authors hypothesize that the silver was trapped inside the SiC grains hence the lack of migration is attributable to the extremely low silver diffusion rate within SiC grains, not a measure of silver grain boundary diffusion. The ion implantation used in this experiment resulted in a shallow silver concentration profile with the peak silver concentration occurring approximately 80 nm, or 0.08 μm, below the SiC surface. Typical SiC grain dimensions on the order of 0.5-1 μm are common, and grain sizes are often larger. The implanted silver, therefore, was probably contained within the first row of grains in the SiC plate. The width of the implanted area, however, was most certainly larger than a single SiC grain, probably on the order of millimeters. The silver implantation beam most likely spanned many SiC grains and their associated grain boundaries. The silver ions were, therefore, not completely contained within SiC grains and those on the grain boundaries should have been free to diffuse, but no evidence of silver transport was observed.

From the small movement of silver atoms in the ion implantation experiment Nabielek et al. derived an upper limit for the diffusion coefficient of silver in silicon carbide at 1180°C as:

$$D_{SiC}(1180°C) << 10^{-19}\,\tfrac{m^2}{s} \tag{A-18}$$

This value is much lower, approximately 3 orders of magnitude lower, than the other diffusion coefficients for silver in silicon carbide reported in the literature. Compared to other experiments reported in the literature, the heat treatment used here, 30 min at 1180°C, is quite short and at a much lower temperature. Although estimates for silver migration in the ion implantation sample

using average diffusion coefficient values in the literature predicted measurable silver movement, given sufficient accuracy of the silver concentration measurement technique, the duration and temperature of the heat treatment may not have been enough to generate silver transport.

Discussion

The lack of cesium release during various irradiation and heating tests argues that most of the fuel particles tested were intact. Thus, it seems reasonable that, in order to escape, silver must have diffused through intact silicon carbide. This view of effective silver release has allowed many authors to compare results from different types of fuels and to categorize their results with diffusion coefficients, useful for estimating total silver release from future operating cores.

Although the reported silver diffusion coefficients agree with each other within about 2 orders of magnitude, the specific path of grain boundary diffusion has been assumed from a comparison of activation energies and not from direct observation. A few observations among the diffusion coefficient experiments and simple calculations aim to look at the process of silver migration in silicon carbide from a different perspective.

Scatter in the Data

Amian and Stöver and other authors propose that the scatter observed in calculated silver diffusion coefficients stems from variations in the silicon carbide microstructure. If silver diffuses along silicon carbide grain boundaries, as commonly suggested, then different microstructures in different particles would produce different total path lengths through each silicon carbide layer. While this explanation makes intuitive sense, it does not represent the available data well.

Given a specific heat treatment duration and silver concentration at the inner SiC surface, the amount of silver released through the SiC coating can be calculated from the analytical solution through a spherical shell, shown in Equation A-19. Equating the mass release from two different scenarios and allowing the overall thickness to vary to represent the total silver path length along SiC grain boundaries, one can calculate the effective change in SiC thickness to match a change in the diffusion coefficient. The maximum and minimum diffusion coefficient values at selected temperatures were taken from the literature values shown in Figure A-4.

$$Q_r = 4\pi\,a\,b\,(b-a)\,C_1 \cdot \left[\frac{D \cdot t}{(b-a)^2} - \frac{1}{6} - \frac{2}{\pi^2} \cdot \sum_{n=1}^{\infty} \frac{(-1)^n}{n^2} \exp\left[-\frac{D n^2 \pi^2 t}{(b-a)^2} \right] \right] \qquad \text{(A-19)}$$

where Q_r = mass released (g),
        a = inner radius of spherical shell (m),
        b = outer radius of spherical shell (m),
        C_1 = source concentration of silver at $r = a$ (g/m^3),
        D = diffusion coefficient of silver in SiC (m^2/s), and
        t = duration of heat treatment (s).

In previous work, authors measured silver release from fuel particles and then calculated effective diffusion coefficients using the duration of the heat treatment and the dimensions of the SiC coating. In either analytical or numerical solutions used to determine the diffusion coefficients, the silver path length is assumed to be, simply, the thickness of the SiC coating. But, if silver travels along a tortuous path through the SiC coating before it escapes, the path length would be longer than the SiC coating thickness and the diffusion coefficient required to "push" the same amount of silver through the coating would have to be greater. If, therefore, the lowest diffusion coefficients are associated with the shortest diffusion paths (i.e., a single SiC grain boundary extending radially from the inner surface to the outer surface of the SiC coating), then one can calculate the total effective path length required to result in a higher diffusion coefficient for the same mass loss.

Equating the silver release using the maximum diffusion coefficient value at a given temperature with the silver release using the minimum diffusion coefficient at the same temperature, one can calculate the difference in effective path length. The values for the effective silver path length required to result in the reported range of diffusion coefficient are listed in Table A-4. The range in values, however, is greater than that expected based on typical SiC grain structures. As discussed above, one SiC grain structure extreme is the case of long, columnar grains with single grains extending through the entire SiC coating. At the other end of the spectrum is a SiC coating with small, equiaxed grains, on the order of 0.5 μm per side, for example. If for every grain-width a silver atom moves in the radial direction it also moves one grain-width in the tangential direction, then the effective path length traveled by the silver atom is twice the SiC coating thickness. For the diffusion coefficient values at 1200°C and 1500°C, where the values differ by more than 1 order of magnitude, the effective path length changes by a factor of roughly 8-10. Although silver would be expected to follow a tortuous path as a result of grain boundary

diffusion, a total path length greater than twice the SiC thickness is not likely. From this assessment of the variation in reported diffusion coefficients, the argument that silver diffusion varies because of the individual SiC microstructures does not reflect the actual data. Another mechanism, therefore, must govern silver transport through silicon carbide coatings resulting in the large variations observed in silver release, both in individual particle measurements and in large batch testing.

Table A-4. The calculated path lengths necessary to explain the range of diffusion coefficients is larger than reasonable tortuous paths through SiC layers.

Temperature (°C)	Lower D (m^2/s)	Assumed Thickness (μm)	Upper D (m^2/s)	Calculated Thickness (μm)	Thickness Ratio (Calculated: Assumed)
1000	1.0E-18	35	1.7E-17	105	3.0
1200	9.8E-18	35	1.5E-15	470	13.4
1500	1.5E-16	35	4.3E-15	290	8.3

Silicon Carbide Diffusion vs. Particle Failure

Most of the silver diffusion coefficients reported in the literature were derived from batch testing of a population of fuel particles. In general, these diffusion coefficients were calculated assuming the collected silver release was due equally to all particles in the batch. But what if the silver release was not uniform? If just a few particles in a batch had a short-circuit diffusion path or connected porosity in the silicon carbide layer, a large portion of that particle's silver inventory could escape. It is possible that almost total release of silver from a few particles in a batch of fuel particles with almost complete retention in the rest would produce the same silver deposition on a cold plate during heating as those previously assumed due to diffusion from the entire batch.

Take, for example, the data reported by Amian and Stöver for a number of post-irradiation anneals. The authors report the diffusion coefficient calculated from release measurements during post-irradiation anneals. The geometry of the fuel and anneal conditions are given, along with the calculated values of fractional release. The number of fuel particles per element tested is not included, but the following demonstration remains instructive.

If the procedure applied to calculate the diffusion coefficients from release measurements is reversed, an estimate of the release detected and silver mass per particle (element) can be

determined. The following analysis assumes that there are 250 particles in each element tested. Using the reported diffusion coefficient for each anneal (D) and the anneal conditions (T, t), the amount of silver released from each element (Q) was calculated using the analytical solution for diffusive release from a thin spherical shell. The total amount of silver released (Q_{total}) from each element was also calculated (using the original assumption that the release was evenly attributed to all of the particles in the element). The total amount of silver in each particle at the beginning of the heat treatment (M_{Ag}) was calculated given the fractional release values listed by Amian and Stöver. The results of this analysis are shown in Table A-5. A comparison of the calculated amount of silver per particle to the calculated amount of silver released from the element shows that it is feasible that in some elements the release is due to a nearly complete loss of silver from a few particles and almost complete retention in the rest.

Table A-5. Equivalent number of failed particles given the fractional release for the batch and assuming 250 particles per batch.

Temp. (K)	Time (h)	D (m^2/s)	FR	Q (g) (particle)	M_{Ag} (g) (particle)	Q_{total} (g) (element)	Failed SiC
1273	2340	4.8E-18	4.0E-03	2.35E-09	5.87E-07	5.87E-07	1.00
1273	700	9.6E-18	4.1E-03	9.53E-12	2.32E-09	2.38E-09	1.03
1273	1000	1.0E-18	7.0E-04	3.34E-21	4.77E-18	8.34E-19	0.18
1373	543	1.4E-16	5.0E-02	1.08E-05	2.16E-04	2.70E-03	12.50
1373	294	1.1E-16	5.3E-03	9.73E-07	1.84E-04	2.43E-04	1.33
1473	162	4.5E-16	3.0E-02	9.84E-06	3.28E-04	2.46E-03	7.50
1473	240	5.6E-17	2.4E-03	9.67E-09	4.03E-06	2.42E-06	0.60
1673	40	7.4E-16	5.3E-03	6.94E-07	1.31E-04	1.74E-04	1.33
1673	75	6.2E-16	9.8E-03	3.19E-06	3.25E-04	7.97E-04	2.45
1673	30	2.0E-15	1.1E-02	6.27E-06	5.70E-04	1.57E-03	2.75
1673	45	1.1E-15	5.0E-03	3.80E-06	7.60E-04	9.50E-04	1.25
1773	30	9.0E-16	4.1E-03	4.77E-07	1.16E-04	1.19E-04	1.03
1773	225	1.5E-15	1.5E-01	1.06E-04	7.09E-04	2.66E-02	37.50
1773	183	2.8E-15	2.9E-01	1.72E-04	5.92E-04	4.29E-02	72.50

* assuming 250 particles per fuel element

Rearranging the numbers somewhat, for a batch of 250 particles, the release of 30% of the silver inventory of just four particles would produce the same results as 0.5% release from each particle, the value attributed to diffusion by Amian and Stöver. This calculation, once again, suggests that silver release could result from a short-circuit path or silicon carbide failure in a few particles per batch rather than diffusion.

Other Possible Silver Migration Pathways

With a melting temperature of 960°C, silver exists as a vapor when released from fuel particles. Nabielek et al. cite previous work when they report that silver is "trapped, nearly quantitatively" when particle surface temperatures are below 1000°C. For all of the results reported in the literature, the fuel surface temperatures exceeded, at least for some portion of the test, 1000°C, so the retention of silver at low temperature cannot be confirmed. This does, however, leave open the possibility that paths allowing the transport of a vapor through the silicon carbide layer may play a role in silver release.

A number of authors have advised some caution relative to the silver diffusion coefficients. Nabielek et al. conclude that migrating fission products will follow grain boundaries in poly-crystalline SiC "through disorganized material via traces of free silicon". If free silicon is present in the silicon carbide layer, Nabielek et al. suggested that it will be stored at the grain boundaries and will aid in silver migration. Additionally, other authors have suggested looking for short-circuit diffusion paths as they may provide significant contributions to enhanced fission product release.

Schenk and Nabielek report that an intermediate stage of silicon carbide failure, beginning around 1600°C, is characterized by non-uniform porosity and cracks. These features could certainly lead to fast silver release from silicon carbide, appearing as diffusion through intact material as long as the pyrocarbon layers are undamaged and still retaining the fission gases and some of the cesium. Nabielek et al. also suggest a deterioration of silicon carbide occurring during operation when fuel temperatures are above 1200°C leading to increased silver release at higher temperatures. Although the assessment of the quality of the fuel used by Nabielek et al. has been challenged in the literature, it is important to note that other pathways and mechanisms resulting in silver release have been suggested and may explain some of the variation in the data.

Although pressure vessel failure (failure of all three structural layers) has been a concern for fuel performance, silicon carbide failure next to intact pyrocarbon layers can occur. During HRB-22 post-irradiation examination, Minato et al. found a partial crack in a single SiC layer. Cracks like this one do not extend completely through the SiC coating so they are not detected by standard burn/leach methods used to detect coating failures. The authors suggest that the crack formed either from mechanical shocks after SiC deposition or during the compact fabrication process. Pathways like this one would provide paths for silver vapor release.

Other Fission Product Behavior

The retention and release of other fission products, namely the noble gases krypton and xenon, and other metallics, primarily cesium, plays an important role in judging the performance of the fuel particles. Intact pyrocarbon layers retain the noble fission gases. As long as either the inner or outer pyrocarbon layer is undamaged, fission gas release will not be observed and this fact is used to categorize fuel as, generally, intact or failed.

One of the initial drivers for adding a silicon carbide layer to coated particle fuels was to improve cesium retention. Cesium escaped from the original pyrocarbon coatings of the BISO particles, but the degree to which pyrocarbon or graphite materials can retain or retard cesium migration is not completely clear.

Brown and Faircloth state that cesium seems to be well retained by the particle coatings, "principally in the inner pyrocarbon layer". Amian and Stöver also had a similar finding stating the "cesium is effectively retained in the HTI-PyC coatings" and that there was no distinct improvement for cesium retention in SiC relative to PyC. Schenk and Nabielek reported that cesium was found mainly in the buffer layer and the matrix graphite around the fuel particles provided enough retention to prevent rapid cesium release from the fuel element. Ketterer et al. found cesium throughout the buffer layer in the particles from the HRB-15B irradiation, indicating some solubility or adsorption of cesium in the low-density graphite buffer and also stated that cesium was retained by the OPyC layer.

These findings suggest that both the pyrocarbon layers and the low-density buffer and matrix materials may provide some retention for cesium, possibly through adsorption in the low-density materials. If cesium is retained, at least somewhat, by the PyC layers or the other graphite materials, then failure of a silicon carbide layer would not automatically result in cesium release. In this way silver release from particles with intact PyC layers and failed SiC layers could be observed while the cesium was still retained.

Conclusions

Although the Arrhenius form of the diffusion equation appears to cover the observed temperature trends regarding silver release from coated fuel particles, other observations suggest that silver

release may depend on mechanisms other than classical diffusion. Nablielek et al. calculate silver diffusion coefficients based on release data, but also caution that the shapes of some of the release curves are not consistent with diffusion. They further propose that silver release may be due to a degradation of the silicon carbide with irradiation and heating.

Amian and Stöver attribute the greater than one order of magnitude scatter in their data to variation in the specific microstructure in each silicon carbide layer. However, as seen in section 0, variations in microstructure alone cannot account for the large range of diffusion coefficients. If silver release from particles is driven by SiC integrity rather than by grain boundary diffusion along specific grain paths, large variations in release per particle and per batch would still be observed with corresponding variations in the calculated effective diffusion coefficient.

Variations in silver release would be expected given a grain boundary diffusion mechanism from individual particles based on specific microstructures and irradiation conditions. However, the large variations observed by Amian and Stöver, Bullock, and Ketterer et al. are greater than can be explained by SiC microstructure and irradiation conditions and do not appear characteristic of a diffusion pathway. When testing particles from a single fabrication batch with nearly identical dimension and irradiation parameters, release due to diffusion should not vary by orders of magnitude. Diffusion does not explain why some particles in Bullock's study released 100% of their silver while others from the same batch in the same test retained all of their silver. These observations suggest that mechanisms other than diffusion are involved with silver release.

The assumption that silver release is governed by grain boundary diffusion attempts to explain a range of data whose span is larger than expected based on typical grain boundary path variations. Without measuring silver concentration profiles or observing direct evidence of diffusion, one must still consider other transport mechanisms. Various authors have expressed doubts about the specific silver migration mechanism and have offered some suggestions of alternative possibilities contributing to silver release, but these paths have not yet been followed.

There is ample uncertainty in the current data to suggest that silver may not only diffuse through silicon carbide, but may escape through failed silicon carbide layers or other defects in the coating. If this is the case, identifying those flawed particles and removing them from operation would decrease silver release. Additional work to identify the specific silver transport mechanism is important for developing methods to reduce or mitigate silver release.

Filename: 7. Appendix A.doc
Directory: C:\Documents and Settings\talbhd\Desktop\FINAL INERI JAN3
Template: C:\Documents and Settings\talbhd\Application
    Data\Microsoft\Templates\Normal.dot
Title: Appendix A
Subject:
Author: test
Keywords:
Comments:
Creation Date: 12/20/2004 5:02:00 PM
Change Number: 81
Last Saved On: 1/11/2005 11:04:00 AM
Last Saved By: test
Total Editing Time: 275 Minutes
Last Printed On: 1/18/2005 11:07:00 AM
As of Last Complete Printing
    Number of Pages: 35
    Number of Words: 12,648 (approx.)
    Number of Characters: 70,580 (approx.)

APPENDIX B (MIT):
Diffusion Coupled Data

The following tables list the heat treatment and fabrication data for the MIT diffusion couple experiments discussed in Section 3. Two different fixtures, shown in Figure B-1 and noted as "clamp" and "plate" in the following tables, were used to hold the diffusion couples during SiC coating.
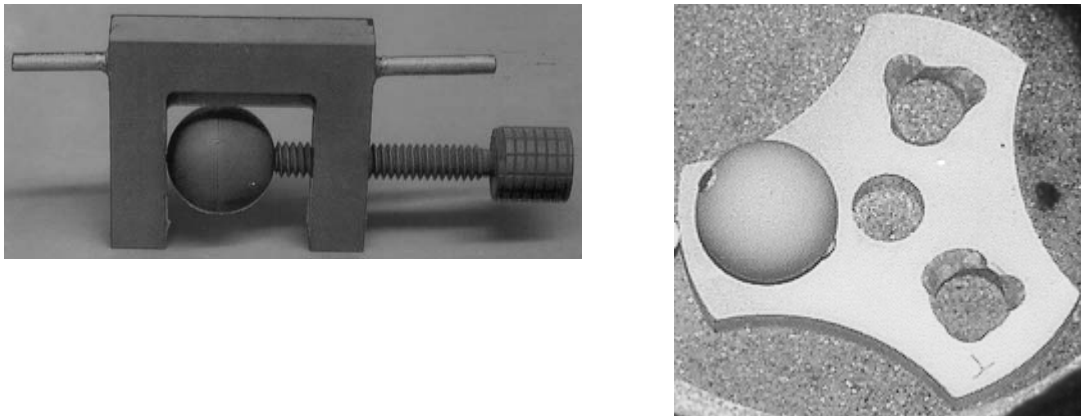
Figure B-1. Two types of fixtures were used during SiC coating: *a*) clamp, *b*) graphite plate.

SIC-1

Table B-1. SiC-1 Diffusion Couple Annealing Data.

ID	Temp (ºC)	Time (hrs)	Start Date	End Date	Notes
			Anneal		
8	1500	24	7/14/00	7/15/00	
9	1400	43.8	7/19/00	7/21/00	
10	1050	1000	7/12/01	8/26/01	
11	1700	50	11/15/01	11/17/01	
12					as-fabricated, not heated
13	1400	276	7/17/01	7/29/01	
14	1500	300	11/15/01	11/30/01	
15	1500	2	8/31/01	8/31/01	bare graphite spot
16					
17	1500	400	10/23/01	11/6/01	control sample, sectioned before heat
19					missing button
20	1500	120	1/17/01	1/22/01	
21	1400	240	1/24/01	2/3/01	
22					missing button
23	1400	276	7/17/01	7/29/01	
24	1050	1000	7/12/01	8/26/01	
28_1	1200	643	7/30/01	8/26/01	1st heat treatment
28_2	1200	1117	12/11/01	1/27/02	2nd heat treatment
28	1200	1760			cumulative
29_1	1500	24			1st heat treatment
29_2	1200	400	2/20/01	3/12/01	2nd heat treatment
30_1	1200	643	7/30/01	8/26/01	1st heat treatment
30_2	1200	1117	12/11/01	1/27/02	2nd heat treatment
30	1200	1760			cumulative
32	1500	100	7/12/01	7/17/01	
33	1500	100	7/12/01	7/17/01	
56	1500	200	2/28/02	3/8/02	control sample, no silver
57	1500	200	2/28/02	3/8/02	
58					
59					
60					
61					
62					
63	1600	550	2/1/02	2/24/02	
64					

Table B-2. SiC-1 Diffusion Couple Mass Loss and Leak Testing Data.

ID	Initial Ag Mass (gm)	Mass before anneal (gm)	Mass after anneal (gm)	dM Total (gm)	dM / initial Ag mass	dM / total mass	pre (atm.cc /sec)	post (atm.cc /sec)
		Mass Loss					**Leak Testing**	
8	0.1366	1.7734	n/a					
9	0.1297	1.7511	n/a					
10	0.1378	1.7728	1.7409	0.0319	0.2315	0.0180		3.0E-02
11	0.1441	1.7672	1.6826	0.0846	0.5871	0.0479		
12	0.1405							
13	0.1358	1.7634	1.7555	0.0079	0.0582	0.0045		
14	0.1219	1.7615	1.6652	0.0963	0.7900	0.0547		
15	0.1249	1.7401	1.7340	0.0061	0.0488	0.0035		1.0E-03
16	0.1289						2.5E-02	
17	0.1090	1.3471	1.3400	0.0071	0.0651	0.0053		
19	0.1294						8.0E-03	
20	0.1383	1.6834	1.6569	0.0265	0.1916	0.0157		
21	0.1615	1.6989	1.6656	0.0333	0.2062	0.0196		
22	0.1700						4.0E-02	
23	0.1581	1.7213	1.7200	0.0013	0.0082	0.0008		
24	0.1750	1.7466	1.7166	0.0300	0.1714	0.0172		2.0E-06
28_1	0.2363	1.8527	1.8460	0.0067	0.0284	0.0036		
28_2	0.2363	1.8497	1.8444	0.0053	0.0224	0.0029		5.0E-04
28	0.2363	1.8527	1.8444	0.0083	0.0351	0.0045		
29_1	0.2363	n/a						
29_2	0.2038	1.8318	n/a					
30_1	0.2029	1.8062	1.7996	0.0066	0.0325	0.0037		
30_2	0.2029	1.8005	1.7987	0.0018	0.0089	0.0010		5.0E-06
30	0.2029	1.8062	1.7987	0.0075	0.0370	0.0042		
32	0.2737	1.9797	1.9781	0.0016	0.0058	0.0008		
33	0.2497	1.9973	1.9959	0.0014	0.0056	0.0007		
56	0.0000	1.6924	1.6864	0.0060		0.0035	5.0E-07	2.0E-04
57	0.3029	1.9801	1.7888	0.1913	0.6316	0.0966	5.0E-07	8.0E-04
58	0.3009						5.0E-07	
59	0.2751						5.0E-07	
60	0.2859						5.5E-07	
61	0.2693						5.0E-07	
62	0.2683						1.5E-05	
63	0.3256	1.9622	1.6325	0.3297	1.0126	0.1680		2.5E-02
64	0.3115						5.0E-07	

Table B-3. SiC-1 Diffusion Couple SiC Coating Data.

ID	CVD fixture	SiC Coating Date	Total Mass (gm)	SiC Mass (gm)	SiC thick (µm)
			SiC Coating		
8	clamp	3/00	1.7734	0.2377	64.5
9	clamp	3/00	1.7511	0.2323	63.1
10	clamp	3/00	1.7730	0.2399	65.1
11	clamp	3/00	1.7676	0.2246	61.0
12	clamp	3/00	1.7270	0.1929	52.4
13	clamp	3/00	1.7636	0.2176	59.1
14	clamp	5/00	1.7606	0.2323	63.1
15	clamp	5/00	1.7599	0.2357	64.0
16	clamp	5/00	1.7725	0.2368	64.3
17	clamp	10/00	1.6337	0.1275	34.7
19	clamp	10/00	1.6500	0.1281	34.9
20	clamp	10/00	1.6834	0.1402	38.2
21	clamp	10/00	1.7014	0.1405	38.2
22	clamp	10/00	1.6856	0.1203	32.8
23	plate	10/00	1.7211	0.1686	45.8
24	plate	10/00	1.7463	0.1824	49.6
28_1	plate	2/01	1.8525	0.2038	55.4
28_2	plate	2/01	1.8525	0.2038	55.4
28	plate	2/01	1.8525	0.2038	55.4
29_1	plate	2/01	1.8318	0.2132	57.9
29_2	plate	2/01	1.8318	0.2132	57.9
30_1	plate	2/01	1.8060	0.1978	53.7
30_2	plate	2/01	1.8060	0.1978	53.7
30	plate	2/01	1.806	0.1978	53.7
32	plate	5/01	1.9972	0.3061	82.9
33	plate	5/01	1.9796	0.3089	83.7
56	plate	11/01	1.6922	0.2750	74.6
57	plate	11/01	1.9800	0.2701	73.2
58	plate	11/01	1.9574	0.2519	68.3
59	plate	11/01	1.9040	0.2206	59.9
60	plate	11/01	1.9034	0.2037	55.3
61	plate	11/01	1.8948	0.2114	57.4
62	plate	12/01	1.8974	0.2208	60.0
63	plate	12/01	1.9602	0.2280	61.9
64	plate	12/01	1.9701	0.2383	64.7

Table B-4. SiC-1 Diffusion Couple Fabrication Data.

ID	Silver Coating Date	Silver Source	Shell Mass (gm)	Male Mass (gm)	M + Ag (gm)	M + Ag + F (gm)	Ag Mass (gm)	Female Mass (gm)	Female Mass (gm)	F + Ag Mass (gm)	F Ag Mass (gm)
									Sample Fabrication / Silver Data		
8	2/1/00	sputter	1.3604	0.7091	0.7737	1.4970			0.6513	0.7233	0.0720
9	2/1/00	sputter	1.3504	0.7095	0.7758	1.4801			0.6409	0.7043	0.0634
10	2/2/00	sputter	1.3568	0.7147	0.7852	1.4944			0.6421	0.7094	0.0673
11	2/2/00	sputter	1.3603	0.7091	0.7813	1.5043			0.6512	0.7231	0.0719
12	2/2/00	sputter	1.3550	0.7073	0.7788	1.4954			0.6477	0.7167	0.0690
13	2/2/00	sputter	1.3715	0.7114	0.7841	1.5073			0.6601	0.7232	0.0631
14	3/23/00	sputter	1.3677	0.7107	0.7724	1.4896			0.6571	0.7173	0.0602
15	3/23/00	sputter	1.3607	0.7085	0.7688	1.4855			0.6522	0.7168	0.0646
16	3/23/00	sputter	1.3680	0.7121	0.7788	1.4970			0.6560	0.7182	0.0622
17	3/23/00	sputter	1.3584	0.7034	0.7679	1.4675			0.6551	0.6996	0.0445
19	3/23/00	sputter	1.3537	0.7137	0.7824	1.4832			0.6401	0.7008	0.0607
20	3/23/00	sputter	1.3665	0.7131	0.7837	1.5045			0.6533	0.7210	0.0677
21	5/3/00	sputter	1.3606	0.7073	0.7929	1.5222			0.6534	0.7293	0.0759
22	5/3/00	sputter	1.3566	0.7036	0.7856	1.5266			0.6531	0.7411	0.0880
23	5/3/00	sputter	1.3558	0.7160	0.7966	1.5138			0.6398	0.7173	0.0775
24	5/3/00	sputter	1.3501	0.7110	0.7997	1.5252			0.6392	0.7255	0.0863
28_1	2/7/01	powder	1.4125	0.7292	0.9655	1.6487	0.2363	0.6832			
28_2	2/7/01	powder	1.4125	0.7292	0.9655	1.6487	0.2363	0.6832			
28	2/7/01	powder	1.4125	0.7292	0.9655	1.6487	0.2363	0.6832			
29_1	2/7/01	powder	1.4148	0.7219	0.9257	1.6186	0.2038	0.6929			
29_2	2/7/01	powder	1.4148	0.7219	0.9257	1.6186	0.2038	0.6929			
30_1	2/7/01	powder	1.4054	0.7238	0.9267	1.6082	0.2029	0.6815			
30_2	2/7/01	powder	1.4054	0.7238	0.9267	1.6082	0.2029	0.6815			
30	2/7/01	powder	1.4054	0.7238	0.9267	1.6082	0.2029	0.6815			
32	3/16/01	powder	1.4166	0.7248	0.9985	1.6911	0.2737	0.6926			
33	3/16/01	powder	1.4210	0.7280	0.9777	1.6707	0.2497	0.6930			
56	11/13/01	powder		0.7257		1.4172		0.6915			
57	11/13/01	powder		0.7221	1.0250	1.7099	0.3029	0.6849			
58	11/13/01	powder		0.7241	1.0250	1.7055	0.3009	0.6805			
59	11/13/01	powder		0.7238	0.9989	1.6834	0.2751	0.6845			
60	11/13/01	powder		0.7206	1.0065	1.6997	0.2859	0.6932			
61	11/13/01	powder		0.7313	1.0006	1.6834	0.2693	0.6828			
62	11/15/01	powder		0.7263	0.9946	1.6766	0.2683	0.682			
63	11/15/01	powder		0.7271	1.0527	1.7322	0.3256	0.6795			
64	11/15/01	powder		0.7281	1.0396	1.7318	0.3115	0.6922			

SIC-2

Table B-5. SiC-2 Diffusion Couple Annealing Data.

	Anneal					
ID	Temp (°C)	Time (hr)	Start Date	End Date	Furnace	Notes
Ag34						no silver
Ag35						no silver
Ag37	1500	80	9/14/01	9/17/01	W4 plate	
Ag38	1400	224	9/14/01	9/23/01	W5 plate	
Ag39	1500	400	10/23/01	11/6/01	W5 plate	
Ag40	1500	140	10/12/01	10/18/01	W4 plate	
Ag50						free Si in SiC
Ag51						free Si in SiC
Ag52						free Si in SiC
Ag53	1600	550	2/1/02	2/25/02	W5 plate	
Ag54						
Ag55						

Table B-6. SiC-2 Diffusion Couple Mass Loss and Leak Testing Data.

	Mass Loss						Leak Testing	
ID	Initial Ag Mass (gm)	Mass before anneal (gm)	Mass after anneal (gm)	dM Total (gm)	dM / initial Ag mass	dM / total mass	pre (atm.cc /sec)	post (atm.cc /sec)
Ag34	0.0000						5.0E-07	
Ag35	0.0000							
Ag37	0.2530	1.8084	1.7974	0.0110	0.0435	0.0061		7.0E-04
Ag38	0.2545	1.8190	1.8052	0.0138	0.0542	0.0076		2.0E-03
Ag39	0.2525	1.8092	1.6732	0.1360	0.5386	0.0752		
Ag40	0.2530	1.9577	1.7297	0.2280	0.9012	0.1165		
Ag50	0.2863							
Ag51	0.2852							
Ag52	0.2836							
Ag53	0.2600	1.9339	1.6330	0.3009	1.1573	0.1556		9.0E-04
Ag54	0.2705						3.0E-02	
Ag55	0.3300						8.0E-04	

Table B-7. SiC-2 Diffusion Couple SiC Coating Data.

ID	SiC Fixture	SiC Coating Date	G + Ag + SiC Mass (gm)	SiC Mass (gm)	SiC thick (um)
			SiC Coating		
Ag34	plate	7/01	1.6065	0.2044	55.5
Ag35	plate	7/01	1.6028	0.1927	52.4
Ag37	plate	8/01	1.8084	0.1448	39.4
Ag38	plate	8/01	1.8190	0.1541	41.9
Ag39	plate	8/01	1.8092	0.1466	39.9
Ag40	plate	9/01	1.9579	0.2929	79.4
Ag50	plate	10/01	1.8321	0.1308	35.6
Ag51	plate	10/01	1.8188	0.1194	32.5
Ag52	plate	10/01	1.8570	0.1703	46.3
Ag53	plate	11/01	1.9343	0.2663	72.2
Ag54	plate	11/01	1.8859	0.2019	54.9
Ag55	plate	11/01	1.8806	0.1329	36.2

Table B-8. SiC-2 Diffusion Couple Fabrication Data.

ID	Silver Source	Silver Date	Shell Mass (gm)	Male Mass (gm)	M + Ag Mass (gm)	M + Ag + F (gm)	Ag Mass (gm)	Female Mass (gm)
			Sample Fabrication / Silver Data					
Ag34	none		1.4021					
Ag35	none		1.4101					
Ag37	powder	7/24/01	1.4107	0.7202	0.9732	1.6636	0.2530	0.6904
Ag38	powder	7/24/01	1.4106	0.7299	0.9844	1.6649	0.2545	0.6805
Ag39	powder	7/24/01	1.4103	0.7227	0.9752	1.6626	0.2525	0.6874
Ag40	powder	7/24/01	1.4122	0.7214	0.9744	1.6650	0.2530	0.6906
Ag50	powder	9/18/01	1.4154	0.7232	1.0095	1.7013	0.2863	0.6918
Ag51	powder	9/18/01	1.4144	0.7295	1.0147	1.6994	0.2852	0.6847
Ag52	powder	9/18/01	1.4035	0.7290	1.0126	1.6867	0.2836	0.6741
Ag53	powder	10/23/01	1.4081	0.7190	0.9790	1.6680	0.2600	0.6890
Ag54	powder	10/23/01	1.4136	0.7212	0.9917	1.6840	0.2705	0.6923
Ag55	powder	10/23/01	1.4177	0.7362	1.0662	1.7477	0.3300	0.6815

SIC-3

Table B-9. SiC-3 Diffusion Couple Annealing, Mass Loss, and Leak Testing Data.

	Anneal				Mass Loss					Leak Testing	
ID	Temp (°C)	Time (hr)	Start Date	End Date	Initial Ag Mass (gm)	Mass before anneal (gm)	Mass after anneal (gm)	dM Total (gm)	dM / initial Ag mass	pre (atm.cc /sec)	post (atm.cc /sec)
S09					0.5153					8.0E-05	
S10	1500	300	7/18/02	7/31/02	0.5072	3.4318	3.4296	0.0022	0.0043	8.0E-07	6.0E-06
	1500	725	8/23/02	9/22/02	0.5072	3.4295	3.4301	-0.0006	-0.0012		5.0E-06
	1500	1025			0.5072	3.4318	3.4301	0.0017	0.0034	8.0E-07	5.0E-06
S11	1500	300	7/18/02	7/31/02	0.5019	3.3225	3.3202	0.0023	0.0046	5.0E-07	5.0E-06
	1500	725	8/23/02	9/22/02	0.5019	3.3203	3.3188	0.0015	0.0030		5.0E-06
	1500	1025			0.5019	3.3225	3.3188	0.0037	0.0074	5.0E-07	5.0E-06
S12	1350	500	7/18/02	8/8/02	0.5024	3.4130	3.4123	0.0007	0.0014	7.0E-07	3.0E-06
	1350	1000	9/24/02	11/5/02	0.5024	3.4121	3.4114	0.0007	0.0014		3.0E-06
	1350	1500			0.5024	3.4130	3.4114	0.0016	0.0032	7.0E-07	3.0E-06
S13	1350	500	7/18/02	8/8/02	0.5064	3.4841	3.4833	0.0008	0.0016	7.0E-07	3.0E-06
	1350	1000	9/24/02	11/5/02	0.5064	3.4831	3.4824	0.0007	0.0014		3.0E-06
	1350	1500			0.5064	3.4841	3.4824	0.0017	0.0034	7.0E-07	3.0E-06
S22	1500	75	4/22/02	4/25/02	0.5007	3.3326	3.3313	0.0013	0.0026	6.5E-07	4.0E-06
	1500	425	6/26/02	7/15/02	0.5007	3.3314	3.3298	0.0016	0.0032		8.0E-06
	1500	500			0.5007	3.3326	3.3298	0.0028	0.0056	6.5E-07	8.0E-06

Table B-10. SiC-3 Diffusion Couple SiC Coating and Fabrication Data.

	SiC Coating					Sample Fabrication / Silver Data					
ID	SiC Coating Date	Total Coated Mass (gm)	SiC Mass (gm)	SiC thick (µm)	Silver Date	Male Shell Mass (gm)	Male + Ag Mass (gm)	Male + Ag + Female (gm)	Ag Mass (gm)	Female Mass (gm)	+ SiC in seam (gm)
S09	7/1/02	3.3911	0.3345	90.5	6/7/02	1.3264	1.8417	3.0566	0.5153	1.2149	3.0614
S10	6/14/02	3.2370	0.2106	57.2	6/13/02	1.3324	1.8396	3.0264	0.5072	1.1868	3.0289
S11	6/14/02	3.1231	0.2302	62.5	6/13/02	1.3182	1.8201	2.8929	0.5019	1.0728	2.8962
S12	6/14/02	3.2126	0.2126	57.7	6/13/02	1.3567	1.8591	3.0000	0.5024	1.1409	3.0033
S13	6/14/02	3.2815	0.2013	54.7	6/13/02	1.3393	1.8457	3.0802	0.5064	1.2345	3.0849
S22	4/2/02	3.3326	0.2322	63.0	3/28/02	1.3321	1.8328	3.1004	0.5007	1.2676	

Table B-11. SiC-3 Diffusion Couple Additional SiC Coating Data.

ID	SiC Coating Date	Additional SiC Coating Data				
		Total Coated Mass (gm)	Previous Coated Mass (gm)	added SiC Mass (gm)	added SiC thickness (μm)	total SiC thick (μm)
S09	7/2/02	3.6049	3.3911	0.2138	58.1	148.6
S10	6/17/02	3.4319	3.2370	0.1949	53.0	110.2
S11	6/17/02	3.3226	3.1231	0.1995	54.2	116.7
S12	6/17/02	3.4133	3.2126	0.2007	54.5	112.3
S13	6/17/02	3.4841	3.2815	0.2026	55.0	109.7
S22	n/a					

Filename: 8. Appendix B.doc
Directory: C:\Documents and Settings\talbhd\Desktop\FINAL INERI JAN3
Template: C:\Documents and Settings\talbhd\Application
    Data\Microsoft\Templates\Normal.dot
Title: Appendix B
Subject:
Author: test
Keywords:
Comments:
Creation Date: 12/20/2004 5:05:00 PM
Change Number: 12
Last Saved On: 1/6/2005 3:07:00 PM
Last Saved By: test
Total Editing Time: 10 Minutes
Last Printed On: 1/18/2005 11:08:00 AM
As of Last Complete Printing
    Number of Pages: 9
    Number of Words: 2,628 (approx.)
    Number of Characters: 13,405 (approx.)

APPENDIX C (MIT):
Vapor Flow Modeling

Flow Regimes

The Knudsen number is the ratio of the mean free path of a molecule to a characteristic dimension of the channel, usually the tube diameter, through which the gas is flowing. The Knudsen number describes the limits between molecular, intermediate, and laminar flow and is defined by (Varian Proceedings 1976):

$$Kn = \frac{\lambda}{d} \qquad\qquad \text{(C-1)}$$

where Kn =   Knudsen number,
           λ =   mean free path (m), and
           d =   channel diameter (m).

The Reynolds number is the ratio for inertial to viscous forces and is used, among other things, to establish the limit between turbulent and laminar flow. The Reynolds number is defined by the following equation (Roth 1976):

$$\text{Re} = \frac{\rho\, v\, d}{\eta} \qquad\qquad \text{(C-2)}$$

where Re =   Reynolds number,
           v =   velocity (cm/s),
           ρ =   gas density (g/cm^3),
           d =   channel diameter (cm), and
           η =   viscosity (poise).

For flow in a circular duct the transport is considered turbulent for Re > 2100 and laminar for Re < 1100. Table C-1 lists the different gas states, flow regimes, and applicable dimensionless number limits.

Table C-1. Conditions for the different flow regimes.

Gas State	Flow Regime	Condition
viscous	turbulent	Re > 2100
	laminar	Re < 1100 Kn < 0.01
transition	intermediate	0.01 < Kn < 1
rarefied	molecular	Kn > 1

In order to calculate the Knudsen number for a specified gas and flow channel, the mean free path of a molecule in the gas is required. For a gas governed by the ideal gas law, the mean free path of a molecule is given by (Mean Free Path 2004):

$$\lambda = \frac{R\,T}{\sqrt{2}\ \pi\ d^2\ N_A\ P}$$
(C-3)

where λ =   mean free path (m),
         R =   universal gas constant (8.314 J/mol-K),
         T =   absolute temperature (K),
         d =   molecular diameter (m),
         N_A =   Avogadro's number (6.02×10^{23} atoms/mol), and
         P =   pressure (Pa).

From the Smithsonian Physical Tables, the atomic radii for helium and silver are 0.93 and 1.44 Å, respectively (Knovel online databases 2004). Using these values, the mean free path of helium and silver can be calculated at any temperature and pressure. Then, for a given crack tube diameter, the Knudsen number can be calculated and the flow regime determined.

The flow equations for viscous, molecular, and transition flow are described in the following sections.

Viscous Flow

At moderate pressures the gas molecules undergo collisions primarily with other gas molecules rather than with the walls of the flow channel; gas viscosity limits flow. Turbulent flow is not usually experienced in leak flow and will not be considered here. For the viscous state, laminar flow is described as follows.

The conductance of a gas governed by laminar flow is (Alcatel Vacuum Technology):

$$C_{\text{laminar}} = \frac{\pi}{8}\left(\frac{d}{2}\right)^4 \frac{P_{avg}}{\eta\,L}$$
(C-4)

where C =   conductance (10^4 liter/sec),
         d =   crack diameter (m),
         P_{avg} =   average of the upstream and downstream pressures (Pa),
         η =   viscosity of the gas (poise), and
         L =   length of the crack tube (m).

To convert from conductance to mass loss, a value measured (or derived) from experiments, the time of the experiment and the molar volume are also needed. The molar volume is calculated from the ideal gas law and is given by:

$$v_{molar} = \frac{R\,T}{P}$$

(C-5)

where v_{molar} = molar volume (m³/mol),
  R = gas constant (8.314 J/mol·K),
  T = absolute temperature (K), and
  P = pressure (Pa).

The following equation converts conductance to mass loss:

$$Q_{\text{laminar}} = \frac{C_{\text{laminar}}\;t}{v_{molar}}\,aw$$

(C-6)

where $Q_{laminar}$ = mass loss (g),
  $C_{laminar}$ = laminar flow conductance (liter/sec),
  t = time (sec),
  v_{molar} = molar volume (m³/mol), and
  aw = atomic weight of the gas (g/mol).

Molecular Flow

At very low pressures, the mean free path of the gas molecules is much larger than the dimensions of the vacuum enclosure. Under these conditions, the gas molecules undergo collisions primarily with the walls of the flow channel rather than with other molecules; this is molecular flow. The conductance of a gas governed by molecular flow is defined as:

$$C_{molecular} = \frac{1}{6}\sqrt{\frac{2\,\pi\,R\,T}{aw}}\,\frac{d^3}{L}$$

(C-7)

where $C_{molecular}$ = conductance (liter/sec),
  R = gas constant (8.314 J/mol·K),
  T = absolute temperature (K),
  d = crack diameter (m),
  aw = atomic weight of the gas (107.87 g/mol for silver), and
  L =   length of the crack tube (assumed equal to the thickness) (m).

Using the molar volume as defined by equation (C-5), the mass loss over a specified time, t, due to molecular flow is given by:

$$Q_{molecular} = \frac{C_{molecular}\, t}{v_{molar}}\, aw$$

(C-8)

where $Q_{molecular}$ =   mass loss (g),
        $C_{molecular}$ =   laminar flow conductance (liter/sec),
        t =   time (sec),
        v_{molar} =   molar volume (m^3/mol), and
        aw =   atomic weight of the gas (g/mol).

The molecular flow equation attributed to Knudsen applies to pipes of circular cross-section. For pipes of equal cross-sectional areas, pipes with non-circular cross-sections will experience lower conduction than those with circular cross-sections.

Transitional Flow
Transitional flow occurs for gas states between laminar and molecular, where both phenomena contribute to the flow. The leak rate for transitional flow is a combination of both the laminar and molecular flow equations:

$$Q_{transition} = \frac{\pi}{8}\left(\frac{d}{2}\right)^4 \frac{P_{avg}}{\eta\, L}\left(P_1 - P_2\right) + \frac{\sqrt{2\,\pi}}{6}\sqrt{\frac{R\,T}{aw}}\,\frac{d^3}{L}\left(P_1 - P_2\right)$$

(C-9)

where $Q_{transition}$ =   leak rate (atm·cm^3/sec),
        d =   crack diameter (m),
        P_{avg} =   average pressure (Pa),
        P_1 =   upstream pressure (Pa),
        P_2 =   downstream pressure (Pa),
        η =   viscosity (poise),
        L =   length of the crack tube (assumed equal to the SiC thickness) (m),
        R =   gas constant (8.314 J/mol·K),
        T =   absolute temperature (K), and
        aw =   atomic weight of the gas (107.87 g/mol for silver).

Filename: 9. Appendix C.doc
Directory: C:\Documents and Settings\talbhd\Desktop\FINAL INERI JAN3
Template: C:\Documents and Settings\talbhd\Application
    Data\Microsoft\Templates\Normal.dot
Title: APPENDIX C
Subject:
Author: test
Keywords:
Comments:
Creation Date: 12/20/2004 5:08:00 PM
Change Number: 11
Last Saved On: 1/6/2005 2:48:00 PM
Last Saved By: test
Total Editing Time: 19 Minutes
Last Printed On: 1/18/2005 11:14:00 AM
As of Last Complete Printing
    Number of Pages: 4
    Number of Words: 945 (approx.)
    Number of Characters: 4,632 (approx.)

APPENDIX D (INEEL):
Project Milestone Summary

Table D-1. Project Milestone/ Deliverable Summary.

Milestone	Deliverable Description	Planned Completion Date	Actual Completion Date
1	Document results of the data exchange and the description of fuel particle models.	Oct 2002	Oct 2002
2	Document the first year modeling accomplishments	Oct 2002	Oct 2002
3	Document interim status of concept improvement, results to date on experiments to measure Ag and Pd diffusion through coating layers, and assessment of failure mechanisms of classical TRISO particles	Oct 2003	Oct 2003
4	Document final results of project including feasibility of extending the coated particle fuel concept to a fast spectrum, and outlining the types of irradiations needed to test prototype particles	Oct 2004	Oct 2003

Table D-2. Task Completion.

	Year 1	Year 2	Year 3
Task 1: Information Exchange	▨		
Task 2: Model Development	▨▨▨		
Task 3: Concept Improvements	▨▨▨▨▨▨		
Task 4: Feasibility of concept in hard spectrum		▨▨▨	
Task 5: Irradiation of prototype particles			▨

Filename: 10. Appendix D.doc
Directory: C:\Documents and Settings\talbhd\Desktop\FINAL INERI JAN3
Template: C:\Documents and Settings\talbhd\Application
     Data\Microsoft\Templates\Normal.dot
Title: APPENDIX D
Subject:
Author: test
Keywords:
Comments:
Creation Date: 1/6/2005 4:20:00 PM
Change Number: 4
Last Saved On: 1/11/2005 12:14:00 PM
Last Saved By: test
Total Editing Time: 2 Minutes
Last Printed On: 1/18/2005 11:15:00 AM
As of Last Complete Printing
     Number of Pages: 2
     Number of Words: 1,182 (approx.)
     Number of Characters: 6,620 (approx.)

REFERENCES:

1) ABAQUS User's Manual Version 5.8, 1998, Hibbitt, Karlsson, and Sorenson, Inc.

2) Alcatel Vacuum Technology (catalog), France.

3) Amian, W., D. Stöver, 1983, "Diffusion of Silver and Cesium in Silicon-Carbide Coatings of Fuel Particles for High-Temperature Gas-Cooled Reactors,"*Nucl. Tech*., Vol. 61, pp.475.

4) ATLAS Facility, Argonne National Laboratory, http://www.phy.anl.gov/atlas/fac-acc.html

5) Baldwin, C. A., et al., 1993, "The New Production Reactor Fuel Post Irradiation Examination Data Report for Capsules NPR1, NPR2, and NPR1A," ORNL/M-2849.

6) Barin, I., Knacke, O., Kubaschewski, O., *Thermochemical Properties of Inorganic Substances: Supplement*, New York: Springer-Verlag, 1977.

7) Bird, R.B., Stewart, W.E., Lightfoot, E.N., "Transport Pheonomena," John Wiley and Sons, 1960.

8) Bisquert, J. and Bikhrenko, V.S., "Analysis of the Kinetics of Ion Intercalation. Two State Model Describing the Coupling of Solid State Ion Diffusion and Ion Binding Processes," Electrochimca Acta, Vol. 47, p. 3977-3988, 2002.

9) Booth, A. H., "A Method of Calculating Fission Gas Release from UO2 Fuel and Its Implication to the X-2-f Loop Test," Atomic Energy of Canada Limited Report – 496, 1957.

10) Braun, C., et al., "Mesure de la Permeabilite aux Gaz des Revetements de Pyrocarbone Isotrope," Journal of Nuclear Materials, Vol. 89, p. 136-142, 1980.

11) Briesmeister, J.F., "MCNP – A General Monte Carlo N-Particle Transport Code, Version 4B," LA-12625-M, Version 4B, Los Alamos National Laboratory, March 1997.

12) Brown, P.E., R.L. Faircloth, 1976, "Metal Fission Product Behaviour in High Temperature Reactors – UO_2 Coated Particle Fuel," *J. Nucl. Mater,* Vol. 59, pp**.** 29-41.

13) Bullock, R.E., "Fission-Product Release During Postirradiation Annealing of Several Types of Coated Fuel Particles," *J. Nucl. Mat.* **125** (1984) 304-319.

14) Carter, Jr., C. H., Davis, R.F., Bentley, J., "Kinetics and Mechanisms of High-Temperature Creep in Silicon Carbide: II, Chemically Vapor Deposited," *J. Am. Ceram. Soc.* **67** (1984) 732-740.

15) CEGA Corporation, 1993, "NP-MHTGR Material Models of Pyrocarbon and Pyrolytic Silicon Carbide," CEGA-002820, Rev. 1.

16) CoorsTek Advanced Silicon Carbides, 2003, C0301 8510-1024 Rev.B. (personal communication with Tom Sibley) www.coorstek.com.

17) Crank, J., 1956, *Mathematics of Diffusion*, New York, NY: Oxford University Press.

18) Department of Defense Test Method Standard, Microcircuits, MIL-STD-883E, December 31, 1996.

19) Förthmann, R. et al., 1982, "Irradiation Performance of Coated Fuel Particles with Fission Product Retaining Kernel Additives,"*High Temp. High Press.* Vol.14**,** pp.477-485.

20) Förthmann, R. et al., "Influence of Material Properties on the Retention of Fission Products by Silicon Carbide Coatings," *High Temp.-High Press.* 14 (1982) 477.

21) Fusamae, H. et al., "Evaluation of Grain-Boundary Groove Profiles and Surface Diffusion Coefficients in SiC Ceramics Using Atomic Force Microscopy," Ceramic Transactions, Vol. 71, 1996, p. 463- 472.

22) Ghoshtagore, R.N., "Decomposition of Single Crystal Silicon Carbide", Solid State Electron., 9, 1966, pp. 178-180.

23) Gontard, R., and Nabielek, H., "Performance Evaluation of Modern HTR TRISO Fuels," HTA-IB-5/90.

24) Heera, V. et al., "Evidence for Diffusion-Limited Kinetics of Ion-Beam-Induced Epitaxial Crystallization in Silicon," *Phys. Rev. B* **52** (1995) 776.

25) Ho, F., *Material Models of Pyrocarbon and Pyrolitic Silicon Carbide*, CEGA-002820, Rev. 1, General Atomics, July 1993.

26) Hofman GL, Hayes SL, Petri MC1996 "Temperature gradient driven constituent redistribution in U-Zr alloys," Journal Of Nuclear Materials 227 (3): 277-286 Jan. 1996.

27) Hollerman et al., "An Infrared Study on CO Intercalated in Solid C60," J. Chem. Physics, Vol. 110, No. 4, Jan. 1999.

28) IAEA, "Fuel Performance and Fission Product Behaviour in Gas Cooled Reactors," IAEA-TECDOC-978, November 1997.

29) INEEL, 2002, "Modular Pebble Reactor LDRD Annual Report 2002", in preparation.

30) Kaae, J., D. Stevens, and C. Luby, 1971, "Predictions of the Irradiation Performance of Coated Particle Fuels by Means of Stress Analysis Models," *Nucl. Tech*., Vol. 10, pp. 44.

31) Ketterer, J.W. and Myers, B.F., "Capsule HRB-16 Postirradiation Examination Report", HTGR-85-053, GA-908012 N/c, September 1985.

32) Lauf, R.J., Lindemer, T.B., and Pearson, R.L., "Out-of-Reactor Studies of Fission Product – Silicon Carbide Interactions in HTGR Fuel Particles", J. Nuc. Mater. 120, 1984, pp. 6-30.

33) Lide, D., *CRC Handbook of Chemistry and Physics*, 71st ed., Boca Raton: CRC Press, 1990.

34) Littmark, U. and Ziegler, J.F., "Handbook of Range Distributions for Energetic Ions in All Elements," Pergamon Press, 1980.

35) Kast, W. and Hohenthanner, C.R., "Mass Transfer with the Gas-Phase of Porous Media," International Journal of Heat and Mass Transfer, Vol. 43, p. 807-823, 2000.

36) Ketterer, J.W. et al., *Capsule HRB-15A Postirradiation Examination Report*, GA-A16758, July 1984.

37) Ketterer, J.W., and Bullock, R. E., *Capsule HRB-15B Postirradiation Examination Report*, GA-A15940, June 1981.

38) Kleykamp, Heiko 2001, "Phase equilibria in the UO_2–PuO_2 system under a temperature gradient," Journal of Nuclear Materials ; April, 2001; vol. 294, no. 1-2, pp. 8-12.

39) Knovel online databases: Smithsonian Physical Tables.

40) Korte, C.; Janek, J.; Timm, H. 1997, Transport processes in temperature gradients: Thermal diffusion and Soret effect in crystalline solids. Solid State Ionics ; November, 1997; vol.101-103, no., pp. 465-470.

41) Levi, M.D., and Aurbach, D., "Frumkin Intercalation Isotherm- a Tool for the Description of Lithium Insertion into Host Materials: A Review," Electrochemica Acta, Vol. 45, p. 167-185, 1999.

42) Littmark, U. and Ziegler, J.F., "Handbook of Range Distributions for Energetic Ions in All Elements," Pergamon Press, 1980.

43) Longhurst, G.R., et al., "TMAP4 User's Manual," EGG-FSP-10315, May 1998.

44) McCardell, R.K. et al., *NP-MHTGR Fuel Development Program Plan*, Idaho National Engineering and Environmental Laboratory EGG-NPR-8971, Rev. C., September 1992, Appendix A.

45) McFarlane J. et al., "Chemical Speciation of Iodine Source Term to Containment," *Nucl. Tech.* **138** (2002) 162-178.

46) Maki, J.T., et al., "NP-MHTGR Fuel Development Program Results", INEEL/EXT-2002-1268, October 2002.

47) Martin, R.C., "Compilation of Fuel Performance and Fission Product Transport Models and Database for MHTGR Design", ORNL /NPR-91/6, October 1993.

48) Martin, D. G., 2001, "Physical and Mechanical Properties of the Constituents of Coated Fuel Particles and the Effect of Irradiation," HTR-F WP3 Meeting Lyon.

49) Mason, E.A., and Malinaukas,A.P., "Gas Transport in Porous Media: The Dusty Gas Model," Elsevier, Amsterdam, 1983.

50) Mathur, R.B. et al., "In-Situ Electrical Resistivity Changes During Bromine Intercalation in Carbon Fibers," Carbon, Vol. 34, No. 10, pp. 1215-1220, 1996.

51) Mean Free Path, Molecular Collisions, http://hyperphysics.phyastr.gsu.edu/hbase/kinetic/menfre.html

52) Miller, G. K. and R. G. Bennett, 1993, "Analytical Solution for Stresses in TRISO-coated Particles," *J. Nucl. Mat.*, Vol. 206, p. 35.

53) Miller, G. K., et al., 2001, "Consideration of the Effects on Fuel Particle Behavior from Shrinkage Cracks in the Inner Pyrocarbon Layer," *J. Nucl. Mat*., Vol. 295, pp. 205.

54) Miller, G. K., Petti, D.A., Maki, J. T., 2002, "Development of an Integrated Performance Model for TRISO-Coated Gas Reactor Particle Fuel," 1st International Topical Meeting on High Temperature Reactor Technology (HTR), Petten, Netherlands.

55) Miller, G. K., Idaho National Engineering and Environmental Laboratory, Stress Analysis for the Thermal Cycling of a Spherical Diffusion Couple, personal communication, June 2003.

56) Minato, K. et al., "Fission Product Palladium – Silicon Carbide Interaction in HTGR Fuel Particles", J. Nuc. Mater. 172, 1990, pp. 184-196.

57) Minato, K. et al., HRB-22 Capsule Irradiation Test for HTGR Fuel (JAERI/USDOE Collaborative Irradiation Test), JAERI-Research 98-021, March 1998.

58) Mishini, Y. and Herzig, C., "Grain Boundary Diffusion: Recent Progress and Future Research," Materials Science and Engineering, A260, P. 55-71, 1999.

59) Montgomery, F., "Fission – Product SiC Reaction in HTGR Fuel", GA-905837/1, July 1981.

60) Morgan, M. T., and Malinauskas, A.P., "Cesium Release and Transport in BISO-coated Fuel Particles," Nuclear Technology, Vol. 35, September 1977, p. 457-464.

61) Nabielek, H., e-mail communication, November 13, 2002, discusses unpublished document: H. Nabielek, "Partikeln und Brennelemente für den HTR", KFA-HTA, January 24, 1991.

62) Nabielek, H., *The Mechanism of Silver Retention in Coated Particle Fuel*, Dragon Project Technical Report DTN/801, April 1976.

63) Nabielek, H., P.E. Brown, P, Offerman, 1977, "Silver Release from Coated Particle Fuel,"*Nucl.Tech.*Vol. 35, pp. 483.

64) Nemeth, N.N., Mandershield, J.M., Gyekenyesi, J.P., 1989, Ceramics Analysis and Reliability Evaluation of Structures (CARES) User's and Programmer's Manual, NASA Technical Paper 2916.

65) Offermann, P., "Ag-Diffusion in PyC," *J. Nucl. Mater.* **64** (1977) 249.Olander, D.R., "Fundamental Aspects of Nuclear Reactor Fuel Elements", ERDA, TID-26711-P1, 1976.

66) Olander, D.R., "Fundamental Aspects of Nuclear Reactor Fuel Elements," NTIS, Springfield, VA, 1976.

67) Ougouag, A.M., Wemple, C.A., and Petti, D.A., "Displacement Kerma Cross Sections for Neutron Interactions in Gas-Cooled Reactor Materials," GLOBAL 2003, November 2003.

68) Pacaud, Y. et al., "Radiation damage and annealing behvaiour of Ge+-implanted SiC," *Nucl. Instr. Meth. B* **120** (1996) 177-180.

69) Palnichenko and Tanuma, S.I., "Effect of Intercalation of Alkali and Halogen Species into the Low Density Carbon Crystal 'Carbolite'", J. Phys. Chem. Solids, Vol. 57, No. 6-8, pp. 1163-1166, 1996.

70) Pearson, R.L., Lindemer, T.B., Beahm, E.C., Simulated Fission Product-SiC Interaction in Triso-Coated LEU or MEU HTGR Fuel Particles, ORNL/TM-6991, November 1980.

71) Pearson, R.L., Lauf, R.J., Lindemer, T.B., The Interaction of Palladium, the Rare Earths, and Silver with Silicon Carbide in HTGR Fuel Particles, ORNL/TM-8059, April 1982.

72) Petti, D.A. et al., "Development of Improved Models and Design of Coated Particle Gas Reactor Fuels: Annual Program Report Under the International Nuclear Energy Research Initiative (I-NERI)," INEEL/EXT-02-0493, Nov. 2002.

73) Petti, D. A., et al., 2001, "Gas Reactor TRISO-Coated Particle Fuel Modeling Activities at the Idaho National Engineering and Environmental Laboratory," *The Second Information Exchange Meeting on Basic Studies in the Field of High Temperature Engineering*, *Paris, France.*

74) Petti, D.A., et al., "Key differences in the fabrication, irradiation and high temperature accident testing of US and German TRISO-coated particle fuel, and their implications on fuel performance," Nuclear Engineering and Design, Vol. 222, p. 281-297, 2003.

75) Petti, D.A., Editor, "Modular Pebble-Bed Reactor Project, Laboratory-Directed Research and Development Program FY 2002 Annual Report", INEEL/EXT-02-01545, November 2002.

76) Price, R.J., "Properties of Silicon Carbide for Nuclear Fuel Particle Coatings", Nuc. Tech. 35, September 1977, pp. 320-336.

77) Projektleitung Hochtemperaturreaktor-Brennstoffkreislauf (HBK), "Projektbericht 1984", 1984.

78) Reid, R.C., Prausnitz, J.M. and Poling, B.E. "The Properties of Gases and Liquids", Fourth Ed., McGraw-Hill, 1987.

79) Röllig, K., "Release of Noble Gases and Halogens from the PBMR Core", Westinghouse Reaktor GmbH, GBRA 052 336, 2001.

80) Roth, A., Vacuum Technology, North-Holland Publishing Company, New York, 1976.

81) Saurwein, J. "Fuel Temperatures in AGR-1", e-mail note to David Petti, May 25, 2004.

82) Schenk, W., Pitzer, D., Nabielek, H., "Fission Product Release Profiles from Spherical HTR Fuel Elements at Accident Temperatures," Jül-2234, September 1988.

83) Schenk, W., and Nabielek,H., "High-Temperature Reactor Fuel Fission Product Release and Distribution at 1600 to 1800°C," *Nucl. Tech.* **96** (1991) 323.

84) Takano, K. et al., "Volume and Dislocation Diffusion of Iron, Chromium, and Cobalt," in CVD beta-SiC," Science and Technology of Advanced Materials, Vol. 2 No. 2 June 2001, p. 381-388.

85) Technical Program Plan for the Advanced Gas Reactor Fuel Development and Qualification Program, ORNL/TM-2002/262, April 2003.

86) Terry, W.K. (ed.), "Modular Pebble-Bed Reactor Project," Laboratory Directed Research and Development Program FY-2001 Annual Report, INEEL/EXT-2001-623, December 2001.Fuel Performance and Fission Product Behaviour in Gas Cooled Reactors, IAEA TECDOC-978, Nov. 1997.

87) Terry, W. K., (ed.), "Modular Pebble-Bed Reactor Project," Laboratory Directed Research and Development Program FY-2001 Annual Report, INEEL/EXT-2001-623, December 2001.

88) Tiegs,T.N., "Fission Product Pd-SiC Interaction in Irradiated Coated – Particle Fuels", Nuc. Tech. 57, June 1982, pp. 389-398.

89) Turnbull, J.A., et al., "The Diffusion Coefficient of Gaseous and Volatile Species During the Irradiation of Uranium Dioxide," Journal of Nuclear Materials, Vol. 107, No. 168, 1982.

90) Varian Proceedings, Leak Detection Seminar/Workshop. June 2-4, 1976.

91) Verfondern, K., Martin, R.C., and Moormann, R., Methods and Data for HTGR Fuel Performance and Radionuclide Release Modeling during Normal Operation and Accidents for Safety Analysis, Jül-2721, Forschungszentrum Jülich GmbH, January 1993.

92) Wang, X. R. et al., "Apparent Anomalous Prefactor Enhancements for Surface Diffusion due to Surface Defects," Surface Science, Vol. 512, p. L361-L366, 2002.

93) Webb, R. D Company Red Devil Furnace, http://www.rdwebb.com/.

94) Webb, R.D., Personal communication with R.D. Webb.

95) Wendler, E., Heft, A., Wesch, W., "Ion-Induced Damage and Annealing Behavior in SiC," *Nucl. Instr. Meth. B* **141** (1998) 105-117.

96) Whitcomb, P., et al., 1993, *Design Expert*, Version 4.0, Stat-Ease Inc.

97) Ziegler, J.F., Biersack, J.P., The Stopping and Range of Ions in Matter (SRIM), www.SRIM.org, Copyright 2003.

98) Zhu, J. et al., "Microstructure Dependence of Diffusional Transport," Computational Materials Science, Vol. 20, p. 37-47, 2001.

Filename: 11. References.doc
Directory: C:\Documents and Settings\talbhd\Desktop\FINAL INERI
     JAN3
Template: C:\Documents and Settings\talbhd\Application
     Data\Microsoft\Templates\Normal.dot
Title: REFERENCES:
Subject:
Author: test
Keywords:
Comments:
Creation Date: 1/6/2005 12:23:00 PM
Change Number: 2
Last Saved On: 1/6/2005 12:23:00 PM
Last Saved By: test
Total Editing Time: 3 Minutes
Last Printed On: 1/18/2005 11:15:00 AM
As of Last Complete Printing
     Number of Pages: 6
     Number of Words: 1,984 (approx.)
     Number of Characters: 11,990 (approx.)